Study on Nip Contact Mechanics and Mold Extraction for Predicting Defects in Roll-to-Roll UV Nanoimprint Lithography

By

XIN CHEN

Bachelor of Science in Mechanical Engineering
Wuhan University of Technology
Wuhan, China
2013

Master of Science in Mechanical Engineering
Northeastern University
Shenyang, China
2017

Submitted to the Faculty of the
Graduate College of the
Oklahoma State University
in partial fulfillment of
the requirements for
the Degree of
DOCTOR OF PHILOSOPHY
December, 2020

A Simulation Study on Nip Contact Mechanics and Extraction for Predicting Defects in Roll-to-roll UV Nanoimprint Lithography

Dissertation Approved:

Dr. James Keith Good

Dissertation Adviser

Dr. Shuodao Wang

Dr. Aurelie Azoug

Dr. Robert Emerson

.

ACKNOWLEDGEMENTS

Throughout the writing of this dissertation, I have received a great deal of support and assistance.

I would first like to thank my advisor, Dr. James Keith Good, whose expertise was invaluable in formulating the research questions and methodology. Your insightful feedback pushed me to edge my thinking and brought my work to a higher level.

I would like to thank my committee chair, Dr. Shuodao Wang, for his valuable guidance throughout my studies. I would also like to thank Dr. Aurelie Azoug for her precious advice on the characterizations of the resin material. You provided me with the tools that I needed to choose the right direction and successfully complete my dissertation. I would like to thanks Dr. Robert Emerson for his discerning suggestions.

I would also like to thanks to J.W. Wallace, Manogna Jambhapuram, Yuan Zhang, Ron Markum, and Dr. Don A. Lucca for their contribution of characterization of the material.

In addition, I would like to thank my parents for their wise counsel and sympathetic ear. You are always there for me.

Name: Xin Chen

Date of Degree: DECEMBER, 2020

Title of Study: A Simulation Study on Nip Contact Mechanics and Extraction for Predicting Defects in Roll-to-roll UV Nanoimprint Lithography

Major Field: Mechanical Engineering

Abstract: Nano-scale or micro-scale structured surfaces have been proven fundamental for high-performance microelectronics. With the development of the microelectronics market, there is an increasing demand for higher-performance, smaller size, energy saving products. Roll-to-roll nanoimprint lithography (R2R UV NIL) provides possibilities for mass production of nanoimprinted surfaces. In the process line, the coated web passes one or more nip sets which are formed by a rigid roller and a rubber roller. The nip mechanics have proven that the nip contact would induce an increase in the web tension, which was called nip-induced tension (NIT). Under some conditions, this increase of web tension causes slippage between the imprint roller and the resin which distort or destroy the nanofeatures. Additionally, successful extraction of imprints from molds on imprint rollers is also an important facet of the R2R UV NIL process. Nanofeatures that fracture during the extraction leave an imperfection in the imprinted surface and the residual may cause an imperfection that repeats with each revolution of the imprint roller. Internal stresses within the imprinted features increase and can exceed the strength of the cured resin which would result in fracture of the feature and an imperfection in the imprinted surface. The objective of this research is to develop simulation tools that can predict whether defect-free nanofeatures will be produced or not. This will enable UV NIL manufacturing to move from a trial-and-error approach to a predictive mode where defect-free processes can be determined prior to moving to the manufacturing industry. Manufacturers of UV resins typically will provide their estimates of shrinkage, tensile strength and modulus properties for their resin. The simulation tools include a macro-scale and a nano-scale numerical models. The first model is developed to predict the slippage in the whole pattern of the R2R NIL processes, while the second one is established to predict the quality of the extraction process. Most of the properties needed for simulations of the UV curable resin system employed in the current project are unknown prior to this work. Methods for characterizing the properties of the UV resin will either be developed or adopted from standards.

TABLE OF CONTENTS

Chapter Page

Chapter Page

Chapter Page

LIST OF TABLES

Table Page

LIST OF FIGURES

Figure Page

Figure Page

Figure Page

Figure Page

Figure Page

Figure Page

Figure Page

Figure Page

Figure Page

Figure Page

CHAPTER I

I. Introduction

Nano-scale or micro-scale structured surfaces have been proven fundamental for high-performance microelectronics[1]. With the development of the microelectronic market, there is an increasing demand for higher-performance, smaller size, energy-saving products. The application of nanostructures is not only beneficial in microelectronics, but has spread into many other fields including biology[2], organic electronics[3], chemistry, medicine, and optical communications[4]. Therefore, the ability to fabricate nanostructures with high accuracy in a wide range of materials is of significance for advancing nanotechnology and nano-science. Due to the huge demand for nanostructured products in many fields, developing a low-cost mass production method has a high priority. In contrast to traditional scanning electron beam lithography, X-ray lithography, a low cost method was first developed in 1995 by Chou[5]. This method is known as nanoimprint lithography (NIL). The NIL can be classified into thermal nanoimprint lithography (T-NIL), and ultraviolet nanoimprint lithography (UV-NIL) by the material used for imprinting nanostructures. The schematic diagram of processes for T-NIL and UV-NIL is shown in Fig. I-1. Compared to T-NIL, UV-NIL has many advantages, such as low imprinting pressure required, no temperature cycle required, and fast fabrication speed. However, with the recent development of nanotechnology, the discrete UV-NIL method cannot satisfy the demand for nanostructured products. Additionally, higher output means lower cost, which is a

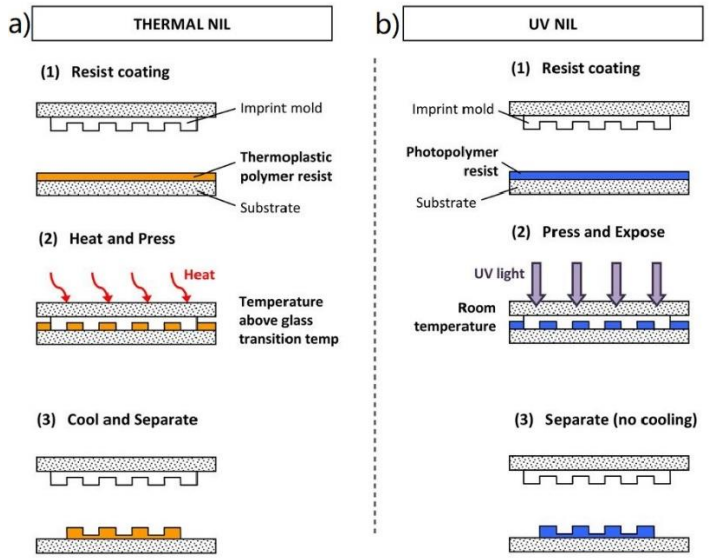

Fig. I-1(a) Schematic of thermal nanoimprint lithography (b) Schematic of UV nanoimprint lithography[6]

consideration for both industry and academic institutions. The discrete stamping fabricating method has limitations to produce nanostructured surfaces. To solve these limitations, a continuous roll-to-roll nanoimprint lithography (R2R NIL) method is in development. This manufacturing method enables imprinting on flexible substrates while drastically increasing the production of nanostructures. This boosts the nanoimprint lithography to an entirely new level, increasing the manufacturing speed at least a hundred times[7]. At the beginning of R2R NIL, the fabrication speed was limited to around 1m/min due to a limited understanding of the whole continuous manufacturing process and the low-curing-rate UV curable resist material. With the development of imprinting materials (UV curable resist), UV light source exposure, mold fabrication, and web transportation, a higher speed of continuous manufacturing is achieved, which leads to higher output and lower cost of the nanostructured products.

The continuous R2R UV NIL process consists of resist mold filling, UV exposure, and releasing or peeling from the mold. A schematic of the R2R UV NIL process is shown in Fig. I-2. Resist mold filling step is fundamental for the successful transfer of the nanofeatures onto the flexible substrate.

To obtain high-quality nanopatterns on the substrate, a backup roller is introduced to provide imprinting pressure for resist filling into the cavities of the mold. The backup roller is pressed to the imprint roller, forming a nip contact zone. Thus, in this document, the backup roller will be referred to as the nip roller. The nip roller not only provides pressure for resist filling but also has several other functions. First, the nip roller induces or prevents slippage between the imprint roller and the flexible substrate, which prevents the destruction of the nanopattern replications. Second, the high-speed winding web causes air entrainment between the web and the imprint roller, which hinders the resist filling into the cavity and causes air bubble defects in the nanostructures. Moreover, the nip roller provides uniform pressure in the traverse direction of the imprint roller, which assures the quality of nanopattern replications across the width of the imprint roller. In the nip contact zone, the low viscosity resist in the liquid state, which combined with the nip pressure, serves to fill the mold cavities. Fluid dynamics has been utilized to analyze the mold filling time[8]. Due to the duplication of the nanostructures, the analysis focused on the filling of one mold feature. The mold filling time is found to be determined by the resist viscosity, the pressure provided by the nip roller, and the geometry of the cavity on the imprinting mold. The mold filling time can be a key to determine the web velocity, which directly affects the production and cost of the nanostructured products.

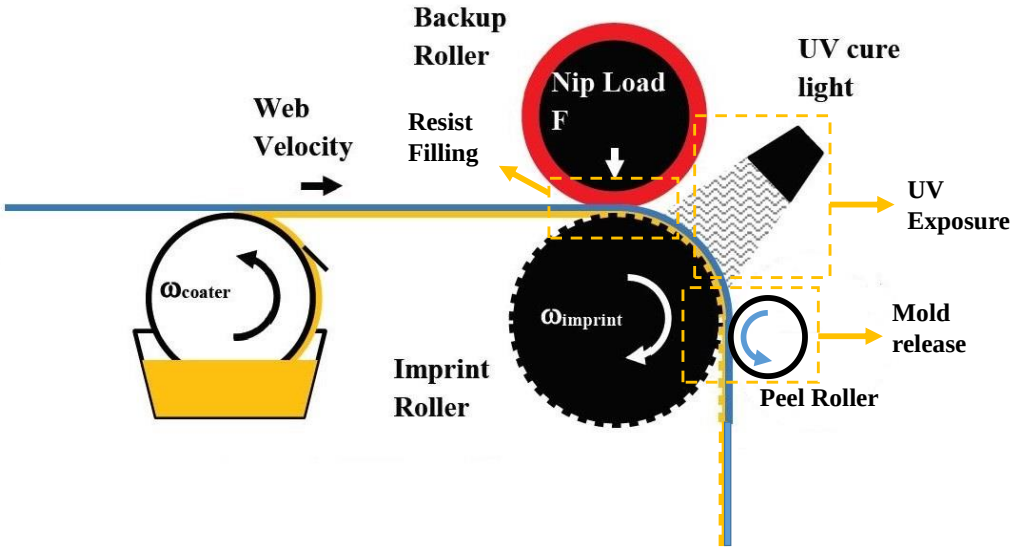

Fig. I-2 Schematic of R2R UV NIL process

Defects can be the result of inadequate mold filling or inadequate curing prior to slippage or peeling. Slippage is common with impinged rubber covered rollers such as the backup and peel rollers in Fig. I-2. The impinged rubber will have a contact surface velocity higher than that of the imprint roller surface and the potential for inducing slip. The pressure provided by the nip roller is one of the parameters which determine the resist filling time. Additionally, the reasons mentioned above explained the importance of the nip roller. Studies pertaining to the science of contact mechanics in the nip contact zone is involved in this report. Many works have been done for the nip mechanics in the nip contact zone since 1966[9]. The nip mechanics have proven that the nip contact would induce an increase in the web tension, which was called nip-induced tension (NIT). The slippage between curing or cured resist should be avoided because it destroys the nanofeatures built on the flexible substrate. The nip is capable of inducing slippage between the resist and the imprint roller, which must be avoided Therefore, a nip roller is required to fill the mold but is also a potential source of defects due to induced change in the web tension and slippage. As a nip roller is required for several reasons in the R2R UV NIL process, it is necessary to deal with the nip-induced tension in the flexible substrate to obtain high-quality nanopatterns. The increase of the web tension induced by NIT can be reduced or eliminated by adjusting the exit tension in the web. To find out if this method can eliminate the slippage, dynamic numerical simulations are developed in several different situations.

The UV curable resist curing process can be separated into stages, such as induction, vitrification, gelation, and post cured[10]. At the induction stage, the photoinitiators are activated by the radiation of the UV light. The reaction rate of polymerization is accelerating. A criterion to determine the vitrification onset is the deceleration of the polymerization rate. After the vitrification, the reaction goes into a diffusion- controlled stage, where $G' = G''$. The resist is in a gel state. For the cationic resist, the reaction keeps going on after the gelation, which is called the “post cured” stage. The first three stages are happening quite faster than the post-cured stage. Moreover, the mechanical properties

of curing resist are changing as a function of exposure of UV light in the first three stages. The varying modulus affects the shear stresses produced by tangential behavior between the resist and the imprint roller. The shear stress and strength of the resist have impacts on the success of nanopattern transfer. Demolding the cured or curing resist from the mold is another issue that causes failure of nanostructures fabrication. To achieve the high production objective, especially for high aspect ratio production, demolding must be reliable and repeatable without any damage to the nanoimprints and the mold. Therefore, more attention must be paid to the demolding process. The demolding of the cross-linked nanostructured polyacrylate from a fluorine-based mold is not an easy job[11]. Two important phenomena of interaction between the UV curable resin and the mold make the demolding complicated. An increase of adhesive strength at the interface as well as the shrinkage due to cross-linking of polymerization occur simultaneously during the UV curing. Excessive UV curing causes the high shrinkage of the polyacrylate and increases the possibility of initiation of the cracks in the nanostructures. Insufficient curing leads to low shear strength which is tremendously important for the cured nanoimprints to maintain a high-fidelity quality. The UV curable resin used in the current project has a max shrinkage ratio of 2%[12], which is relatively low to other materials[13, 14]. The adhesive strength has also been studied vastly in the thermal NIL[11, 15-19]. Finding an optimal way to release the mold is also of importance to obtain high-quality outcome of nanostructured products. Simulations performed for roll-to-roll NIL has been studied little due to its recent development as well as the complexity by introducing the dynamic effect. When the interface between the mold and UV curable resin breaks apart, the friction behavior at the interface performs a role to affect the mechanic in the nanoimprints. Therefore, the demolding process of roll-to-roll NIL is a study combining the adhesive strength, shrinkage, as well as friction behavior at the interface. The defects that are witnessed result from the shearing and tensile stresses while in contact and during peeling from the imprint roller, as shown in Fig. I-3. The ability of the resin without failing depends on

strength of the resin which is dependent on the level of curing. Therefore, numerical models are developed to study the mechanism during the peeling and in contact with the imprint roller.

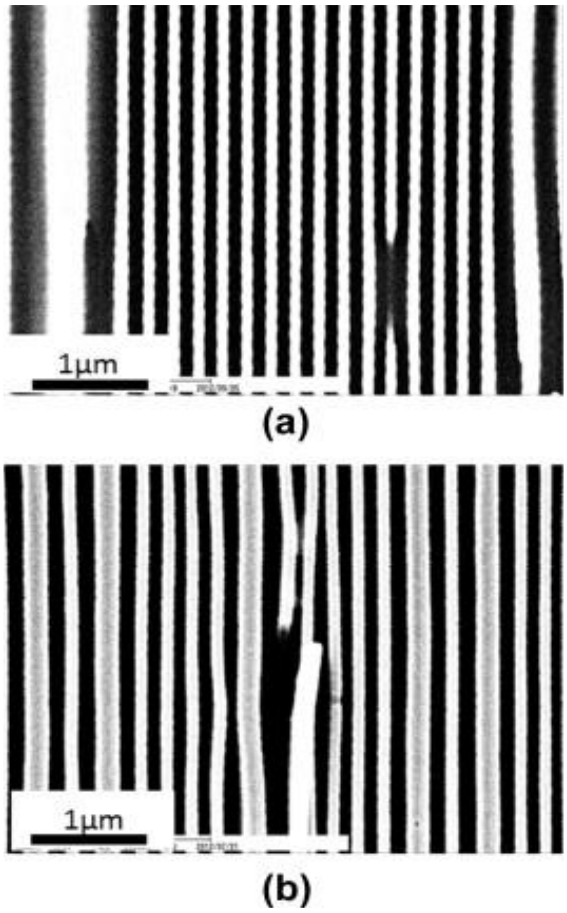

Fig. I-3 (a) and (b) peel defects by Scanning electron microscope (SEM)

To compute tearing failures, the modulus and tensile and shear strength and the shrinkage of the resin in addition to the adhesion toughness and friction at the interfaces between the resin and the mold must be known. The maximum principal stress criterion is used to determine if the nanoimprints are distorted or fall apart. The maximum principal stress is defined as the highest value of principal stress all over the nanoimprints through the history of the demolding in the numerical model. This maximum principal stress will then be compared to the ultimate tensile and shear strength of the resin which is also tested under various process speeds. In this paper, the UV curable resin we used in the

current project (funded by NSF) is UV15[1], an acrylate-based cationic epoxy. The mechanical properties mentioned above are varied by increasing the curing level. Additionally, the acrylate-based cationic epoxy UV curable system has a "dark-curing" effect[20, 21]. Once the polymerization started, the reaction continued until the cross-linking was done. However, the high process speed of production provides a relatively narrow time-span for the demolding process. The UV curable resin cannot reach its fully cured state when the demolding process starts. Therefore, the properties during the demolding are what we concerned. The tensile and shear strength, shrinkage, adhesion toughness, and friction for a consistent cure level for demolding are measured in this study. A numerical simulation model is established to analyze the stress distribution caused by shrinkage, adhesion as well as friction. If the maximum principal stress exceeds the ultimate strength, the demolding process can be considered unsuccessful due to the failure of some part of the nanoimprints. This comparison provides a quantitative way to estimate the success of demolding.

The focus of this research is to develop simulation tools that can predict whether defect-free production can be produced. The simulation tools include macro-scale and nano-scale in dimension. This will enable those who design imprinted surfaces based on geometric requirements to predict whether that surface can be commercially produced. This will enable UV-NIL manufacturing to move from a trial-and-error approach to a predictive mode where extraction success can be known prior to moving to the manufacturing environment. Manufacturers of UV resins typically will provide their estimates of shrinkage, full cured tensile strength, and modulus properties for their resin.

In this report, literature describing the whole R2R UV NIL process has been reviewed in chapter 2. A series of experiments for determining the mechanical properties including rheology, shear strength, friction and adhesive properties at the interface between the resin and the mold as a function of

[1] Master Bond Inc., 154 Hobart St, Hackensack, NJ 07601, USA

exposure dosage of UV light has been done in chapter 3. The results of the mechanical property tests are used for improving the accuracy of the simulation model. In chapter 4 and 5, the numerical models are used to analyze the mechanism during the nanoimprint lithography (NIL). To thoroughly study the whole process, micro-scale and nano-scale numerical models are established. In chapter 4, we have built a macro-scale model to simulate the continuous R2R UV NIL process. The simulations for different situations have been investigated to reduce or even eliminate slippage between the resist and imprint roller. In chapter 5, a nano-scale numerical model is established to analyze the stress distribution of the nanofeatures imprinted on the flexible substrate. Moreover, a series of preliminary trial tests for continuous R2R UV NIL have been done which will be shown in chapter 6. And a 20m/min manufacturing speed has been achieved. The parameters, such as nip pressure, downstream web tension, set for operation of R2R UV NIL will be optimized by the results of the simulations.

CHAPTER II

II. Literature Survey

The nanostructure patterning technology is fundamental for all high-performance microelectronics. The semiconductor industry and integrated circuits (ICs) industry has a great need for high-resolution nanostructured products. The application for nanostructure has also spread to many other fields, such as, biology[2, 22], organic electronic[3], chemistry, medicine[23], and optical communications[4]. 5G (5th generation of cellular mobile communications) targets at high data rate, reduced latency, cost efficiency and massive device connectivity. With the development of 5G, there will be a huge demand for microchips, organic electronic products, optical elements in light-emitting diodes (LED) and patterned media. Therefore, it is urgent to develop a low-cost high precision nanostructured patterning technology.

Nanoimprint lithography (NIL) is a promising method to massively produce surfaces with nanofeatures. It is a process method which uses a hard mold that contains nanostructures to emboss a thermoplastic material under certain temperature and pressure, thereby creating different thickness[24]. The schematic of nanoimprint lithography is shown in Fig. II-1(a). NIL was first published by Chou[5, 23, 25] in 1995. This method is also known as thermal-NIL (T-NIL). It is an attractive and widely researched field because it demonstrated ultrahigh

resolutions[26], and high reliability. However, the resist, a thermal plastic, would be deformed by embossing the mold with nanostructures on its surface during the imprint step. Therefore, the resist is required to be heated above its glass transition temperature to get low viscosity. Later, the mold will be removed, when the plastic is cooled down below glass transition temperature. An etching process is followed to remove the residual resist to complete pattern transfer[23]. The whole process of NIL is time-consuming due to the cycling of temperature. To build uniform patterns, maintaining pressure uniformly is required through the whole process. Avoiding stick and defect problems due to traditional contact printing is also required for successful demolding for the large-area imprint. Residual stresses will be produced associated with wide change of temperature during the imprinting.

In 1996, Haisma[27] from Philips Research Laboratories, first introduced Ultraviolet Nanoimprint Lithography (UV-NIL). The schematic of UV nanoimprint lithography is shown in Fig. II-1(b). They used UV curable resin which has a high curing rate, sufficiently low viscosity and good adhesive to the substrate. An essential addition in the UV curable resist as photoinitiator can absorb UV light and then initiate the photopolymerization process. The resist used in UV-NIL will be further discussed in the next subsection. Similar to T-NIL process, there are two steps for replication in UV NIL. A thin layer of UV curable material is spin coated on a silicon substrate due to the low viscosity of resin. Then a mold with the nanostructure is pressed on the thin resin layer while it is still in a liquid state. The resist is solidified under UV curing with exposure of UV light, followed by removing of the mold. An etching process is applied after removing the mold. The pattern transfer process is completed. Contrary to the T-NIL process, the mold is imprinting on a liquid layer of the resist in the UV-NIL process. The solidification of resist is a cross-linking reaction in a polymer instead of controlling phase change of a thermoplastic with temperature[28]. The UV-NIL process, thus, has several advantages to the T-NIL. First, while the T-NIL process requires to elevate the temperature, the UV-NIL process can

be conducted at room temperature, which helps to avoid the issues due to thermal expansion variations between the resist, the mold and the substrate [28-32]. Furthermore, imprinting on a low viscosity photoresist requires lower pressure conducted on the mold compared to T-NIL [33-38]. In addition, lower viscosity photoresist also has a better capability to fill the cavity of the mold in a shorter time. Additionally, elimination of temperature cycle can increase process output[34]. However, the sticking and defects produced by traditional contact printing cannot be avoided. Residual stress due to polymerization has appeared in nanostructures[39]. The UV-NIL process is also known as step and flash imprint lithography (SFIL). The process is also attractive to IC semiconductor industry, because it can be carried out at room temperature[40].

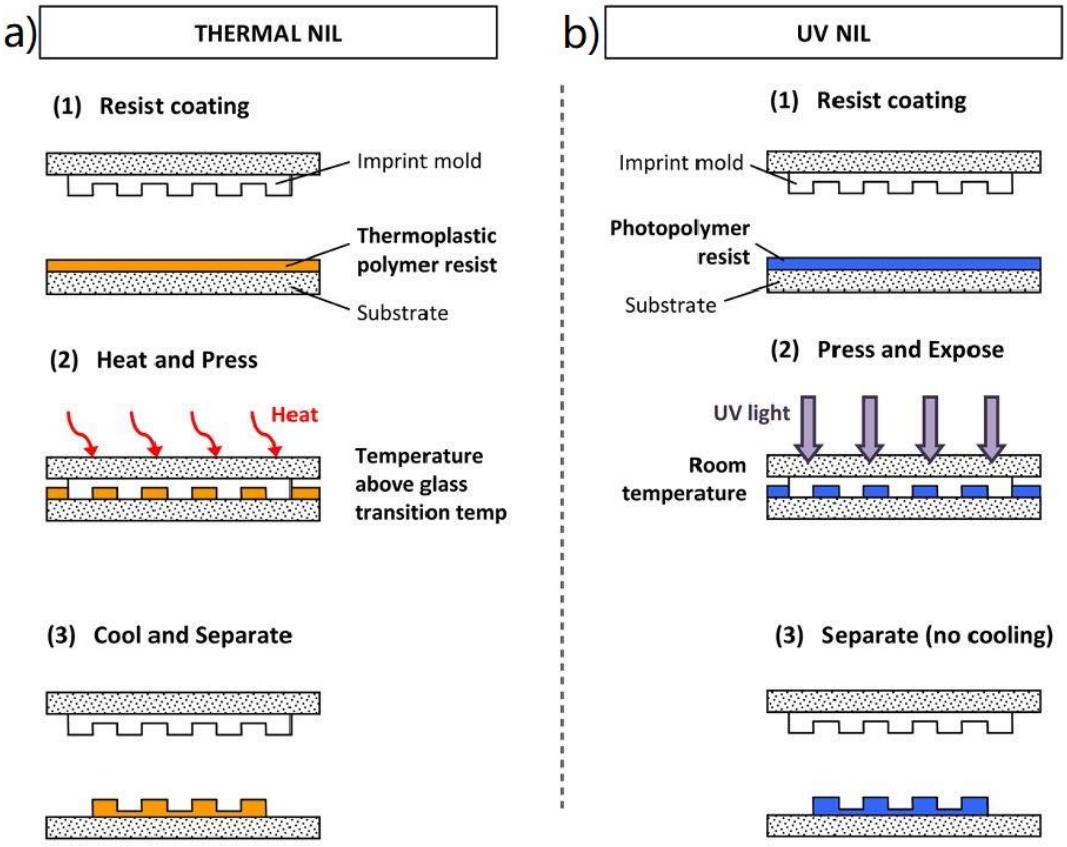

Fig. II-1 (a) Schematic of nanoimprint lithography (b) Schematic of UV nanoimprint lithography[6]

The T-NIL and UV-NIL methods discussed thus far have the same contact type. They both are plate to plate contact (P2P). To meet the requirement for high throughput and low cost, the imprint area needs to be large. The entire imprinting area is imprinted in a single imprint cycle. However, the imprint process typically requires large forces to provide uniform pressure for the entire imprint area, which may reach to 20kN for an 8-in wafer[41]. Air bubble entrapment problems have been reported in P2P NIL[41]. As the air in the gaps between the imprint mold cavity and the resist have no room to escape, it is trapped in the resist, resulting in defects on nanostructures. To avoid the air entrapment problem, some researchers observed that conducting the imprint process under vacuum can effectively prevent the trapping of air bubbles[36, 41]. However, it is hard to achieve vacuum or reduced air environment when applying a continuous nanoimprint on the web. Hiroshima and his team introduced a method to eliminate air bubbles by conducting the nanoimprint in a condensable gas ambient environment [42-45]. They eliminated the air bubble defects by using pentafluoropropane gas, which has a vapor pressure of 0.15 MPa at 25 Celsius degree. Increasing the gas pressure can effectively reduce the pressing time[46]. In 2016, Lai and his team from Shanghai Jiao Tong University thoroughly reported parameters which cause air bubble defects by both experiment and simulation[47, 48]. The temperature and the web speed play more important roles for air bubble defects. They also reported a method to produce bubble free products.

Chou's team[49] introduced roller nanoimprint lithography as an alternative method to plate to plate imprint in 1998. They reported two approaches for roller nanoimprint. One of them imprints using a cylinder mold, the other using a flat mold which is pressed by a rotating roller. The schematic of roller nanoimprint lithography is shown in Fig. II-2.The cylinder mold was made by a bended thin metal film mold on a roller. During the roller NIL, the cylinder mold is pressed into the resist and the rotation of roller will push the sample forward, shown in Fig. II-2 (a). The mold and imprint result are shown in Fig. II-2 (b). This method is able to replicate the mold pattern into

the PMMA resist continuously. The flat mold method uses a flat Si wafer mold of 0.5mm thickness placed directly on the substrate. A smooth roller is rotated over the mold, then the patterns on the flat mold is imprinted onto the resist under pressure, shown in Fig. II-2 (c). The flat mold has a large grating pattern of 190nm period and 180nm height. After roll NIL, the imprinted pattern has 190nm period and 40nm depth. The imprinted results are shown in Fig. II-2 (d). However, the accuracy of the replication of the rolling method is not as good as the flat mold method. Because the whole process is still T-NIL. It needs long period of time to complete the pattern transferring process due to temperature cycling, while the rotating roller mold has limited time contacting on the PMMA. Nevertheless, the flat method is actually P2P T-NIL. It has enough time for the PMMA to fill into the cavity of flat mold. Although the results obtained by Chou's team showed limited accuracy, this roller nanoimprinting method does provide a possibility of continuous manufacturing process and has an inspiration for the next generation of roll-to-roll nanoimprint lithography (R2R NIL).

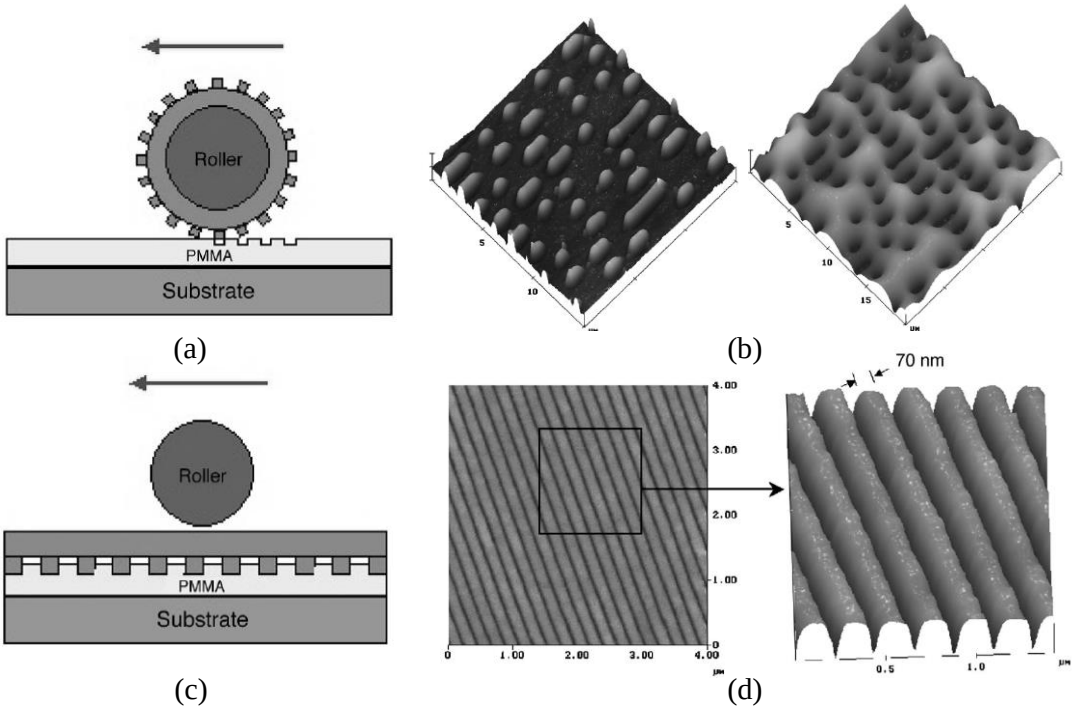

Fig. II-2 Schematic of roller nanoimprint lithography (a) imprint using a cylinder mold: bending a compact master disk into cylinder shape, mounting it around the roller, and rolling the roller on the substrate (b) Left: AFM graph of a compact disk mold before bending into a cylinder; Right: PMMA imprinted by a cylinder mold, showing sub-100nm accuracy in pattern transfer. (c) imprint with a flat mold: putting the mold directly on the substrate, and rotating the roller on top of the mold (d) PMMA imprinted by flat mold: it has large area grating with 190nm period and 40nm depth [49]

In the contrary to conventional nanoimprint lithography facing the high cost of large-scale flat mold and uniformity and releasing problems, R2R NIL has been introduced by Shinill Kang and his team from Yonsei University in 2006[50]. The schematic diagrams of the UV roll nanoimprinting system are shown in Fig. II-3. The UV roll nanoimprinting system can be identified as rigid substrates or flexible substrates (shown in Fig. II-3 (a) and (b) respectively). Both UV nanoimprinting system have similar components. A dispensing unit is used for coating UV curable resins onto the substrate; the thickness of coating material is controlled by viscosity of UV curable resin, nozzle size, ejection pressure as well as the feeding speed of substrate. A pair of flattening rollers are introduced to ensure the uniformity of resin on the substrate. The thickness of the final replica can be controlled by varying the contact pressure of the contact roller with the substrate and indirectly with the roller stamper. It can also be controlled by choosing various UV curable resins with different viscosity. The contact roller and pattern roll stamper form a passive gap control system. The UV light illumination unit exposes UV light onto the curing region where roller stamper and photopolymer contact. The cavity of the roll stamper is filled by photopolymer. An ellipsoidal reflector is used to collimate the UV light from the lamp with wavelength ranging from 265 to 420nm. The condensing lens is used to concentrate UV light to a narrower region where contact happens. For the flexible substrate system, the contact region increases significantly, because the flexible substrate can be wrapped on the pattern roll stamper. Increased contact region means faster feeding speed, which also means higher throughput. Shinill Kang and his team demonstrated the imprinting results on a flexible substrate. Polyethylene terephthalate film was used as the substrate. Pattern roller stampers with two different nanopatterns were used to test the replication ability of nanopatterns for their device.

The pattern roller mold is fabricated by the electroforming process which is the traditional nano-forming technology. Scanning electron microscope (SEM) and focused ion beam (FIB) section images of line structures with width of 500nm, pitch of 1000nm, height of 900nm on stamper and imprinted pattern. The nanopattern of line structure was transferred on the resist by UV roll nanoimprinting, shown in Fig. II-3 (c). SEM images and atomic force microscope (AFM) profiles of imprinted nanopillars with diameter of 50nm, pitch of 150nm and height of 35nm are shown in Fig. II-3 (d). The deviations of nanopillars on the stamper and imprinted pattern were found to be less than 3nm. Therefore, the results shows UV roll nanoimprinting process has the ability to replicate sub-100nm scale nanopatterns with high surface quality. Lan and several researchers[51] published a survey on the international conference on smart manufacturing application in 2008. They introduced development of roller-type nanoimprint lithography process at that time. It mainly included Chou's and Kang's setup.

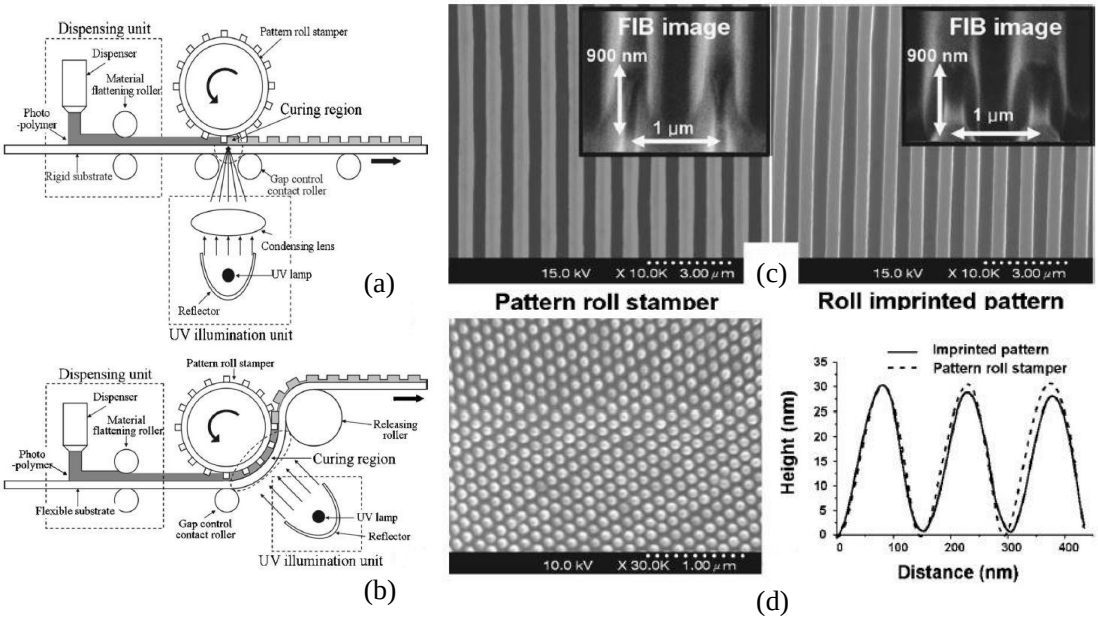

Fig. II-3 Schematic diagrams of UV roll nanoimprint system (a) for a rigid substrate and (b) for a flexible substrate. This UV roll nanoimprinting system can be used to replicating the large-scale nano- and micro-patterns on both rigid and flexible substrates (c) SEM and FIB section images of line structures on roll stamper and imprinted patterns, respectively (d) SEM images and AFM profiles of imprinted

nanopillars[50]

Later in the same year, Guo and Ahn reported high speed R2R NIL on the flexible plastic substrates[7]. The ability to coat nanometer-scale structures on flexible substrates can enable new applications in the field of photonics and organic electronic. The process and production of NIL (on the order of minutes per wafer) still cannot meet the huge demand of many applications. This is another reason to move to the continuous manufacturing process. R2R NIL can enable imprinting nanostructures on a flexible film with drastically increased output, leading the nanoimprint lithography to a brand new level. It inherits the high-resolution feature from traditional NIL process because it is still based on an embossing approach. However, the manufacturing speed of the nanofeature can be increased up to one hundred times [7]. On the other hand, by contrast to conventional NIL process, R2R NIL have several other advantages:

In conventional NIL process, embossing a large-area mold into the resist requires a large force applied uniformly. R2R NIL requires a much smaller force to transfer nanopatterns because the imprinting conducted in a narrow region transverse to the web moving direction.

Large-contact area between mold and nanostructures also produces a large adhesive force, which makes demolding from the substrate without damaging substrates or nanostructures difficult or even impossible. R2R NIL uses the roller mold which makes demolding like a “peeling” process. Thus, it is much easier to demold and causes less defects produced by demolding. In addition, fluorinated anti-stick coatings are always used on the mold surface to reduce the detachment force required under NIL. However, in the continuous manufacturing process, the small demolding force does not require anti-stick coatings except when imprinting of high aspect ratio nanostructures. Furthermore, spraying the fluorinated anti-stick coatings can also increase the cycle time since anti-stick coating is required for each imprint. Anti-stick coatings can be sprayed continuously on the imprint roller in the R2R UV NIL process.

In T-NIL, if the mold and the substrate made by different thermal expansion coefficients materials, the residual stress between the mold and the substrate may be built up during a thermal cycle, which may damage the imprint when releasing from the mold.

In the large area NIL, presence of dust particles can affect uniformity around the large surrounding area, while it can be potentially limited in one dimension by the contact linewidth in R2R NIL. The other issue is the air entrapment. Gas can be trapped under the entire imprinting mold since there is no path to escape for the gas trapped away from the edge. However, in R2R NIL, gas can only be trapped along the contact linewidth. The applied pressure by backup roller tends to squeeze out air bubbles along either side of the contact line[52].

Guo reported the schematic of their R2R NIL method including a coating process and an imprint process. The schematic is shown in Fig. II-4 (a). A roller keeps rotating in the resist. The resist adherents on the roller then transfers onto a continuous feeding flexible substrate (PET web) after being flatted by a doctor blade. The coating unit is shown in Fig. II-4 (b). The web with coating resist then goes through the imprinting unit, which contains an imprint roller and backup rollers as well as radiation of UV light. The contact zone between backup roller and imprint roller is commonly called nip, which will be discussed in the next section. The imprint unit is shown in Fig. II-4 (c).

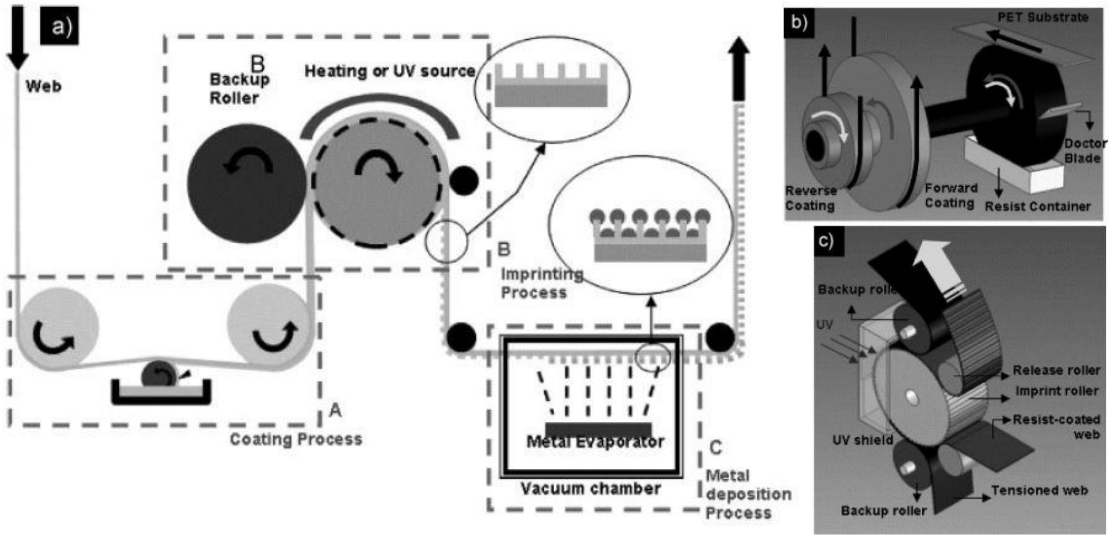

Fig. II-4 (a) Schematic of the R2R NIL process, and the continuous fabrication of a metal wire-grid polarizer as one of its applications (the metal deposition process is carried out in a separate evaporator) (b) Schematic of coating unit and (c) imprinting unit of R2R NIL[7]

In the work of Guo, they introduced R2R NIL including R2R thermal NIL[7] and R2R UV NIL. For thermal R2R NIL, a thermal curable liquid resist based on modified PDMS was used. The material can be crosslinked within a few seconds at 120 ºC. However, using a UV-curable low viscosity liquid epoxy silicone as the imprint resist can further increase the imprinting speed. They did experiments on both methods of R2R NIL. For easy visualization of the imprinting results, they chose a grating pattern of 700nm period in the initial experiment, because a well-replicated grating structure shows strong light diffraction, and therefore, the pattern quality can be easily estimated by eye. The flexible substrate used for both tests was a PET web. A 200mm long, 300nm line-width and 700nm period grating imprinted by thermal imprinting is shown in Fig. II-5(a, b). A 570mm long, 700nm period grating structure imprinted by UV NIL is shown in Fig. II-5 (c-e). It is not hard to see that the epoxy silicone resist pattern has a higher quality than thermally cured PDMS resist, which is attributed to the lower viscosity of UV curable resist that facilitates the filling process.

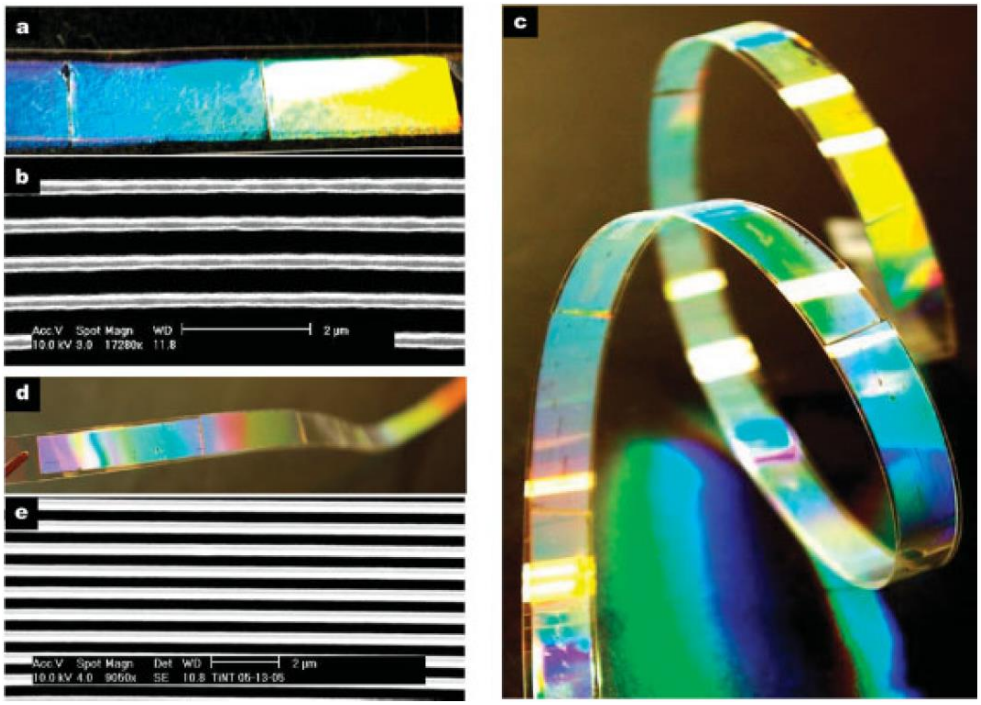

Fig. II-5 R2R T-NIL results: (a) Photograph of 700nm period, 300nm width PDMS grating pattern imprinted on PET web by using thermal R2R NIL (b) SEM image of grating structure; R2R UV NIL results: (c, d) Photograph of 700nm period, 300nm line width epoxy silicone grating pattern imprinted on PET web by R2R UV NIL, showing better quality than T-NIL (e) SEM image for the replicated pattern[7]

After the initial experiment, they tried to imprint high-aspect-ratio (AR =5.4: 1) grating structures. Faithfully replicated epoxy silicone pattern imprinted by ETFE mold should have the same geometry parameters with the original Si mold. Because the ETFE mold has the exact inverse pattern of Si mold, we can observe a good shape of pattern replication for fine details at the bottom of grating trenches, by comparing the original Si mold (Fig. II-6 (a)) and the replicated pattern (Fig. II-6 (c)). Fig. II-6 (d-f) shows their results for thinner and denser grating structures which are fabricated by R2R UV NIL. However, like we discussed before, the speed of feeding web determines the output of nanopatterns. When Shinill Kang and his team introduced R2R NIL process, the optimal imprinting speed was set as 13mm/s[50]. They also mentioned that the increasing of UV light intensity will increase the manufacturing speed. In later work of Guo from University of Michigan, their web velocity was 1.3-23.5mm/s[7, 53, 54]. Maury et al.[55] reported they build flexible electronic by R2R UV NIL. Their manufacturing speed is at

0.1m/min (1.6mm/s). Apparently, the manufacturing speed is relatively low, which limits the output of process. It is mainly limited by UV exposure during the resist curing in the cavity of the mold. The resist cure level is affected by UV exposing intensity and UV exposure dosage. In 2013, H. Yoshikawa and his team successfully increased the speed to 18m/min[56]. The goal speed in our project is set to 20m/min, which has been achieved. This will be discussed in chapter 5. The relation between resist cured level and UV exposure will be discussed in subsections.

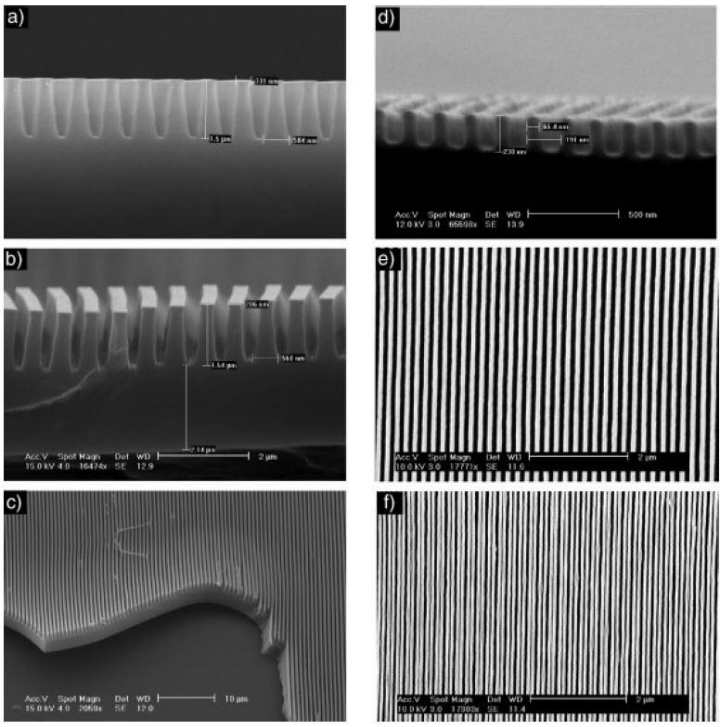

Fig. II-6 (a) Original Si mold (b, c) Epoxysilicone gratings replicated from the ETFE mold (d, e) SEM images of 200nm period, 70nm line width epoxysilicone pattern (f) 100nm period, 70nm line width epoxysilicone pattern fabricated by UV R2R NIL[7]

The schematic of the testbed for R2R UV NIL used by Good[57] is shown in Fig. II-7 (a).The main components of apparatus for R2R UV NIL process involves dispensing unit (also called coating unit), imprint unit (imprint mold, flexible substrate (usually using web), backup roller, and peel roller), UV illumination unit, as well as storage unit (winding roller). As shown in Fig. II-7(b), the mechanics in the nip contact zone and flexible substrate will affect the quality of final nanopatterns transferring. This part will be discussed in next sections. On the other hand, the

continuous R2R UV NIL process can be separated into filling the cavity of the mold, UV exposure, peeling from the imprint roller. The properties of UV resist will determine the filling of the mold, UV curing and release from the mold. We will discuss the UV resist first, followed by the process review.

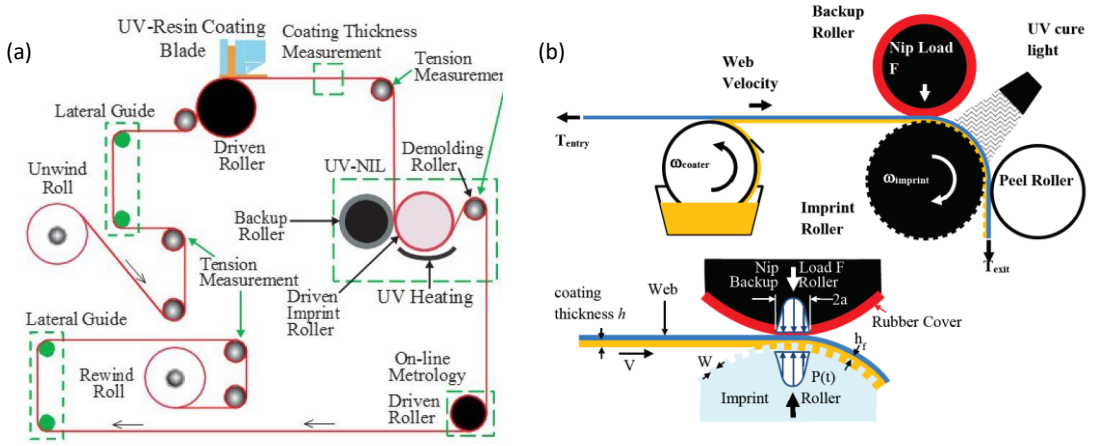

Fig. II-7 (a) Schematic of nanopattern fabrication producing line for R2R UV NIL (b) Schematic of R2R UV NIL and nip mechanics in nip contact zone[57]

2.1 UV resin

The UV curing resist (also called resin), used in R2R UV NIL, typically contains monomers, cross-linking agents, photo-initiator, and may contain photosensitizer. Monomers are the basic of a resist, which are acrylic and epoxy monomers. Cross-linking agents are molecules similar to monomers but contain more functional group to enable chain reaction for polymer. Photo-initiators are a kind of molecules which can absorb certain wavelength UV light to activate the reaction. The resist may also contain a photosensitizer, which is used to widen the absorbing wavelength of UV light. When the photo-initiator is irradiated by high energy and suitable wavelength UV light, it can generate free radical or photo-acid, which can activate the cross-linking and polymerization[39]. Depending on the monomer, the resist can be classified into a radical curing system (contains acrylic monomers) and a cationic curing system (contains epoxy

monomers) [39, 52, 58, 59]. The process of photo-polymerization can be classified into initiation (also called induction), propagation and termination by reaction kinetic[60], as shown below.

$$P \rightarrow P+M(\text{initiation}) \rightarrow M+M(\text{propagation}) \rightarrow \text{Polymer(termination)}$$

P: photoinitiator M: monomer

The polymerization process can be identified into induction, gelation, and vitrification processes by rheological behavior[61, 62]. The rheological behavior can affect the process of polymerization. In the first stage at a low degree of conversion, the conversion can be considered as an autocatalytic or auto-accelerated (kinetics controlled) model with propagation reaction accelerating up to a maximum before decelerating. When the storage modulus equals to loss modulus ($\tan\delta=1$), it reaches the gel point. The second stage at the high degree of conversion would be considered as diffusion controlled and occurring partially cross-linked polymer upon vitrification below the glass transition temperature. A criterion to determine the vitrification onset from photo differential scanning calorimeter(p-DSC) results was proposed by Schmidt[61] as the inflexion point between the first and the second stage in the conversion rate versus the conversion curve tangents crossover point between the deceleration and diffusion governed zones.

The advantages and disadvantages for both types of resist are listed in Table II-1[58]. Iyoshi and his team reported a hybrid resist which contains both radical and cationic free polymerization type. The resist showed relatively low shrinkage and less inhibition by oxygen. It also showed a good mold removability[58].

Table II-1 Comparison between radical curing system and cationic curing system[58]

	Radical curing system	Cationic curing system
Advantages	1. Storage ability 2. Quick curing rate 3. Uninfluenced by moisture 4. Easy formation of thick film 5. A wide range of	1. Small or controlled shrinkage 2. No oxygen inhibition 3. Generally better adhesion to substrates

	monomers available	
Disadvantages	1. Large cured shrinkage 2. Oxygen inhibition 3. High volatility	1. Relatively slow curing rate 2. Inhibited by moisture

Comparing to the free-radical photo-polymerization, the ring-opening polymerization epoxy resist does not have issues with oxygen inhibition, resulting in very low shrinkage, excellent adhesion and chemical resistance. Additionally, it also allows dark-curing after photo-initiation and thermal post-cure due to cationic active centers[63]. The cationic epoxy resist is suitable for curing in the ambient air, which means it is preferred for continuous R2R manufacturing process. A vacuum environment for the whole process will increase the cost and inconvenience of R2R UV NIL. Benefiting from the recent availability of diaryliodonum salt photoinitiators that are "benzene free", the cationic systems are stable at room temperature. To achieve higher manufacturing speed, the process requires higher web feeding speed. It means that the curing time for resist while the resin in the cavity of the mold has been shortened. The reaction rate, thus, should be increased to shorten the curing time. L. Yang and J. Yang et al.[63]proposed a temperature controlled method to shorten the conversion time. During the induction period at room temperature, the photo initiator transforms to a secondary oxoinium ion species. The secondary oxoinium ion species are the triggers for chain reaction forming the resin. Moreover, studies[64] revealed that secondary oxonium ion species are much more stable under low temperature conditions. The researchers stirred and irradiated the monomer solution with a cationic initiator at low temperature. The cationic initiator, thus can be photo-activated and form secondary oxonium ion species. When the temperature control was removed, the secondary oxonium ions became active with the increasing temperature to the room, which induced fast polymerization, and the released heat due to exothermal reaction of polymerization further propelled the reaction. The whole process has a "snow balling" effect.

The resist we are using in the current project is UV 15 supplied by MasterBond Co. Ltd[12]. It is a high strength, low viscosity, epoxy-based UV curable system for bonding, sealing and coating.

It is 100% reactive and does not contain any solvents or other volatiles. As it is an epoxy-based UV curing system, it is completely free of any oxygen inhibition. The photo reactive wavelength of UV light for UV 15 ranges 320-365nm, with optimum at 365nm. The curing rate depends on the intensity of the light source and exposure time as well as thickness of the resin. Typically, it takes 15-30 seconds to cure a few microns to 0.015-0.020 inches resin with a 20-40 mW/cm2 UV light. The UV 15 also has lower shrinkage (1-2%) and higher temperature resistance than majority of resin which cures by a free radical mechanism. UV15 has excellent resistance to a wide variety of chemicals including water, acids, bases, fuels and many solvents. It also has excellent optical clarity and light transmission properties. As a cationic UV curing system, one interesting feature needs to be noted. The UV resin can continue reacting even after removing the UV light source, which is called dark curing. This suggests that the mechanical properties of UV resin may keep changing after entirely exiting the wrap on imprint roller. UV15 can also be post cured. The post cure can enhance UV15's chemical resistance. Both dark curing effect and post cure can influent the study of storage of our product. Typical properties for UV15 are shown in Table II-2[12].

Table II-2 Typical properties for UV15

Viscosity, 75 ºF	115-350 cps
Tensile strength, 75ºF	6,000-7,000 psi
Tensile modulus, 75ºF	250,000-300,000 psi
Hardness, 75ºF	>75 Shore D
Hardness after 1000 hours 85ºC/85% RH	>75 Shore D
Glass transition temperature, 75ºF without post cure	90-95ºC
Glass transition temperature, 75ºF with post cure	125-130ºC
Refractive index, 75ºF	1.517
Shrinkage	1-2%
Shelf life, in original, unopened containers at 75ºF	6 months
Service temperature range	-80ºF to +350ºF (-62ºC to +177ºC)

As we are using a cationic UV curing system, there is no oxygen inhibition. Therefore, it is convenient for the roll-to-roll process since no vacuum environment is required. Furthermore, as we discussed above, low shrinkage of this resist also leads to a reliable pattern replication.

Additionally, the resist can be imprinted with low pressure due to its low viscosity. In addition, the resist can be cured in seconds by focused UV light.

The mold filling process

The resist must completely fill the mold to produce high-quality nanopatterns. Thus, hydrodynamics plays a key role studying the filling of the cavity on the mold with resist. Before filling resist into the mold, coating resist on flexible substrate (PET web in current work) is a topic to be considered. Too thick a resist coating can cause a residual on the imprint mold which hampers the continuous imprinting. In addition, the imprint roller and backup roller will squeeze out the excess resist resulting in waste. Too thin a resist coating will cause insufficient resist filling into the cavity of the mold or cause coating fractures during the demolding process[7]. In the current apparatus of the project, we adopt a doctor blade on the gravure roller to control the thickness of resist coating which comes from a resist container, shown in Fig. II-4 (b). Therefore, sufficient resist needs to be provided to get high-quality nanostructures.

Other than the coating thickness, filling time is also a main parameter for the resist filling process. Additionally, filling time can be controlled by adjusting web feeding speed and contact region length. The filling time is also affected by resin viscosity, applied pressure, initial coating thickness, web width, contacting length, final coating thickness. The length of the contact region is directly dependent on Young's modulus, Poisson's ratio and thickness of rubber cover for nip roller, applied pressure, radius of both imprint roller and nip roller. In R2R UV NIL, low viscosity UV curable resins are used as patterning media. The simplest and most adopted assumption is that resin spreads as a uniform thin coating on the substrate in contact with the imprint roller. This arrangement would give simplest flow behavior and most predictable results in practice. As the thin coating of resist spreads uniformly between substrate and the imprint roller, the setup can be described as a one-dimensional squeezing flow of a thin coating into a long channel cavity[52]. In 2004, H. Schift and L. J. Heyderman[65] presented a method to

calculate the resist filling time by considering NIL as a liquid flow squeezing model. The two-dimensional model gives $\partial / \partial x = 0$. Therefore, both plates should have length $L \gg s$ in x direction. For an infinitesimal cuboid of the size $2L\delta_y\delta_z$ at the axis $z = 0$, shown in Fig. II-8(b).

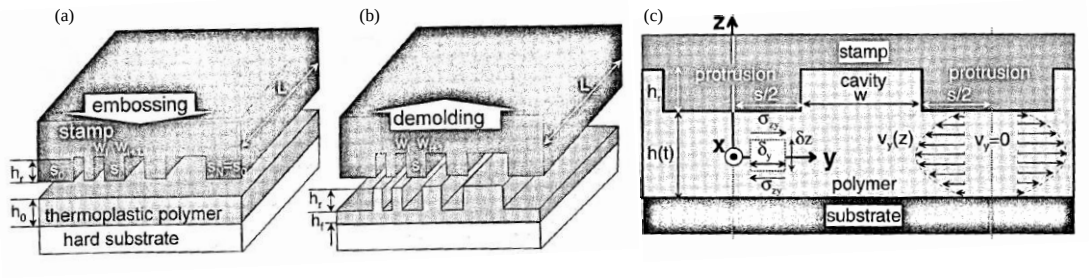

Fig. II-8 Geometrical definitions used for the description of flow process (a) before molding (b) after demolding (c) Model describes the flow process. Left side: Flow element. Right side: Velocity distribution in a Newtonian flow. Only the flow of polymer between the centers of two protrusions contribute to the filling of the cavity of the stamp mold[65]

From the quasi-stationary flow motion equation:

$$-\partial_j p + \nabla_i \sigma_{ij} = 0 \qquad (\text{II-1})$$

the shear stress in y-direction can be derived:

$$\sigma_{zy} = \frac{dp(y)}{dy} z \qquad (\text{II-2})$$

If we consider the flow as a Newtonian flow, here the pressure *p* is considered to be independent from the z axis. Newton's friction law is applied as follows:

$$\frac{dv_y}{dz} = \dot{\gamma}_{zy} = \frac{1}{\eta_0}\sigma_{zy} = \frac{1}{\eta_0}\frac{dp}{dy} z \qquad (\text{II-3})$$

Integrating equation (II-3) over *z* gives velocity field:

$$v_y(y,z,t) = \frac{1}{2\eta_0}\left[z^2 - \left(\frac{h(t)}{2}\right)^2\right]\frac{dp(y,t)}{dy} \qquad (\text{II-4})$$

with the boundary condition, $v_y = 0, at\,|z| = h(t)/2$. The equation (II-4) showed the distribution of flow velocity of y direction across the z axis. Integration of equation (II-5)(II-4)

over *z* with the boundary condition, $v_y = 0, at \left|z\right| = h(t)/2$, we introduced the dependence on time. The half volume flow in y direction, $q_y(y,t)$, is calculated as follow:

$$q_y(y,t) = \int_0^{h(t)/2} v_y(y,z,t)dz = \int_0^{h(t)/2} \frac{1}{2\eta_0}\left[z^2 - \left(\frac{h(t)}{2}\right)^2\right]\frac{dp(y,t)}{dy}dz$$
$$= \frac{1}{2\eta_0}\frac{dp(y,t)}{dy}\left[\frac{1}{3}z^3 - \frac{h^2(t)}{4}z\right]\Bigg|_0^{h(t)/2} = -\frac{h^3(t)}{24\eta_0}\frac{dp(y,t)}{dt} \qquad \text{(II-5)}$$

The volume flow in the slot $q(y,t)$ through area $y = const$ results in:

$$q(y,t) = 2Lq_y = -\frac{L}{12\eta_0}h^3(t)\frac{dp(y,t)}{dy} \qquad \text{(II-6)}$$

The volume flow in the slot $q(y,t)$ can also be calculated by

$$q(y,t) = -Ly\frac{dh(t)}{dt} \qquad \text{(II-7)}$$

Since the direction of flow is toward negative y direction, thus there is a negative sign for the volume flow. Combining equation (II-6) and (II-7),

$$q(y,t) = -\frac{L}{12\eta_0}h^3(t)\frac{dp(y,t)}{dy} = -Ly\frac{dh(t)}{dt} \qquad \text{(II-8)}$$

Integrating over *y* results in hydrostatic pressure as a function of the film thickness *h(t)*:

$$\frac{dp(y,t)}{dy} = \frac{12\eta_0 y}{h^3(t)}\frac{dh(t)}{dt} \qquad \text{(II-9)}$$

$$p(y,t) = \int_0^{s/2}\frac{12\eta_0 y}{h^3(t)}\frac{dh(t)}{dt}dy = \frac{6\eta_0}{h^3(t)}\frac{dh(t)}{dt}\left\{y^2 - \left(\frac{s}{2}\right)^2\right\} \qquad \text{(II-10)}$$

with the boundary condition $p(s/2,t) = 0$.

Integrating equation (II-10) over the width of a single stamp and multiply the length of mold, we get force:

$$F = L\int_{-s/2}^{s/2} p(y,t) = -L\eta_0 \left[\frac{s}{h(t)}\right]^3 \quad \text{(II-11)}$$

Finally, from equation (II-11) we can solve for film thickness $h(t)$ as a function of time under a constant force F.

$$\frac{1}{h^2(t)} = \frac{1}{h_0^2} + \frac{2F}{\eta_0 L s^3} t \quad \text{(II-12)}$$

When the resist has fully inserted into the cavity of the imprint mold, the height of film thickness is $h_f = h(t_f)$. Combining with equation (II-12), we get the embossing time:

$$t_f = \frac{\eta_0 L s^3}{2F}\left(\frac{1}{h_f{}^2} - \frac{1}{h_0^2}\right) \quad \text{(II-13)}$$

For most practical cases, we applied pressure on the imprint mold. Then we can get resist filling time as format of equation (II-13).

Other research based on work of H. Schift and L. J. Heyderman[65], developed the UV NIL resist filling time calculation method. Hong. H. Lee and his team reported filling time for R2R UV NIL[66].To obtain the equation for filling time, several assumptions should be made. First, the diameter of the imprint roller should be much bigger than contact length L so that the curvature of the mold does not affect flow behavior. Second, the distribution of the press is assumed to be uniform through the length of the contact region. Third, the flow of resist is assumed to be purely viscous, the resin is incompressible. Then, we get the following equation for t_f

$$t_f = \frac{\eta(T) S^2}{2P(t)}\left(\frac{1}{h_f{}^2} - \frac{1}{h_0^2}\right) \quad \text{(II-14)}$$

η (T) is the resist viscosity at temperature, T, P(t) is applied pressure by a backup roller, hf and h0 are the final and initial thickness of resist coating, respectively, S is the pattern size in the machine direction. The viscosity is considered as a variable dependent on temperature, while the applied pressure is thought to be dependent on time. Fig. II-9(a) shows that the PUA mold as a

substrate film is flexible, but is rigid enough to be a mold for imprinting. If the cavity is filled entirely, the final thickness can be calculated by

$$h_f = h_0 - \frac{WH}{S+W} \qquad \text{(II-15)}$$

W is line width, *S* is pattern width, *H* is depth of pattern, shown in Fig. II-9(b).

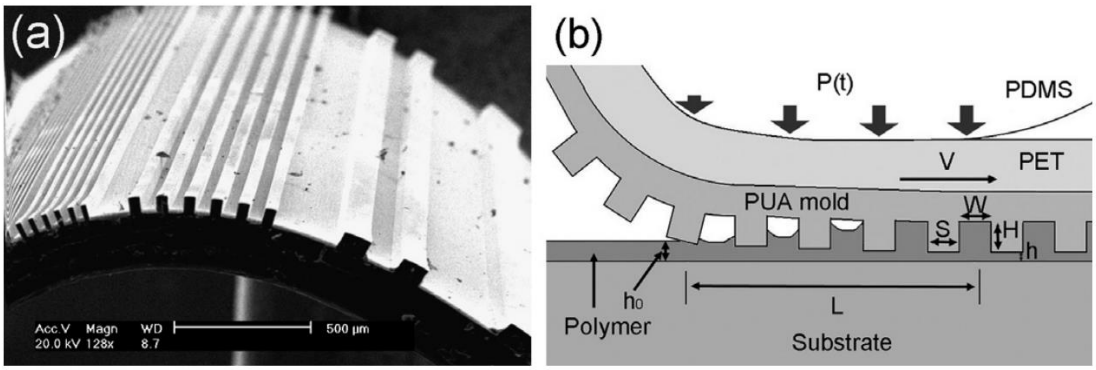

Fig. II-9 (a) SEM image of a flexible PUA mold that was replicated from a hard mold. (b) Schematic illustration of imprinting with PUA mold. The PUA mold moves at a speed of V and the pressure is applied to the PDMS buffer layer.[66]

Hong. H. Lee and his team reported filling time for R2R UV NIL[66]. They developed equation (II-14) to predict if the filling time is adequate. For continuous imprinting, L is the length of the contact region, and V is the web speed. Thus, the time from web moving into the contact zone to out of the contact zone should be greater than the filling time required to fill resist into the cavity. It can be described as

$$\frac{L}{V} = \frac{\eta(T)S^2}{2P(t)}\left(\frac{1}{h_f^{\,2}} - \frac{1}{h_0^2}\right) \qquad \text{(II-16)}$$

As shown in Fig. II-9 (b), the protruding part of the imprint roller obliquely penetrates into the resist when it first contacts the resist on the substrate. This oblique contact can help reduce entrapment of air bubbles. This is another reason that a backup roller is required for the resist filling unit of R2R UV NIL additionally providing pressure.

Heyderman et al. also used this model to calculate the filling time for NIL[67]. Heyderman used this method for plate to plate nanoimprint of thermal plastic. It is obvious that the increasing embossing pressure or reducing the viscosity of the polymer (by increasing temperature) can decrease the filling time by equation (II-14). Furthermore, to reduce the filling time, we can increase the polymer thickness or decrease the ratio of cavity volume to stamp width. Similar to thickness of the resist coating we discussed before, the film thickness should be thin enough for subsequent pattern transfer but thick enough to fill into the mold. All of these factors should be taken account to optimize the NIL mold filling process.

We mentioned above that a backup roller is required for providing pressure, and eliminating air bubbles. The imprint roller and backup roller form a contact zone which would commonly be called the nip contact zone. In 2009, S. H. Ahn and L. J. Guo from University of Michigan created dynamic elastic roller contact model[53]. The thickness of the product or residual layer thickness (RLT) is of importance for metal wire-grid polarizer and solar cells in optical applications since they will affect the absorption of light or film birefringence. In addition, most semiconductor applications generally need thinner RLT to decrease the impact on nanostructured profile. Guo and Ahn zoomed in the contact area between the imprint roller and the backup roller, regarding the contact region as two planar plates squeezing the liquid resist. The schematic of liquid resist being squeezed by contact rollers is shown in Fig. II-10 (a). Thus, resist filling time can be calculated by similar method of NIL.

$$t = \frac{\eta a^2}{2P}\left(\frac{1}{h^2} - \frac{1}{h_0^2}\right) = \frac{\eta a^3 L}{2F}\left(\frac{1}{h^2} - \frac{1}{h_0^2}\right) \qquad \text{(II-17)}$$

Where η is the resist viscosity. In the UV nanoimprint process, the reaction can produce heat, however the temperature cycle is not as much as the T-NIL process. Thus, an average viscosity is adopted in the equation. P is applied pressure by backup roller, F is the applied force for the plates, a is the length of contact area, L is the width of planar panel. h and h0 are final and initial

thickness of resist coating, respectively. Since they are impacted by the residual layer thickness (RLT), therefore, the equation for calculating RLT is as follows.

$$h = \left(\frac{2F}{\eta a^2 LV} + \frac{1}{h_0^2} \right)^{-1/2} \qquad \text{(II-18)}$$

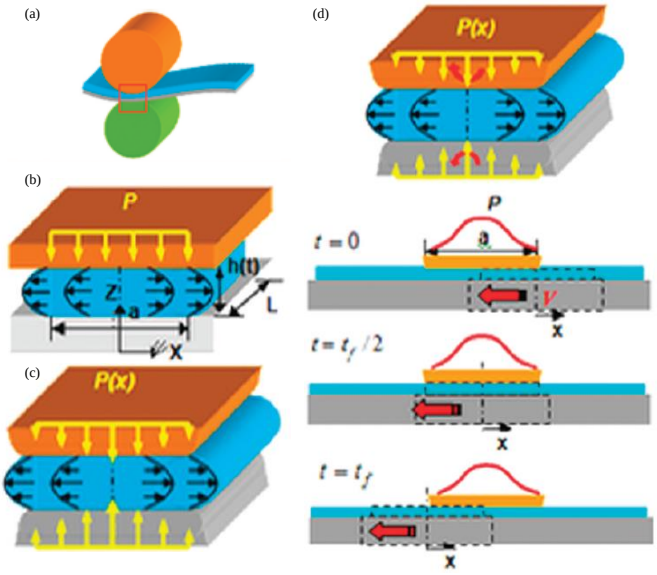

Fig. II-10 (a) Schematic diagram of the liquid resist being squeezed by the contact rollers (b) modeled as rigid plates (c) modeled as elastic cushion layers (the pressure distribution is given by Hertz contact solution). (d) the dynamic elastic roller contact model[53]

Many researchers worked on the study of residual layer thickness. In 2005, Lee worked on exploring the effect of imprinting pressure and viscosity of resist polymer. He found that a near-zero-residual layer can be achieved with assists of high-pressure imprint, regardless of the initial resin thickness. Additionally, highly fluidic imprint resin is helpful to achieve a near-zero-residual layer[68]. Lee et al. reported a specular x-ray reflectivity as a powerful metrology to quantify the nanostructure height, residual layer thickness as well as aspect ratio[69]. Later in 2007, Schimiit et al. also used equation (II-14) to predict the resist filling time[70]. However, they suggested that in the case of the initial resist thickness being much bigger than final resist thickness, the final thickness of resist can be simplified as

$$h = \sqrt{s^2 / 2Pt_f}\sqrt{\eta}$$
$$h \propto \sqrt{\eta} \qquad \text{(II-19)}$$

In 2019 IWEB conference hold by Oklahoma State University, Dr. Pagilla from Texas A&M University reported their progress in the mold filling process in R2R NIL[71]. A model utilized to investigate the effect of web speed, fluid film thickness, viscosity, stress relaxation time, mold pattern geometry and size was developed. Time-dependent pressure distribution was applied in the model instead of existing results where a priori assumption were made. The mold filling process is highly dependent on the interactions between the material properties, especially the stress-relaxation time λ and free-surface energy γ.

Many scholars also showed interests in simulating resist filling process by molecular dynamic method (also known as stochastic simulation). In 2007, K.W. Kim et al. reported using molecular dynamic method to study the pattern transfer of NIL. They studied adhesion and frictional force for different aspect ratio pattern[72]. Masaaki et al. from Osaka Prefecture University studied the relation between the press force required to fill the resist in the cavity and the size of the cavity[73].They also reported that the sidewall roughness may affect the press force. M. Koyama et al. simulated the resist filling process. They mainly considered reactions between monomers[74]. This finding shows that the effect of film thickness on conversion ratio is much smaller than the data obtained by experiments.

The resist filling process has been studied by many researchers with different methods. In summary, sufficient resin should be provided to entirely fill the cavity of the mold. A backup roller (nip roller) is necessary for continuous roll-to-roll nanoimprint lithography. Since introducing a nip roller is unavoidable, a model to deal with nip pressure and resist flow has been reviewed.

UV exposure

The curing process of UV curable resist is directly influenced by UV dosage received during imprinting process. Too low the dosage will result in unmatured resist which may lead to pattern transfer failure, while too much the dosage will cause overcooking, resulting in higher shrinkage ratio, brittleness, residual stress, and difficulty of the demolding. Therefore, proper UV light exposure is strongly recommended for high-quality nanostructures. It also limits web transporting speed to achieve high-speed roll-to-roll nanoimprint lithography. On the other hand, UV light intensity can affect the curing rates. Generally, higher UV light intensity can increase the curing rate of UV resist. In this section, we will consider the distribution of UV intensity.

Jian and Zhao reported simulation of light distribution of a UV lamp with a parabolic cylinder reflector on the workpiece surface[75]. They built a physical model, which had a good agreement with the real situation. In addition, the simulation can help adjust the parameters of the UV radiation system. Many researchers studied UV light intensity distribution in UV disinfection, which is similar to Jian and Zhao's work[76-78]. Zhang and Chen reported a unique radiation characteristic of UV LED array for inquiring the photocatalytic odor abatement process[79]. They neglected the scattering and reflection due to their narrow-slit gaseous reactor. The photon flux overlapping can affect the radiation field due to directivity of LED lamps. Additionally, the LED lamps are assembled as arrays. They built a model to calculate the intensity distribution of LED array based on geometric relationship. Zhang and Chen reported a photocatalytic degradation in a LED continuous reactor[80]. Their LED lamp is 3*9 arrays. The directivity of the LEDs was 20ºfor 50% of total irradiation energy. They fixed the LED at a distance of 3.5cm directly above the reactive film. They determined light intensity projected onto reactive film by averaging 20 measurements at varying positions on the plate. The uniformity of UV light distribution is determined by the standard deviation of measured intensity which is within ±20%. Moreover, Shibata[4] and Hirai[81] reported simulation of UV distribution throughout the profile of resist.

Maxwell's equation was numerically solved by finite-difference time-domain method (FDTD). It shows the electromagnetic propagation of the UV light irradiation.

To successfully obtain nanostructures, we want the UV light exposing on resist as much as possible when the resist is pressed into the cavity of the imprint roller. However, other areas, especially resist coating area prior to imprint roller, can be under unintentional exposure. Such exposure could cause chain reaction in the resist prior to resist filling process, which would increase viscosity of resin and lead to unsuccessful pattern transferring. Guo also mentioned about this pre-exposure effect in his work[53]. Kirchner et al. reported the influence on resist pre-exposure[82]. They used demolding force as an indirect measurement of resist curing. Successful pattern transfer can be achieved before a threshold value of accumulated UV light dose.

It is also important to understand the UV curing process since we need rapid curing, less shrinkage, and low adhesion. Obviously, there is a relation between UV light intensity and conversion rate, UV light dosage and final conversion ratio. This part of review is closely related to another group of papers which is about measurement of mechanical properties as a function of percent cured. Thus, we will discuss the UV curing in the following section.

Based on current review of UV light distribution, it is not enough to build a model for our project since we are using two LED lamps with arrays. The reactive film is not a plate but a lateral surface of a cylinder. However, experimental measurement could be a good solution to obtain the accurate UV light intensity distribution around the cylinder.

Demolding process

After the resist filling process and UV curing process, there is another challenge to accomplish successful pattern transferring, which is the mold releasing step. When the UV resist fills into cavity of mold, it is in liquid phase. Thus, it is easy for the resin to be filled into the nano-channel on the mold, resulting in promising high aspect ratio nanostructures. Successful demolding of the

pattern from the mold without any damage will be hard after resist is cured by UV exposure. The challenge will be even greater when the aspect ratio is increasing. Considerable research works have been done in this field. These studies are mainly classified into two groups by considering whether the anti-stick additive is added or not.

The crosslinking level determines both shrinkage and modulus of cured resist. With the increase of crosslinking level, the shrinkage as well as modulus will be increased. Shrinkage can either impede demolding or break the interface between mold and resist to assist demolding. Furthermore, a relatively high modulus of resist can help avoid damage from demolding[39]. Therefore, shrinkage level needs a compromise consideration.

A large volume of studies for optimizing the demolding process of thermal NIL has been conducted[16, 17, 19, 83-86]. The demolding of the cross-linked nanostructured polyacrylate from a fluorine-based mold is not an easy job[11]. Two important phenomena of interaction between the UV curable resin and the mold make the demolding complicated. An increase of adhesive strength at the interface as well as the shrinkage due to cross-linking of polymerization occur simultaneously during the UV curing. Excessive UV curing causes the high shrinkage of the polyacrylate and increases the possibility of initiation of the cracks in the nanostructures. Insufficient curing leads to low shear strength which is tremendously important for the cured nanoimprints to maintain a high-fidelity quality. The UV curable resin used in the current project has a max shrinkage ratio of 2%[12], which is relatively low to other materials[13, 14]. The adhesive strength has also been studied vastly in the thermal NIL[11, 15-19]. Amirsadeghi et al. reported a parallel demolding process in UV NIL by numerical simulation[87]. The parameter needed for simulation involving Young's modulus, coefficient of friction, crack initiation stress, fracture toughness and demolding energy were obtained by experiments. The fracture strength would increase with higher concentration of cross-linking agents since the cross-linking net

structure can increase the mechanical properties of the resin. Meanwhile the fracture stress also increases with an increase of the concentration of cross-linking agents due to the increasing Young's modulus. When both curing and demolding stresses were considered, the optimum cross-linking agent concentration had been found out, seen in Fig. II-11. Yeo et al. reported peel demolding instead of parallel demolding for a micro-pattern with an aspect ratio of 14[15]. The parameters governing the demolding process were peel angle, pre-crack condition, tensile modulus and strength, shrinkage, and interface fracture toughness. They used a numerical analysis of cohesive zone modeling (CZM) to simulate the demolding process. They used thermal strain effects to mimic shrinkage caused by UV curing. The fully cured polymer was peeled off by applying displacement. The failure criterion was the ultimate tensile strength. However, in their simulation, they considered polymer as a liner elastic polymer which affect the accuracy of simulation. Later, Yeo et al. used a hyper elastic material model and rate-dependent cohesive zone modelling in the simulation[88]. The accuracy of simulation was enhanced. They also increased the aspect ratio from 5 to 10, and the results indicated optimal shrinkage increased from 0.9% to 1.9%. T. Tochino et al. reported the impact of shrinkage on template releasing process in UV NIL[89]. Unlike Amirsadeghi and Yeo, they built a single symmetric structure and focused on shrinkage induced residual stress and partial separation. As a result, the demolding force increases as the thickness of residual layer decreases. The maximum demolding force depended on aspect ratio. The release force increases as aspect ratio increases. This finding is in line with that of previous researchers' work. Y. Hirai et al. reported impact of stiffness of template for NIL[90]. They used both numerical analysis and experiments to compare failure rate with different stiffness templates. They reported release force is not the only factor to take into account. The stiffness of template is another factor which impacts the demolding. Furthermore, Z.C. Song et al. reported that simulation for demolding process of T-NIL[91]. They also built a

simple structure with only one single symmetric model and studied the stress and deformation in polymer during cooling and demolding process.

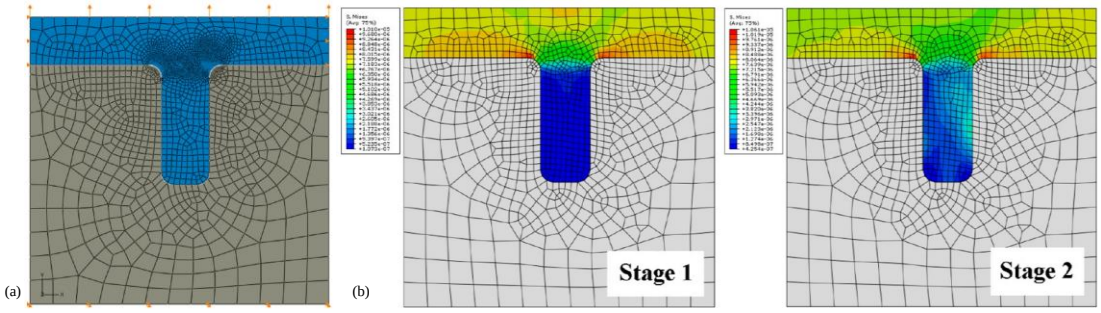

Fig. II-11(a) FEM model and the boundary conditions: The interface between resist (top) and silicon stamp (bottom) was modeled as cohesive zone elements. Simulation was done in two steps: First, a pseudothermal contraction was used to simulate the polymerization shrinkage upon curing while resist was constraint on x direction. Second, the resist was pulled out of the stamp cavity by applying a vertical displacement. (b) Von Mises stress evolution during curing (stage1) and demolding (stage 2)[87]

The numerical analysis method for parallel demolding and peel demolding for UV NIL has been discussed earlier in this report. Some other researches also reported demolding process by experimental method. Ye et al. reported effects of exposure time on defects and demolding force[92]. With increasing exposure time, the degree of curing and demolding force was measured. They modelled the resist as a linear viscoelastic material, which helped explain the increase of demolding force when curing time was increased. M.Shira et al. reported effects of elastic modulus on demolding force[93]. They measured storage modulus and demolding force by a rheometer. They suggested that the increase of demolding force is mainly caused by vertical surface of nanostructures. The optimization of elastic modulus of cured resist is important for defect-free demolding process in UV NIL. On the other hand, some researchers also pointed out a novel multi-step demolding process. They suggested that unfully cured resist could not only successfully transfer pattern but also reduce the demolding force. Jiang et al. presented a two-step curing method for demolding[94]. In the first UV exposure, they released mold when the pattern could stay stable. After demolding, a second UV exposure was applied to acquire sufficient pattern rigidity. Later, the same team proposed the two-step curing method with multistep loading

and demolding process[95, 96]. This method increased output with reducing demolding force and avoiding to pull up the residual layer.

To reduce the demolding force, some scholars proposed using anti-sticky coatings. Many kinds of antiadhesion coatings have been reported.[26, 97]. As a specific imprint mold and a substrate are used in this work, other antiadhesion coatings are not discuss here. The imprint mold we are using is made of a flexible fluoropolymer, ethylene-tetrafluoroethylene (ETFE). ETFE mold is replicated from an original Si mold by a thermal NIL process. In addition, ETFE mold has an exceptional anti-sticky property (surface energy of 15.6 dyn/cm). However, it is also challenging when the high aspect ratio patterns are continuously imprinted by roll-to-roll method. Therefore, a few drops of fluorosurfactant were added into the resist[7]. Additionally, L. J. Guo et al. reported that traverse or parallel peeling can affect the pattern transferring[98], shown in Fig. II-12. The energy release rate kept constant where peeling was perpendicular to the nanostructures. In the contrary, when peeling direction is parallel to nanostructures on the mold, the energy release rate changes with time. Thus, they concluded peeling perpendicular to the nanostructure orientation results in better quality than the parallel one. In roll-to-roll nanoimprint lithography, the demolding process can seem as a peeling process. During the whole R2R UV NIL process, we need to avoid slippage between the imprint roller and the uncured resist, because the slippage can destroy the nanopatterns.

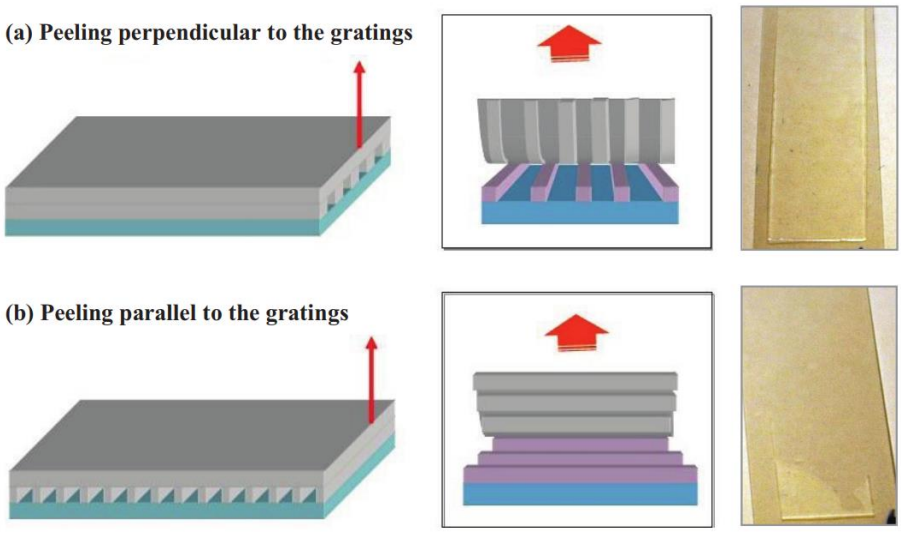

Fig. II-12 Schematic of two different mold separation methods: (a) peeling parallel to the grating orientation and (b) peeling perpendicular to the grating orientation. Pictures on the right show that "peeling perpendicular to the grating orientation" provides better pattern quality for 200nm period grating pattern[98]

2.2 Nip Mechanics

In the continuous R2R UV NIL process, a backup roller is required for several reasons: (1) a backup roller can provide pressure required to fill UV curable resist into cavity of the mold on the imprint roller. (2) To achieve our high-speed continuous manufacturing goal, the air entrainment can happen on the web substrate. Thus, a backup roller is needed to effectively squeeze out the incoming air layer[99]. On the other hand, the backup roller can also help eliminate air bubble defects in the resist filling process. (3) In the continuous manufacturing process, the nanostructures need to be replicated on a web substrate. Therefore, the contact between the imprint roller and the web is a line-contact. Thus, a cross machine direction (CMD) needs to be considered. A backup roller can provide uniform pressure across the substrate. Based on the above reasons, a backup roller is required for the R2R UV NIL process. As mentioned in section 1.1 of the literature review, the apparatus of R2R UV NIL always contains a backup roller.

Nip Contact Mechanics

A backup roller covered with elastomer and an imprint roller with hard surface form a rolling nip pair. The rolling nip pairs have been widely used in web manufacture for a long time. It was mainly used for preventing slip between rollers. Such roller pairs are also used for pressing two or more sheets together for manufacturing laminated products. The rolling nip pairs can remove air on the surface layer of web and increase web tension through the nip contact zone. The increased web tension will increase wound roll tightness, which could prevent failure during wound roll storage and transportation. How to control this increased web tension drew researches' and manufactures' attention at earlier times. Studies about the nip contact mechanics have been done by many researchers. The rolling contact can be traced back to 1882. The Hertz theory[100] assumed elastic contact of frictionless surface. Thus, there was no tangential surface traction across the interface. E.I. Radzimovshy[101] developed Hertz theory. He reported stress distribution and strength condition of two rolling cylinders pressed together. To determine the strength in contact zone of two cylinders rolling together, the variation of stress during loading cycle should be taken into account. He also presented progresses made by other researchers at that time (1953). Bentall and Johnson reported slip in the rolling contact of two unidentical elastic rollers[102]. They considered unsymmetrical stress distribution due to tangential forces transmitted or micro-slip occurring in the contact zone. After the numerical computation, they reported that there were three regions for micro-slip in the contact zone of two dissimilar rolling elastic cylinders: one at each edge of the contact and a third toward the opposite of slip direction. A difference in elastic constants can lead to a different peripheral speed. In the next year, Bentall and Johnson[103] presented an elastic strip passing through a rolling nip pair. They first assumed there was no slip between contacting surfaces. Thus, a shear stress was produced on interface. A micro-slip must exist within nip contact zone by comparing these shear stresses with the normal

stresses. They also reported their results of contact stresses, the indentation of strip, contact width, and the speed of strip passing through rolling nip pair with relation to nip roller rotating speed. Hahn and Levinson[104, 105] reported a frictionless contact between an elastic layer covered cylinder and a rigid cylinder without strip. They also analyzed the situation which assumed slipping over the entire contact surface based on Coulomb's friction law. Batra [106, 107] studied a compressible rubberlike layer bonded to a rigid roller and indented by a rigid rolling using boundary element method. He found out the pressure on contact surface depended on thickness of rubberlike layer and the Poisson's ratio of the layer. Soong and Li [108] studied steady rolling state for two cylinders with a thin sheet in the nip, each covered with an elastic layer to a rigid core. The thin sheet was incompressible in its thickness. They found out that the speed differential would develop an asymmetric shear stress on the contact surface and the nip geometry would be adjusted. The local slippage would not affect the speed ratios when the coefficient of friction was not too low. Later they considered that the asymmetric stress distribution was caused by a pushing or pulling force applied on end tail of the sheet. The local slippage in the contact interface was studied by enforcing exact contact conditions[109].

Nip Induced Tension in Web

Many researchers have conducted studies on the mechanism inside the rolling nip contact zone. On the other hand, the tension in web can be increased after the web passes through the nip. Pfeiffer first described this phenomenon of increasing tension due to nip pressure called nip-induced tension in 1966[9]. He also gave a new term to describe nip-induced tension as wound-in tension (WIT). In the later literature, Good introduced the definition as the tension in the outermost lap of a winding roll and renamed the term as wound-on-tension (WOT). The term WIT and WOT are identical. Since the WOT is more commonly used, thus it is preferred in this document.

One group of studies in the literature mainly focus on empirical study of WOT with various ways to measure WOT in a winding roll. Rand and Eriksson [110], and Pfeiffer [111] introduced a direct measurement method for WOT. Pfeiffer' arrangement is shown in Fig. II-13 (a). The web tension before entering nip contact zone was measured by a load cell which was located at the upstream of web. The nip-induced tension was measured by another load cell after the web went through the nip contact zone. The nip load was controlled by a cylinder/cable system. However, later in 1999, Good et al. [112] proved it was a interfering method. Shortcomings include (1) the inability to determine if the WIT was constant throughout the wind and (2) the signal to noise ratio in the experimental measurement blocked it to be a candidate for measuring WIT during winding. A WIT apparatus was developed at the Web Handling Research Center, as shown in Fig. II-13 (b). The web tension was controlled by a tension controlling unit. The brake at unwinding roll provided the braking torque resulting in tension in web which was measured by a load cell. Then, the web went through the nip contact zone. An idle roller and the nip roller travelled together on a mount which could move on a rail. The nip load was closed-loop controlled by a swing arm. Since the web wrapped the nip roller 180 degrees, the setup prevented web tension affecting the nip load. The WIT at the outer layer of web was measured by another load cell. Pfeiffer reported experimental data of a rolling nip on a stack of paper, which simulated a rolling nip cylinder with an infinite radius cylinder[113]. He observed the outer layer of paper stack moved towards the direction of rolling nip, while the layer beneath outer layer moved the opposite direction. He concluded that there must be an instantaneous center rotation under the contact interface. To understand the mechanism of nip-induced tension in wound rolls, Good and Wu used the same apparatus to measure web tension, which is shown in Fig. II-13 (c). To minimize the effects of elastic hysteresis, an aluminum strip was employed instead of rubber or plastic due to its lower hysteresis but relatively high Young's modulus. Since the deformations of the aluminum strip would be small, a precise method to measure the elongation and nip-induced

tension was necessary. In the experiment apparatus, an aluminum strip was rigidly clamped at one end of the test table. A dead weight was applied to the opposite end of the aluminum strip to provide tension in the web. Aluminum nip roller with different diameters rolled through the strip at various nip loads. The nip-induced tension was measured using strain gages on the aluminum strip. Good and Fikes [114] proposed an indirect measurement method for measuring the wound-on-tension (WOT) with winding models. They used force sensing resistor (FSR) to measure the WOT. The increase of nip pressure resulted in increasing of radial pressures and also increasing the winding tension in constant tension center-wound rolls. With known web properties, a modified Haklel's model[115, 116] can be used to predict winding tension. The maximum wound-on-tension, WOT, for a center roller with an undriven nip roller is

$$WOT = T_w + NIT = T_w + \frac{\mu N}{h} \tag{II-20}$$

where NIT is the nip induced tension, μ is the coefficient of friction, N is the nip pressure in units of load per unit width, and h is the web caliper which yields units of stress for the tension. The expression worked well for kinds of web materials and winding conditions. The limitations of the expression were unknown. Later, Good et al. [112] and Steve [117] found that the estimation of expression (II-20) was too large for increasing nip load.

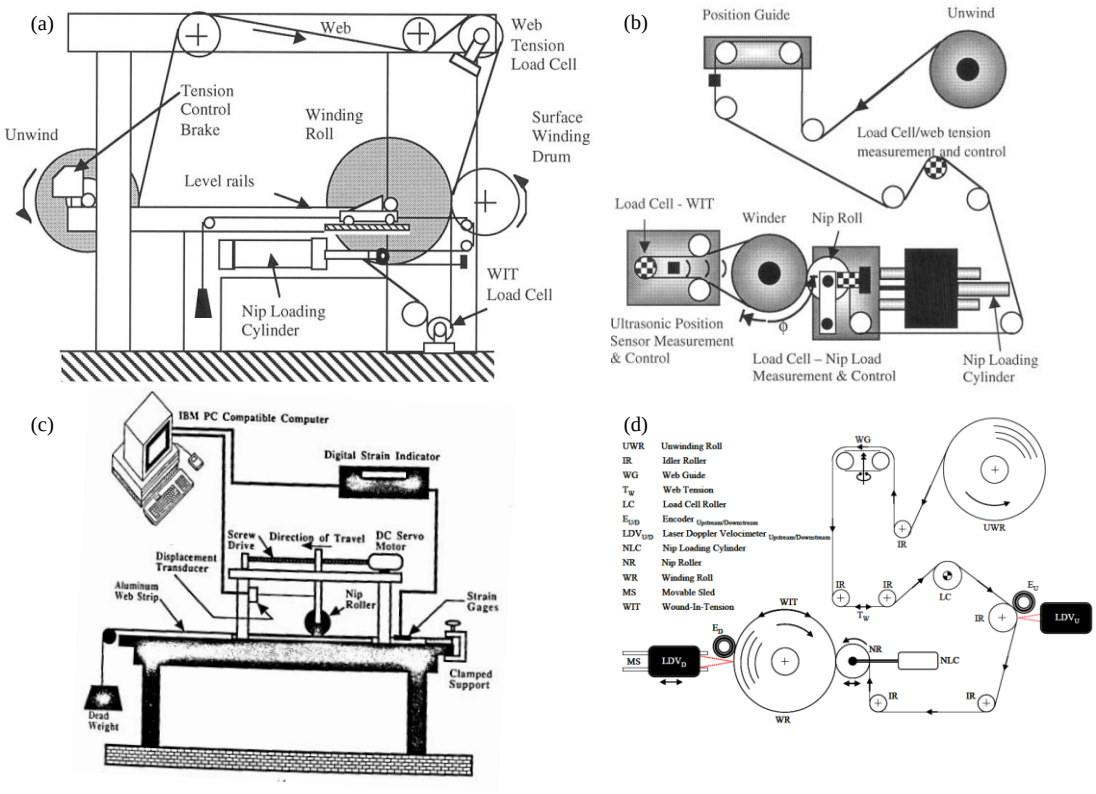

Fig. II-13 (a) Schematic of Pfeiffer's experiment apparatus[111] (b) Schematic of test equipment developed by WHRC[112] (c) Schematic of measurement of nip-induced tension in aluminum strip [116] (d) Schematic of non-contact laser doppler velocimetry method[118]

Good, Kandadai and Markum [118] developed a non-contact method to measure the WOT by applying laser doppler velocimetry (LDV). The method is based on change in deformation of the web. It picked up a first location upstream of the winder where the tension could be measured and a second point where the web had become the outer layer of a wound roll. The difference of velocity divided by upstream velocity gave an approximate MD strain change between two picked sites. Using the strain change multiplied by Young's modulus and cross section can produce the estimated change of web tension between the upstream location where the tension is known and the site where it had become the outer layer of a wound roll. Thus, the final WOT can be the sum of the tension known at the first point and the change of the web tension. The method is based on no slippage between the outer layer of a wound roll and the layer beneath. However, the slippage does exist. Therefore, the second site for velocity measurement must be picked at

several different points to determine where the slippage is located. Jiang [119] developed a non-interfering method to measure the WOT. He used the core pressure and the winding model to infer WOT.

Many researchers also tried to explain the mechanism of WOT or nip-induced tension (NIT). Good and Wu [120] gave their explanation of NIT in their paper published in 1993. A Hertzian normal stress distribution moves along the machine direction on the upper surface of the web in finite element analysis. On the other hand, the lower web surface was refrained by frictional force. An elongating machine direction strain due to compressive Hertzian-like contact stress, which is under the nip roll location, is distributed through the depth of web. As the elongating strain advanced with the moving nip roll, web material attempted to advance in front of the nip. If the web material in the back of the nip is constrained, a net increase in the web tension will result. Good and Wu first provide a basic understanding of elongating machine direction strain. However, their model used Hertzian contact model which does not consider the shear stress at the upper surface of web material due to rolling contact with friction. Later work done by Jorkama [121, 122] showed that Poisson's ratio is not responsible for the slippage. He developed a rigorous contact model for the winding nip, which can calculate the slippage and the NIT in the outer layer. He found out NIT is nearly independent of Poisson's ratio but sensitive to the shear modulus of rigidity. This indicated shear stress and strain are the main reasons for the slippage which results in NIT. In 2001, Good [123] developed a model for predicting NIT which had been proving to agree with trends measured in the laboratory. The model required the input of Poisson's ratio, which is small and difficult to measure. It assumed slippage between the nip roller and the web hardly affected the NIT since the coefficient of friction between web layers is smaller than the one between the web and the nip roller. Arola and Hertzen [124, 125] used the FEM method to analyze the mechanism of NIT by studying layered structure of the paper stack like Pfeiffer's experiment[113]. The slip-and-stick pattern in all contacting surface had been

presented. A detailed movement of interlayer paper sheets is given. They identified the mechanism of NIT as a result of shear stress and opposing frictional force. Kandadai and Good [126, 127] presented a new method of wound roll analysis using an explicit finite element method. In their model, the results showed NIT is proportional to the coefficient of friction of the web layers and the nip load.

Literatures about the pressure distribution in the rolling nip contact zone and nip induced tension (NIT) have been reviewed. To successfully obtain nanopatterns in continuous R2R UV NIL process, slippage between the resist and the web, which can significantly destroy the nanofeatures, must be avoided. The pressure distribution affects the filling time of the resist and also NIT in the web. In addition, the increasing web tension due to NIT could cause slippage in the wrapped area other than the nip contact zone. This slippage also needs to be avoided.

2.3 Measurement of curing UV resist

To accomplish the goal of high speed R2R UV NIL with high-quality nanofeatures on the substrate, it is significant to characterize the mechanical properties of UV curable resist during curing. As we have mentioned above, the resist is filling into the cavity of the mold when it is in liquid phase. Right after the resist-filling step, exposure of UV light will initialize the photo-polymerization. The resist will keep reacting till fully cured. Mechanical properties including Young's modulus, shear modulus, tensile strength and shear strength are of interest because the resist would be deformed and have interaction with the imprint roller during the imprinting step. Due to the interaction between the resist and the imprint roller happening when the resist is reacting, the mechanical properties need to be measured as a function of percent cure. In addition, there could also exist tensile failure of cured or pre-cured nanofeatures during the de-molding process, especially when nanostructures have a high aspect ratio. The pre-cured state of nanostructures is due to the lack of exposure time or low UV light intensity. It is also feasible to reduce the demolding force by releasing mold when the resist is at a pre-cured state[94], followed

by an additional UV exposure step after the demolding process. Additionally, the cationic epoxy curing resin has a dark-curing effect, resulting in polymerization of resin remaining even out of irradiation of the UV source, which would increase the mechanical properties of nano-pattern on the substrates. On the other hand, the shrinkage of the resist by polymerization could affect the demolding process[89], and it may reduce the demolding force and stresses in the nanostructures. The shear behavior between the resist and the imprint roller is due to the friction. Therefore, measuring the coefficient of friction as a function of the conversion ratio would be helpful to increase the accuracy of predicting shear stresses on the resist surface while the nanofeatures are leaving the imprint roller. Comparing the shear stress on the resist surface and the shear strength of a certain percent cured resist can help us to evaluate the potential damage of nanofeatures.

Measuring mechanical properties as a function of the conversion ratio is difficult to accomplish, because the conversion ratio of the polymerization of the resist needs to be measured by equipment, such as a photo differential scanning calorimeter (pDSC)[128-130], a fourier transform infrared spectroscopy (FT-IS)[59, 131, 132] and etc. The conversion rate and the final conversion ratio are directly affected by the UV light intensity as well as the exposure time. A. Maffezzoli et al. [128]reported time-temperature and time-irradiation intensity superposition for photo-polymerization of an epoxy based resin in 2005. They proposed a new time-intensity superposition principle for a cationic epoxy resin to associate a more traditional time-temperature superposition principle. The master curve obtained by experimental data indicated that the temperature or the irradiation intensity have similar effects on the curing process. J.E Manson et al. presented time-intensity transformation[10, 129]. They drew the same conclusions. Additionally, they found there are three stages for the polymerization: the initial stage, gelation, and vitrification. During the gelation, the monomers can move freely with diffusion, while the monomers are relatively fixed in the vitrification stage. Higher intensity increases the rate of the polymerization, which would develop the internal stress. However, the stress built-up can help to

delay the vitrification, thereby higher final conversion ratio. Many researchers reported the same phenomena[133, 134]. Additionally, scholars who cared about mechanical properties as a function of conversion ratio conducted the tests with the x-axis as exposure time under a certain UV intensity. Thus, the production of the exposure time and the UV light intensity will result in the UV exposure dosage.

Measurement of modulus and demolding force

R2R UV NIL was first introduced by Shinill Kang in 2006[50]. Before 2006, most researchers devoted their focus on UV NIL, as a stationary molding process. Therefore, the variation of modulus by conversion ratio did not raise the attention of scholars who studied on UV NIL. However, the curable resist has been widely used for coating, lithography and other fields. S. A. Khan and his team first published the device for measuring rheological parameters of UV curing resist in 1992[135]. They presented a controlled, in situ method to rheologically monitor the material properties when the resin transforms from liquid state through gel point to a solid state. They also use differential photocalorimetry as a complementary method to relate the mechanical properties to reaction conversion. Their device is shown in Fig. II-14(a). J. E. Manson et al.[136] used a rheometer coupled with a UV-light generator to characterize UV curable systems for coating. They measured storage modulus and loss modulus as a function of time. Due to the high reaction rate (50% conversion in less than 0.3s) of the UV curable resist, they also measured viscosity with UV-pulse irradiation. The setup called photo-rheometer was also used to measure rheological and viscoelastic properties of a series of star-branched polyester resins[137]. The setup is shown in Fig. II-14(b). F.A. Houle et al.[130, 138] used a rheometer to measure the storage modulus, but they did not give out the setup. They also did nanoindentation on fully cured resin to measure the viscoelasticity. Other than the modulus they also measure the demolding force and the fracture energy release rate with or without anti-stick layer. R. Suzuki et al.[131] reported storage modulus and loss modulus measured by a rheometer. The setup used a quartz

stage as a substrate for rheometer due to ability of high transmittance of UV light. See Fig. II-14(c). The UV source irradiated to the resist through the quartz stage beneath the substrate. This setup is simpler than J.E. Manson's since they need to introduce light through a mirror and a tube inside the rheometer. They also presented the viscoelastic modulus is a function of the effective exposure time $\sqrt{I}t$ (I is the intensity of the UV source, t is the exposure time). Later in 2012, they proposed the kinetic of polymerization and developed a model of conversion ratio as a function of $\sqrt{I}t$ [139].

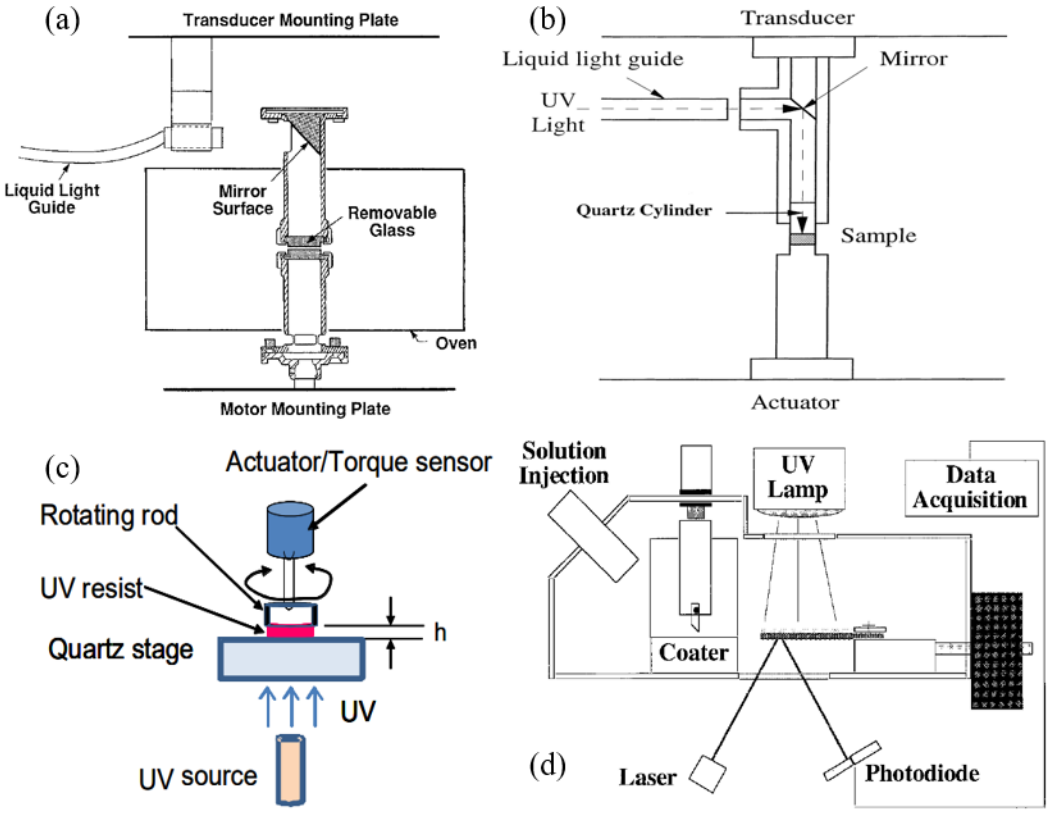

Fig. II-14 (a) Schematic diagram of rheological setup that allows *in situ* gelation of photosensitive materials. UV radiation from the liquid light guide is reflected by the mirror onto the sample placed between two quartz windows[135] (b) Photo-rheometer by J.E. Manson[136] (c) Rheometer by R. Suzuki[131](d) The stress measurement apparatus: a controlled environment combination draw-down coater and cantilever stress measurement device[140]

The kinetics of photo polymerization is briefly explained as follows[141]: Radical chain polymerization is a chain reaction consisting of a sequence of three steps, namely, initiation,

propagation, and termination. The derivation of the rate expression for this polymerization is under a steady-state condition, where the rate of initiation is equal to the rate of termination.

The initiation reaction velocity VR is expressed as

$$V_R = \frac{d[R]}{dt} = 2k_d f [C_i] \tag{II-21}$$

where k_d, f, $[R]$ and $[Ci]$ are reaction velocity constant (decomposition rate constant, typically measured by experiments), coefficient of UV absorption, radical concentration and initiator concentration, respectively.

On the other hand, the velocity of polymerization reaction V_p is expressed as

$$V_p = -\frac{d[M]}{dt} = k_p [R][M] \tag{II-22}$$

where k_p and $[M]$ are propagation rate constant and monomer concentration, respectively. Also, the termination velocity V_t is expressed as

$$V_t = k_t [R][R] \tag{II-23}$$

where k_t is reaction rate constant. In steady state, V_p and V_t are balanced with each other. Thus, radical concentration $[R]$ is expressed as

$$[R] = \left[\frac{2k_d f}{k_t}\right]^{1/2} \sqrt{[C_i]} \tag{II-24}$$

Substituting (II-24) into equation (II-22), V_p can be expressed as

$$\begin{aligned} V_p &= -\frac{d[M]}{dt} = k_p \left[\frac{2k_d f}{k_t}\right][M]\sqrt{[C_i]} \\ &= K[M]\sqrt{[C_i]} \end{aligned} \tag{II-25}$$

Where $K = k_p \left[\frac{2k_d f}{k_t}\right]^{1/2}$

As a result of the polymerization between the monomers, the reaction rate of monomers can be expressed as

$$V_p = -\frac{d[M]}{dt} \tag{II-26}$$

Then, the time dependent monomer concentration is expressed as

$$-\frac{d[M]}{dt} = K[M]\sqrt{[C_i]} \tag{II-27}$$

When the photo initiator is enough in the resin and degradation is ignored, the monomer concentration is derived as

$$[M] = [M_0]\exp\left(-K\sqrt{[C_i]}\cdot t\right) \tag{II-28}$$

Where $[M_0]$ is initial concentration of monomer. As a result the monomer conversion ratio CR can be expressed as

$$CR = 1-\frac{[M]}{[M_0]} = 1-\exp\left(-K\sqrt{[C_i]}\cdot t\right) \tag{II-29}$$

In addition, the rate of photochemical ignition is given by

$$R_i = 2\Phi I_a \tag{II-30}$$

Where I_a is intensity of absorbed light and Φ is the number of propagating chains initiated per light photon absorbed. Then the photo initiator concentration $[C_i]$ is given as

$$R_i = 2\Phi I_a \tag{II-31}$$

$$[C_i] \propto 2\Phi I \propto [C_0]I \tag{II-32}$$

Where $[C_0]$ is the concentration of primary initiator in the resin. Therefore, the conversion ratio can be expressed as

$$CR = 1-\exp\left(-\sqrt{I}\cdot t/\tau\right) \tag{II-33}$$

Like we mentioned above, $\sqrt{I}\cdot t$ is effective time, and τ is related time constant of the polymerization. The thickness shrinkage was also measured in each experiment which can be

calculate total shrinkage ratio for the resist. For the cationic epoxy resin, the polymerization rate was yielded as:

$$R_p = k_p [M] \left(\frac{R_i}{k_{t'}} \right)^{1/2} = k_p [M]^{3/2} \left(\frac{GI}{k_{t'}} \right)^{1/2} \quad \text{(II-34)}$$

A method of measuring stress development is also reported by J.A Payne and L.Francis[140]. They measured the curing resin as a coating on a rigid substrate. The stress measurement apparatus was based on a cantilever deflection measurement principle to study the stress development.

The final conversion ratio and the conversion rate are also strongly dependent on the thickness of resin. B. Golaz and V. Michaud et al.[10] reported the conversion rate and the final conversion ratio decreased with the increasing thickness. Most of activated photoinitiator molecules for the polymerization are produced near the irradiated surface due to light absorbance and must diffuse through the thickness of curing the bulk, especially, in the case of low light intensity. The thickness dependence of conversion was assumed to result from absorption of light described by the Beer-Lamber equation,

$$I(\lambda, z) = I_0(\lambda) \cdot \exp(-\mu z) \quad \text{(II-35)}$$

Where I is the transmitted light intensity after a path length z, I0 is the incident light intensity of wavelength λ, and μ is the attenuation coefficient. The average conversion $\bar{\alpha}$ in a sample of thickness h was obtained by integrating and averaging equation(II-35) through the thickness. Other assumptions are also made. A conversion rate constant is dependent on the UV intensity[133, 142], and the UV light is assumed as a monochromatic light, as expressed in equation

$$\bar{\alpha}\big|_{\lambda,i} \propto \left(\frac{I_0(1-\exp(-\mu h))}{\mu h} \right)^{\beta} \quad \text{(II-36)}$$

Where the exponent β is the power-law parameter that will further be determined by p-DSC results. Their conversion ratio versus thickness results are shown in Fig. II-15.

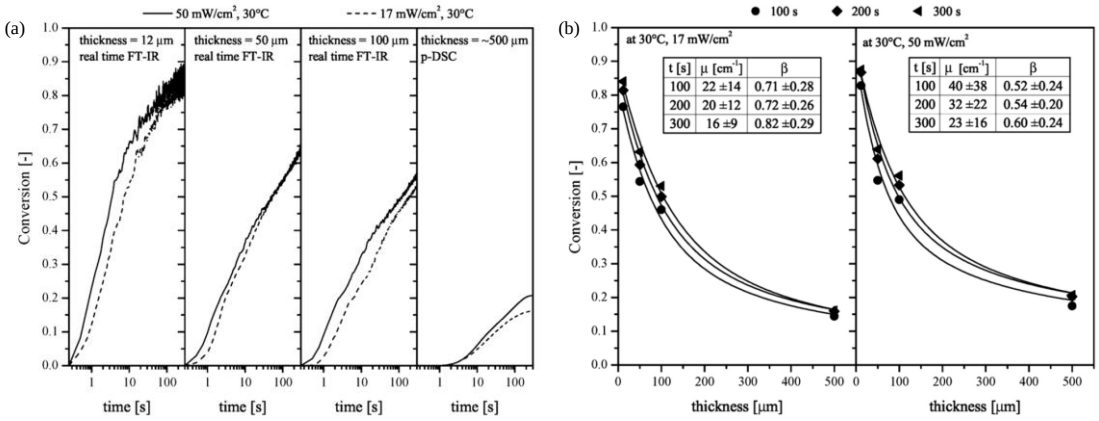

Fig. II-15(a) Conversion ratio versus time for epoxy at 30ºC for two UV intensities (17 and 50 mW/cm^2) and four sample thickness; (b) Conversion versus thickness for epoxy at 30ºC for two UV intensities (17 and 50 mW/cm^2) and three UV-exposure time. The lines are fits in equation (II-36).[10]

S. Nobuji et al. also reported a measuring method for the uniaxial demolding force. They measured the demolding force for a flat mold. The schematic diagram of demolding force measurement is shown in Fig. II-16 (a).The photo of experimental setup is shown in Fig. II-16 (b) The resist underwent spin coating on the quartz substrate, and Si mold was pressed on the resist with an anti-stick layer (fluorocarbon molecular layer) coating. The UV source was put beneath the quartz substrate. The UV light, thus, can expose through the quartz substrate. The demolding force as a function of dosage was reported [143]. Y. Hirai et al. from the same university investigated the relation between the conversion ratio of resist, the demolding force and the elastic modulus. They used storage shear modulus as the elastic modulus. They reported that the increment of the elastic modulus was not synchronized with the conversion ratio. Additionally, the demolding force was not stable till 90% cured. Moreover, the elastic modulus of cured resist before this point was not hard enough for a successful nanopattern transferring. R.Suzuki et al.[144] used the same setup to measure the demolding force and suggested the demolding force as a function of effective exposure time. They made a modification of the setup by adding a

flexible joint between the force gauge and the base of the substrate. The schematic of the setup is shown in Fig. II-16 (c). M. Shirai et al. [93] also studied the relation between the demolding force and the elastic modulus. They measured the demolding force on the same apparatus for measuring rheological behavior and shear moduli, which would reduce the interfering parameter to increase the accuracy of measurement. The demolding force is measured right after the UV resist is cured on the quartz plate. However, it may not be applicable when they were curing a rather thin sample due to its high conversion ratio leading to a higher demolding force. They found out that the demolding force decreased with increasing storage modulus for a smooth surface. One interesting phenomenon they reported is that the demolding force would increase with increasing storage modulus when using a L/S (similar to the line grating pattern) patterned mold. The demolding force required for the vertical surface is ten times higher than the one for the horizontal surface. The demolding force for vertical surface would produce shear stress for the resist.

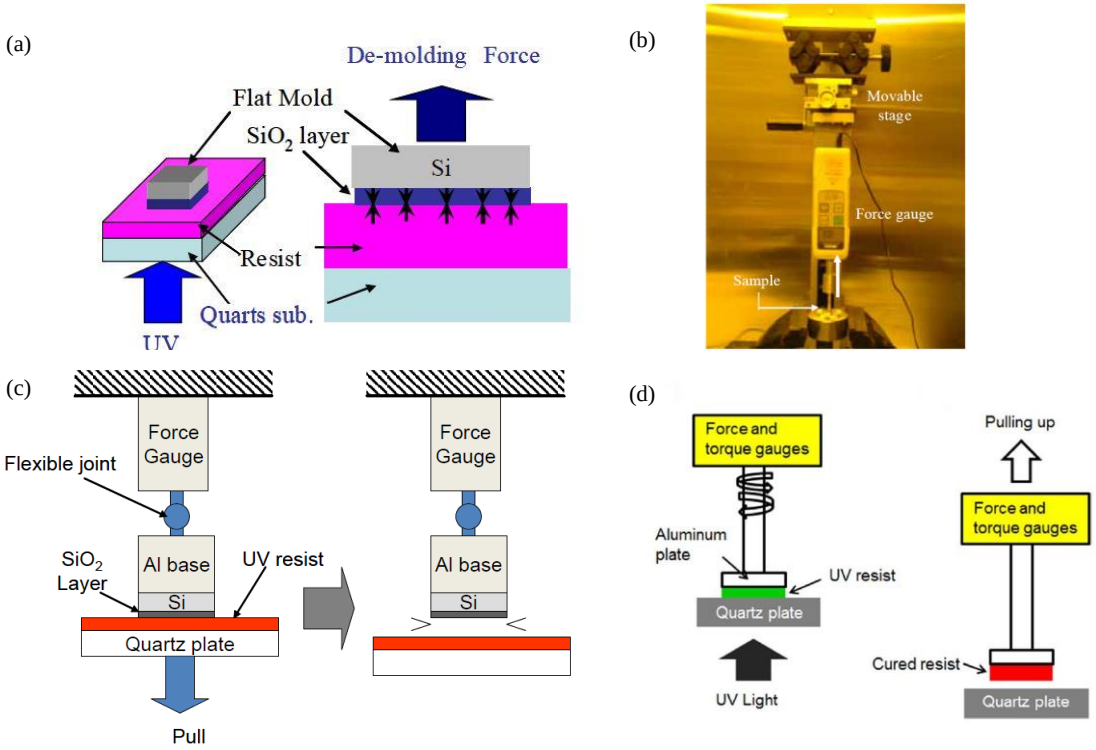

Fig. II-16 (a) Schematic diagram of the demolding force measurement (b) Exact experimental

equipment for measuring the demolding force[143] (c) Schematic diagram of demolding measuring apparatus[144] (d) Measuring the demolding force after curing process on rheometer[93]

The demolding process for continuous R2R UV NIL is more like a peel process. Although uniaxial demolding forces can be a tentative reference, a more accurate measuring method and relative parameters for the demolding process need to be provided. Additionally, an anti-adhesion layer have been applied for the imprint mold to acquire promising nanopatterns transferring. F. A. Houle et al.[97, 130], studied various anti-adhesion layers. They concluded that low reactivity but not low surface energy was of importance for effective releasing. They measured adhesion energies using a double cantilever beam method (DCB) and X-ray photoemission spectroscopy (XPS) to determine the location of the crack path. However, a more specific method to evaluate the demolding process would provide promising accuracy for describing the releasing step. It also increases the complexity of the assessment system. A comprehensive on-line measuring method is lacking now. As we discussed above, the elastic modulus and tensile strength should be enough to evaluate if the nanopatterns can be transferred successfully. On the other hand, shrinkage is also an important factor to affect the demolding process, which we will discuss later.

Measurement of shear strength and shrinkage

The shear strength of the resist plays an important role since frictional behavior and potential slippage could occur in the interaction between the curing resist and the mold on the imprint roller. The shear strength can be measured in many ways, such as single lap joint test, thin wall tubular test and etc. However, the shear strength of resist needs to be measured at different UV dosages, in another word, the conversion ratio. Therefore, the test adherend must be UV transmissible. The UV curable resist, as an adhesive, drew attention of researchers for a long time. R.W. Bryant and W. A. Dukes [145] proposed the design of adhesive joints in 1964. When two thin-walled tubes are jointed coaxially by an adhesive which is normal to axis and of uniform thickness, a simple shear stress distribution would occur. They did the test on steel adherends of various dimensions and reported several parameters which would affect the strength of the joint.

Now this method has developed to a standard measuring method, as known ASTM E229[146]. Other scholars preferred single lap joint tests, because the required test machine is more common. Only universe tensile test machine is needed for this kind of test. Lu and Youngblood [60] reported shear strength measurement for carbon fiber reinforced composite. They did the test to estimate the strength of repaired carbon fiber reinforced composite structure. ASTM D5868 was followed due to the adherend material. One of interesting point they suggested is dark curing of resist as we mentioned before. Since the carbon fiber would block UV lights, they can only cure the resist by exposing it to the UV light for a certain time and then press the adherend on the adhesive to complete the curing process. P. Jojibabu et al. [147]explored shear strength of an adhesive based on epoxy matrix. They followed ASTM D1002[148] since the adhesive can be cured without UV light. A similar standard in Europe is AFERA 4012[149]. The literature of measuring shear strength for UV curable resist with increasing exposure dosage is lacking. However, as the single lap joint test has been widely applied to measure the shear strength of adhesives, a series of standards can help us to determine the test method for the current project. The method will be discussed in the next chapter.

The shrinkage of UV curable resist must happen due to cross-linking of monomers in both cationic epoxy system and free radical system. The shrinkage of resist is of importance because it can affect many mechanical properties and the final quality of nanopatterns. On micro scale level, a correct size of nanopatterns cannot be achieve due to excessive shrinkage. Too much shrinkage would also cause distortion for the nanofeatures as well as internal residual stress which could affect the durability of commercial products. In the demolding step, too low a shrinkage level cannot break mold-resist interface to assist demolding, too high a shrinkage level could lead to higher demolding displacement. Therefore, shrinkage level has been always concerned by researchers as we mentioned in previous sections. Only measuring method will be discussed here. R. Suzuki et al. [131]used their rheometer to measure the storage modulus and shrinkage in

thickness as well. To measure the shrinkage in a more precise way, Gee and Davidson [150] designed a modified dilatometer for continuous recording of volumetric polymerization shrinkage of composite restorative materials. Measurement of volume change can also be applied by using a dilatometer with a mercury-filled capillary for monitoring polymerization processes[151]. Other researchers test the shrinkage by assessing the change of thickness like R. Suzuki. J.A Manson used a laser interferometer to measure the change of thickness of resist[152]. J. Park et al. [153]measured the shrinkage of thickness by a linometer. Briefly, a certain amount of resist was placed on a stainless steel plate and covered with a slide of glass which is fixed. The axial shrinkage would be measured by movement of the steel plate by a displacement sensor and transducer over time.

Measurement of adhesion behavior

A huge volume of methods to estimate the strength of adhesive bonds at the interface between the materials have been developed[154-156]. Researchers made a distinction between methods. The intrinsic and unvarying property of the material pair measured by one specific method[154, 156], may be different from the strength measured by other method[155, 157]. Therefore, a method of assessing adhesion strength in a more accurate way to simulate the conditions of the real situation of interest is a key criterion for selecting the test method. Some of the well-established adhesion measurement methods are evaluated by how well they emulate the conditions of the demolding in practical applications.

Tension or pull tests are straightforward in concept and simple in execution. There are standards came from ASTM C633, D2095. The ends of two cylinders are bonded, and specimen is subjected to a normal tensile load. Then tensile strength at where the bond fails is taken to be the strength of the adhesive joint. Tension test have a significant advantage of simplicity. However, the specimen we are testing needs to be exposed to the UV light. The cylinders cannot be transmittable for the specific range of UV light. Pull tests have been applied to measure the

intrinsic adhesion between polymers and mold materials in nanoimprint lithography[87, 158, 159], and to measure the demolding forces in NIL[18, 91, 93, 96, 160]. However, in the practical roll-to-roll situation, the nanoimprints are always peeled from the mold roller. The separation starts by the edge of exit area of the imprint roller, rather than pure normal forces.

Blister test is another common test to evaluate the adhesive strength of a resin. The hydrostatic pressure is applied to the adherend through an hole in the substrate in a blister test[155, 161]. As the UV 15 is a low viscosity liquid before irradiating by the UV light, the uniformity of UV 15 cannot be assured during applying the fluid pressure. Moreover, the strain energy release rate increases with increasing blister radius, resulting in unstable test condition[161].

Razorblade or wedge test (ASTM D3762) as well as cantilever beam test (ASTM D3433, D3807) are requiring the substrates have a certain thickness, which is not the practical situation for roll-to-roll NIL.

Peel test is commonly used to assess the strength of adhesion. Some peel tests are applicable for a stiff substrate and a flexible adherend. For example, pressure-sensitive tape test (ASTM D3330), 90 degree peel test, 180 degree peel test for adhesion to metals (ASTM D903). Peel tests have been applied to evaluate the adhesive strength in flexible materials such as UV-cured acrylate [15] and PDMS[162]. T-peel testing was used to assess the failure modes of PDMS-PDMS integrity[163]. In the T-peel test, the adherends are both flexible substrates. The bonded area is easily to be accessed for the UV light. The bonding strength characterization in terms of two parameters are commonly used in linear elastic fracture mechanics (LEFM): fracture energy and the surface energy at the bonded interface (toughness). The T-peel test is applied in this report and described in details.

2.4 Research Summary

Literature Summary

From the above literature review, the development of continuous R2R UV NIL process and the main challenges we are facing have been shown. In the first part of review, it is obvious that R2R UV NIL process can be a promising high-output manufacturing method for high-quality, low cost nanostructured products. Many studies have been done for various steps in the R2R UV NIL process. The resist filling quality can be determined by adjusting the resist filling time. The nip contact is required for several reasons and it would be a potential source of defects in the manufacturing process. Therefore, in the second part of the review, the nip mechanics has been discussed for this reason. After the resist fills into the mold, it passes to the UV curing step, which is affected by the distribution of the UV light. Works for simulating and calculating UV light distribution of LED arrays and the cylindrical mercury vapor lamps have been reviewed. The resist is in contact with the ETFE mold wrapped on the imprint roller. The mechanical properties which would have impact on tensile or shear stress and strain are necessary to be measured as a function of curing level. The curing level is directly related to the process speed. In the third part of the review, the research focused on measuring mechanical properties have been reviewed. However, some of the mechanical properties measuring methods are lacking. The demolding step is of importance, though it is the last step of the continuous manufacturing. To accomplish high-quality nanopatterns transferring, the nanofeatures cannot be destroyed by demolding force. Many studies have been done for the nanoimprint lithography in last decades since it was first invented. There are still blanks and new challenges for the R2R UV NIL.

- Since the resist is an adhesive, it thus may stick into the cavity of the mold. Therefore, the coefficient of friction and the adhesive properties at the interface between the resist and the imprint roller is of importance to be measured for perfecting our model of simulation. The measurement

of coefficient of friction for a curing resist or some other materials whose properties vary with UV exposure dosage is lacking.

- The shear strength of the curing resin is an important criterion to determine if there is damage or distortion on the nanoimprints. The method to measure the shear strength of a curing resin at a certain strain-rate is lacking.
- The demolding of the cross-linked nanostructured polyacrylate from a fluorine-based mold is not an easy job. To study the mechanism during the demolding process, a nano-scale numerical model involving adhesive and friction properties at the interface, shrinkage of the polyacrylate needs to be established. Literatures about this kind of numerical model for roll-to-roll NIL process is lacking.

Research Objectives

The focus of this research is to develop simulation tools that can predict whether defect-free production can be produced. The simulation tools include two dimensional scales: macro-scale and nano-scale. The simulation tools will enable those who design imprinted surfaces based on geometric requirements to predict whether that surface can be commercially produced. This will also enable UV-NIL manufacturing to move from a trial-and-error approach to a predictive mode where extraction success can be known prior to moving to the manufacturing environment. Manufacturers of UV resins typically will provide their estimates of shrinkage, tensile strength and modulus properties for their resin. The research objectives will be to:

- Characterize the properties of a UV resin (UV 15) as a function of process speed. Establish a material model which can describe the material behaviors on the manufacturing process line.
- Conduct macro-scale simulations with practical contact conditions, where the objective is to adjust operating parameters to eliminate slip between the cured resin and the imprint roller.
- Establish a nano-scale numerical model to analyze the mechanism during the demolding process, where the objective is to predict if defect-free nanoimprints can be produced.
- Conduct R2R UV NIL trials in the laboratory to validate the prediction of the simulation tools.

CHAPTER III

III. Characterization of UV 15

The characterization of UV curable resist as a function of the curing level is important for conducting meaningful simulations. The curing level is mainly determined by the process speed. Based on the literature review, the curing rate and final cured ratio are determined by UV intensity and dosage. In this chapter, the experimental equipment and methods used to characterize the properties of UV curable resist are described. Based on the literature survey, the UV resin has an optimal wavelength for curing, which is centered about 365nm. Cationic resins that curing is also related to the square root of the UV light intensity (I) times time (t). UV exposure is typically quantified as the product of UV intensity and exposure time. The rheometer UV light accessory has a limit to a maximum intensity of 150mW/cm^2 which is much less than the UV light intensity used on the process line. Currently, in our UV-NIL R2R tests in the laboratory, an intensity of 2600mW/cm^2 is used. This find allows us to project the storage and loss modulus data taken in the rheometer to the intensity of 2600mW/cm2, which is the practical condition in the R2R UV-NIL tests that are being conducted in the lab. To compute the stress distribution, the shrinkage, modulus, and adhesion toughness, as well as the friction at the interfaces between the resin and the mold are necessary to be studied. The tensile strength and shear strength are necessary to analyze the tearing failure of the nanoimprints. As the UV resin

have different properties at the various curing levels. A consistent curing level is determined by the effective irradiation energy dosage of UV light. The UV curable resin used in the current project is called “UV 15” which is provided by Master Bond Inc. It is a low viscosity, one component, UV curable epoxy-based system. However, most of the mechanical properties of this UV curable system are blank. Therefore, various methods for characterizing the properties of the UV resin is applied. As we have mentioned in the introduction, the epoxy-based UV curable system has a so-called “dark-curing” effect. Once the cross-linking of the polymer has started, the reaction will continue until the end of cross-linking even if the UV irradiation source is removed. Additionally, the high speed of the manufacturing process narrows the time-span for curing the UV resin. Therefore, traditional measuring methods may not be applicable to this project. The functional requirements and detailed arrangement of the experimental apparatus are discussed, and the fabrication methods of producing specimens are presented. The procedures of experiments are described which are according to ASTM standards.

3.1 Measurement of rheology behavior of UV 15

The UV 15 is a kind of UV curable resist which has a low viscosity. Therefore, measuring its viscoelastic modulus by a rheometer is a good choice to determine its rheology behavior. Meanwhile, to measure the storage modulus as a function of percent cure, continuous UV exposure is required to maintain the polymerization of the resin. To accomplish the measurement of mechanical modulation of resin characteristics by UV exposure, a traditional rheology meter with a quartz stage is used.

Rheology meter setup

The setup of the experiment is similar to R.suzuki’s[131]. The schematic diagram of the UV rheometer is shown in Fig. III-1 (a). The UV resin is dropped on the quartz stage which has a high capability to transmit 365nm UV light. A rotating rod with a steel plate is placed on the resin. This rotating rod is connected to the actuator and torque sensor. Then the rod starts to

rotate, the torque is applied to the resin by the steel plate. The response torque signal which is used to calculate the stress is recorded by the same rotating rod. After a few seconds, the rheological response of the resin tends to be steady. Then UV LED light switches on and irradiates through the quartz. The applied torque and the response including phase lag are measured by the sensor under a certain rotational frequency.

All the rheology tests were conducted using a strain-controlled rheometer (TA Instruments) with a UV curing accessory, as shown in Fig. III-1(b) and (c). The diameter of the parallel plate is 20 mm. Note that large plate sizes are not commercially available since it is difficult to provide radially uniform intensity at larger diameters through LED arrays. The UV LED in the UV curing accessory can provide a 365nm wavelength with peak intensity of 150mW/cm^2. There is no decay in the intensity of UV light. All the experiments were monitored using small amplitude dynamic oscillatory time sweeps, where time 30s represents the start of UV irradiation.

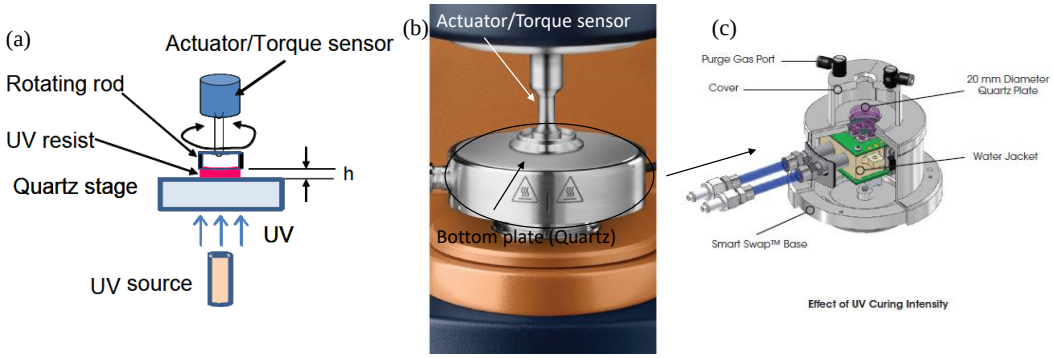

Fig. III-1 (a) Schematic diagram of apparatus of UV-Rheometer (b) Photograph of rheometer (bottom part in the circle was replaced to UV curing accessory (c) Schematic of the structure of the UV curing accessory (contains purge gas unit, Quartz plate, UV LED unit, and output cables)

All rheological experiments were conducted by J. Wallace from Mechanics of Smart and Soft materials lab in OSU.

Experiment results and discussion

The reaction rate is related to the intensity of the UV light. It is also beneficial for us to find out if higher intensity can accelerate the polymerization. Therefore, the tests are conducted under different intensities, which is shown in Table III-1.

Table III-1 Intensity of UV irradiation source for tests

Test number	Intensity (mW/cm^2)
1	5.8
2	30.8

The storage modulus and loss modulus are mainly concerned. The results of test 1 and 2 are shown in Fig. III-2. Time zero is when the monitoring starts. A 30s period is used for the test machine to reach a steady state. After the 30s, the UV irradiation source is switched on. Based on the results of rheology tests, when the UV light does not turn on, the UV resin is still in a liquid state. The sample behavior shows typical solution characteristics. The loss modulus is higher than the storage modulus. When the UV light is switched on, the storage modulus and loss modulus increased steeply. The results showed its value for the time-intensity superposition. Based on the kinetics of polymerization for cationic resins, the reaction ratio is related to the effective exposures instead of the energy of exposure[141]. In section 0 of the literature review, the deduction was shown.

$$R_p = k_p [M] \left(\frac{R_i}{k_{t'}} \right)^{1/2} = k_p [M]^{3/2} \left(\frac{GI}{k_{t'}} \right)^{1/2} \quad \text{(III-1)}$$

where R_p, k_p, $[M]$, k_t ,R_i are ratio of polymerization, reaction velocity constant, the concentration of monomer, UV absorption constant, and polymerization ratio for the initial stage, respectively. Therefore, the polymerization ratio is directly related to$\sqrt{I} \cdot t$ instead of the energy of exposure, $I \cdot t$.

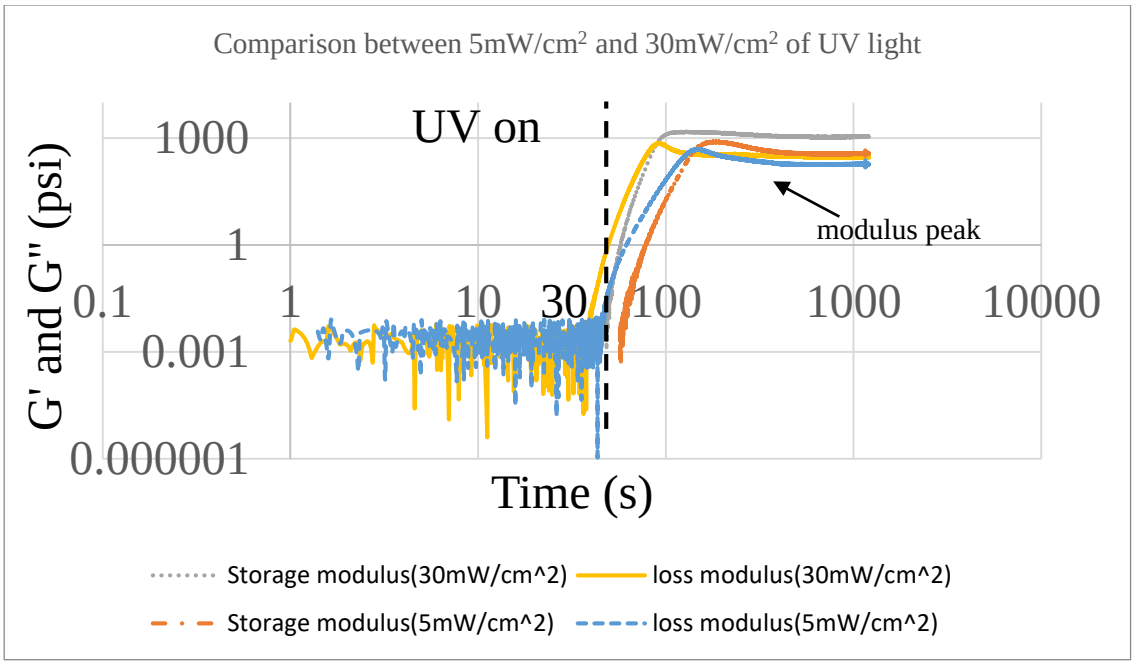

Fig. III-2 Time sweep at 62.8 rad/s during constant UV irradiation. The UV light was turned on after 30s sweeping.

An equation that can predict the reaction ratio for different UV intensity is given.

$$t = \sqrt{\frac{I_0}{I}} t_0 \qquad \text{(III-2)}$$

where t and t_0 are superposed time and test time, respectively. I is the objective intensity, and I_0 is test intensity. In Fig. III-2, it takes 200s when storage modulus and loss modulus reach its peak for 5mW/cm^2, while 100s for 30mW/cm^2. The comparison of the effective energy and the energy are shown in Table III-2. Obviously, the effective energy of both tests is close to each other. Therefore, equation (III-2) can be a valid method for time-intensity superposition.

Table III-2 Comparison of effective energy and energy

	5mW/cm^2	30mW/cm^2
Effective energy$\sqrt{I} * t$	383	380
Energy$I * t$	2100	850

Rheology test is a practical and continuous method to measure the mechanical properties of UV 15 with its phase transfer. In the manufacturing line, the process speeds of 6, 10, and 14mpm are

most concerned. The process speeds are corresponding to the exposure time of 5, 3, and 2 seconds. The storage modulus and loss modulus for the equivalent exposure time are shown in Fig. III-3 and Fig. III-4. The equivalent exposure time is calculated by equation(III-2). The superposed storage modulus and loss modulus show a good agreement.

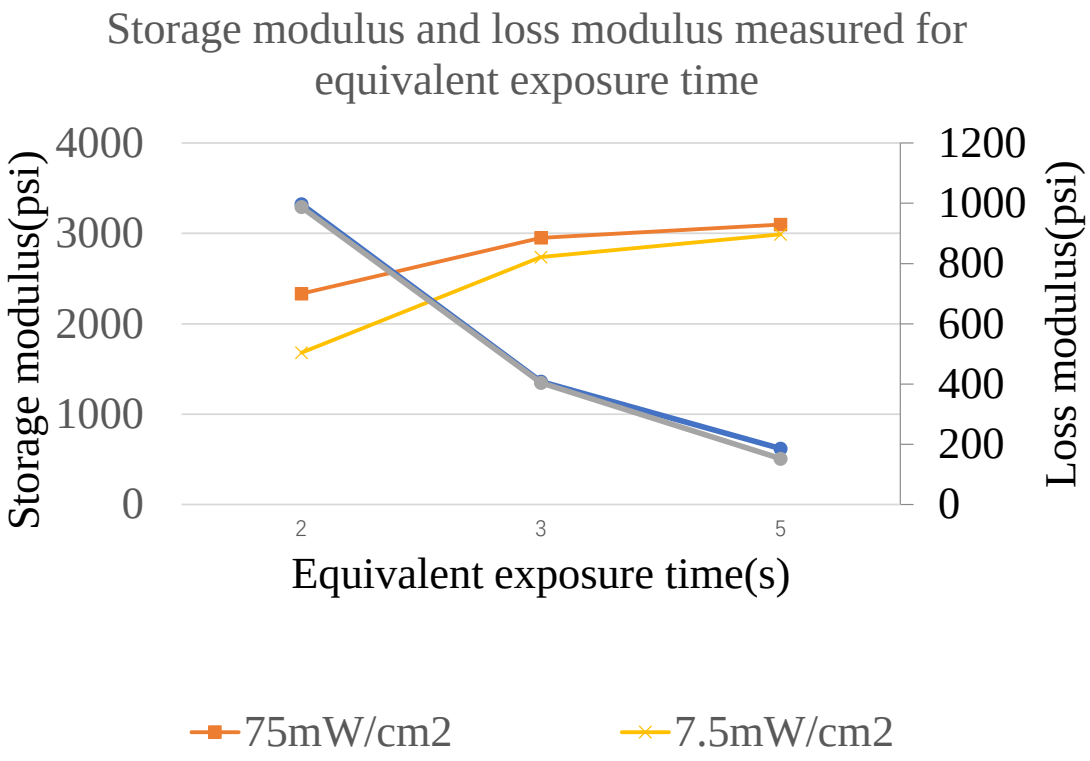

Fig. III-3 Storage modulus and modulus for intensity of 7.5 and 75mW/cm^2 at the equivalent exposure time of 2, 3, 5s

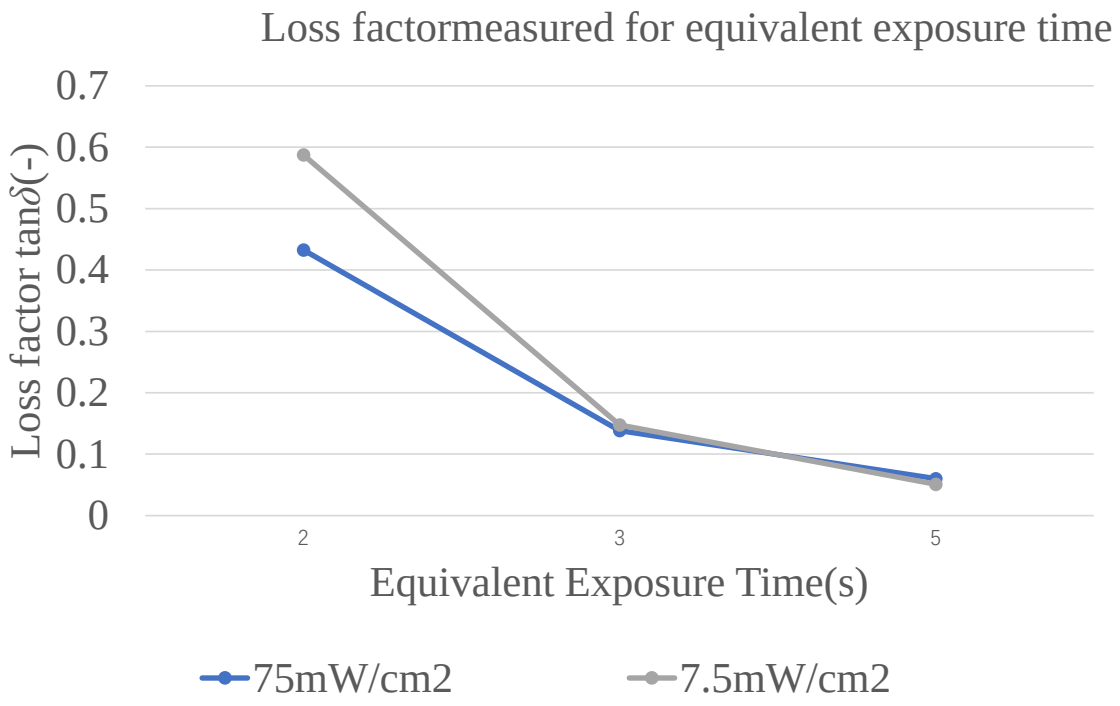

Fig. III-4 Tan delta for intensity of 7.5 and 75mW/cm^2 at the equivalent exposure time of 2, 3, 5s

3.2 Experimental characterization method considering dark curing

The UV curable resin is, once cured, easily characterized with classical viscoelastic measurements such as Dynamic Mechanical Analysis tests, measuring the storage and loss moduli, which can lead to the identification of the Generalized Maxwell model parameters. Generally, curing of resin with UV radiation is divided into four stages: Induction, vitrification, gelation, and post-cured[10]. In the UV-NIL process, UV curable resin reaches the post-cured stage when it is still in contact with the imprint rollers after the UV exposure. The extremely short and high energy UV exposure initiates the crosslinking process but the curing keeps occurring after this exposure and the material properties evolve for a day after curing. This phenomenon, called dark curing, is accentuated by the extremely short time scale of the UV exposure in the nanoimprinting process. Because web handling processes happen at a relatively high speed to increase productivity, the nanoimprinted web will be subject to mechanical loading in a short

time after the UV exposure. The high process speed will result in a high strain-rate in the nanoimprints during the extraction. To characterize the viscoelasticity of the UV 15, a multi-wave method specifically addressing the concerns raised by the presence of substantial dark curing in the UV resin was designed.

Experimental method

The experiments are performed using a Dynamic Mechanical Analysis apparatus (TA Instruments RSA-G2). The time decoupling is achieved by using the normal time scale as the dark curing time and the frequency of the imposed strain sinusoidal waves as the viscoelastic time.

A specimen of resin of 30mm length, 9.6mm width, and 1.183mm thickness is placed in the apparatus right after UV exposure (67 seconds). An arbitrary wave $\varepsilon(t)$ combining multiple sinusoidal signals of varying frequency (equation(III-3)) is imposed to the material for a period of 60 minutes.

$$\varepsilon(t) = \sum_{i=1}^{N} a_i \sin(2\pi f_i t) \qquad \text{(III-3)}$$

where f_i and a_i are the chosen frequencies and corresponding signal amplitude constants. The coefficients defining the imposed wave are $a_i = 0.05\%$ for all terms and $f_1 = 1$Hz, $f_2 = 5$Hz, $f_3 = 10$Hz, and $f_4 = 15$Hz.

The stress is continuously recorded through time during 60 minutes. During these 60 minutes, dark curing occurs in the resin, influencing its stress response to the arbitrary strain wave. By the definition of linear viscoelasticity, the stress response will be of the form

$$\sigma(t) = \sum_{i=1}^{N} b_i \sin\left(2\pi f_i t + \delta_i\right) \qquad \text{(III-4)}$$

The stress signal is then processed in MATLAB® with a Fast Fourier Transform to isolate the response to each frequency and determine the norm of the complex modulus $\|E_i^*\| = b_i/a_i$, and loss factor $\tan \delta_i$.

From the norm of the complex modulus and the loss factor, one can compute the storage modulus *E'* and the loss modulus *E''*. which are material properties fully characterizing the viscoelastic behavior. Finally, the coefficients of the resin relaxation modulus can be identified from the storage and loss moduli using equation(III-5) and (III-6).

$$E'(\omega) = E_{\infty} + \sum_{i=1}^{n} \frac{E_i \omega^2 \tau_i^2}{1+\omega^2 \tau_i^2} \qquad \text{(III-5)}$$

$$E''(\omega) = \sum_{i=1}^{n} \frac{E_i \omega \tau_i}{1+\omega^2 \tau_i^2} \qquad \text{(III-6)}$$

where ω is the angular frequency.

The experiments were conducted by Manogna Jambhapuram[164] from Mechanics of Smart and Soft materials lab in OSU.

Results and discussion

The data has been acquired on UV15 resin and shows the increase of modulus during dark curing for all frequencies from 1 to 15Hz. The evolution of the storage modulus and the loss factor of the resin during dark curing are shown in Fig. III-5 and Fig. III-6, respectively. In all time scale, the storage modulus shows a trend of increasing with the increase of frequency. The loss factor shows a decreasing trend with the increase of frequency. An assumption that the trend of the loss factor will continue with a higher frequency. In the practical process line, the UV resin will mainly show elastic behavior due to the high strain-rate of the nanoimprint during the extraction. The material model used in the simulation of the extraction is based upon this assumption.

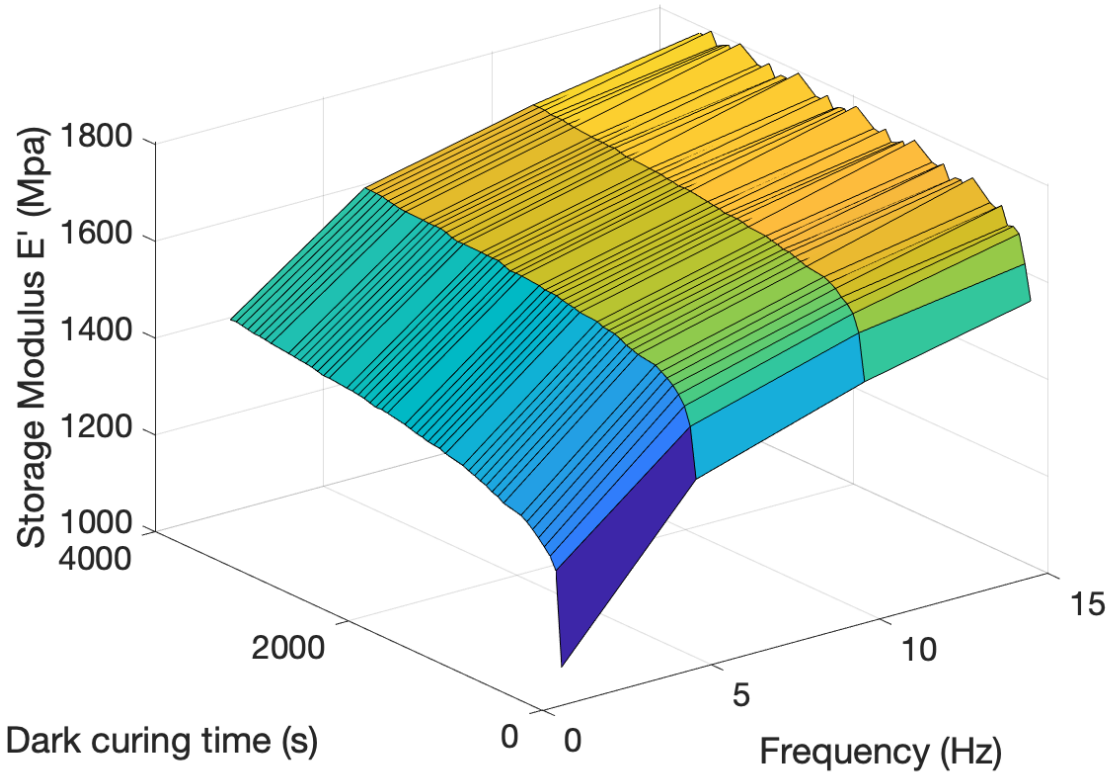

Fig. III-5 Evolution of the storage modulus of the resin during dark curing.

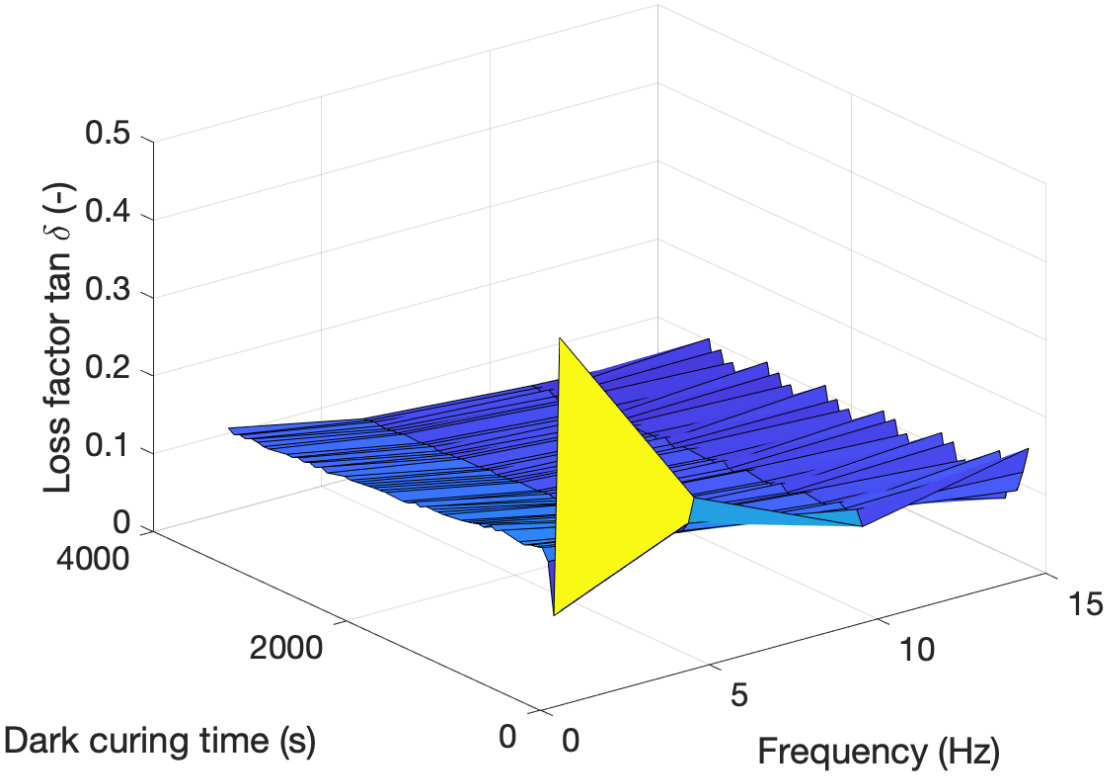

Fig. III-6 Evolution of the loss factor of the resin during dark curing

3.3 Measurement of shear strength and modulus for UV 15

Since there can be shear stress between the curing resin and the mold on the imprint roller, knowledge of the shear strength of the resin is important in determining if the nanofeatures could be fractured by these shear stresses. There are several methods to measure the shear strength for adhesives, such as lap joints test, thin-wall tubular test, and so on. However, measuring shear strength as a function of curing level for resist needs the adherend to be UV transmittable. Due to the limitation of choice for adherend and feasibility of the test, a single lap test is conducted in this document.

Single lap joint setup

UV 15 is a low-viscosity UV curable epoxy-based system. The UV 15 is in a liquid state without any adhesion at the interface between the flexible substrate and the mold. A vertical single lap joint is not only facing the difficulty of self-alignment but also hard to produce the specimen assembles without pre-irradiation of the UV light. Therefore, a vertical single lap joint with a continuous UV source is not feasible. To conquer the difficulties, a horizontal single lap joint is designed, shown in Fig. III-7. The platform is driven by a DC motor and a screwed driven system. The speed of the platform is controlled by an adjustable power supply system. The measurement of the testbed is monitored by a program of LabView. The schematic diagram of the control and monitor program is shown in Fig. III-8. The picture of the testbed is shown in Fig. III-9.

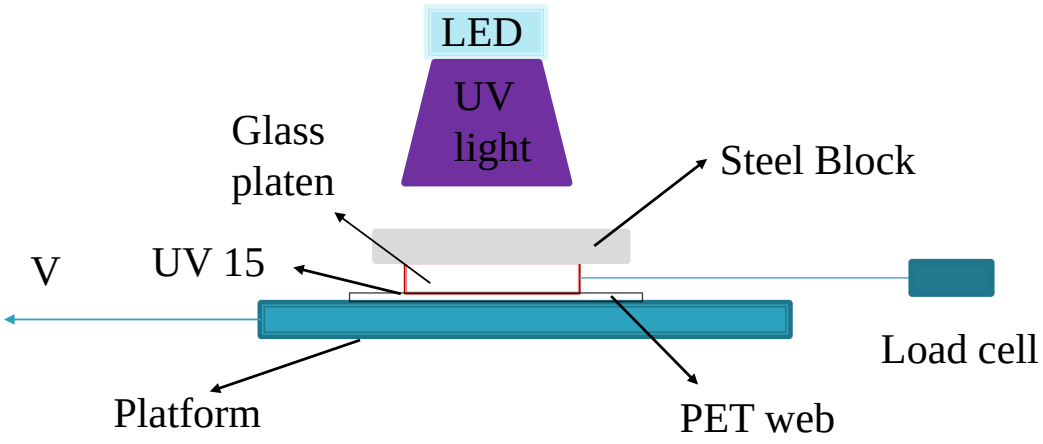

Fig. III-7 Setup of horizontal single lap joint shear test

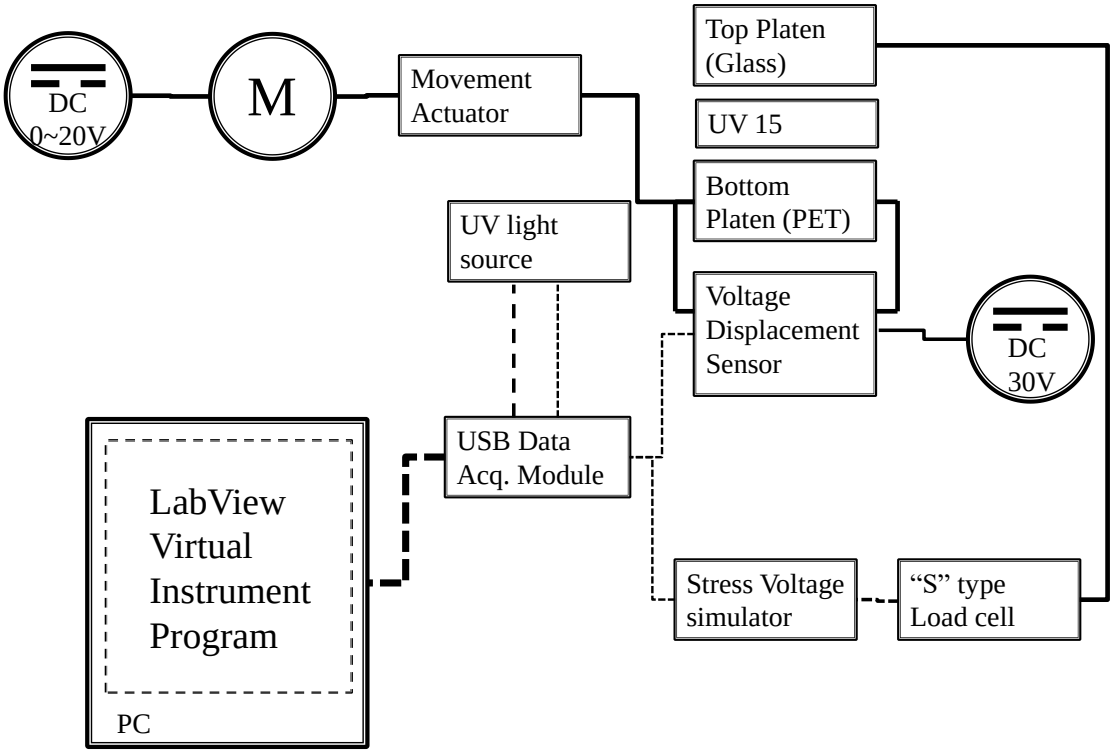

Fig. III-8 Control program flowchart

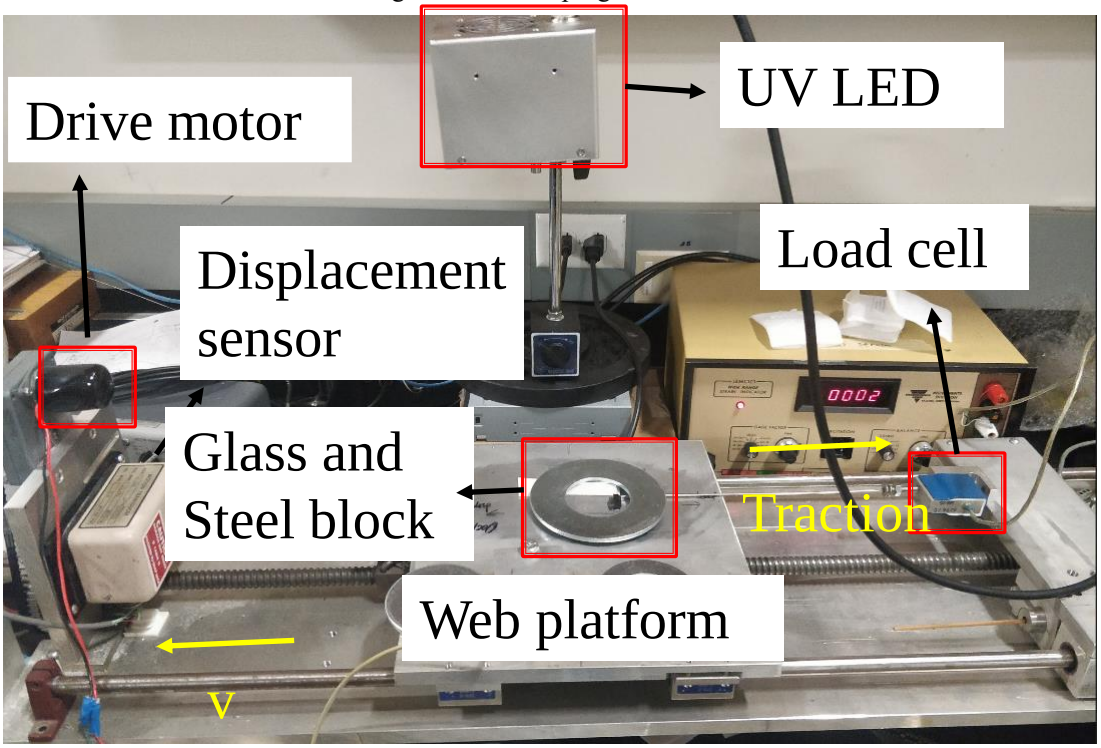

Fig. III-9 Photo showing testbed including plates mounted on the screw, motion system, UV irradiation source

In the technique sheet of UV 15, there is no requirement for surface treatment for clear glass, acrylics, and polycarbonates. Nevertheless, it is better to clear the surface of the webs. Physical treatment by wiping with methanol at room temperature is required according to ASTM D2093. After clearing the surface, a small drop of UV15 is dropped onto the PET web, followed by putting the glass top plate on the adhesive as settled in Fig. III-9. The UV LED array moved right above on the glass plate to assure the intensity of the UV light was 2600mW/cm^2.

Before an experiment, the computers that monitor the test are booted and the software is executed (LabView). The glass plate is mounted to the load cell. The PET web is mounted on the steel platform of the testbed. The bottom plate is aligned to a suitable position. The displacement is zeroed by adjusting the parameter in the LabView. Once the testbed is prepared as above, a drop of UV 15 is placed onto the PET web. The glass plate is aligned by eye.

Results of the shear test

The load at failure and the type of failure (cohesion or adhesion) for each specimen were recorded by the software. All failing loads were expressed in the unit of psi. Calculate the shear stress and shear strain with the equation (III-7)**Error! Reference source not found.**.

$$\tau = \frac{V}{bL}$$
$$\gamma = \frac{d}{t} \qquad \text{(III-7)}$$

where V is the failure load, bL is the area in shear, d is the failure displacement and t is the thickness of the resin. A typical shear force versus displacement curve at a process speed of 6mpm was shown in Fig. III-10. The shear force increased monotonically once the bottom plate started to move until the upper plate was pulled apart from the PET web. The maximum shear load was the load of UV 15 that can withstand under the condition of 2600mW/cm^2 for 5s. The typical failure mode of the single lap joint test was a cohesive failure, as shown in Fig. III-11,

which provided a good estimate of the shear strength. Table III-3. The shear strength is calculated by equation(III-7), as shown in Table III-3.

Table III-3Shear modulus and shear strength under process speeds

Process speed(mpm)	Exposure time(s)	Shear modulus(psi)	Shear strength(psi)
6	4.8	2861	511
10	2.88	2519	302
14	2.05	1464	208

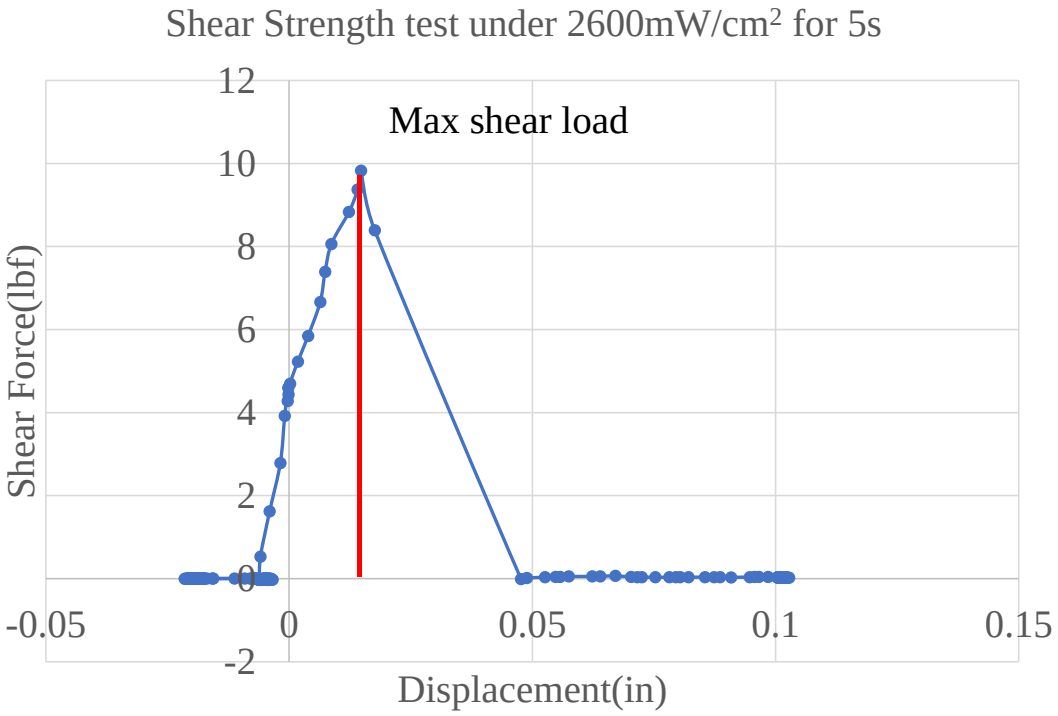

Fig. III-10 Shear force versus displacement under 2600mW/cm^2 for 5s

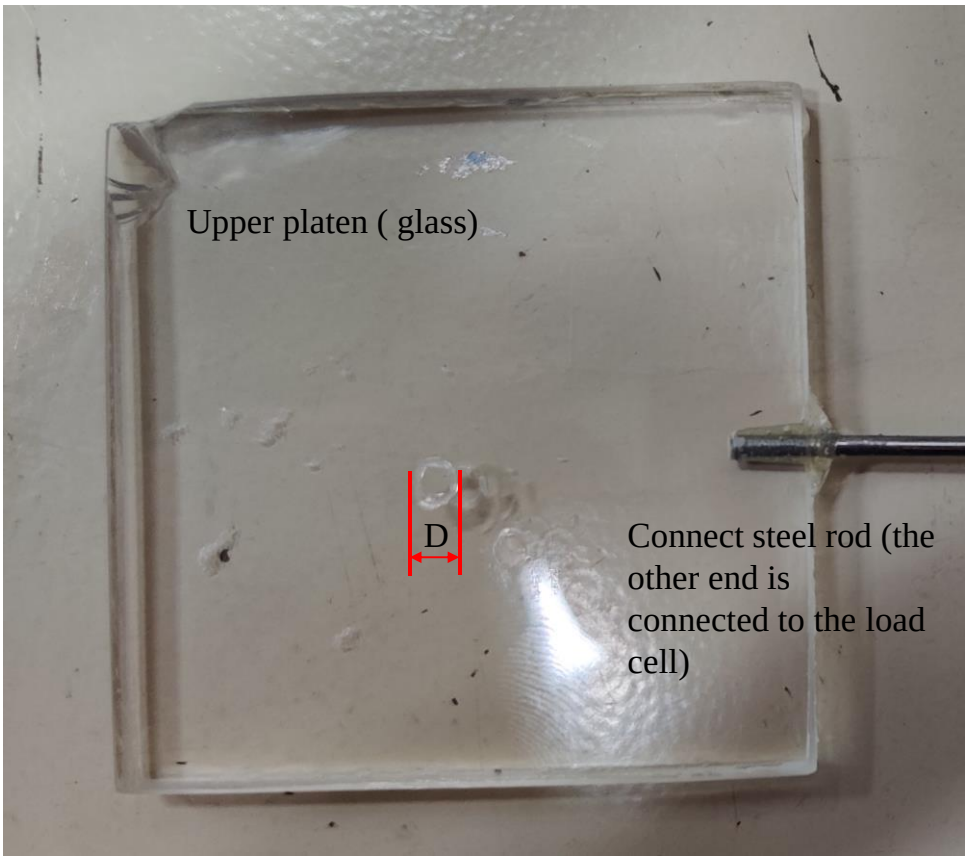

Fig. III-11 The diameter measurement of the single lap joint. The failure mode is cohesive failure.

Since the strain-rate for a shear test is a parameter that we concerned, the shear test for different shear strain-rates were conducted as well. Due to the limitation of the capability of the testing equipment, the strain-rate was ranged from $0.26s^{-1}$ to $0.75s^{-1}$. The shear strength was plotted in Fig. III-12. The shear strength under the strain-rate range from $0.26s^{-1}$ to $0.75s^{-1}$ does not show a big difference. Since on the practical process line, the strain-rate of the nanoimprint is much higher, the elastic behavior will be shown in the material is assumed. Thus, the shear strength of UV under various process speed will be used, as shown in Table III-3.

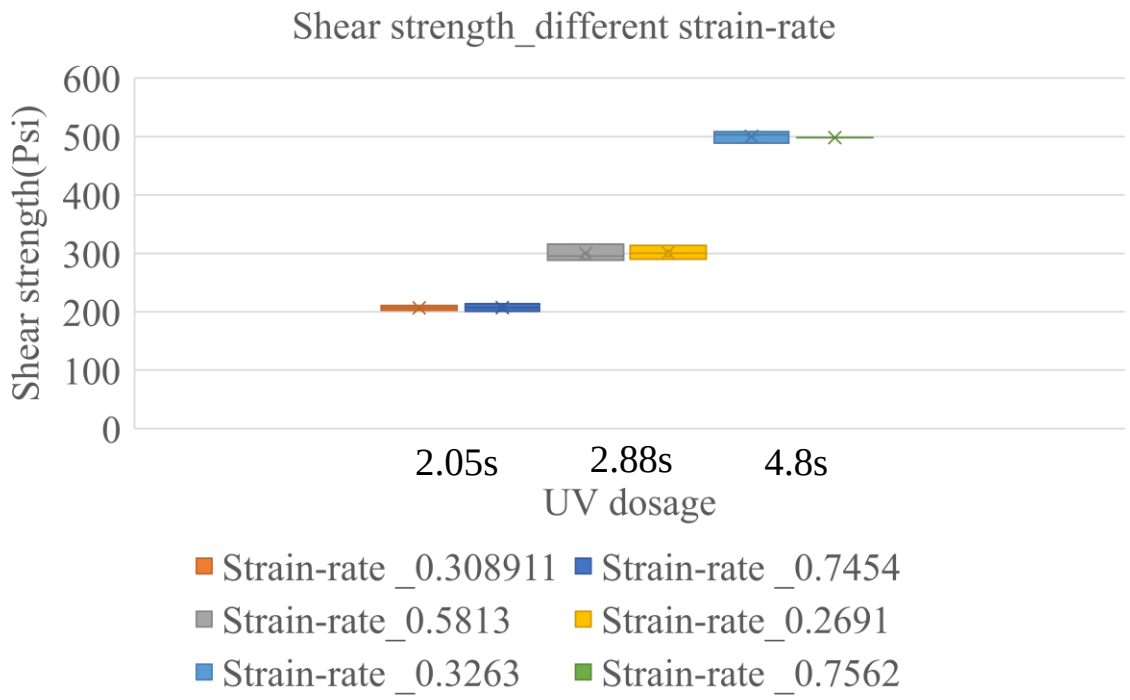

Fig. III-12 Shear strength of UV 15 under exposure time of 2, 3, 5s with different strain-rate

3.4 Measurement of coefficient of friction

With the increase of curing level of the UV 15, the friction behavior at the interface between the resin and the mold differs. The variation of coefficient of friction plays an important role in affecting the stress distribution in the nanoimprint. To predict the failure of the nanoimprint, a measurement of coefficient of friction shows necessity. In the current numerical simulation, Coulomb friction in user subroutine FRIC using the penalty method is applied. Therefore, a measure of Coulomb friction according to ASTM D1894 is designed to satisfy the requirement.

Experimental setup

As we have discussed in section 0, UV 15 is a low-viscosity UV curable epoxy-based system. According to ASTM D1894, a testbed is built to complete the experiment. It is the same testbed we used in the shear strength measure test, shown in 0.(Fig. III-7, Fig. III-8and Fig. III-9). In the shear strength test, the area coating with resin is relatively much smaller than the friction test. The resin will be applied to the whole area of the glass plate to assure that the measurement of the

friction is the interface of resin (UV15)/substrate (PET). Additionally, based on Coulomb's friction law, the area does not affect to the coefficient of friction.

The motion system was started once the UV light was switched on. Therefore, an increase in the dynamic coefficient of friction was monitored by the software. The specimen was placed on the desktop under the UV LED. A dropper was used to place the UV 15 at the coating area. The UV 15 flowed for a few seconds and bubbles were removed inside the coating. The glass plate was put on the coating area, and then a steel block which weighs (1.2lb) was placed onto the glass plate to provide load in the normal direction. The residual resin was wiped by clear cloth with methanol. The UV light was irradiated on the specimen with the time recorded. At the same time, the motion system was driven by a speed of approximately 150 mm/min. The load and displacement were monitored by the software program.

Results of friction test

The friction coefficient measurement of UV 15 under 2600mW/cm^2 was as shown in Fig. III-13. Before the UV resin was irradiated, the resin showed a function as a lubricant. The friction coefficient was as low as less than 0.1. Comparing the tests without any UV resin, the coefficient was much smaller. When the UV light turned on, the cross-linking of the UV resin was initiated. At the beginning of the curing, the coefficient did not increase steeply. Once the cross-linking reached a certain degree, the coefficient started to surge. As shown in Fig. III-13, a linear part was shown after the coefficient increased steeply. During the linear part, the ETFE film was stuck with the PET web. The load cell was measuring the shear deformation of the cross-linking UV resin. Thus, the coefficient friction of this test is 0.132 to 4.24 for purpose of simulation.

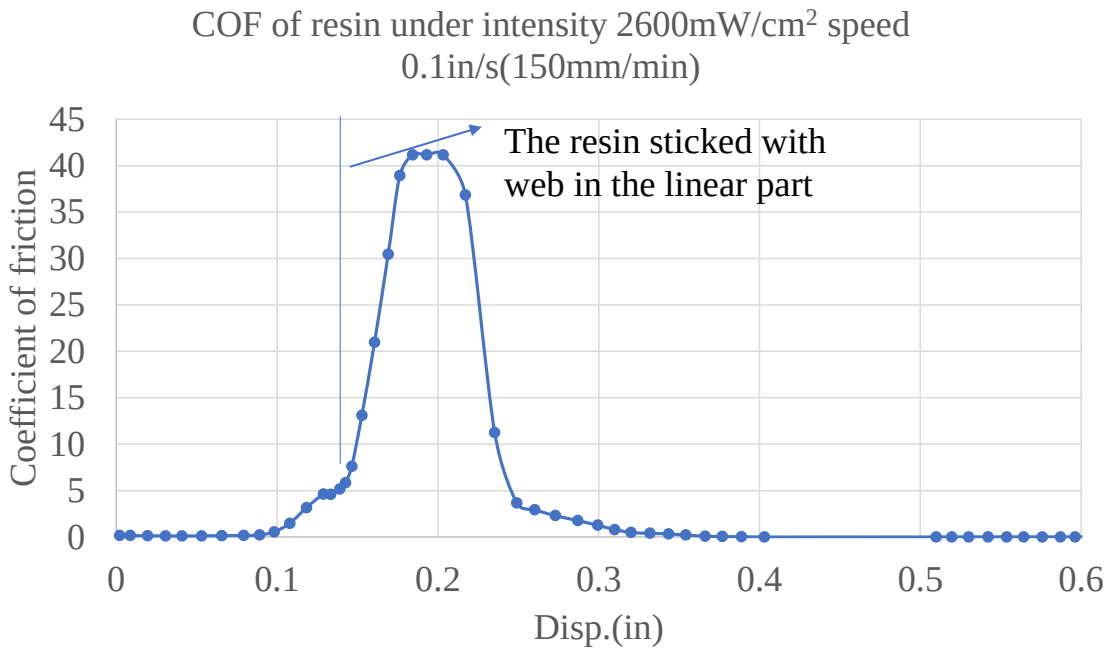

Fig. III-13 Friction coefficient measurement of UV 15 under 2600mW/cm2 for 1s

3.5 Measurement of adhesion behavior of UV 15

A huge volume of methods to estimate the strength of adhesive bonds at the interface between the materials has been developed[154-156]. Researchers made a distinction between methods. The intrinsic and unvarying property of the material pair measured by one specific method[154, 156], may be different from the strength measured by other methods[155, 157]. Therefore, a method of assessing adhesion strength in a more accurate way to simulate the conditions of the real situation of interest is a key criterion for selecting the test method. Some of the well-established adhesion measurement methods are evaluated by how well they emulate the conditions of the demolding in practical applications.

Tension or pull tests are straightforward in concept and simple in execution. There are standards that came from ASTM C633, D2095. The ends of two cylinders are bonded, and the specimen is subjected to a normal tensile load. Then tensile strength at where the bond fails is taken to be the strength of the adhesive joint. Tension tests have a significant advantage of simplicity. However,

the specimen we are testing needs to be exposed to UV light. The cylinders cannot be transmittable for a specific range of UV light. Pull tests have been applied to measure the intrinsic adhesion between polymers and mold materials in nanoimprint lithography[87, 158, 159], and to measure the demolding forces in NIL[18, 91, 93, 96, 160]. However, in the practical roll-to-roll situation, the nanoimprints are always peeled from the mold roller. The separation starts with the edge of the exit area of the imprint roller, rather than pure normal forces.

Blister test is another common test to evaluate the adhesive strength of a resin. The hydrostatic pressure is applied to the adherend through a hole in the substrate in a blister test[155, 161]. As the UV 15 is a low viscosity liquid before irradiating by the UV light, the uniformity of UV 15 cannot be assured during applying the fluid pressure. Moreover, the strain energy release rate increases with increasing blister radius, resulting in unstable test conditions[161].

Razorblade or wedge test (ASTM D3762), as well as cantilever beam test (ASTM D3433, D3807) are requiring the substrates to have a certain thickness, which is not practical situation for roll-to-roll NIL.

Peel test is commonly used to assess the strength of adhesion. Some peel tests are applicable for a stiff substrate and a flexible adherend. For example, pressure-sensitive tape test (ASTM D3330), 90-degree peel test, 180-degree peel test for adhesion to metals (ASTM D903). Peel tests have been applied to evaluate the adhesive strength in flexible materials such as UV-cured acrylate [15] and PDMS[162]. T-peel testing was used to assess the failure modes of PDMS-PDMS integrity[163]. In the T-peel test, the adherends are both flexible substrates. The bonded area is easy to be accessed for the UV light. The bonding strength characterization in terms of two parameters are commonly used in linear elastic fracture mechanics (LEFM): fracture energy and the surface energy at the bonded interface (toughness). The T-peel test is applied in this report and described in detail.

Experimental preparation

The nanoimprint mold used in the current project was ETFE, and the PET web was used as the flexible substrate. The bonding between the ETFE web and the PET web was carefully made by placing a piece of paper between the contact region. The UV 15 was placed at the ends of both webs, as shown in Fig. III-14(a). The dimension of the bonding area was shown in Fig. III-14(b). The bonding area was 30 mm2. The UV irradiation source was placed on one side of the bonding specimen from a certain distance. The detailed intensity and irradiation time will be elaborated on in the next subsection. One should notice that the UV 15 was a low viscosity liquid with low adhesive ability. Thus, the PET web and the ETFE web cannot be bonded together before irradiation. The alignment of the two strips was the key to assure the liquid UV 15 remaining in the bonding area. Additionally, the gap between two pneumatic grips was small to make the webs bending, as shown in Fig. III-15 (a) and (b). After the UV light irradiating on the bonding area for a certain time, the upper grip started to move up till the failure of the adhesive joint of PET and ETFE webs. The assembled specimens were exposed to the ambient environment while in a queue for testing. The specimens prepared from the same batch of UV 15 were tested on the same day.

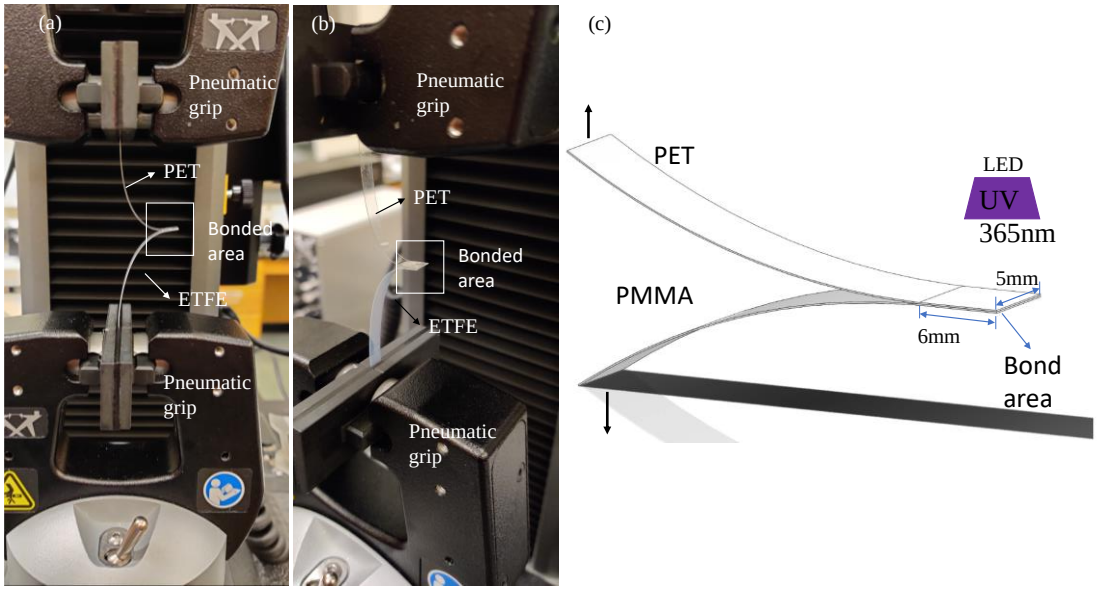

Fig. III-14 (a) PET and ETFE sample on Instron 5942 machine (b) Schematic diagram of the setup of T-peel test.

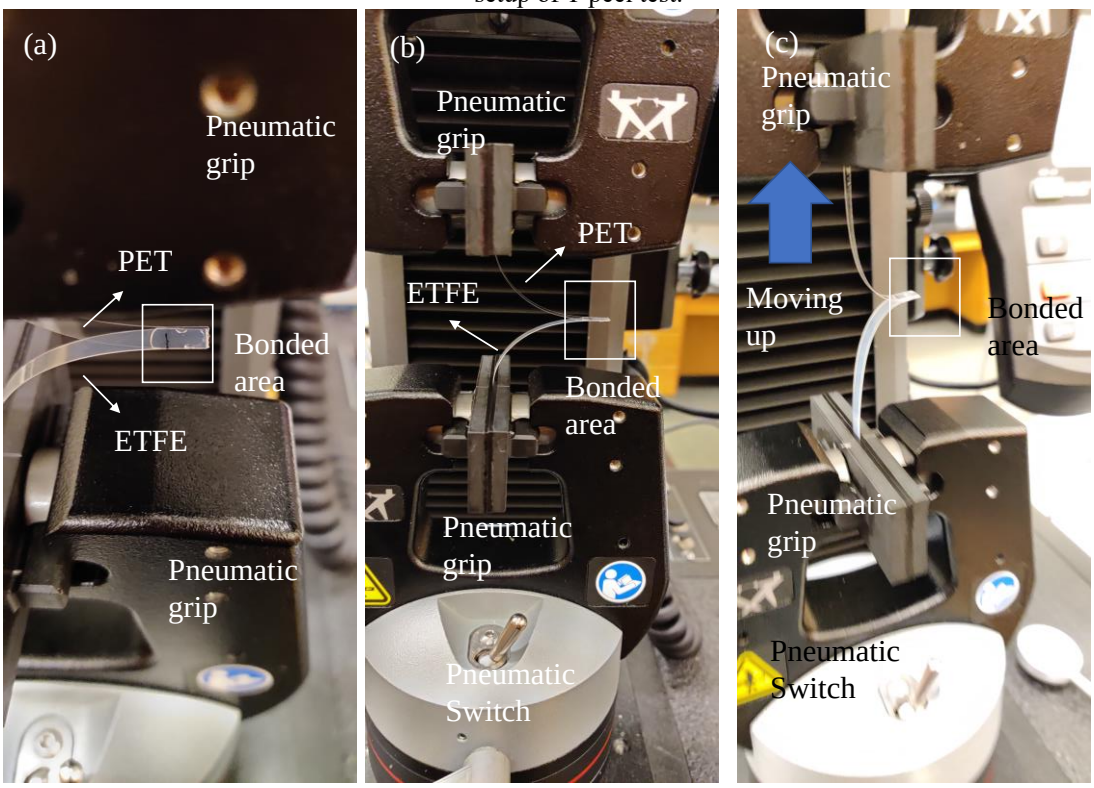

Fig. III-15 Photo showing mounting specimen onto the Instron machine including (a) slack specimen, liquid UV 15 at the bonding area between PET and ETFE webs (b) front look of the mounting the specimen (c) specimen under loading

The T-peel test is conducted to pull apart the assembled PET and ETFE specimen at a constant displacement rate, which is different from the traditional peel test in that a constant load is applied for measuring the fracture toughness of the adhesive joint[165]. In each test, the PET and ETFE web were clamped with the grips of the Instron machine (Instron 5942 system) at about 44 mm from the edge of bonding, and loading is applied as shown in Fig. III-14 (b). Each test specimen remained slack while installing on the clamps as well as placing the UV 15. Then the UV light started to irradiate the bonding area. Once the test started, the specimen became taut by moving the upper grip at a constant rate of 100mm/min until the assembly was pulled apart. Since the UV 15 had a short time to be cured on the process line of roll-to-roll NIL, the fracture toughness of the adhesive approaching the time when the UV light stopped irradiating on the

bonding area was preferred. Because the UV 15 has a “dark-curing” effect, which means the UV 15 remained cross-linking once irradiated by the UV light until all the molecules had done the reaction. The Instron machine automatically recorded a load-extension curve.

The two grips were moved to a gap of around 50mm to make sure the PET web and ETFE web bending to have a contact area. Then, a small drop of UV 15 was placed at the bonding area, and the UV 15 spread to fill the whole bonding area. Next, a UV irradiation source was provided to the bonding area, as shown in Fig. III-16 (b). The upper grip started to move upward until the assembly was pulled apart.

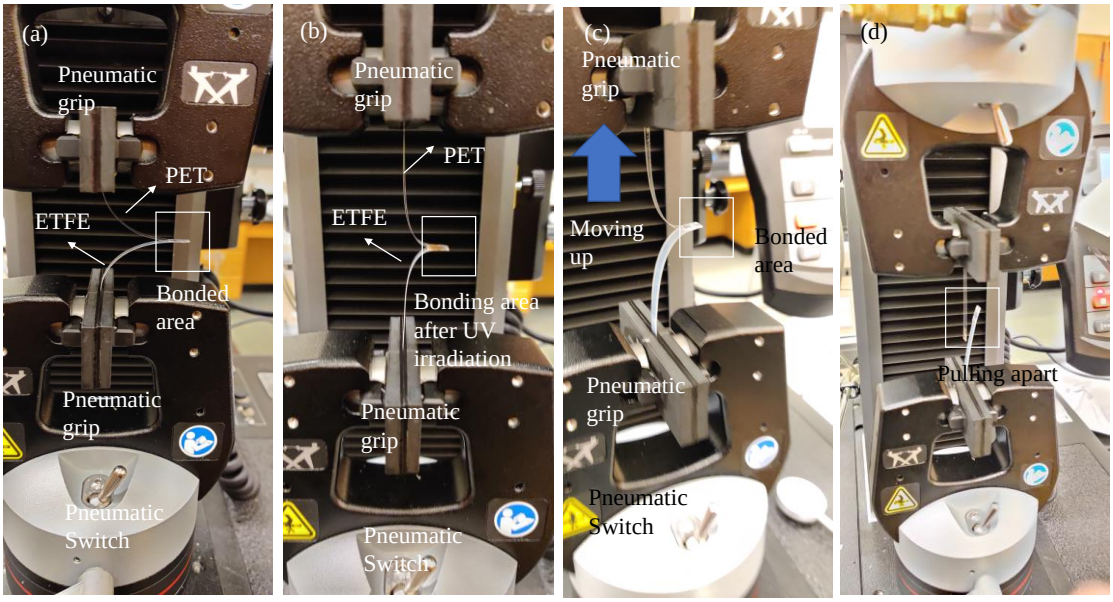

Fig. III-16 Photos of the test procedure (a) installing the PET and ETFE web onto the Instron machine and create a contact area (b) Place the UV 15 in the contact area and UV irradiation on the bonding area (c) Start the test (upper grip moving upward as a constant displacement rate) (d) the test stops until the assembly specimen was pulled apart

Due to the space limitation of the Instron machine, a high UV intensity (2600mW/cm2) cannot be provided to the bonding area. Thus, the UV LED was placed as close as possible under the condition of avoiding interfering with the test. The UV intensity was measured by a radiometer (provided by DYMAX cooperation), read as 430~460mW/cm2. Based on the equation we have discussed before,

$$\sqrt{I_1}t_1 = \sqrt{I_2}t_2 \qquad \text{(III-8)}$$

One can calculate

$$t_2 = \frac{\sqrt{I_1}}{\sqrt{I_2}}t_1 \qquad \text{(III-9)}$$

Where I1 and I2 are UV intensity of the UV source, t1 and t2 are exposing time of UV source, respectively. Since in the practical situation, we were using the UV exposure dosage as 2600mW/cm2*5s. By calculation, the time for exposing under the intensity of 450mW/cm2 was 13s. This calculation was limited to the current UV curable resin.

Results of the T-peel test

All the test results of the load-extension curve showed a common shape as schematically shown in Fig. III-17. When the test started, the load increased monotonically until reaching the maximum value. The specimens became taut until the load reached its maximum value as shown in Fig. III-16. After reaching the maximum load, the slope became zero or negative, which means the stiffness of the assembly was reducing. The extension at point “b” in Fig. III-17 marks the end-point of the test, while the specimen was completely pull-apart. The max load and the initiating maximum nominal stress of 10 tests are shown in Table III-4 Max load and max nominal stress for T-peel tests. The average max nominal stress for initiating crack was 0.006MPa.

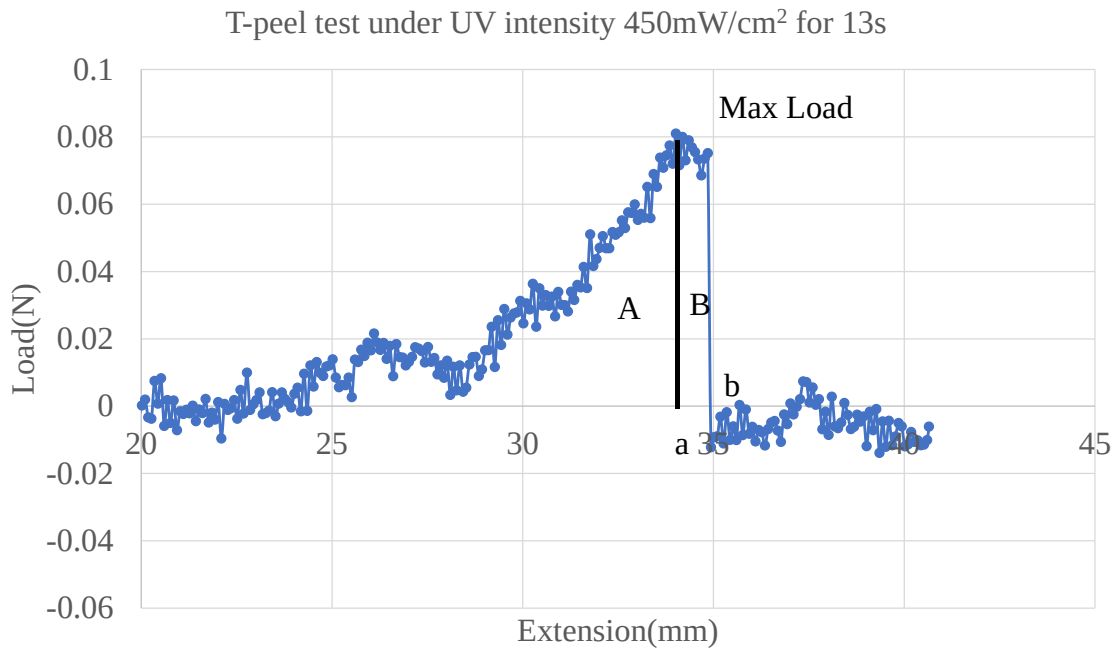

Fig. III-17 Load-extension curve of T-peel test for PET and ETFE substrate

Table III-4 Max load and max nominal stress for T-peel tests

	1	2	3	4	5	6	7	8	9	10	Average
Max load(N)	0.796	0.140	0.087	0.274	0.052	0.204	0.101	0.060	0.070	0.029	0.181
Max nominal stress (MPa)	0.0261	0.004	0.002	0.0091	0.001	0.007	0.003	0.002	0.002	0.001	0.006

Fracture energy is also called critical strain energy. During the test, the uniaxial tensile load was completely converted into strain energy stored in the assembled specimen, which is area A shown in Fig. III-17. The area under the load-extension curve before point “a” (area A) represents the maximum strain energy that a specimen can withstand before cracking, debonding, or a mixed-mode of failure. Therefore, the value of area A can be served as a metric for the resistance of the bonded specimen to failure. The strain energy in area A is defined as critical strain energy. This definition of critical strain energy was the same as the definition of fracture energy [166, 167] in linear elastic fracture mechanism (LEFM). The fracture energy was the maximum elastic energy a bulk material can withhold before a crack initiate. The critical strain energy density was attained by divided by the bonding area (which is 30mm2) in the current experiment.

All tests terminated at the point when the specimens were pulled apart. Only one failure mode was shown in all the test results: adhesive failure, as shown in Fig. III-18. Due to the low surface energy of ETFE, the failure mode was an adhesive failure. The cured UV resin remained on the PET substrate, as shown in Fig. III-18 (a) and (b). On the bonded area of the ETFE substrate, there is no UV cured resin left, as shown in Fig. III-18 (c). The pulled apart specimens were shown in Fig. III-18 (d).

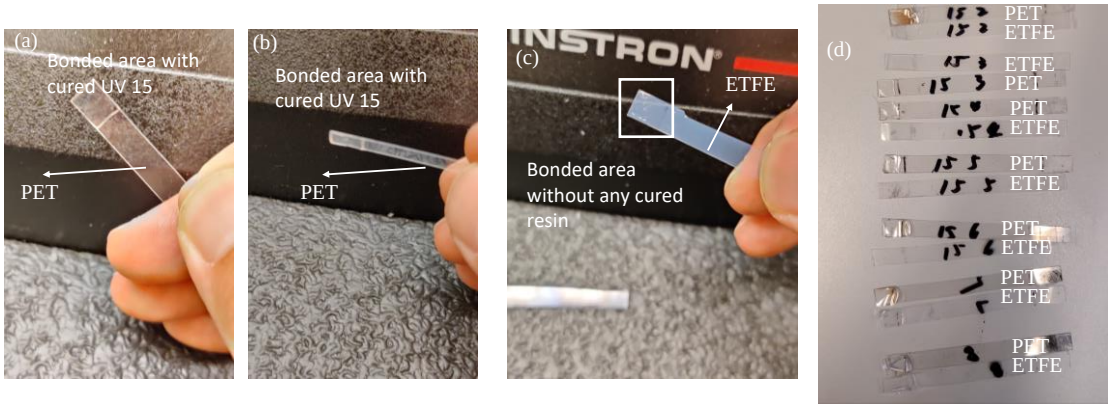

Fig. III-18 Adhesive failure mode on the substrates (a) Front look of bonded area on PET web (b) side look of the bonded area on PET web (c) the bonded area on ETFE web (without any cured UV resin on the bonded area) (d) All test specimens (adhesive failure mode)

Since the adhesive failure mode is the only failure mode occurred in the peel tests, the surface energy at the bonding interface can be estimated. The surface energy of the bonding area was estimated by using the energy balance principle from LEFM for a specimen that failed by adhesive failure. As shown in Fig. III-17, the debonding of adhesive started at the point "a" where the specimen reached the maximum load. The debonding process was unstable as evidenced by decreasing load in a very short time at a constant peeling rate. The debonding process continued until the load was reduced to zero when the specimen was completely deboned. In the energy balance principle (Griffith theory)[168, 169], the total work done by Instron during the debonding process (δW) is equal to the change of in strain energy (δU) and the energy required to create an additional cracking surface ($G\delta a$):

$$\delta W = \delta U + G\delta a \quad \text{(III-10)}$$

Where G is toughness or critical strain energy release rate in fracture mechanics, has a unit of J/m^2 (also N/m). Here $G\delta a$ is the surface energy at the bonding interface. The work done to the specimen during the debonding process is area B (from point a to point b under the load-extension curve), as shown in Fig. III-17.

$$\delta W = \text{areaB} \quad \text{(III-11)}$$

For simplicity, no plastic work[170] was stored in the strain energy so that the strain energy stored in the specimen was completely released at the end of tests. Therefore, the change of strain energy in the bonding area at the interface is

$$\delta U = -\text{areaA} \quad \text{(III-12)}$$

Therefore, the surface energy is

$$G\delta a = \delta W - \delta U = \text{areaB} + \text{areaA} \quad \text{(III-13)}$$

Where area A and area B are referring to Fig. III-17. Equation(III-13) shows the surface energy $G\delta a$ of at the bonding interface. In the calculation, δa is the bonding area (30mm^2), which can be used to estimate the critical strain energy release rate G. The calculated surface energy of 10 runs for the same UV intensity and exposing time is shown in Fig. III-19. The toughness at the interface between the resin and the ETFE was calculated by averaging the toughness of 10 samples. The average adhesive toughness for the interface of PET/ETFE was 0.011mJ/mm2, which would be input into the Abaqus numerical model in the next section chapter.

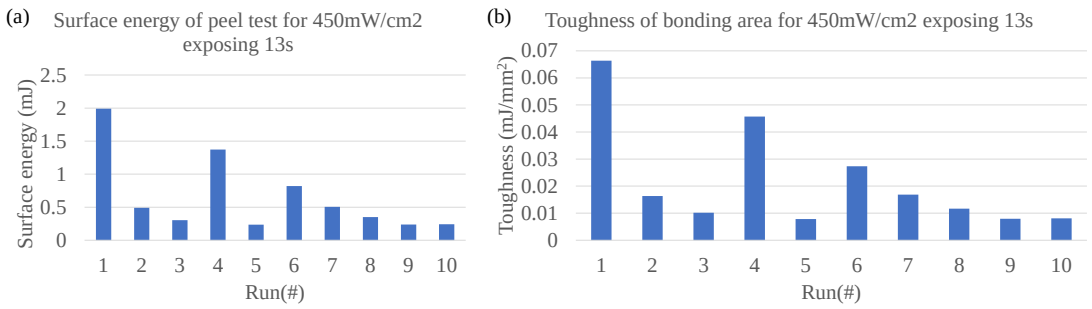

Fig. III-19 Adhesive properties of the bonding interface of PET and ETFE (a) surface energy of the

bonding area (b) Toughness (or surface energy density of the bonding area)

3.6 Summary

Characterization of UV 15 with the curing level is necessary and challenging. Based on the tests of rheological measurement, viscoelasticity, shear strength test, coefficient measurement as well as adhesive toughness test, a full characterization of the resin is established. The parameters can be used to build a numerical model to simulate the real-world process of roll-to-roll NIL. Based on the comparison of the results of the ultimate shear strength data and the dynamic simulation, we can tell if the UV resin can produce defect-free nanostructures during the imprinting.

CHAPTER IV

IV. Dynamic simulation of R2R UV NIL

Finite element simulation was used for predicting the quality of nanoimprints on the product. The numerical simulation for the roll-to-roll NIL process should include the whole pattern of the process. As we have discussed in the introduction, the roll-to-roll NIL process consisted of three steps, such as resist filling, UV exposing as well as demolding. The backup roller, also known as nip roller, was necessary for not only assisting the resist filling into the cavities on the mold, but also broaden the contact area for the resist and the mold. However, the nip roller caused nip-induced tension on the flexible substrate, which would induce slipping at the interface between the resin and the imprint roller. The nip-induced tension would be studied in the roll-to-roll NIL dynamic simulations which included imprint roller, nip roller with a rubber cover, peel roller as well as the flexible web in macro-scale. The demolding process was also a key step to determine if we can obtain high-quality products. Even if the resin could fill into the cavities on the mold perfectly, the damage or distortion during the demolding step would lead to defects on the nanoimprints. Two important phenomena of interaction between the UV curable resin and the mold contributed to the complexity of the demolding step. An increase of adhesive strength at the interface as well as the shrinkage due to cross-linking of polymerization occur simultaneously during the UV curing. Excessive UV curing caused the high shrinkage of the polyacrylate and

increased the possibility of initiation of the cracks in the nanostructures. Insufficient curing led to low shear strength which was tremendously important for the cured nanoimprints to maintain a high-fidelity quality. To study the combination of the friction and adhesive as well as shrinkage, a simulation in nano-scale should be established. It was apparent that only dynamic simulation of the R2R NIL process line or nano-scale simulation would not be enough to study the mechanics. Since the numerical simulations were not in the same geometry scale, a macro-scale and a nano-scale simulation were proposed. The macro-scale numerical simulation was conducted for the whole NIL process. The nano-scale numerical simulation was built for the demolding process. As we have mentioned in the literature review, numerical models for predicting the quality of nanopatterns on the surface of the products for roll-to-roll NIL process were lacking. Combination analysis of the macro-scale and nano-scale numerical model was built to predict the quality of the nanopatterns on the flexible substrate.

The main goal of the dynamic simulation was to predict the slippage and shear stresses which would potentially distort or destroy the nanofeatures. In the current project, the machine direction (MD) stress in the web and the contact stress produced by the interaction between the resist surface and the imprint roller were the points we mainly pay attention to. Therefore, defects of cross machine direction (CMD), such as buckling or wrinkling for the web which may cause the failure of the imprinting nanofeatures, were not considered in this report. The assumption that the web had no thickness variation across the roll width, and alignment of rollers was perfect was made to simplify the model. Thus, it was reasonable to simulate the continuous R2R UV NIL process as a two-dimensional model, which can significantly reduce the computation cost. Thus, this less computational resource required model allows us to simulate the process implicitly, which can provide unconditional stable solutions to analyze the equilibrium state of the process. Moreover, the reduced dimensional model would help us focus on the interaction between the nip roller and the imprint roller, the resist and the imprint roller, slip-stick behavior, and the shear

deformation of the resist during wrapping on the imprint roller and in the nip contact zone. The R2R UV NIL process simulations using commercial finite element software were capable of modeling the real process with the assumptions. In the R2R UV NIL process, an imprint roller and a rubber covered nip roller were built as a nip contact zone. A web with a thin layer of resist coating was built to go through the nip contact zone and to wrap on the imprint roller till it exits the imprint roller. The web and the resin layer were first subjected to the web tension and then pressed by nip, finally wound on the imprint roller when the process initiated. It allowed the quantities like stresses and strains through the web and the resist to respond as the process goes on. The slippage was allowed between the imprint roller and the resist, and the bottom web surface and the rubber cover by contact algorithms. Nevertheless, there were several limitations of this model. First, the UV curable resin was a low viscosity liquid at room temperature before being exposed to UV light. The resin was modeled as an elastic isotropic solid. It mainly affected the results of simulation because the nip contact would produce the shear traction for tension on wound roll which was called nip-induced tension. In the current situation, it was the best choice for us to simulate the liquid state resin as a low Young's modulus solid. The dimension of the nanofeatures was another limitation of this simulation. The height of nanofeatures was at the order of magnitude to tens of nanometers. It was much smaller than the dimension of the R2R NIL process line. Therefore, modeling the imprinting mold and the resist surface as a flat surface with frictional behavior was a compromise. Focusing on the shear deformation due to tangential behavior and potential slippage was the main goal to predict if the nanofeatures would be destroyed or distorted.

The difficulties of the simulation mainly include dealing with the expensive computational cost while modeling the material of the resin with high accuracy. Interactions between the surface of the resist and the imprint roller as well as the web and the rubber cover introduce nonlinearity into the boundary conditions. The stable time increment is set to a small number due to the thin

thickness of the web and the resist layer, which results in a large computation time. The nonlinearity and small stable time increment may cause convergence difficulty in the implicit method. Moreover, the mechanical properties of the resin are changing during the curing process. Predicting the slippage and the shear deformation on the resist surface is the main goal of this simulation. Based on the results of the simulation, controlling the external parameters of the setup can help us reduce or eliminate the slippage between the resist and the imprint roller. Therefore, how to create a balance between the accuracy of the simulation and computational cost, how to model the varying mechanical properties of resin material, how to reduce or eliminate the slippage and the shear deformation need to be explored.

In the macro-scale numerical model, a theory calculation is used to validate if the simulation is correct. Then, to explore the best control of slippage and frictional behavior, various operational parameters were applied to the simulation. After the previous research period, an improvement of the process line was made. Thus, an improvement of the numerical simulation was also updated. Finally, by the finding of simulation, the tangential behavior between the UV resin and the imprint roller was mainly affected by the coefficient of friction at the interface. A numerical model that describe the varying COF in the process line was established. Based on the results of this varying COF numerical model, a relatively precise simulation that can predict the tangential behavior in the manufacturing environment was developed.

4.1 Model setup

Geometry

A 2D model is built to simulate the R2R UV NIL process. A 2D model adopts a plane condition assumption to describe the web behavior of the CMD dimension. The web has a thin membrane geometry subjected to the web tension. Before entry of the imprint roller, the web already has a negative CMD strain due to web tension and Poisson’s effect. This negative CMD strain remains

constant since the web has enough width. Therefore, the web is under a pseudo plane strain condition.

The geometry of the R2R NIL model is shown in Fig. IV-1(a). The web first goes through the nip zone formed by the rubber covered nip roller and the imprint roller. The web then wraps the imprint roller. After the web exits the imprint roller, an idle roller is used for guiding the direction of the web. The material of the thin web is chosen as PET. The thickness of the web is 0.004" to approach reality. The length of the web is sufficient for the simulation to achieve an equilibrium state. The schematic diagram of the model and the detailed dimensions of the apparatus are shown in Fig. IV-1(b). The wrapping angle of the web on the imprint roller is around 260° to provide more time for the resin to be cured.

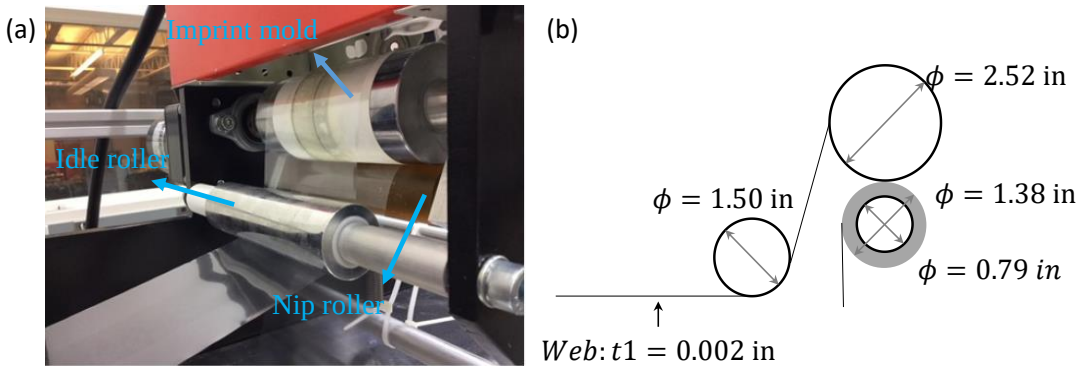

Fig. IV-1 (a) Practical apparatus for R2R UV NIL (b) Schematic of geometry for the model

Material

The web in these simulations was given properties that are common for PET films. Since the core used for imprinting the mold and the rubber cover is far stiffer than the web and the rubber cover, the core of the imprint roller and the nip roller are simplified as rigid analytical surfaces in Abaqus. The resin is curing uniformly on the flexible substrate. The strain of the resin should be equal to the strain of the web due to the formation of the resin happening when the web is stretched. The web and the resin thus are modeled as a part with two partitions in the simulation. However, the thickness of the UV resin is one thousand thinner than the PET web. The contact

behavior of the UV resin may be ignorable. Thus, the necessity of a thin layer of UV resin needs to be explored. The interaction properties between the resin and the ETFE mold will be further explored.

The rubber cover on the nip roller is modeled as an isotropic elastic material. It is completely defined by Young's modulus and Poisson's ratio. Rubber is often characterized by hardness in units of international rubber hardness degree (equivalent to Shore A). Good [171] provided the following equation to convert rubber hardness to Young's modulus of elasticity which is proved by the testing of many synthetic rubber types and samples.

$$E_0 = 20.97e^{0.0564*IRHD} \quad \text{(IV-1)}$$

Good also proved Poisson's ratio for rubber was 0.458 through additional tests for the same group of test samples. The characterization of this method has been proven to be accurate for large deformations while other characterizing methods have convergence difficulties for the implicit scheme. The properties of the web and rubber are shown in Table IV-1.

Table IV-1 Mechanical properties for web and rubber

Young's modulus of web E_w	700000psi
Poisson's ratio of web v_w	0.3
Young's modulus of rubber (IRHD 50) E_r	350psi
Poisson's ratio of rubber v_r	0.458

Solution techniques, boundary conditions, loadings, and interactions

Since the main goal of these simulations is to predict the tangential behavior between the resist and the imprint roller, it can be regarded as a static or a quasi-static problems. There is a "Static General" analysis in Abaqus to solve static problem. When the problem involves nonlinear large deformation and dynamic problems, the "Dynamic implicit" method can be used to solve quasi-static problems in Abaqus. There are two solver codes in Abaqus, one is Abaqus/Standard and the other is Abaqus/ Explicit. They can be used to solve different types of problems.

Abaqus/Standard uses an implicit scheme, specifically the New-Raphson method or quasi-

Newton method. Linear and nonlinear static problems are solved by this method. The governing equation used in a static problem is the equilibrium equation (IV-2). K is the stiffness matrix, u is the displacement vector, and R is the external force of the system. For the nonlinear situation, these three terms of matrix or vector become variables dependent on deformation history. The tangential stiffness matrix and iteration are required to get a converged solution. The advantages of this method are more accurate solutions and bigger time increments. One drawback of the method is that during the Newton-Raphson iterations one must update and reconstruct the stiffness matrix for each iteration, which can be computationally costly.

$$Ku = R \qquad \text{(IV-2)}$$

Moreover, Abaqus/Explicit solver is designed to solve dynamic and transient problems. It can be used when the implicit method meets a convergence difficulty. We will not discuss this method further since it is not a focus in this report.

When a R2R NIL process initiates, tension is introduced into the web on both ends. Then the nip load is applied by pressing the nip roller upward to contact with the imprint roller. After the nip load is applied, the imprint roller starts rotating to continuously imprint nanofeatures on the web. To approach the real situation of the manufacturing process, the loading procedure is divided into three steps: pretension, applying the nip load, and rotating the imprint roller. The boundary conditions and loads are shown in Fig. IV-2 and Fig. IV-3. In the pretension step, the horizontal displacement is allowed for both ends of the web, while all degree of freedoms (DOFs) of cores are restrained. The vertical or rotational displacements of the web are also restrained to avoid introducing dynamic effects into the whole model. A constant tension T_w is prescribed on both ends of the web and is maintained through the whole simulation. In the second step, the vertical displacement of the core of the nip roller is released and a concentrated force is applied on the center point of the core. The other restraints remain the same. In the third step, the rotational DOF of z-axis for all the cores is released. An angular velocity ω is introduced to the core. All other

loads and boundary conditions propagated from the previous step. The value of web tension and angular velocity used in the simulation is shown in Table IV-2.

Table IV-2 Loads and BCs

Web Tension, T_w	500psi
Angular Velocity, ω	4rad/s
Nip load	10pli

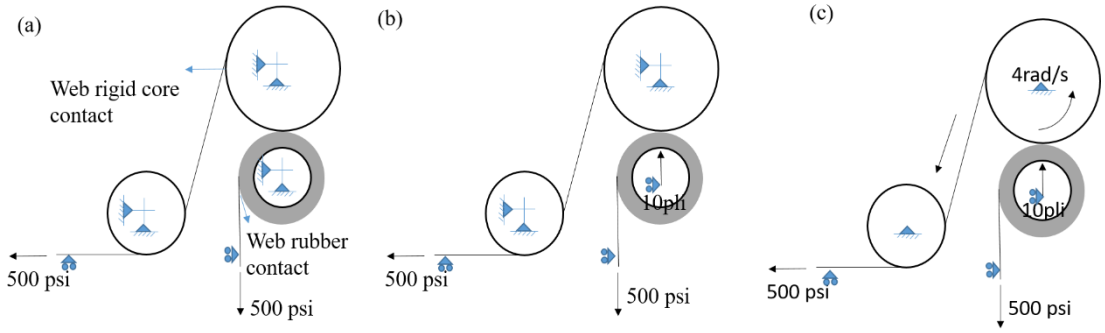

Fig. IV-2 (a) Boundary conditions for the pretension step (b) Applying nip load step (c) Applying rotating speed for the imprint roller

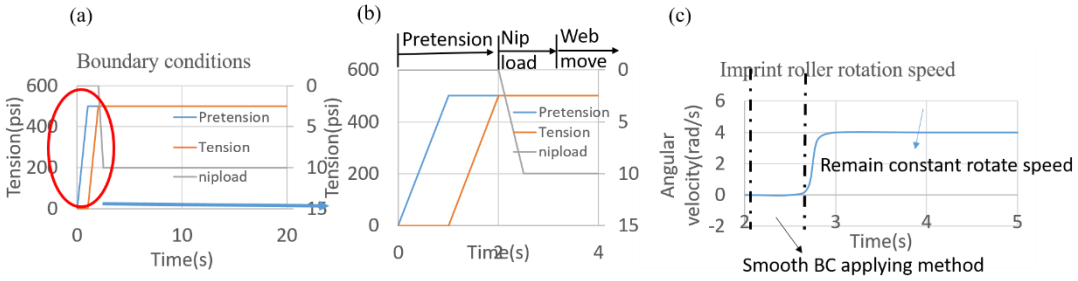

Fig. IV-3(a) Boundary conditions of tension on both ends of the web and the nip load applied on the nip roller (b) Zooming in the tension applying step (c) Boundary condition of rotating speed of the imprint roller

The rubber cover and the core of the nip roller is bonded together. All other contacts are defined by a penalty contact pair algorithm and the coefficient of friction is 0.3 both for the web to the rubber cover and the resist surface to the imprint roller. Here is another inaccurate factor which would be introduced into the model. As we discussed above, the mechanical properties of the resist can be varied by different curing level. The coefficient of friction should also be spatial-depended for the resin.

The relation between maximum frictional (shear) stresses across an interface to the contact pressure between contacting bodies is modeled by Coulomb friction law. Two contacting surfaces can react shear stress up to a certain magnitude before the slipping happened, which is the state of stick. Coulomb's friction model defines this certain magnitude as critical shear stress. When the shear stress is smaller than the critical shear stress, two surfaces are at a stick state, otherwise, they are slipping.

$$\begin{aligned} \tau_c &= \mu P(x) \Rightarrow \text{slip} \\ \tau_c &< \mu P(x) \Rightarrow \text{stick} \end{aligned} \qquad \text{(IV-3)}$$

The equation (IV-3) determines the slip/stick state for a point in the contact region.

Elements and Mesh

Abaqus has a wide range of elements in the library providing flexibility in modeling different geometries and structures, such as continuum (solid) elements, shell elements, beam elements, etc. A family of continuum quadrilateral elements is used to model plane problems. Second-order quadrilateral elements are not suitable for contact problems. Convergence difficulties may arise with these elements. First-order elements were used in the project. Quadrilateral elements with full integration may cause a problem which shearing the element rather than bending it. This problem is called "shear locking". Abaqus provides a reduced integration form of elements which is known as CPE4R or CPS4R for plane problems. These elements eliminate shear locking but they have a defect which is called hourglassing. The deformation of this kind of element consumes zero-energy. Hourglassing can propagate easily through a mesh of first-order reduced integration elements, which can cause unreliable solutions. The method to solve this problem is a finer mesh and multiple elements through the thickness. Therefore, a study of mesh convergence is necessary for the model.

To test the mesh convergence, a simpler case that can achieve the equilibrium state faster was developed. The geometry of the model is shown in Fig. IV-4. This model avoids the contact

between the bottom surface of the web and the rubber cover. It significantly reduces the cost of computation for nonlinear contact. For this reason, the model can achieve the equilibrium state faster than the former case. In the reality, the resin is a coating on the web. Therefore, a 0.0006in thickness resin is coating on the PET web. The dimension of the imprint roller and nip roller remain the same. The diameter of the idle roller which is also called peel roller is 1 in due to the arrangement of the whole apparatus. Other than the geometry, the boundary conditions, loadings, interactions, and analysis steps remain the same. To accurately approximate the deformation and stress state of the web on machine direction, the length of elements on machine direction is set to 0.009 in. As we discussed earlier, CPE4R elements are not reliable on the thickness direction due to unlimited propagated deformation. Therefore, the number of elements through the thickness of the web affects the accuracy of the simulation. Hence, the mesh convergence in the thickness direction is studied. The dimension and type of elements are shown in Table IV-3.

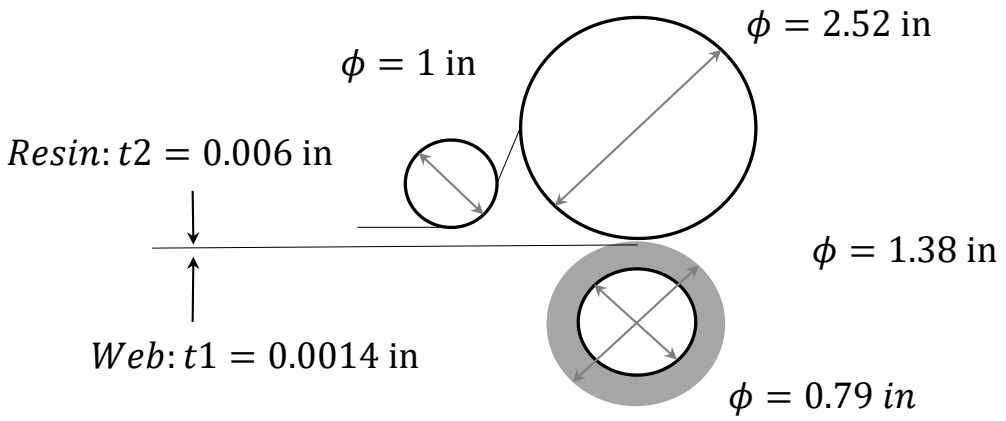

Fig. IV-4 Schematic diagram of geometry for the study of mesh convergence

Table IV-3 Element size in convergence study

Mesh Type	Mesh Size (in)
CPE4R: 0.009X1	Web: 0.009*0.0014; Resin: 0.009*0.0006
CPE4R: 0.009X2	Web: 0.009*0.0007; Resin: 0.009*0.0003
CPE4R: 0.009X3	Web: 0.009*0.0046; Resin: 0.009*0.0003
CPE4R: 0.009X4	Web: 0.009*0.0035; Resin: 0.009*0.0002

It was found that the stress on thickness direction was not affected by the layers of the element. The tangential stresses (MD stress) were affected by the varying layers of elements. Additionally,

the tangential stresses were the key parameters to determine the slippage between the resist and the imprint roller. Therefore, the MD stress was selected as the criterion for evaluating the performance of the mesh size in Table IV-3. In the Abaqus, the calculation was based on the integration point of each element. The values of stresses and strains on nodes of an element were obtained by interpolation. Thus, in this study, the average values of the bottom nodes and top nodes of the web and the resin were used to represent the MD stress at that location. Fig. IV-5 (a) showed the MD stress varies with different mesh sizes, especially when there was just one layer of the element both for the web and the resin. The MD stress had a little difference when the layer of element for the web increase from 2 to 4. It showed the MD stress convergence. The impact of mesh size on contact pressure in the nip contact zone was much less than the MD stress. In other words, the contact pressure also showed convergence by increasing the density of the mesh. For purpose of balancing the saving of the computational source and accuracy of the solution, mesh size 0.009*3 was chosen in the current study.

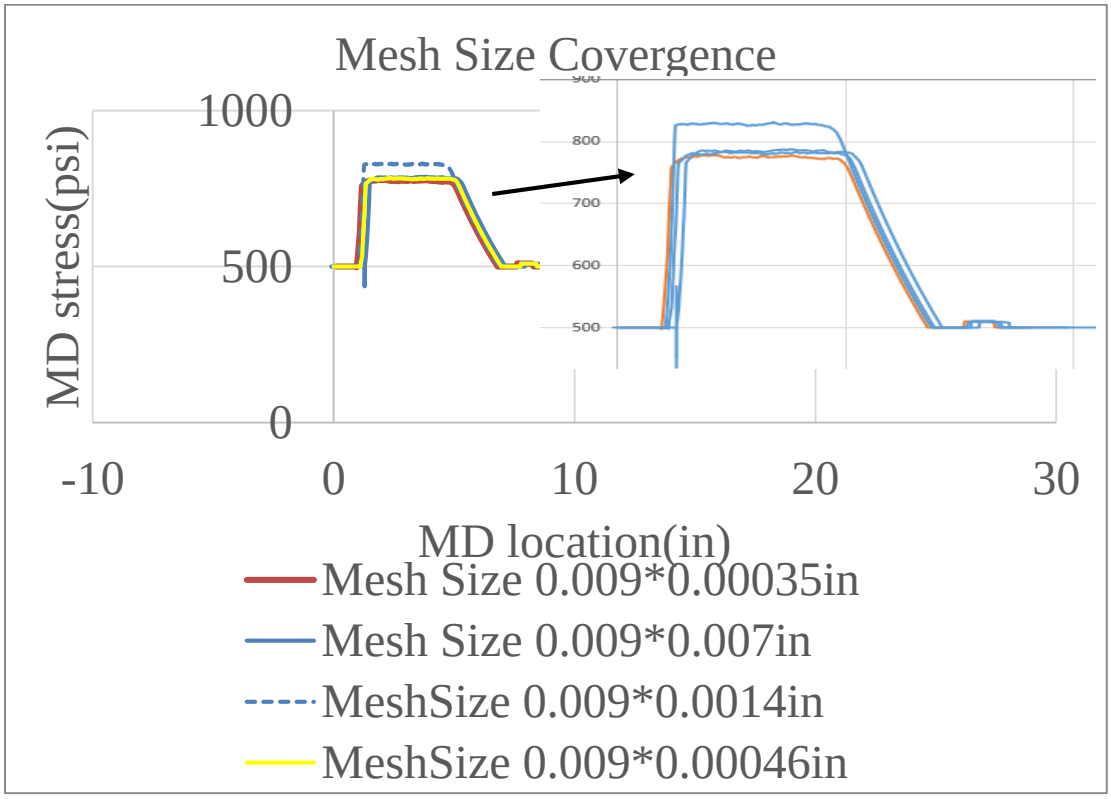

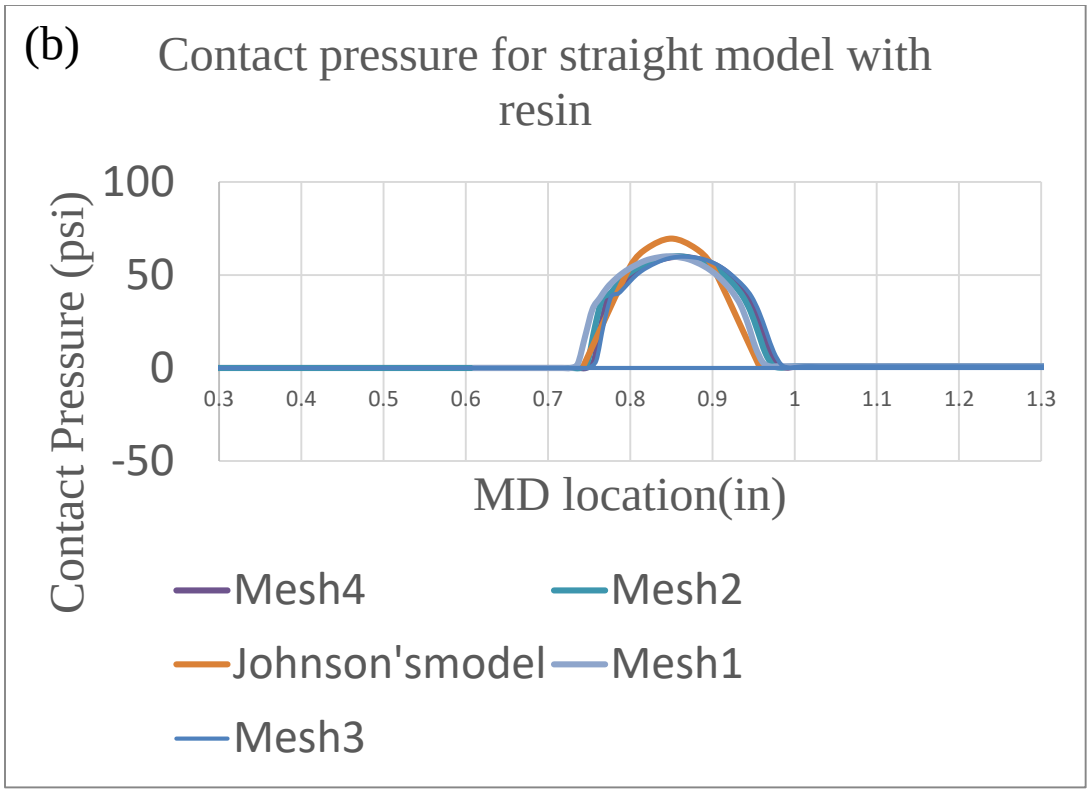

Fig. IV-5 (a) MD stress for different mesh sizes through the contact zone (b) Contact pressure for different mesh size at the nip contact zone.

4.2 Results and discussion

Results of numerical simulation of R2R NIL

The PET web went through the nip contact zone formed by rubber covered nip roller and the imprint roller. Then, the web wrapped on the imprint roller till exiting. Nip load applying step was first analyzed to assure that the pressure was provided steady. Additionally, the analysis of the nip load and the deformation of the rubber could help to find a suitable model for the nip contact zone. The MD stress was used to analyze the tension in the web. The contact pressure and tangential stresses were used to analyze the slippage zone between the web and the imprint roller. To show the tangential behavior of the web, 3 layers of mesh were adopted. The data was harvested by averaging the values of nodes of the top and the bottom surface of the web.

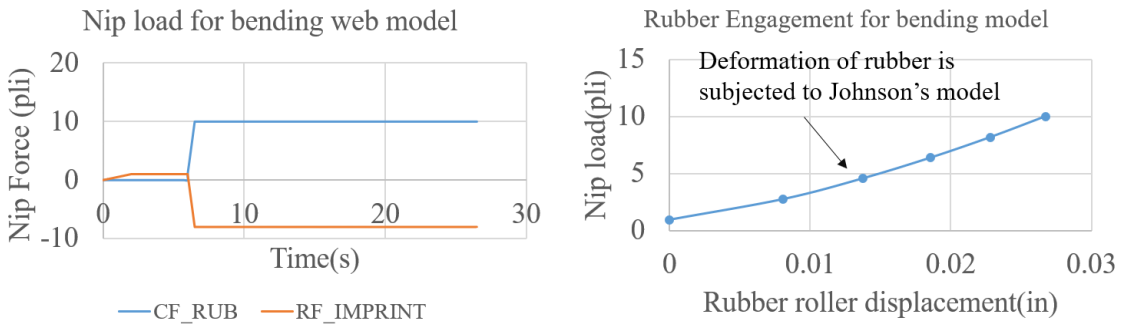

Fig. IV-6 (a) Nip load applied by the backup roller and reaction force on the center of the imprint roller (b) Rubber cover deformation correspond to the nip load

The nip load was applied up to 10pli by the nip roller with a ramp step starting at 5.5s. It remained 10pli till the end of the simulation, shown in Fig. IV-6(a). The reaction force at the center of the imprint roller was also shown in Fig. IV-6(a). There was the reaction force when the tension was first introduced onto the web. The reaction force reached 1.7pli due to the tension in the web. The direction of the reaction force was determined by the tension in the web. At the time when nip load was applied onto the imprint roller, the reaction force was determined by the vector sum of web tension and the nip load, which was 8.3pli as shown in Fig. IV-6(a). The change of reaction was 10pli which equaled the nip load applied by the nip roller. The rubber cover on the nip roller would be deformed while applying force on the rubber. The deformation in the normal direction of rubber had a direct relation to the applied nip load. In Fig. IV-6(b), the relation between nip load and rubber deformation on the normal direction as shown. The nip contact zone was shown in Fig. IV-7 (a). This relation was a contact model created by Johnson in 1985[172] in his book " Contact Mechanics". By his contact model, we can also analyze the contact pressure distribution at the nip contact region:

$$P(x)=\frac{(1-\upsilon_r)}{1-2\upsilon_r}\frac{E_0}{1-\upsilon_r^2}\frac{a}{2Rt_r}\left(1-\frac{x^2}{a^2}\right) \qquad \text{(IV-4)}$$

Where the nip contact zone width is 2a, R is the equivalent radius in contact defined as:

$$R = \frac{1}{\frac{1}{R_{nip}} + \frac{1}{R_{imprint}}} \qquad \text{(IV-5)}$$

R_{nip} and $R_{imprint}$ are the radius of the nip roller and the imprint roller, respectively. x is a coordinate whose original point is centered in the contact zone and ranges from –a to +a, shown in Fig. IV-7(b). t_r is the thickness of the rubber cover. E_0 is Young's modulus of the rubber cover. From the equation (IV-4), an average pressure of the contact can be obtained which will be used to determine the resist filling time.

$$P_{avg} = \frac{(1-\upsilon_r)}{1-2\upsilon_r}\frac{E_0}{1-\upsilon_r^2}\frac{a}{3Rt_r} \qquad \text{(IV-6)}$$

The half width of the contact zone can be calculated by

$$a = \sqrt[3]{\frac{3FRt_r(1-2\upsilon_r)(1-\upsilon_r^2)}{2E_0(1-\upsilon_r)^2}} \qquad \text{(IV-7)}$$

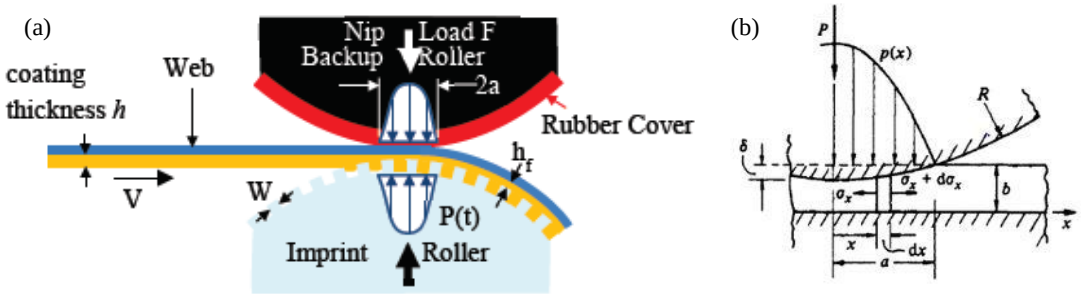

Fig. IV-7 (a) the schematic of the nip contact zone formed by the imprint roller and the nip roller[57] (b) an elastic layer on a rigid substrate indented by a rigid cylinder[172]

Fig. IV-8(a) showed the numerical simulation of the nip contact zone. The length of the contact width was calculated by Johnson's contact model. The contact pressure calculated by equation (IV-7) is shown in Fig. IV-8 (b). The contact pressure on the top and bottom surface of the web approximately equaled to each other. However, the contact pressure for the top surface of the web was oscillating, while the one for the bottom surface was smooth. This was because the top surface contacted with the rigid roller. Since the rigid roller cannot be deformed, the rubber covered nip roller deformed and contacted with the rigid roller. Thus, the web contacted the

deformed rubber cover prior to entry of the nip contact zone. This entrance condition was one of the reasons causing oscillatory behavior. Moreover, the mesh size for the tangential direction was 0.09 in. This rough mesh size also contributed to the vibration of the contact pressure for the top surface of the web. On the other hand, the contact pressure for the bottom surface was much smoother than the one for the top surface. Both contact pressures had a good agreement with Johnson's model. The maximum contact pressure calculated by the model was a little bigger than the one of the simulations. However, the lengths of the contact width were almost the same. We could also see that the contact pressure for the bottom surface was not zero at the entering point of the nip contact zone. This was because the web wrapped the rubber covered nip roller. Therefore, the bottom surface of the web contact with the rubber before entering the nip contact zone.

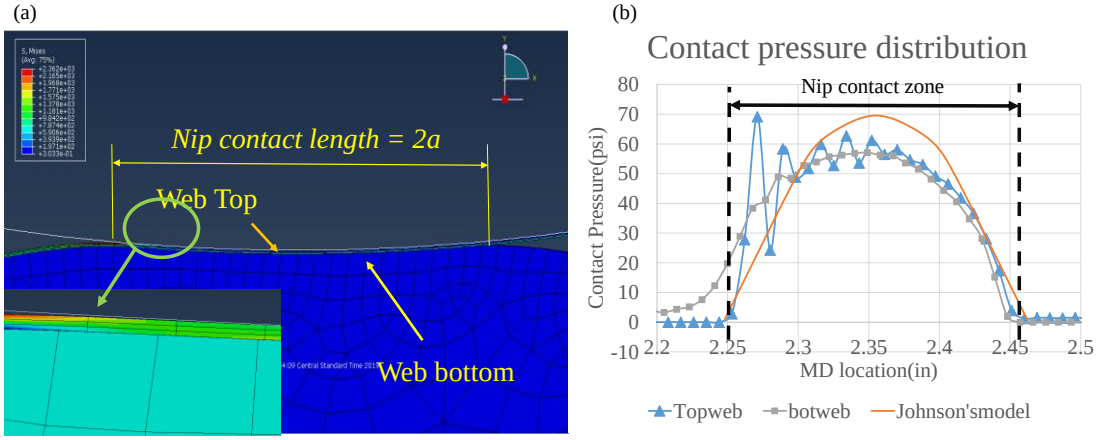

Fig. IV-8 (a) numerical simulation of the nip contact zone; the bottom left picture is the amplified area of resin and the web (b) contact pressure distribution along with the MD location in the nip contact zone (Topweb: top surface of the web, botweb: bottom surface of the web)

The contact width of the simulation was 0.12 in, while the width calculated by equation (IV-7) was 0.107in. The results of the contact width showed good agreement. The average contact pressure calculated by equation (IV-6) was in line with that of the numerical simulation, shown in Table IV-4. The average pressure for the simulation was calculated by

$$P_{avg} = \int_{-a}^{a} Cpress * dx \qquad \text{(IV-8)}$$

Where C_{press} is the contact pressure for each node on the top or bottom surface. dx is the length of each element. By comparing the average pressure and distribution of contact pressure, the contact pressure for the top and bottom surfaces were the same. The average pressure obtained from the simulation and the equation (IV-7) showed a good agreement with each other. Therefore, the average pressure calculated from Johnson's model could be used for purpose of designing the time for resist filling into the model.

Table IV-4 Average contact pressure of simulation and Johnson's model

Average pressure (psi)	Top surface	Bottom surface
Simulation	42.3	42.5
Johnson's model	46.3	46.3

The normal contact behavior was studied by both numerical simulation and theoretical calculation. Compared to the normal contact behavior, the tangential behavior of the web was more concerned. However, a suitable theoretical model for the current dynamic situation was lacking. Thus, a dynamic implicit method was used to analyze the tangential behavior of the web. Moreover, the slippage between the web and the imprint roller was examined by simulation and Capstan formula. Before we evaluated the MD stress in the web, a steady-state of all parameters needed to be achieved in the simulation. Fig. IV-9 (a) showed that several points at different locations when the web was wrapping on the imprint roller. The MD stress for the points at various locations was the criterion if the whole model achieved a steady-state. As shown in Fig. IV-9 (b), the MD stresses at each point achieved plateau at the time of the third second. This phenomenon shows that the simulation reaches the equilibrium state. The solution of the simulation can be used to analyze the dynamic tangential behavior of the web.

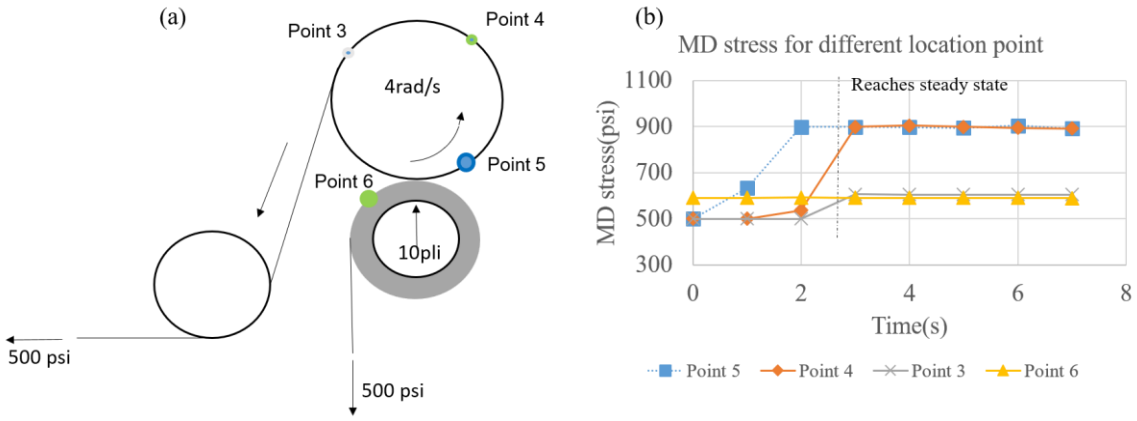

Fig. IV-9(a) Pick 4 points at different locations on the web during the web wrapping on the imprint roller (b) MD stresses for the points at different locations

In the dynamic simulations, the MD stress varied at different locations. Therefore, the web was separated into several zones by different locations, shown in Fig. IV-10 (a). The MD stress at different locations showed various stress levels, shown in Fig. IV-10(b). The upstream tension kept constant at 500 psi. Therefore, at the beginning location of the web, the MD stress started at 500 psi due to the tension applied on both ends of the web. The tension is required for web transportation. Then, the MD stress increased to 780 psi during the bottom surface of the web slipping on the rubber covered nip roller prior to the web entering the nip contact zone. Later, the MD stress increased to 900 psi after the web went through the nip contact zone. This increase in MD stress was due to the nip induced tension (NIT) phenomenon[111, 113]. The NIT and the impact of NIT on the web tension after the nip contact zone are shown in Fig. IV-10 (b). The NIT is affected by the slippage in the nip contact zone. The slippage will be shown in Fig. IV-11(c). The web tension, in the units of stress, can be calculated as followed:

$$T_{out} = T_{entry} + NIT \qquad (\text{IV-9})$$

The MD stress remains steady during the web wrapping on the imprint roller. The increase in MD stress must decrease to the MD stress associated with the downstream web tension to achieve an equilibrium state. This could occur only by slippage for the thin webs. The spatial slippage between the web and the imprint roller is shown in Fig. IV-10 (a).

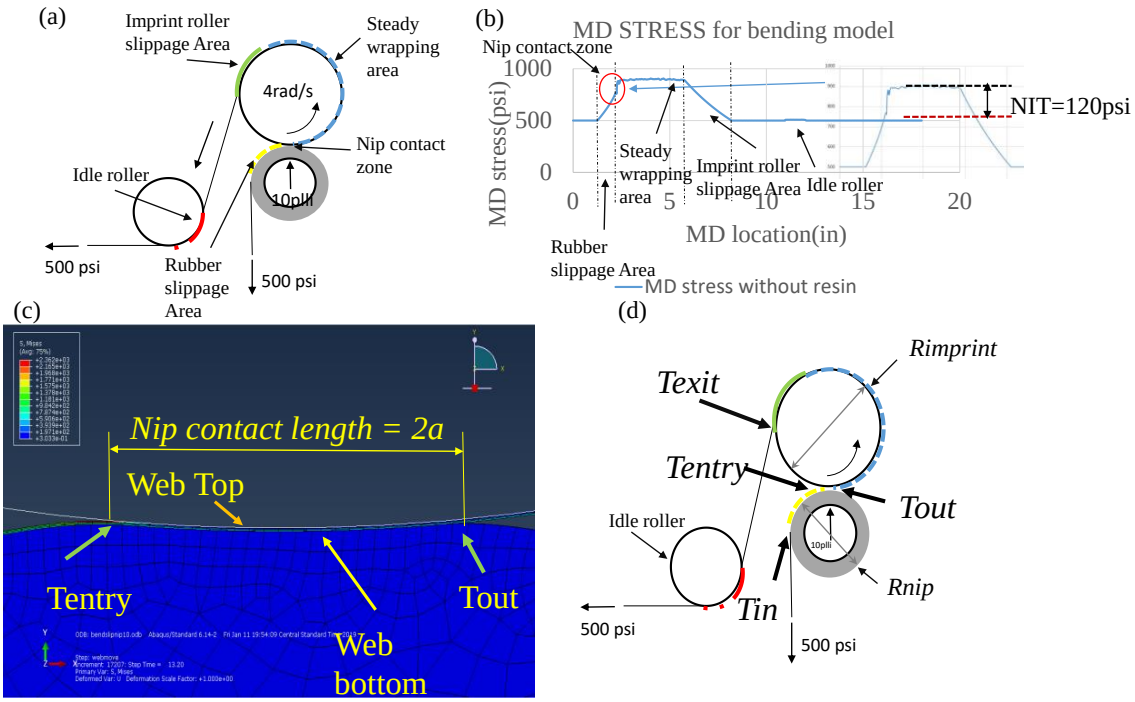

Fig. IV-10 MD (a) various contact situation of the web going through the processing different locations on the web (b) MD stress at different locations on the web (zoomed picture on the right: the impact of NIT on the web tension) (c) numerical simulation results at the nip contact zone (d) The name for web tensions at different locations

The increase of the MD stress at the rubber slippage area was coincident with the slippage shown in Fig. IV-11(b). The slippage could also be calculated by Capstan formula. The equation relates the hold-force to the load-force if a flexible line is wound around a cylinder.

$$T_{in} = T_{entry} e^{\mu\theta} \qquad (\text{IV-10})$$

Where T_{in} is the applied tension on downstream of the web. T_{entry} is the resulting tension on the upstream of the web. μ is the coefficient of friction between the web and the imprint roller. θ is the angle of the arc of slippage. The slippage, therefore, can be predicted by:

$$slippage = \frac{R_{nip}}{\mu} \ln\left(\frac{T_{in}}{T_{entry}}\right) \qquad (\text{IV-11})$$

The slippage at the rubber slippage area was 0.900in obtained by the simulation, while the slippage acquired by the equation (IV-10) was 0.9326in. The results obtained by the dynamic

simulation and the estimated method showed a good agreement with each other. The increase in MD stress was also coincident with the slippage at the entry and exit regions of the contact zone, shown in Fig. IV-11(c). As we mentioned, the increased MD stress must decrease to the MD stress associated with the web tension to achieve equilibrium, the slippage was happening at the exiting area of the imprint roller. The slippage zone was evident as shown in Fig. IV-11(d). The slippage at the exiting area can be evaluated by:

$$slippage = \frac{R_{imprint}}{\mu} \ln\left(\frac{T_{out}}{T_{exit}}\right) \qquad \text{(IV-12)}$$

The slippage at the exiting area was 2.376in by the simulation, while the slippage was 2.46in calculated by Capstan formula. At this slippage zone, the imprinted nanofeatures should be cured by the time the web exits the imprint roller so that they can release without damage. The contact shear stresses must be minimized to avoid damage to the imprinted nanofeatures. Therefore, the slippage zone at the exiting area could be a potential part to damage or ruin the imprinted nanofeatures.

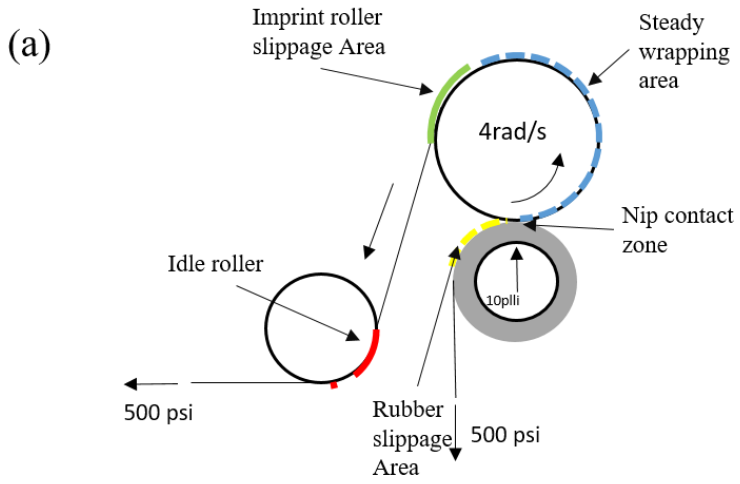

(b)

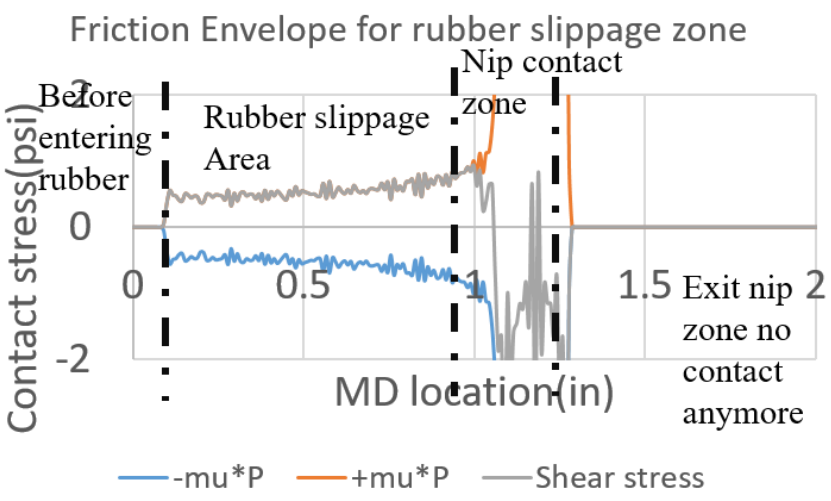
Friction Envelope for rubber slippage zone
Nip contact zone
Before entering rubber
Rubber slippage Area
Exit nip zone no contact anymore
Contact stress(psi)
2
0
-2
0
0.5
1
1.5
2
MD location(in)
-mu*P
+mu*P
Shear stress

(c)

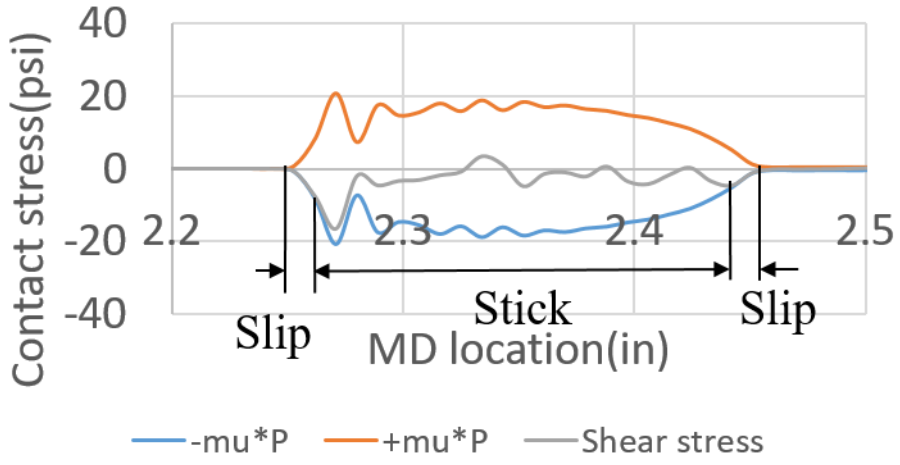
Shear traction and friction at the nip contact zone
Contact stress(psi)
40
20
0
-20
-40
2.2
2.3
2.4
2.5
Slip
Stick
Slip
MD location(in)
-mu*P
+mu*P
Shear stress

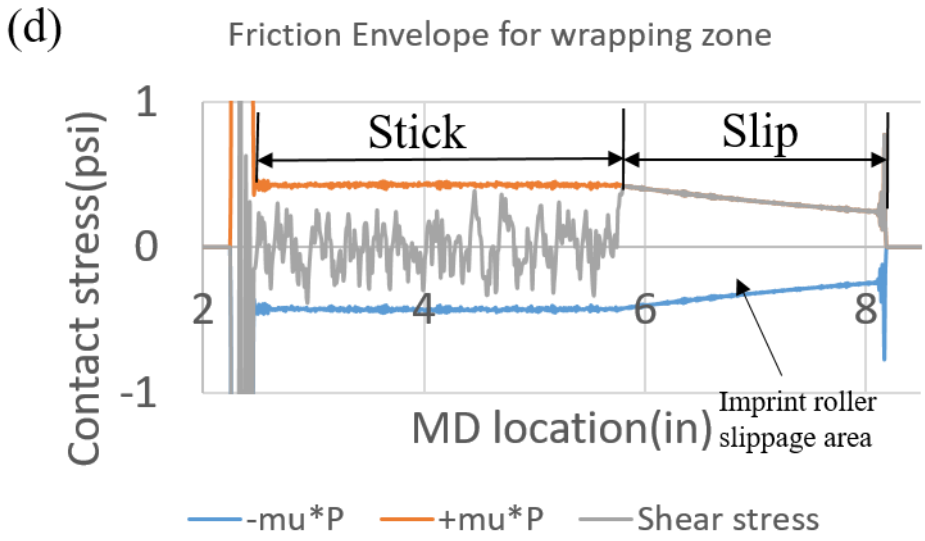

Fig. IV-11(a) Spatial contact zone classified by contact situation (b)Shear traction and friction envelope for the bottom surface of the web and rubber covered nip roller (c) Shear traction and friction envelope for the top surface of the web and the imprint roller (d) Shear traction and friction envelope when the web was wrapping on the imprint roller

After the web exited the imprint roller, the tension in the web remains 500psi except passing through the idle roller as shown in Fig. IV-10 (b). It is because the bending of the web being restricted by the frictional force as it conforms to the roller. It is obvious that this minor increase in MD stress also decayed back to the tension level at the exit of the peel roller. However, this part of slippage was not concerned because the surface that being contacting the peel roller was the bottom surface of the web. The bottom surface does not have the imprinted nanofeartures. Nevertheless, this does not mean the slippage can always be ignored since imprinted features may be in contact with the roller in the process line.

Parameters affect the MD stress

To determine the parameters which can affect the tangential behavior of the web, several cases were established. Each of these cases just changed one of the parameters but remained the rest. Therefore, one could find out which parameters would affect the stress state of the web. The evaluation of results included tangential behavior of the web, average normal contact pressure in

the nip contact zone, and the length of the slippage area. The change of parameters in each case was shown in Table IV-5.

Table IV-5 Cases of simulation for different parameters

Case	*Nip load* (pli)	T_{exit}(psi)	v_r	E_r(IRHD)	*Cof1*
1	10	500	0.458	50	0.3
2	10	500	0.458	40	0.3
3	10	500	0.458	30	0.3
4	10	500	0.3	50	0.3
5	10	500	0.2	50	0.3
6	10	990	0.458	50	0.3
7	10	500	0.458	50	0.1
8	10	500	0.458	50	0.5
9	2	500	0.458	50	0.3
10	5	500	0.458	50	0.3

Case 2 and 3 were similar to Case 1. These two cases were built to explore the influence of different rubber cover hardness for the nip roller. Case 4 and 5 were to explore the effect of low Poisson's ratio elastomers that were achievable with open and closed cell foams. As we have discussed in the literature review, Poisson's ratio is one of the key parameters which could induce the NIT (nip-induced-tension). Case 6 was built to explore if one can reduce and even eliminate the slippage by controlling the downstream web tension. Case 7 and 8 were to explore the effect of frictional behavior between the resin and the imprint roller. The coefficient of friction between the resin and the imprint roller would change while the resin was curing. Therefore, Case 7 and 8 could give results of the effect of the frictional behavior. Case 9 and 10 were to study the influence of the nip load.

Table IV-6 Results of simulation cases

Case	Average Pressure (pli)		Nip contact area *a* (in)		Slip (in)	
	Simulation	Equation(IV-6)	Simulation	Equation(IV-7)	Simulation	Equation(IV-11)
1	43.97	46.39	0.216	0.216	-2.83	-2.91
2	33.94	38.49	0.140	0.130	-2.61	-2.83
3	34.20	32.01	0.324	0.312	-2.91	-3.08
4	41.88	31.20	0.225	0.320	-0.93	-1.19
5	40.25	29.27	0.234	0.341	-0.54	-0.73
6	42.09	46.39	0.225	0.216	0	0
7	41.86	46.39	0.225	0.216	-5.58	-5.57

8	41.97	46.39	0.225	0.216	-1.58	-1.77
9	5.97	10.94	0.182	0.276	-0.75	-0.85
10	19.63	20.17	0.171	0.188	-1.62	-1.81

The results of these simulations were shown numerically in Table IV-6. The average pressure in the nip contact zone, the width of the contact area, and the slip of the web at the exit of the imprint roller were the main parameters to be concerned. Table IV-6 also showed the ability of equation (IV-6) and (IV-7) to predict the average pressure and the width of the contact region. The equations performed well except Case 4 and 5 which has lower Poisson's ratio. Equation (IV-11) was used to predict the length of slippage at the exit of the imprint roller. The results of the simulation for slipping showed a good agreement with the equation. Based upon all the results of numerical simulations presented in Table IV-6, they are useful for predicting the mold filling process. Also, note that the slip results in Table IV-6 had signs. A positive sign was defined as slippage of the web forward with respect to the imprint roller surface towards the exit. A negative slip was defined as the web slipping upstream with respect to the imprint roller surface.

The slip results in Table IV-6 showed the effect of variables on slip while other parameters remained constant. The effect of hardness of the rubber cover for the nip roller was small since the length of the slippage varied not much. The comparison of MD stress in the web was shown in Fig. IV-12 (a). The MD stress in Case 1, 2, and 3 showed little sensitivity to the different hardness of rubber cover. Additionally, it was impossible to force the slippage to vanish by selecting various elastomers. Based on the results of Case 1, 4, and 5, lower Poisson's ratio would reduce the slippage. It is noticeable that even the Poisson's ratio was as low as 0.2, the slippage still happened at the exit of the imprint roller. As shown in Fig. IV-12 (b), one interesting phenomenon was that the direction of the slippage between the bottom surface of the web and the rubber cover was the opposite. This opposite slippage caused a decrease in the web tension. However, lower Poisson's ratio elastomer caused higher nip-induced tension in the web during going through the nip contact region. This phenomenon is in line with the literature of

Johnson[102, 103]. Based on the results, even the Poisson's ratio was 0.2, it was still impossible to eliminate the slippage at the exit of the imprint roller. Additionally, the bottom surface of the web would slip drastically when the web enters the nip contact zone. Thus, the selection of low Poisson's ratio elastomer was not a preferred way to eliminate the slippage. Case 6, 7, and 8 showed that controlling the downstream web tension could be an effective way to reduce or eliminate the slippage. The MD stress distribution for various downstream web tension was shown in Fig. IV-12 (c). It was apparent that the MD stress in the web and the slippage area at the exit of the imprint roller could be controlled by manipulating the downstream web tension. As shown in Fig. IV-12 (c), the slippage at the exit of the imprint roller was controlled by manipulating the downstream web tension. One interesting phenomenon was that there was slippage at the idle roller. The slippage on the idle roller was controlled by the tangential properties of the interaction between the web and the rigid idle roller. The slipping angle on the idle roller was 34.83º, which means the downstream web tension was 1.2 times to the exit web tension on the imprint roller, calculated by equation (IV-10). Therefore, controlling the downstream web tension could be a very effective way to eliminate the slippage. Case 9 and 10 showed the slippage was strongly affected by the coefficient of friction between the resin and the imprint roller.

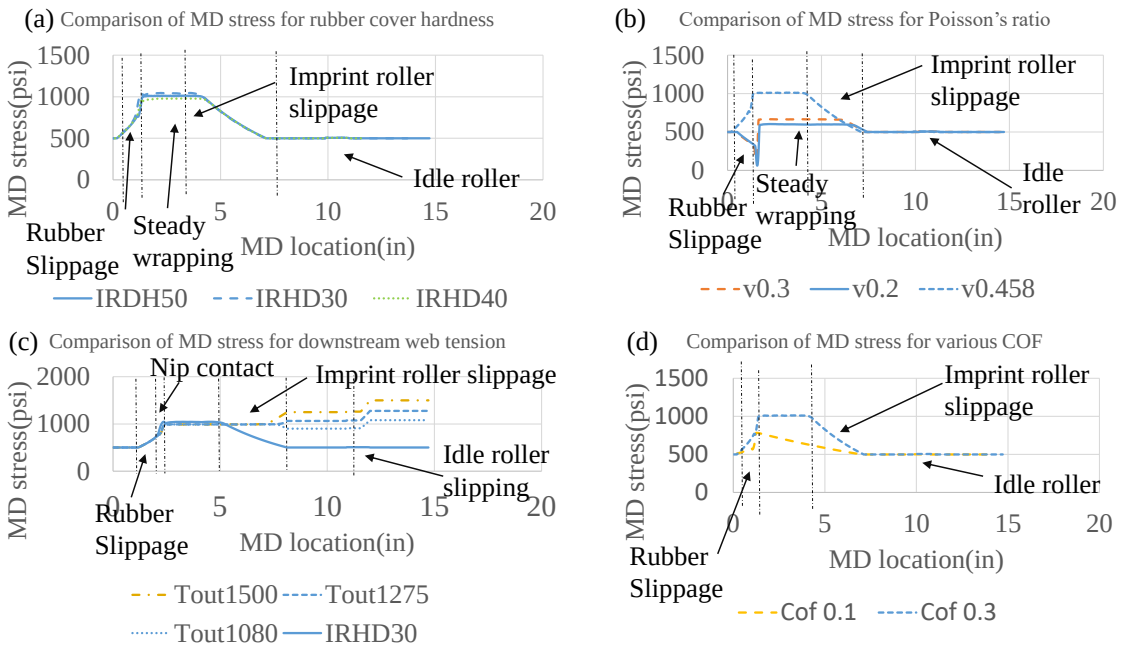

Fig. IV-12 (a) Comparison of MD stress for various rubber cover hardness (b) Comparison of MD stress for regular rubber and lower Poisson's ratio elastomers (c) Comparison of MD stress for various downstream web tension (d) Comparison of MD stress for various interaction properties

4.3 Improvement of UV-NIL process machine and simulation

The roll-to-roll UV NIL project is concerned with scaling UV NIL to production levels by performing the process continuously with a speed of 20 m/min on R2R machines. The results of our trial tests in the laboratory indicate that inadequate curing level of UV resin prior to slippage or peeling will result in defects on the nanofeatures. The rubber cover is required to broaden the nip contact zone and provide the pressure and contact duration needed to force the uncured resin into the cavities on the mold. The slippage and shear motion are beneficial for filling the cavities on the mold. However, this shearing slippage after the nip contact zone will induce defects which depends on the curing level of the UV resin. These defects can be reduced by curing the resin to a higher level and increasing the strength of the nanoimprinted features prior to extraction from the mold. The slippage between the resin surface and the imprint roller prior to extraction from the mold has been discussed in section 0. The ability of the resin to react stresses without failing

depends on the strength of the resin which is dependent on the curing level of the resin. Increased process speed has a result of decreasing exposure and strength of resin prior to peeling. The inadequate curing level on the previous testbed is mainly caused by a short time of irradiation. Therefore, a new R2R UV NIL process testbed was built at Web Handling Research Center (WHRC) in Oklahoma state university, which is shown in Fig. IV-13(a). Fig. IV-13(b) shows the diagram of the geometry of the new testbed. Comparing to the previous testbed, the diameter of the imprint roller is increased to 8 inches, which will provide higher irradiation energy due to the increase of irradiating time. Since the geometry of the imprinting process line has been changed, a new numerical model had to be established to provide accurate simulation. Additionally, to improve the precision, a code that can provide friction coefficient varying as a function of cure level is introduced into the numerical model.

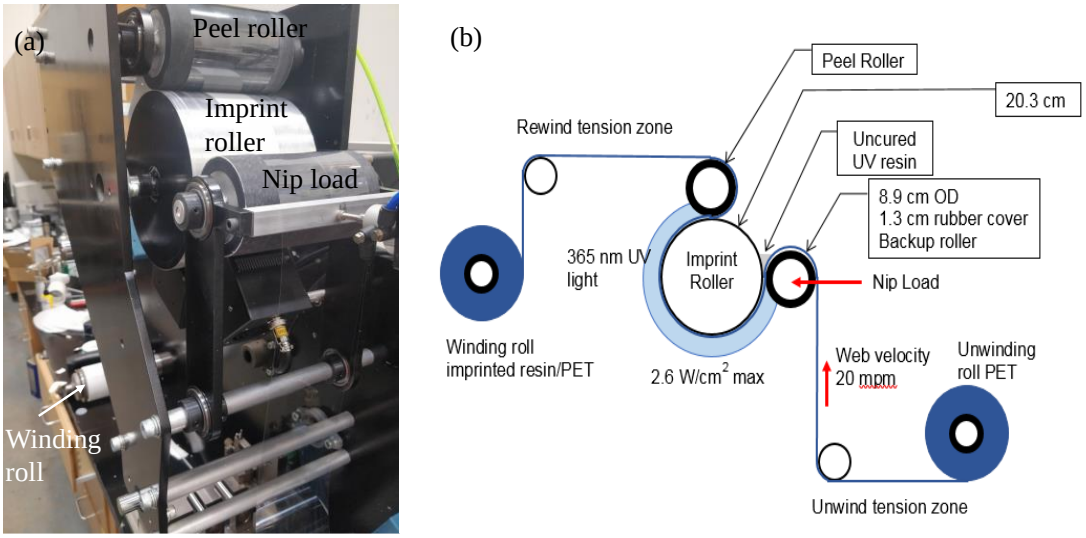

Fig. IV-13 (a) New UV NIL process testbed (b) diagram of the new testbed

As we have discussed in section 0, the main goal of the simulation is to predict the slippage and shear stresses which can potentially distort or destroy the nanofeature on the flexible substrate. The machine direction (MD) stress in the web and the contact stress produced by interactions between the resist surface and imprint roller are mainly concerned. Therefore, simulating the

continuous R2R UV NIL process as a two-dimensional model is reasonable. The two-dimensional model can also significantly reduce the computational cost, which allows us to simulate the process implicitly. The complexity in the simulation arises from the changing physics and properties of the resin between the entry and exit of the imprint roller. The resin is a liquid which serves potentially as a hydrodynamic lubricant between the polyester web and the imprint roller in the nip contact zone. After exiting the nip contact zone, UV exposure begins, and the resin first transfers to a gel state and finally a solid with strength increasing with the curing level. Comparing to the wrapping area of the web on the imprint roller, the broaden nip contact zone caused by the rubber cover is relatively ignorable. The liquid state of the resin plays a tiny important part in the whole process line. Therefore, the resin is treated as a layer of continuum elastic elements that is attached to other layers of finite elements that represent the polyester web.

The friction property between the polyester web and the imprint roller starts very low while the resin has a liquid physical form, it serves as a hydrodynamic lubricant. As the curing level increasing during the UV exposure, the cured resin is adhered to the mold before peeling. The results in 0 show that the coefficient of friction between the resin surface and the imprint roller affects the slippage and stresses in the web. A user subroutine where the friction coefficient can vary as a function of curing level results in a more accurate numerical model. When the contact pressure reduces to zero, the web with imprinted nanofeatures is free to release from the mold on the imprint roller. However, this simulation cannot study the peeling tensile and shear defects resulting from the extraction of nanoimprints from the mold. To study the defects -resulting from the demolding, a numerical model in a nanometer scale is helpful. The nano-scale demolding numerical model will be discussed in the next chapter.

Model setup of the improved numerical model

As we have discussed thoroughly the numerical model in section 0, the details of the new model would not be elaborated. Except for the geometry, the rest of the model remained the same. The geometry of the new numerical model is shown in Fig. IV-14.

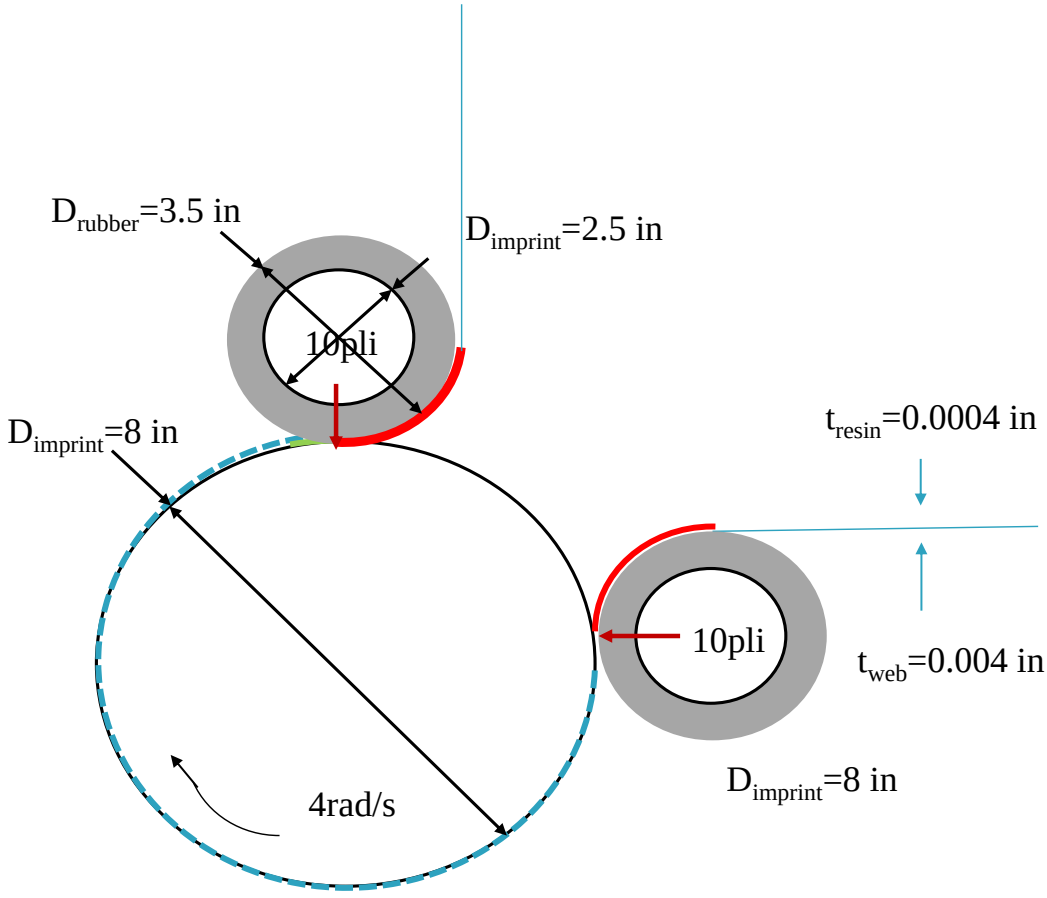

Fig. IV-14 Schematic of geometry for the model

As the reduced integrational elements are not reliable on the thickness direction due to unlimited propagated deformation, the number of elements through the thickness of the web affects the accuracy of the simulation. The mesh convergence in thickness direction has been studied in section 0. The major difficulty of the simulation is dealing with the expensive computational cost while modeling the material of the resin with high accuracy. To pursue the most efficient mesh

size with the highest computational accuracy, the convergence test for mesh length was also applied. The stress in the machine direction is the parameter we concerned most, thus, S11 was used to examine the convergence. The mesh length as 0.04 was chosen as the mesh size with the best efficiency.

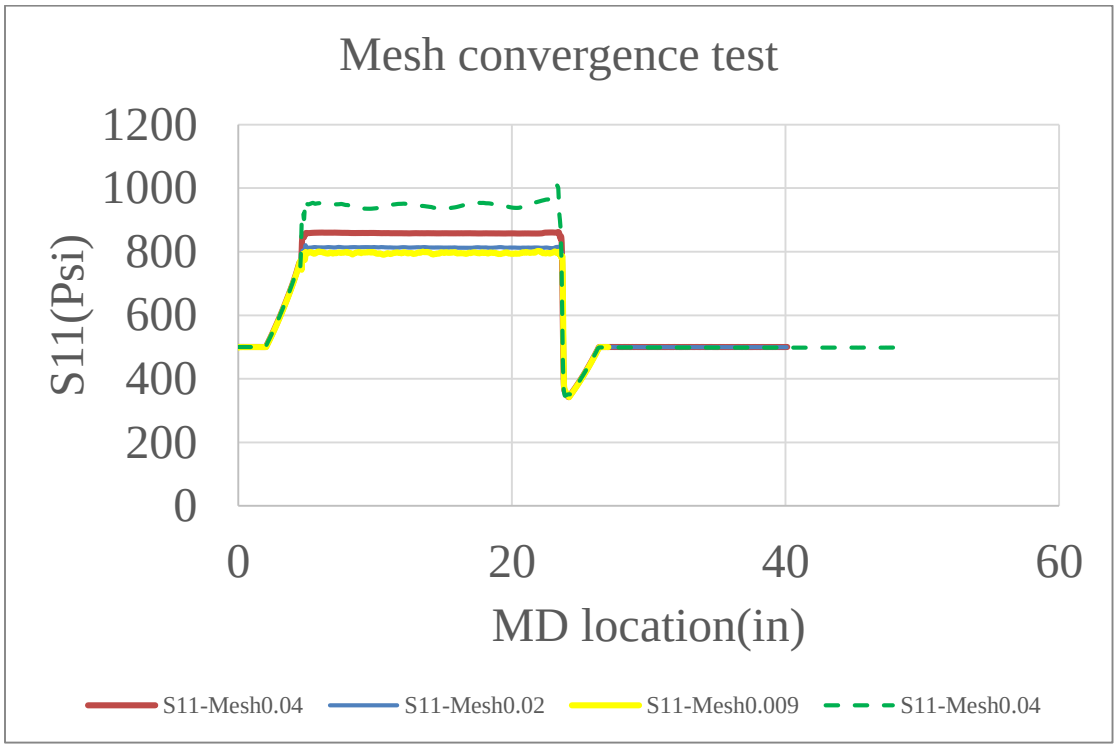

Fig. IV-15 Mesh convergence test for new numerical model

Results of new setup simulation

The case without resin coating was always a good start to learn the mechanism in the process of UV NIL. The slippage at the rubber cover part and nip induced tension at nip contact zone 1 was the same as the previous model, as shown in Fig. IV-16 (a). One should notice that there was a phenomenon that happened at the nip contact zone 2. The MD stress decreases down below 500 psi first and then returned to 500 psi by the slippage between the web and the top rubber. Based on the nip contact mechanism, the impinged rubber will have a contact surface velocity higher than that of the imprint roller surface. The tangential contact stress was negative at the negative x-axis and increased to positive due to the difference of velocity for the rubber surface and the

imprint roller, as shown in Fig. IV-16(b). In the chart, the only way to adjust the tension variation in a thin web was slippage. Therefore, the slippage happened at the exit area of the imprint roller.

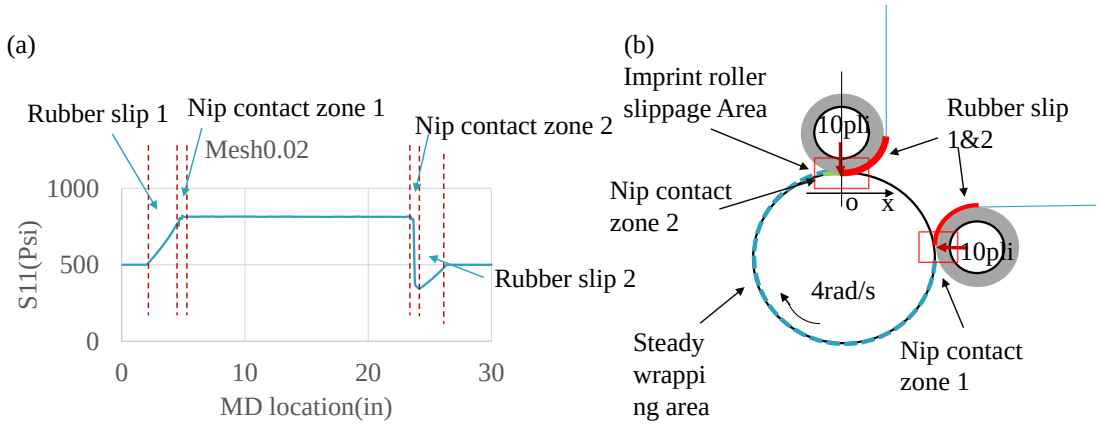

Fig. IV-16 (a) MD stress distribution for the case without resin coating (b) instruction for the corresponding area for the MD stress distribution

The MD stress distribution of the case with resin coating on the flexible substrate was shown in Fig. IV-17(a). It was obvious that there was a linear decrease right before the exit area of the imprint roller, which was called “imprint slip”. This slippage was in line with the contact friction envelope, which was shown in Fig. IV-17(c). The slippage length was 3.37in which was in line with the S11 chart. The slippage that caused increase tension at nip contact zone 1 was shown in Fig. IV-17(b). The comparison between the cases with and without resin coating showed a good agreement in the MD stress distribution, as shown in Fig. IV-18. Therefore, simulating the UV resin as a thin layer was not necessary.

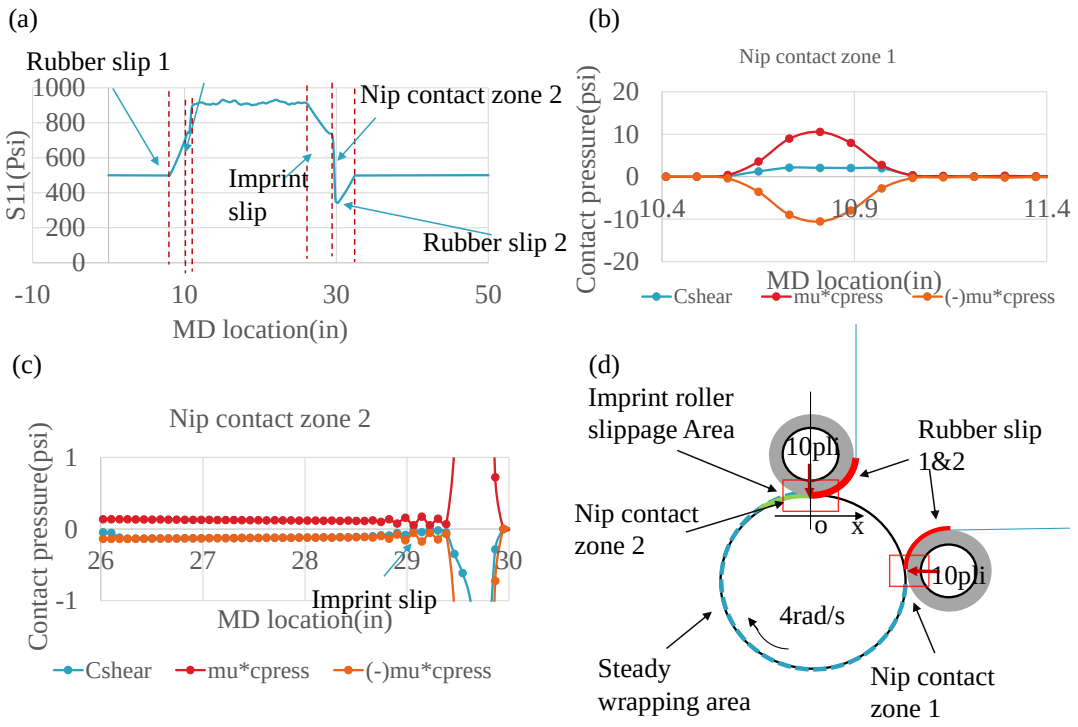

Fig. IV-17 (a) MD stress for the web with the coating resin at different locations (b) shear traction and friction envelope at the nip contact zone 1(c) shear traction and friction envelope at the wrapping contact zone (d) instruction for the corresponding area for the MD stress distribution

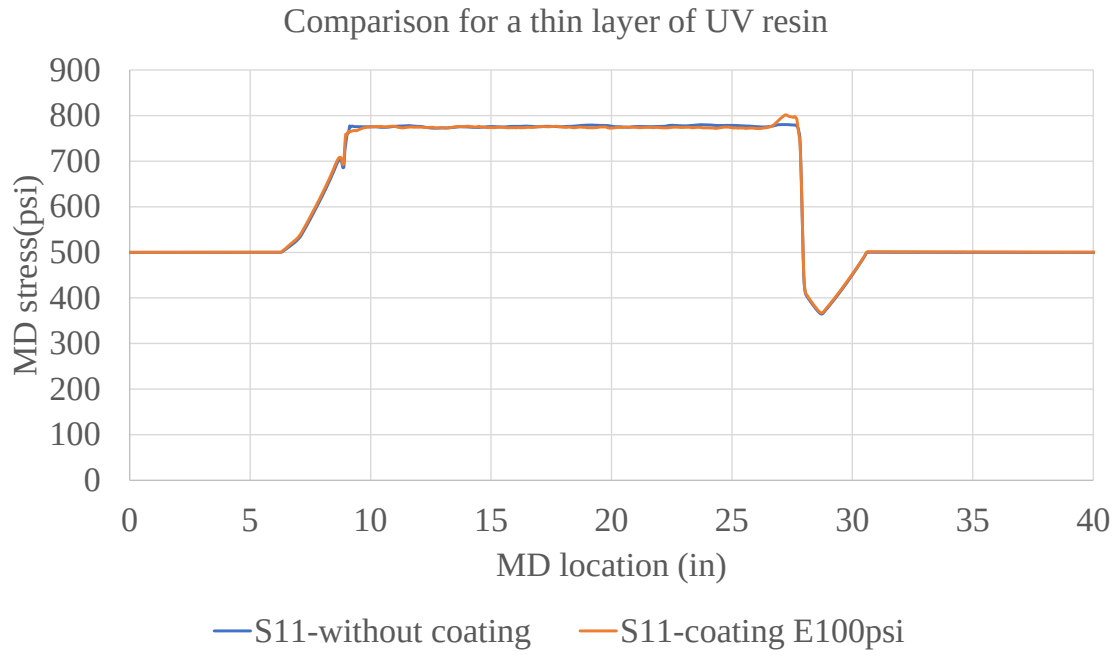

Fig. IV-18Comparison of MD stress distribution between the case with and without resin coating

As shown in Fig. IV-14, a rubber covered peel roller was arranged on the top of the imprint roller. Since a vertical load was applied on the rubber cover, a nip induced tension was also introduced at the top nip set. As shown in Fig. IV-19, the nip roller truly reduced the slippage length between the resin and the imprint roller. However, the slippage still happened in the nip contact area. This slippage at the nip contact zone 2 could also destroy or distort the nanofeatures on the substrate. If we replaced rubber covered roller with a rigid roller, and adjusted the downstream tension to 770 psi, the slippage at the exit part of the imprint roller was eliminated, which was in line with the results of section 0. Thus, by adjusting the operating parameters and arrangement of the process machine, the slippage between the resin and the imprint roller can be eliminated.

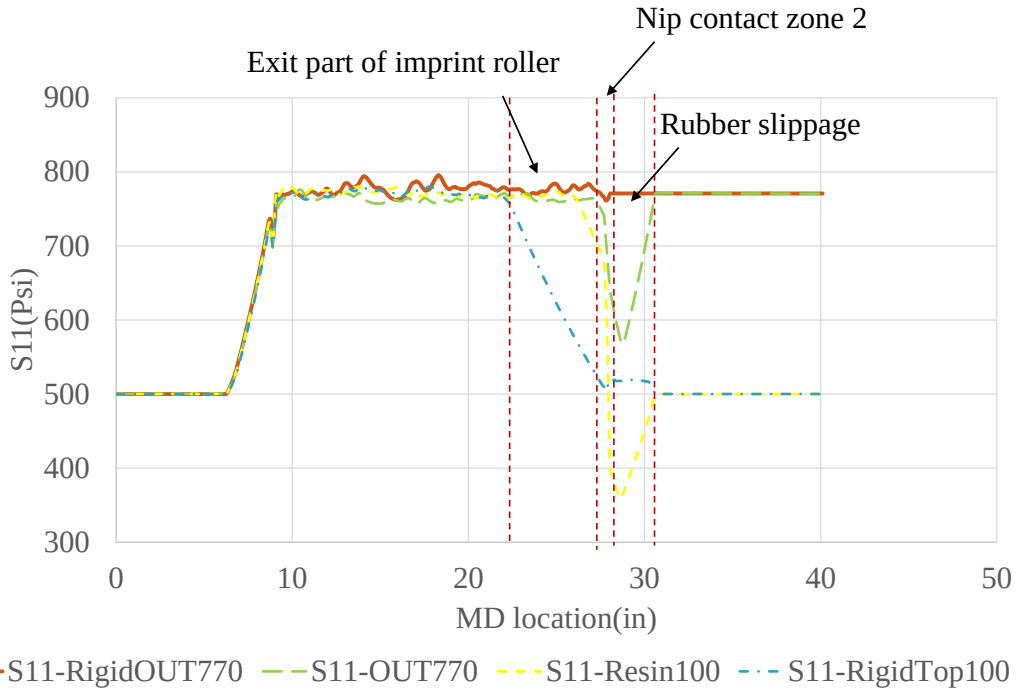

Fig. IV-19 MD stress distribution for finding optimal operation parameters

4.4 Spatial-dependent COF

In the previous section, we have shown that the results are the same between the case with modeling the resin coating as a thin layer and the case without a resin coating. In chapter 3, we have demonstrated how the properties of the UV cured resin are not attained instantaneously on

exposure to UV light[173]. Modulus and tensile strength as well as the contact properties at the interface between the resin and the ETFE mold increase initially with exposure where cross-linking of the polymer resins initiate but also increase with dark curing time where the cross-linking between polymer chains continue after exposure. To characterize the tangential behavior at the interface between the UV resin and ETFE mold on the roll-to-roll manufacturing process line, a coulomb friction contact model is established as a function of curing level. The curing level is directly related to the UV intensity and exposure time (see section 0). Since the UV light is provided by four LED UV arrays arranged uniformly on the process line, the UV intensity is assumed to be constant on the roll-to-roll process line. Commercial UV-NIL processes that are economically successful require speed and productivity which are attributes of roll-to-roll (R2R) manufacturing processes. The exposure time of the UV light is inverse proportional to the process speed. Thus, a coulomb friction contact model is developed as a function of process speed. To apply the contact model in the commercial finite element package Abaqus/standard, a user subroutine named FRIC is necessary. By applying the user subroutine FRIC, a practically numerical simulation of the roll-to-roll NIL manufacturing process is established.

Coulomb friction in user subroutine FRIC with penalty method

The ideal frictional behavior between two contacting bodies is following the coulomb friction law, as shown in Fig. IV-20. In Fig. IV-20, it is apparent that if the tangential shear stress less than critical shear stress, there will be no relative motion. In the penalty formulation method of the friction, a condition of no relative motion is approximated as a stiff elastic behavior, as shown in Fig. IV-21. Thus, a small amount of elastic slip $\left|\gamma^{el}\right| \leq \gamma_{crit}$ is allowed although there should be no slippage at all. The elastic slip is, therefore, related to the frictional shear stress through the relation

$$\tau = k_s \gamma^{el} \qquad \text{(IV-13)}$$

where

$$k_s(p) = \frac{\tau_{crit}}{\gamma_{crit}} = \frac{\mu p}{\gamma_{crit}} \qquad \text{(IV-14)}$$

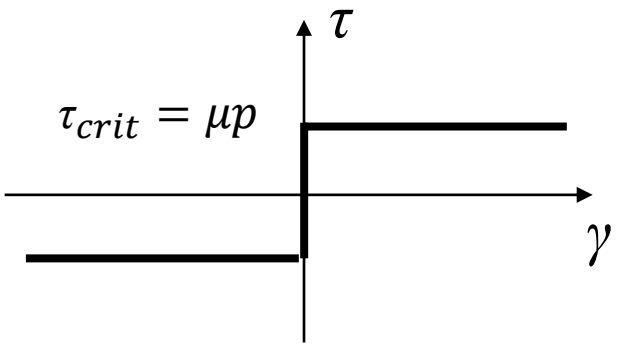

Fig. IV-20 Ideal frictional behavior between two contact surfaces

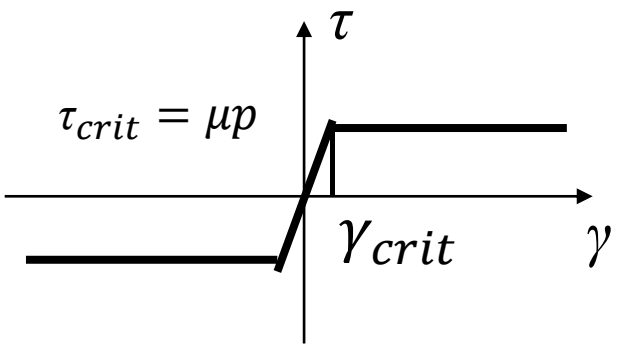

Fig. IV-21 Stiff elastic friction behavior when applying penalty formulation of Coulomb friction model

The behavior remains elastic until $|\tau| \leq \tau_{crit}$. Linearize the equation(IV-14),

$$d\tau = k_s d\gamma^{el} + \frac{\gamma^{el}}{\gamma_{crit}} \mu dp \qquad \text{(IV-15)}$$

The equation (IV-15) is valid in the stiff elastic region, $|\tau| \leq \tau_{crit}$. If $|\tau| \geq \tau_{crit}$, the frictional shear stress is given by

$$\tau = \frac{\gamma}{|\gamma|} \tau_{crit} = \frac{\gamma}{|\gamma|} \mu p \qquad \text{(IV-16)}$$

where γ is the total slip. Note that the $\gamma/|\gamma|$ is the direction of the frictional shear stress. The elastic slip is calculated by

$$\gamma^{el} = \frac{\tau}{k_s} \qquad \text{(IV-17)}$$

The incremental plastic slip which is denoted as $\Delta\gamma^{sl}$ is calculated as

$$\Delta\gamma^{sl} = \bar{\gamma}^{el} + \Delta\gamma - \frac{\tau}{k_s} \qquad \text{(IV-18)}$$

where $\bar{\gamma}^{el}$ is the elastic slip at the start of the iteration, and $\Delta\gamma$ is the current slip increment passed to user subroutine FRIC. The elastic predictor is defined as

$$\tau^{pr} = k_s\left(\bar{\gamma}^{el} + \Delta\gamma\right) \qquad \text{(IV-19)}$$

The increment of the plastic slip can also be written as

$$\Delta\gamma^{sl} = \frac{\tau^{pr} - \tau}{k_s} \qquad \text{(IV-20)}$$

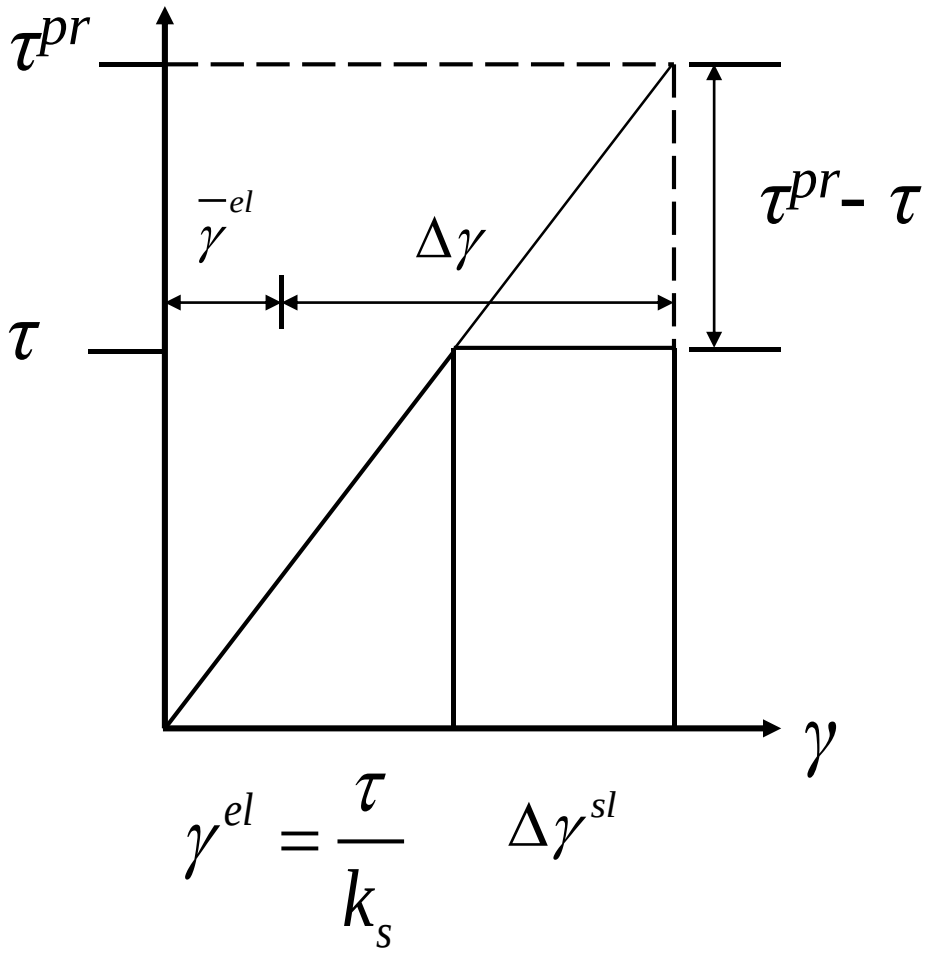

Fig. IV-22 Computation of incremental slip

Characterization of contact properties in the simulation

The tangential behavior at the interface between the UV resin and ETFE mold on the roll-to-roll manufacturing process line is characterized by a coulomb friction contact model as a function of curing level. The coefficient of friction at the interface increases with the curing level, which has been discussed in chapter 3. Moreover, the curing level is directly related to the intensity of the UV light and the exposure time. Since the UV irradiation source is uniformly provided by four LED arrays, the UV intensity on the process line can be regarded as constant. The exposure time is dependent on the process speed. To characterize the coefficient of friction (COF) as a function of the curing level, a spatial-dependent coefficient of friction method is applied. This method

precisely describes the increasing COF as a function of the curing level of the UV resin. As we have shown in section 0, the COF is defined as a function of exposure time. Since the process speed is known, the exposure time can be defined as a function of spatial coordinate. The contact properties at the interface between the resin and the ETFE mold increase initially with exposure where cross-linking of the polymer resins initiate and increases steeply in a few seconds. It is reasonable to use the average COF to represent the transit COF in a short range of time, as shown in Fig. IV-23. The polymerization causes the UV resin to transfer from liquid to gel to solid. In the COF test, it is apparent that the phase transfer phenomenon is occurring. The linear part of the curve is measuring the shear deformation of solid resin, as we discussed in section 0. Thus, the UV resin is tangentially bonded with the imprint roller when the COF reaches the linear part. One should note that the purpose of this simulation is to predict if the slippage will occur on the process line. Thus, the COF is defined as a constant after the point to predict whether the contact shear stress at the interface will exceed the shear strength of the UV resin or not. If the contact shear stress exceeds the shear strength, the failure of the resin would happen, then the slippage would occur. The spatial-depend COF under process speed of 14mpm, 10mpm, and 6mpm are shown in Fig. IV-23,Fig. IV-24 and Fig. IV-25, respectively.

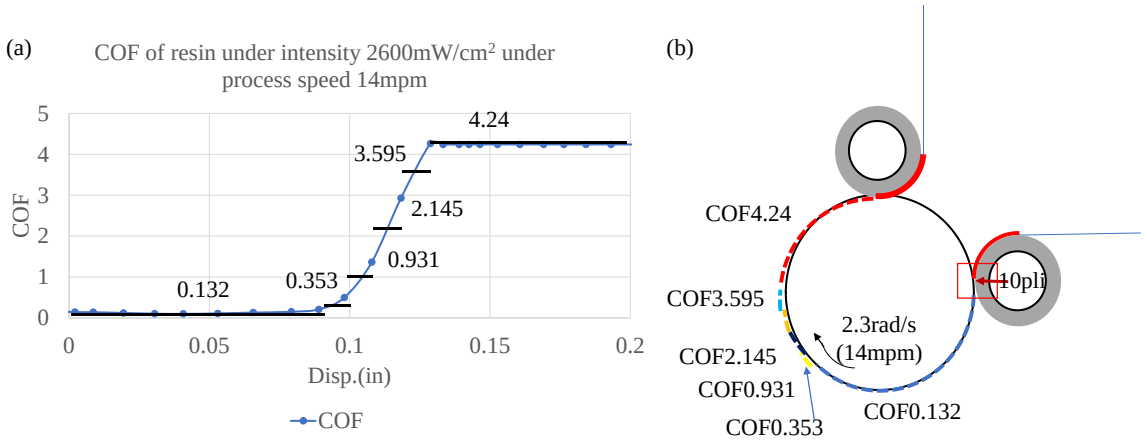

Fig. IV-23 (a) Spatial-depend coefficient of friction in the roll-to-roll nip mechanics simulation under process speed 14mpm (b) corresponding coordinate with the average COF in a short range of time

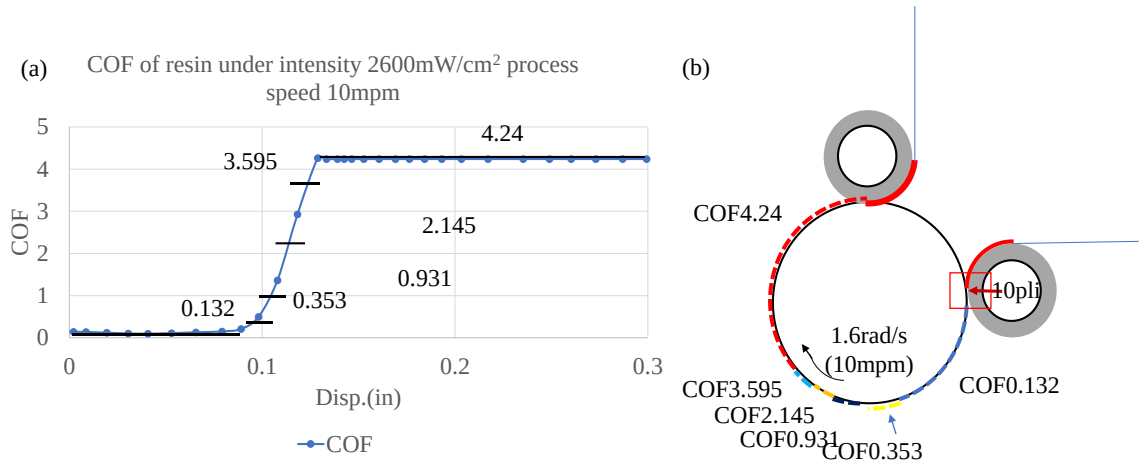

Fig. IV-24(a) Spatial-depend coefficient of friction in the roll-to-roll nip mechanics simulation under process speed 10mpm (b) corresponding coordinate with the average COF in a short range of time

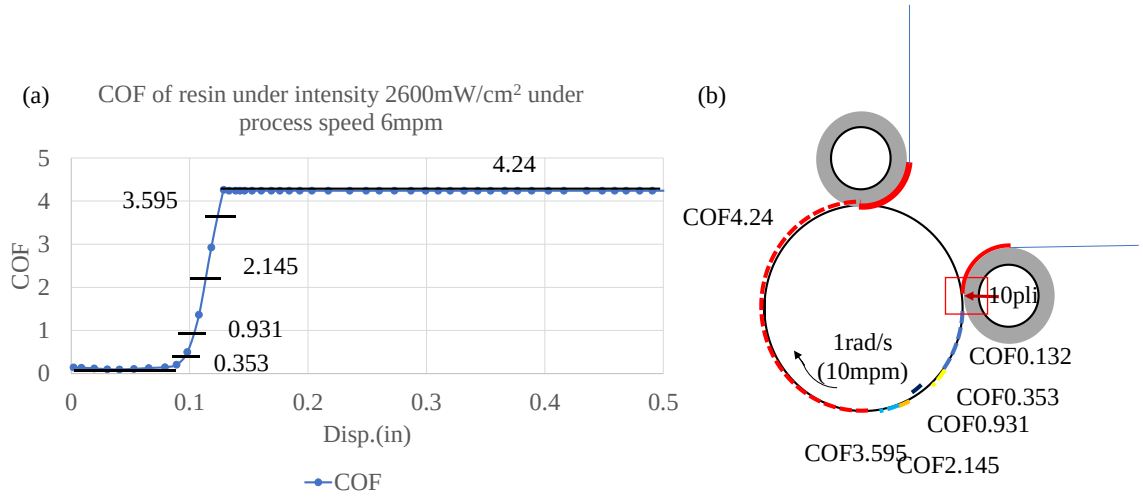

Fig. IV-25(a) Spatial-depend coefficient of friction in the roll-to-roll nip mechanics simulation under process speed 6mpm (b) corresponding coordinate with the average COF in a short range of time

Results of spatial-depend COF model

Since the tangential behavior at the interface between the UV resin and the imprint roller, the stress in the machine direction is mainly concerned. The stress distribution in the machine direction on the process line for a process speed of 14mpm is shown in Fig. IV-26. To find out if the thin resin layer will affect the MD stress distribution through the process line, a comparison between the models with and without a resin layer is made. As shown in Fig. IV-26, the MD

stress distribution is close for both models. Thus, it is reasonable to regard the resin coating layer as a spatial-dependent COF tangential behavior.

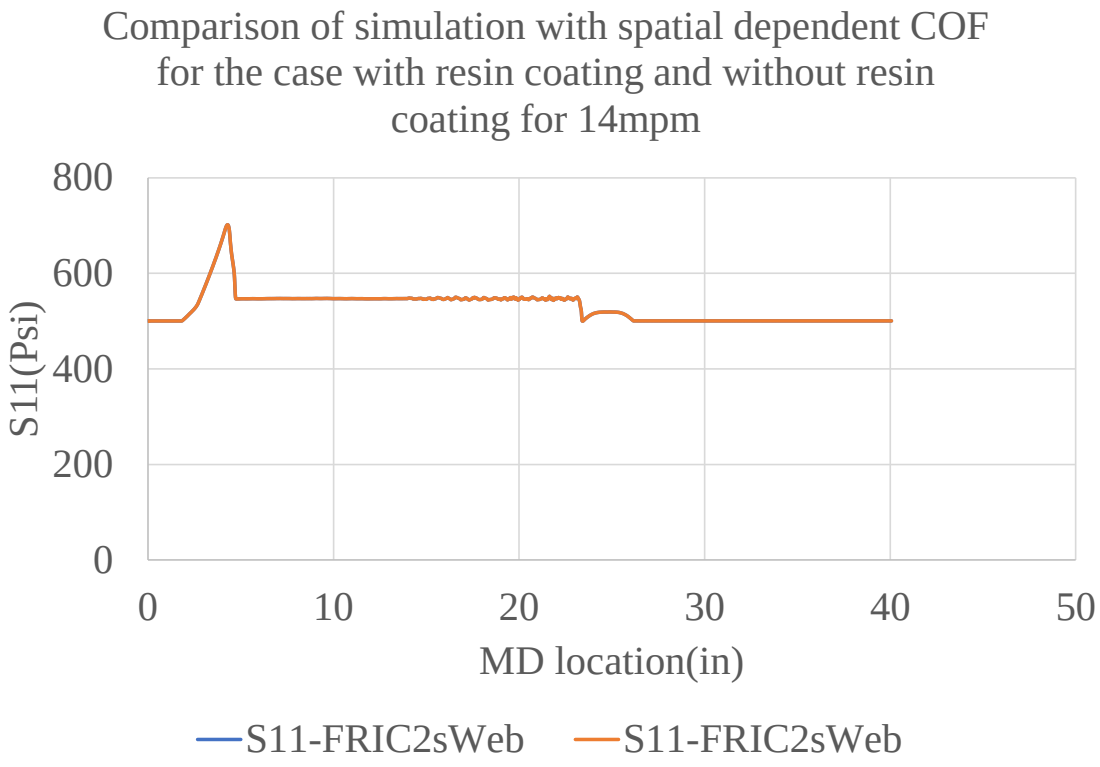

Fig. IV-26 Comparison of MD stress distribution for the case with and without resin coating under process speed 14mpm

To find out if there is any slippage occurring adjacent to the exit area of the imprint roller, the friction envelope plot is shown in Fig. IV-27(a). The slippage is occurring in the nip contact zone, which will assistant the liquid UV resin to fill into the cavities of the ETFE mold. The stepped increase of normal contact pressure reflects that the COF increases with the curing level of the UV resin. The contact shear stress is always less than the COF times normal contact pressure at a certain location. Thus, the slippage will not happen until the web traveling through the tangential exit point of the imprint roller. Moreover, the maximum contact shear stress is 5.63psi located adjacent to the tangential exit point, which is still much smaller than the shear strength (approximately 205 psi) of UV resin under the process speed of 14mpm. Therefore, the adhesive

between the UV resin and the imprint roller will not fracture, which prove that using the upper limit of the COF is acceptable.

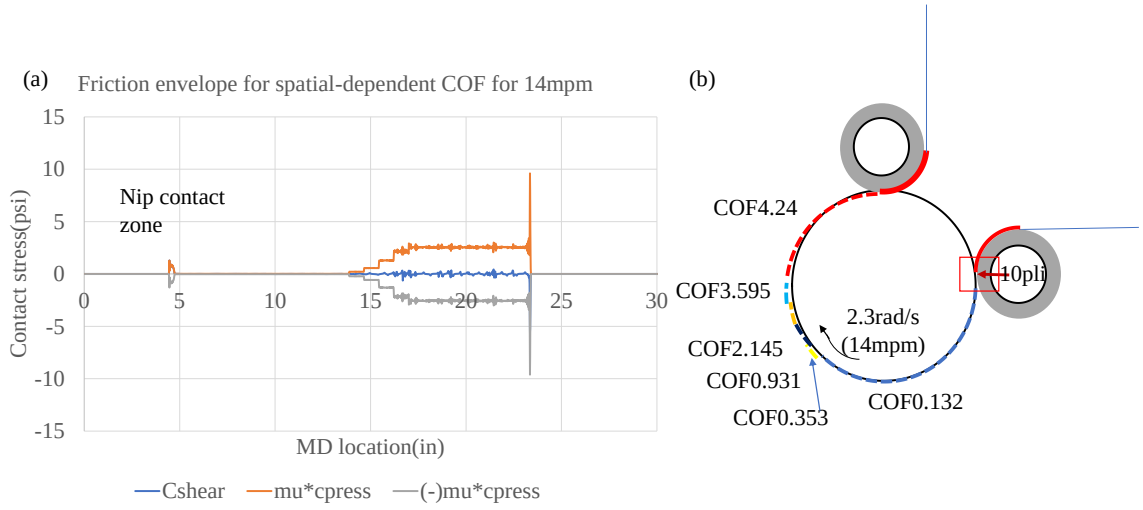

Fig. IV-27 (a) Friction envelope for the model with spatial-dependent COF under the process speed 14mpm (b) Corresponding spatial-dependent distribution of COF

The MD stress distribution for models under process speed 10mpm and 6mpm are shown in Fig. IV-28 and Fig. IV-29, respectively. The comparisons validate that a spatial-dependent COF contact model is adequate to study the stress distribution on the process line for various process speed.

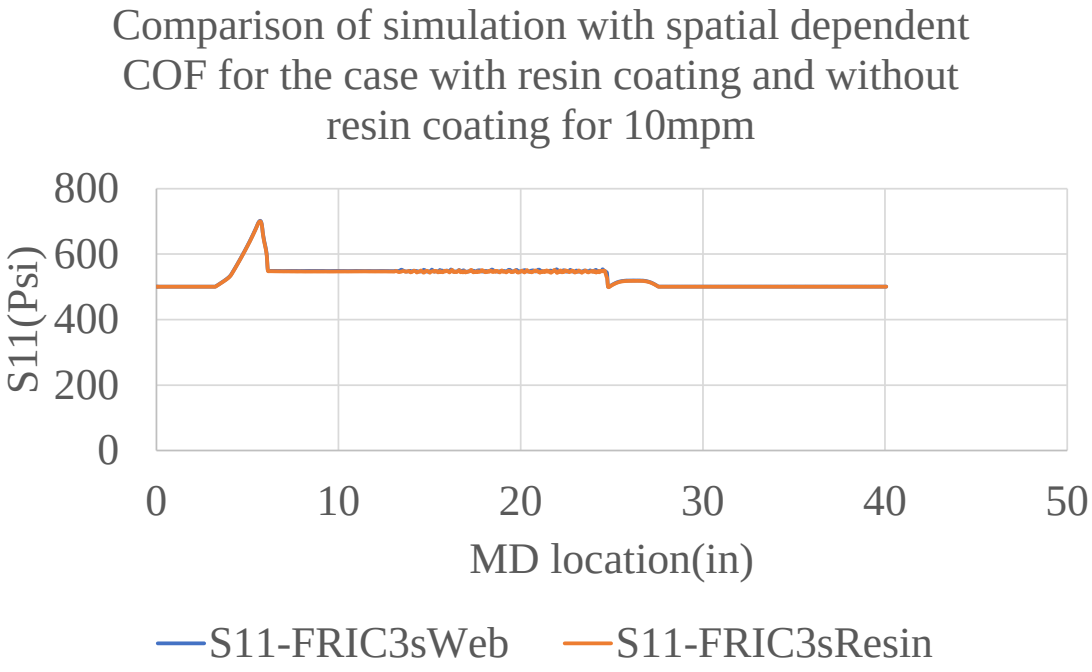

Fig. IV-28 Comparison of MD stress distribution for the case with and without resin coating under process speed 10mpm

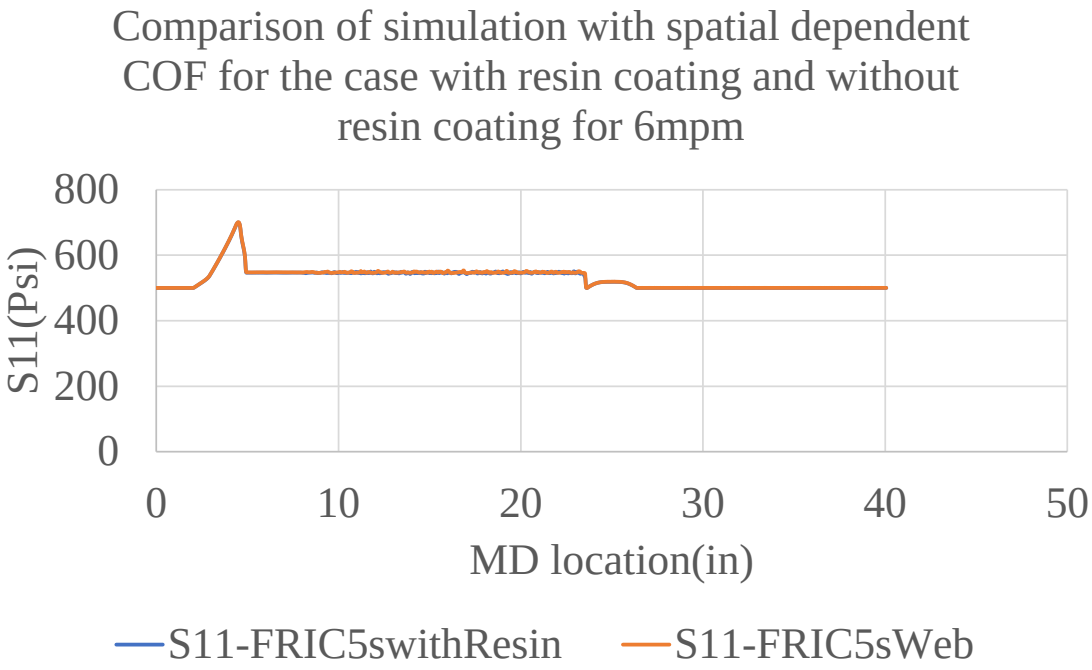

Fig. IV-29 Comparison of MD stress distribution for the case with and without resin coating under process speed 6mpm

The friction envelope plots for the model with process speed 10mpm and 6mpm are shown in Fig. IV-30 and Fig. IV-31, respectively. Both plots show that no slippage occurring until the web traveling to the tangential exit point of the process line. Thus, the defects viewed in the nanoimprints is occurring during the extraction. This is the reason that a nano-scale extraction simulation needs to be established to predict whether defect-free production can be produced. The nano-scale simulation will be elaborated in the next chapter.

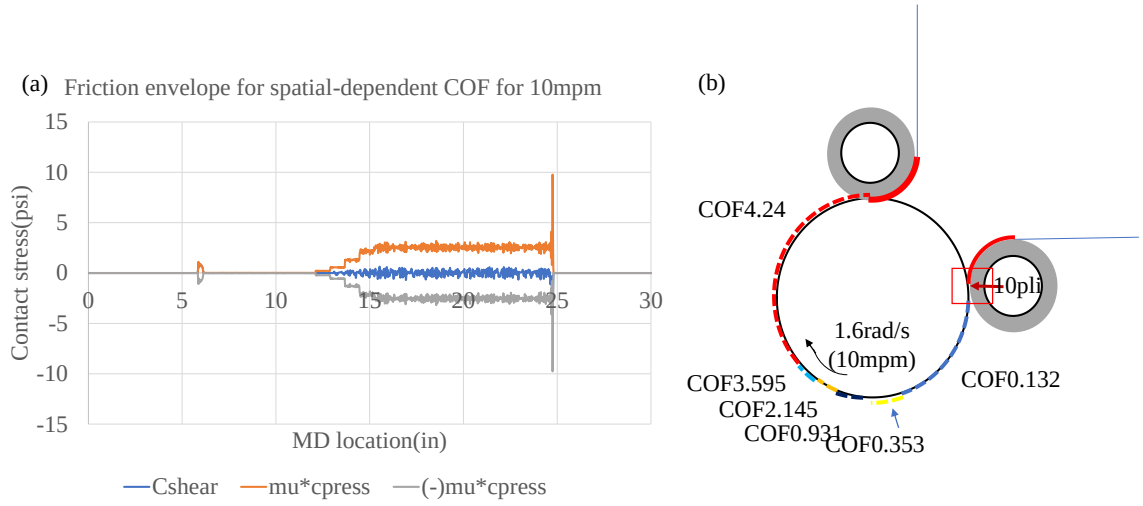

Fig. IV-30 (a) Friction envelope for the model with spatial-dependent COF under the process speed 10mpm (b) Corresponding spatial-dependent distribution of COF

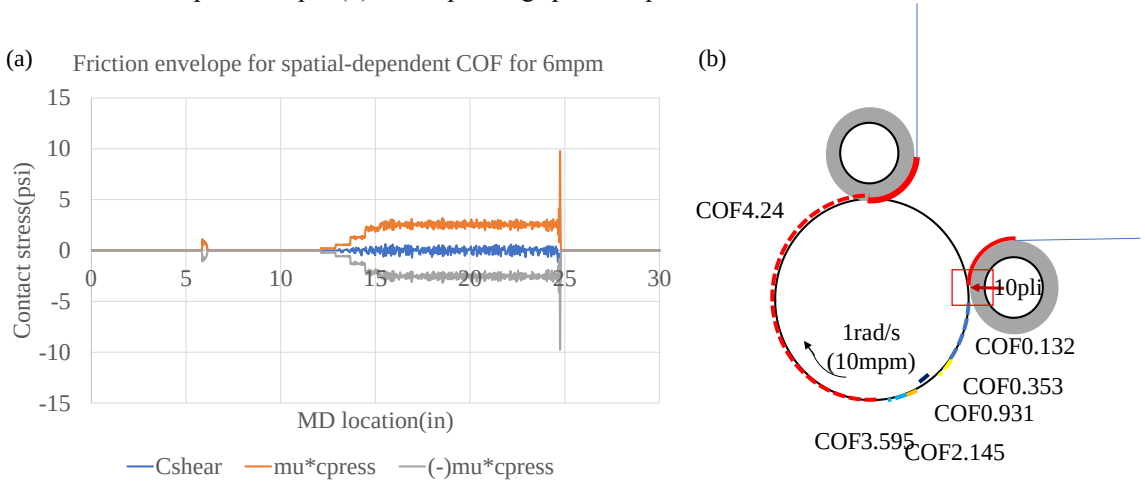

Fig. IV-31 (a) Friction envelope for the model with spatial-dependent COF under the process speed 6mpm (b) Corresponding spatial-dependent distribution of COF

Higher commercial process speed leads to higher production output. The simulation tool has the capability the predict the slippage due to the nip mechanics in the manufacturing process line. A representative prediction by the simulation at process speed of 28mpm is plotted in Fig. IV-32and Fig. IV-33. In the friction envelope, the contact shear stress is equal to the product of the coefficient of friction and contact normal stress. Based on Coulomb's friction law, the corresponding area is slipping at the interface. The length of the slippage predicted by the simulation is 0.420in. By calculating the variation of web tension with Capstan Formula (IV-11), the slippage length is 0.419in, which has a good agreement with the prediction by friction envelope.

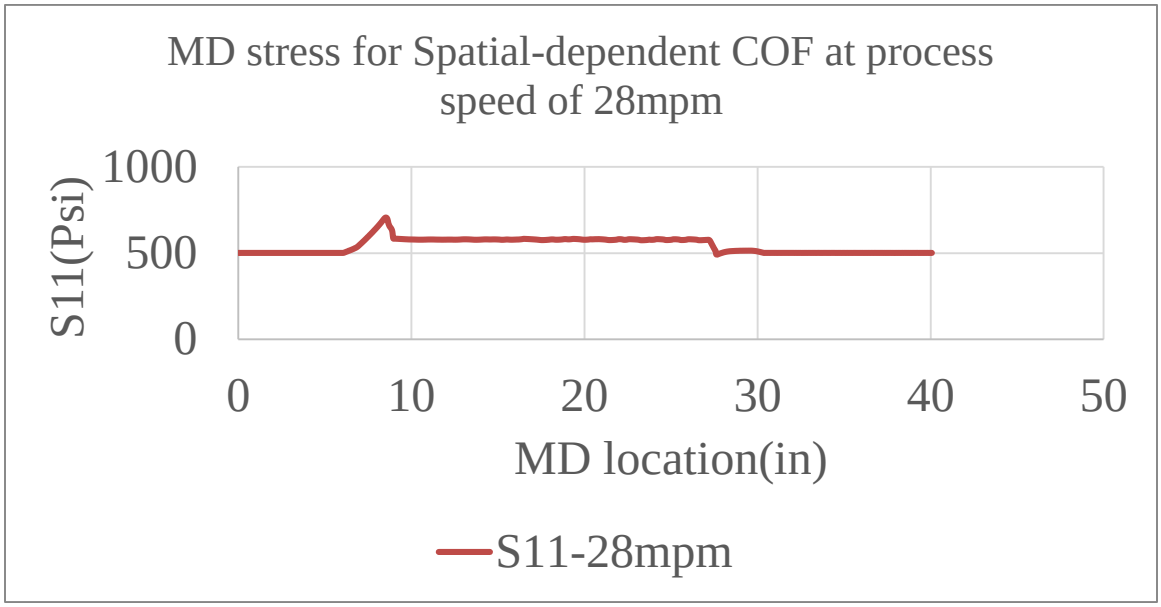

Fig. IV-32 MD stress distribution for the case at process speed 28mpm

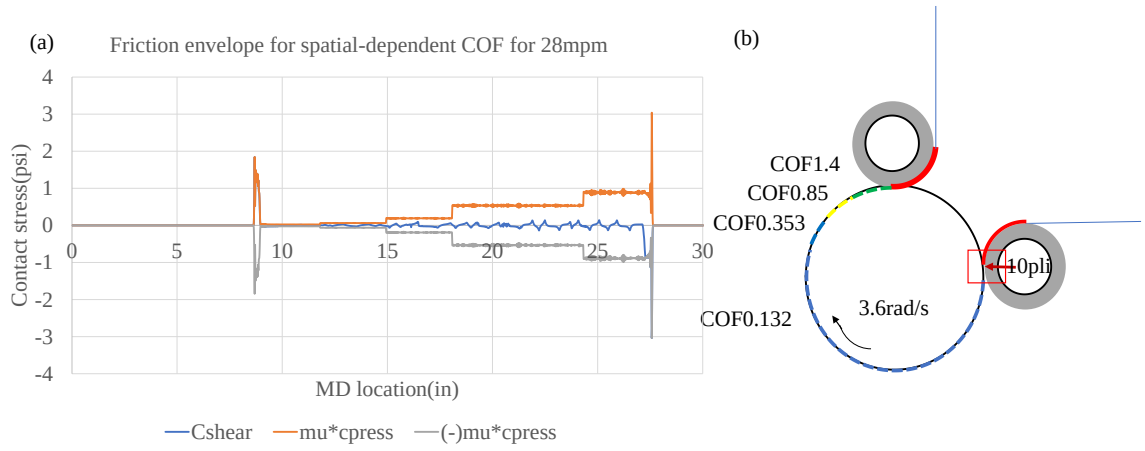

Fig. IV-33 Friction envelope for the model with spatial-dependent COF at the process speed 28mpm (b) Corresponding spatial-dependent distribution of COF

4.5 Summary

In this chapter, a series of numerical simulations were built to predict the normal and tangential behavior of the web and the resin coating. The normal contact behavior and the slippage were verified by theoretical calculations. The main purpose of the simulation is to study the tangential behavior at the interface of the resin and ETFE mold. To conquer the limitations of the simulation, the tangential behavior of the resin was regarded as a spatial-dependent contact property. To the best of our knowledge, the spatial-dependent COF model described the tangential behavior of the resin closely to reality.

As we have discussed at the beginning of this chapter, a macro-scale numerical model helps us study the whole pattern of the roll-to-roll NIL manufacturing process. The simulations guided us that the slippage induced by the nip mechanism can be eliminated. However, the macro-scale model cannot reach the details of the topology of the nanofeatures during the demolding step. To study the mechanics in the demolding step, a nano-scale numerical model had to be established. This part would be elaborated on in the next chapter.

CHAPTER V

V. Nano-scale simulation of the mold extraction process

As we have discussed in Chapter 0, the dynamic simulation for the roll-to-roll NIL process can describe the whole pattern of the process line. In this chapter, the mechanism during the demolding step will be focused on. A nano-scale numerical model will be established to study the stress distribution for the nanofeatures imprinted on the flexible substrate. The shrinkage of the resin induced normal and shear stress at the interface between the resin and the mold. The adhesive properties also contribute to the stress distribution during the demolding process. When the interface between the mold and UV curable resin breaks apart, the friction behavior at the interface performs a role to affect the mechanic in the nanoimprints. The demolding process of roll-to-roll NIL is a study combining the adhesive strength, shrinkage, as well as friction behavior at the interface. To compute tearing failures, the modulus and tensile and shear strength and the shrinkage of the resin in addition to the adhesion toughness and friction at the interfaces between the resin and the mold must be known. The maximum principal stress criterion is used to determine if the nanoimprints are distorted or fall apart. The maximum principal stress is defined as the highest value of principal stress all over the nanoimprints through the history of the demolding in the numerical model. This maximum principal stress will then be compared to the

ultimate tensile and shear strength of the resin which is also tested. In this paper, the UV curable resin we used in the current project is UV15, an acrylate-based cationic epoxy. The mechanical properties mentioned above are varied by increasing the curing level. Additionally, the acrylate-based cationic epoxy UV curable system has a “dark-curing” effect[20, 21]. Once the polymerization started, the reaction continued until the cross-linking was done. However, the high process speed of production provides a relatively narrow time-span for the demolding process. The UV curable resin cannot reach its fully cured state when the demolding process starts. Therefore, the properties during the demolding are what we concerned. The tensile and shear strength, shrinkage, adhesion toughness, and friction for a consistent cure level for demolding are measured in this study. A numerical simulation model is established to analyze the stress distribution caused by shrinkage, adhesion as well as friction. If the maximum principal stress exceeds the ultimate strength, the demolding process can be considered unsuccessful due to the failure of some part of the nanoimprints. This comparison provides a quantitative way to estimate the success of demolding.

5.1 Description of the model

A 2-dimensional model shown in Fig. V-1 was consisted of a PET web, a UV curable resin layer as well as an ETFE mold in a sandwich structure. A plane strain assumption is justified by the fact that the dimension of the grating channels was in higher orders of magnitude than the width and height of the ETFE mold and the PET web. Since the resin can freely shrink in the direction parallel to the channels, the plane stress assumption was applied to the nanoimprints. A web with a thin layer of resin coating was built to go through the nip contact zone and wrap on the imprint roller till it exited the imprint roller. The web and the resin layer then peeled from the imprint roller. Since the radius of the peel roller is five orders of magnitude larger than the thickness of the PET web, it was reasonable to regard the boundary condition on the top surface of the PET web as a vertical displacement instead of the peeling with a certain angle. To study the stress

distribution experienced through history during the demolding in the nanoimprints, a single nanofeature was built. The schematic diagram and dimension for the numerical model is shown in Fig. V-1 (c). The model consisted of an ETFE mold with a 180nm cavity at the center. The UV curable resin filled into the cavity with a 360nm residual thickness. The PET web was the flexible substrate with a thickness of 10μm. The simulation was conducted in three steps: In the first step, a pseudothermal contraction was applied to mimic the shrinkage of the UV curable resin during the curing process. The mold was constrained at the bottom surface and left side; In the second step, a bending load was applied on the PET web to simulation the bending caused by peel roller; In the third step, the resin was pulled out vertically by applying a real-time velocity on the PET web to simulate the peeling action by the peel roller.

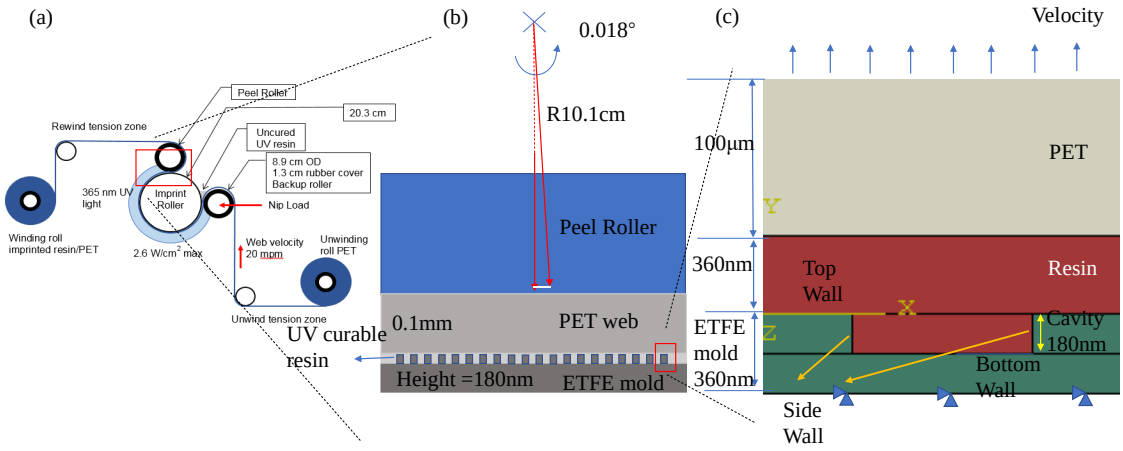

Fig. V-1 (a) Schematic diagram of the roll-to-roll NIL process line (b) amplified demolding process (c) amplified a single nanofeature and boundary conditions. (the interface between the resin and the mold was modeled as surface-based cohesive property. Simulation was conducted in two steps: 1st Pseudothermal contraction was applied to mimic the shrinkage of the UV curable resin during curing process. The mold was constrained at the bottom surface. 2nd the resin was pulled out vertically by applying a displacement on the PET web.)

Line gratings have horizontal and vertical contact walls. The release of these walls had different fracture modes and time sequence during extraction. The elaborated fracture mode will be described in interaction property. For clarity, the name for each wall is identified here. As shown in Fig. V-1, the interface between the residual layer of resin and the mold was called “top wall”,

which will be first fractured by shrinkage of the UV curable resin due to the curing process. The vertical contact surface between the nanoimprints and the mold was regarded as “sidewall”, which will suffer shear stress combining the adhesive and friction behavior. The bottom surface of the nanoimprints was named after “bottom wall”, which had similar property to the top wall.

Abaqus provides a huge variety of elements in its library. A family of continuum quadrilateral elements was used to model plane problems. Second-order quadrilateral elements were not suitable for contact problems due to the convergence difficulties. Reduced integration form of elements which were known as CPE4R and CPS4R for plane strain and plane stress problems. These elements eliminate shear locking but they had a defect which is called hourglassing. The deformation of this kind of element consumes zero-energy. Hourglassing can propagate easily through a mesh of first-order reduced integration elements, which can cause unreliable solutions. However, multiple layers of the reduced integration elements can overcome the problem for causing unreliable solutions. The element was controlled by an algorithm of the structured quadrilateral. The element size was balanced by considering the accuracy and the computational cost.

Interactions between the resin surface and the mold including adhesive and friction behavior introduced nonlinearity in the numerical model. The stable time increment was set to a small number due to the small dimensions of the nanoimprints, which resulted in a large computation time. The nonlinearity and small stable time increment may cause convergence difficulty in the implicit method. Predicting the distortion, deformation, and internal stresses within the nanoimprints was the goal of these simulations. When the internal stresses surpassed the strength of the resin in its cure state at extraction, failures of imprint features could be expected which would degrade the quality of the imprint.

5.2 Material property

The PET web and the ETFE mold in the simulation were given properties that are common for PET films and fluorine-based plastic. The resin was liquid before UV exposure. Under UV irradiation, the resin started polymerization from liquid to solid. The UV curable resin is under the phase transition in the process line. Different process speed provided different exposure time of UV light. At the point in time where extraction of the imprint from the mold occurs, the resin had achieved a state of curing level that provides strength. This is achieved by ensuring adequate UV exposure of the resin by adjusting UV intensity, the wrap of the resin/web about the imprint roller, the diameter of the imprint roller to sustain a desired R2R production velocity. In the extraction process, the strain-rate of the nanoimprint is high due to the high process speed. The average strain-rate of the nanoimprint during the demolding process is shown in Table V-2.

Table V-1 Mechanical properties for web and rubber

Young's modulus of ETFE mold E_m	1500Mpa
Poisson's ratio of ETFE mold v_m	0.45
Young's modulus of PET web E_w	4826Mpa
Poisson's ratio of PET web v_w	0.3

Table V-2 Material property of UV resin under different process speed

Process speed(mpm)	Exposure time(s)	Extraction time(s)	Strain-rate(s^{-1})	Shear modulus(psi)	Shear strength(psi)
6	4.8	0.0011	88	2861	511
10	2.88	0.00066	139	2519	302
14	2.05	0.00047	208	1464	208

Based on the DMA test results, the loss factor of the UV 15 showed a trend of decreasing when applying higher frequency load. As discussed in section 3.2, an assumption that the UV 15 follows the trend that the loss factor would decrease with increasing frequency was made. Since the strain-rate in the process line is several orders of magnitude higher than the DMA test, an assumption that the UV 15 behaved its elastic property in the process line during the demolding

process was made. Thus, the UV curable resin was modeled as an elastic solid as shown in Table V-2.

5.3 Interaction property

The surface energy at the interface between the resin and the PET web was much higher than that between the ETFE and the resin, as proven by the T-peel tests. The PET web was bonded with the resin, while the interaction between the resin and the mold was defined as surface-based cohesive behavior. The cohesive surface was zero thickness cohesive elements embedded at the interface[174]. The property of the cohesive behavior involves two parameters: (1) initiation crack stress which is regarded as fracture strength obtained by experiments; (2) Fracture energy which is the adhesive toughness (see section0). The traction-separation law was applied to the cohesive surface, which is shown in

Fig. **V-2**. The element behaves elastically before reaching the initial failure stress, which is also known as maximum nominal stress in the ABAQUS. Before the point A (see

Fig. **V-2**), the unloading curve follows the path of loading and this is called “elastic region”[11]. Beyond the initial failure stress, the unloading path goes directly back to the point O, as path BO shown in Fig. V-2, which is called “softening region”. In this region, the cohesive elements are not pulled apart. While the separation continues to increase, reaching point C, the elements fail. This is the “fail region”. The properties of the cohesive surface tested in section 0 are not time-dependent. The loading is assumed to be taken place in a way that the equilibrium condition was reached instantaneously at every point in the system. Adhesive failure is applied to the mixed-mode fracture (Mode I and II) in the model. Mode I fracture is known as opening mode and occurs when tensile stress is perpendicular to the plane of the crack area. Mode II fracture happens when the shear stress acts parallel to the plane of the propagating crack. The dominant fracture mode of the demolding process on the horizontal interface is mode I. The fracture mode

on the vertical interface is mixed by mode I and II. On the vertical sidewalls, the shrinkage of the UV curable resin causes normal stresses which will lead to a mode I fracture. The vertical displacement boundary condition induces shear stresses, resulting in mode II fracture. The properties of mode I and II fracture were assumed to be similar for simplification. Based on the results of literature [11, 18, 175, 176], this simplification is reasonable to get a reliable result of numerical simulation. Based on the results of the experiments in section0, the average maximum nominal stress was 0.006MPa, the fracture toughness was taken as 0.011 mJ/mm2. The traction separation stiffness coefficient was adjusted to acquire convergence[19].

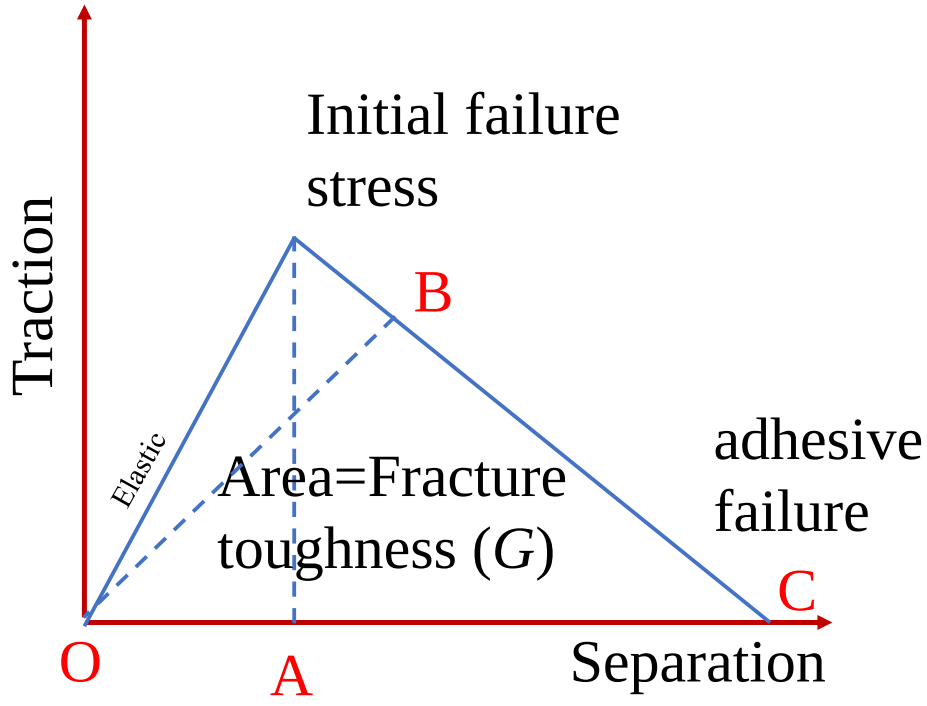

Fig. V-2 Loading and unloading curve of the cohesive area applied by traction-separation law.

The numerical modeling faced difficulties due to the nonlinearity by introducing the cohesive behavior. At the point where the interface started to break, only a small stable increment of load and time can be obtained. However, the small increment would cause the failure of the cohesive element occurred in a sudden way. The maximum principal stresses were expected just before the

failure of the cohesive surface because the stress cannot increase any further when the interface started to break. A small time increment for the expected breaking period was required to obtain the maximum principal stress.

After the adhesive failure occurred at the interface between the resin and the ETFE mold, the resin may suffer friction at the interface. Here, the UV curable resin reached the same curing level as the tests conducted for adhesive toughness. The relation between maximum frictional (shear) stresses across an interface to the contact pressure between contacting bodies is modeled by Coulomb friction law. Two contacting surfaces can react shear stress up to a certain magnitude before the slipping happened, which is the state of the stick. Coulomb's friction model defines this certain magnitude as critical shear stress. When the shear stress is smaller than the critical shear stress, two surfaces are at a stick state, otherwise, they are slipping.

$$\begin{aligned} \tau_c &= \mu P(x) \Rightarrow \text{slip} \\ \tau_c &< \mu P(x) \Rightarrow \text{stick} \end{aligned} \qquad \text{(V-1)}$$

The equation (IV-3) determines the slip/stick state for a point in the contact region.

5.4 Boundary conditions for the extraction process of roll-to-roll manufacturing

Moving the discrete UV nanoimprint lithography (UV NIL) manufacturing method to the continuous roll-to-roll manufacturing method yields higher efficiency. The demolding process of the discrete UV NIL was simulated as a uniform vertical velocity applied to the whole surface of the substrate. However, moving this discrete method in the roll-to-roll process line caused the extraction speed to be nonuniform. The extraction movement of the boundary condition was in compliance with the roll-to-roll process. The vertical component of the peripherical line speed of the imprint roller and peel roller. The diverging speed of the imprint roller and the peel roller was near zero adjacent to the tangent exit of the imprint roller, and then rose rapidly as the imprint roller and peel roller surfaces diverge. The diverging vertical velocity of two rollers increased as a

function of process speed. Since the dimension of the nanoimprints is several orders of magnitude smaller than the imprint roller and peel roller, the variation of the velocity distribution across one nanoimprint is negligible. As shown in Fig. V-1 (b), the extraction of a single nanoimprint just yields 0.018°. Thus, an assumption that the velocity on the surface of the substrate was uniformly distributed was made. A schematic diagram of the diverging velocity of the imprint roller and peel roller is shown in Fig. V-3.

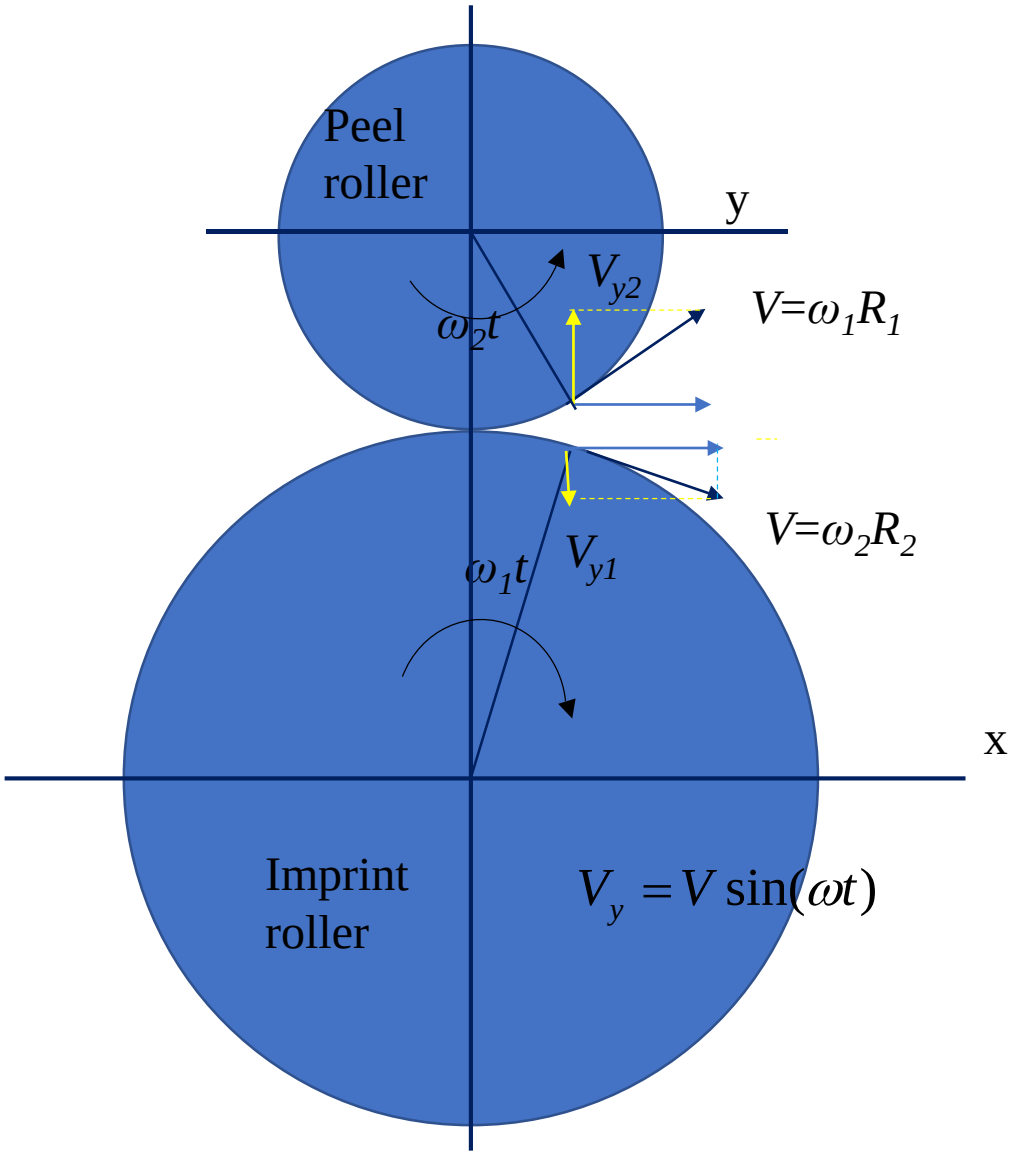

Fig. V-3 Schematic diagram of the diverging velocity applied on the surface of the substrate

The diverging velocity was calculated by

$$\begin{cases} V_y = V_{y_1} + V_{y_2} = V\sin(\omega_1 t) + V\sin(\omega_2 t) \\ \omega_1 R_1 = \omega_2 R_2 \end{cases} \quad \text{(V-2)}$$

where V_y is the diverging velocity of the imprint roller and the peel roller, V_{y1} and V_{y2} are the vertical component of the line speed of the imprint roller and the peel roller, respectively. The ω_1 and ω_2 are the angular speed of the imprint roller and the peel roller, respectively. t is the time when the substrate traveling through the process line.

The equation (V-2) yields

$$V_y = V\sin(\omega_1 t) + V\sin\left(\frac{7}{16}\omega_1 t\right) = V\sin\left(\frac{23}{32}\omega_1 t\right)\cos\left(\frac{9}{32}\omega_1 t\right) \quad \text{(V-3)}$$

Thus, equation (V-3) shows the diverging velocity for extraction on the roll-to-roll nanoimprint lithography process line.

The commercial finite element package Abaqus does not have the capability to directly describe the calculated diverging velocity. Therefore, a user subroutine named UAMP was coded to satisfy this boundary condition. The UAMP allows to define the current value of amplitude definition as a function of time. All data passed in the subroutine for information or to be updated are values at the beginning of that increment. AmpValueNew defines the current value of the amplitude. Time(iStepTime) and time(ITotalTime) define the current value of step time and total time, respectively. The diverging speed applied in the simulation had a close agreement with the equation (V-3), as shown in Fig. V-4.

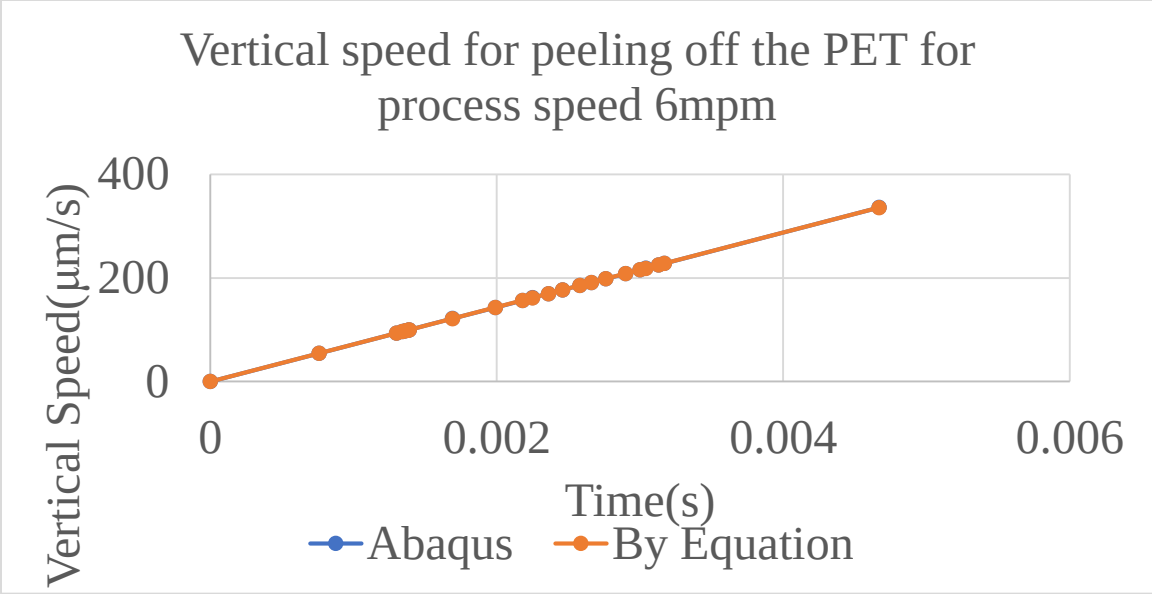

Fig. V-4 Comparison of diverging speed by equation (V-3) and the simulation

In the roll-to-roll manufacturing process, the UV curable resist was a coating on the flexible substrate. The polymerization was occurring in the UV resist while the coating layer was traveling through the process line with the substrate. As the uncured resin is applied to the web there is no internal strain. The web coated with resin conforms to the imprint roller and the resin is exposed to UV light and curing begins. As the imprinted web approaches the exit of the imprint roller we will first consider the case where no peel roller is present. As the web leaves the imprint roller and moves into the exit span, tensile bending strains of approximate magnitude h/(2R_{IR}) will occur in the resin. Here *h* is the thickness of the web and is assumed very largely compared to the resin coating thickness and R_{IR} is the radius of the imprint roller. If a peel roller is employed the bending strain will increase to a higher level of $h/(2R_{IR})$ plus $h/(2R_{PR})$ where R_{PR} is the radius of the peel roller. The bending strain is calculated by

$$\varepsilon = \frac{h}{2 * R_{IR}} + \frac{h}{2 * R_{PR}} \qquad \text{(V-4)}$$

The bending strain at the interface of the PET web and UV resin is 0.0016. The bending stress in the resin will be whatever the modulus of the resin is at the stage of curing at the exit (*E*) times

the total bending strain. If that bending stress exceeds the ultimate tensile stress of the resin, also dependent on the stage of curing at the exit, cracks will result in defects in the imprinted resin. To simulate the bending strain caused by the roll-to-roll process line, pressure is applied to the PET web which assures the resin is under the equivalent bending strain.

5.5 Results and discussion

One goal of developing this numerical model is to explore an imprint which is known to be challenging to extract. High aspect ratio nanoimprints are known to be such a challenge. The success of imprint mold extraction is important in producing high-quality imprints and maintaining the cleanliness of the mold, resin debris left in the mold from unsuccessful extractions will cause additional imprint defects. The liquid UV curable resin was first filled into the cavity of the mold with the assistance of shear force provided by the nip contact between the backup and imprint roller (see Fig. I-2&Fig. IV-13). As the resin is exposed to UV light, the liquid resin gel will shrink proportionately with the curing level. The factors such as adhesive and friction at the interface, the shrinkage of the resin, as well as the parameters of the materials are investigated. The principle maximum stress in the nanoimprints experienced throughout the whole history during the demolding was studied by the numerical simulations.

Simulation of the mold extraction process

As discussed in the description of the numerical model (see section 0), the simulation was separated into two steps. In the first step, the shrinkage of the resin caused by UV exposure was simulated. This shrinkage was increasing in process as the web/resin transited the wrap of the imprint roller during which the UV exposure kept increasing. The shrinkage was simulated by thermal contraction which can provide a uniform and homogeneous shrinkage typical during the polymerization of the UV resins. This method was widely applied by works done for thermal or UV NIL demolding simulation by Yeo[18], Chan-Park[11], Shibata[177], and Dirckx[19]. The UV curable resin was regarded as part which was assigned a pseudothermal expansion

coefficient. Master Bond specifies the maximum shrinkage of UV15 during curing to be 2%. The equivalent shrinkage of 2% was applied by providing a linear temperature decrease in the resin part. Although the polymerization of the resin is an exothermic process[31, 63], the actual heat produced by the reaction was negligible because the heat was dissipated fast through the thin layer of the mold to the steel imprint roller. Therefore, it was reasonable to assign the pseudothermal expansion coefficient to the resin to simulate the shrinkage phenomenon. A contraction strain contour plot was shown in Fig. V-5(a). Due to the bonded interface between the PET web and the resin, the contraction strain adjacent to the interface was small. However, the nanoimprints which were relatively far from the interface had little influence by the bonded interface. Global polymerization shrinkage of the UV curable resin with curing level was measured by a method developed by Hudson et al[178]. The shrinkage was measured in volume after curing. This volumetric shrinkage needed a cubic root to be converted to linear shrinkage strain for the simulation purposes[87]. The relationship between volumetric and linear shrinkage was as follows:

$$1-\varepsilon_l = \sqrt[3]{1-\varepsilon_v} \qquad \text{(V-5)}$$

where ε_l and ε_v are linear and volumetric shrinkage, respectively. In the 1st step of the simulation, the adhesive layer was not fractured. The strain in the first (e11) and second direction (e22) shown in Fig. V-5(b) was a description of the shrinkage due to polymerization.

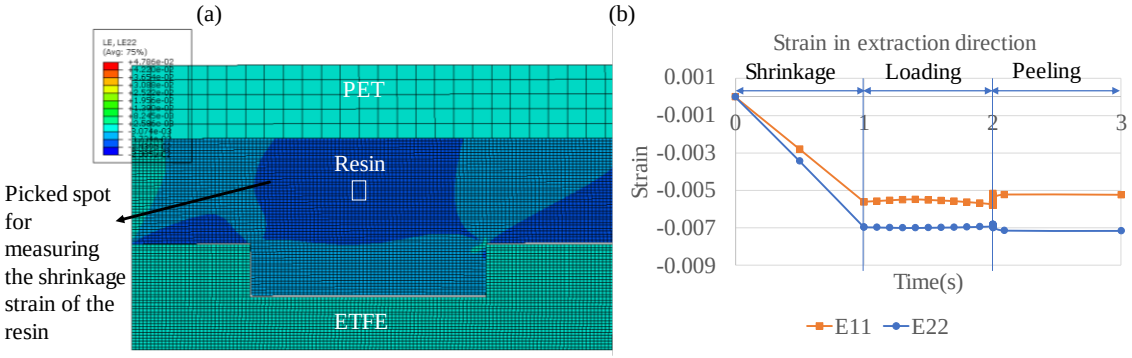

Fig. V-5(a) Shrinkage strain during the cross-linking process loading and demolding. The strain was caused by polymerization shrinkage of the resin in step 1. A spot that has little impact by the bonded PET web was chosen. (b) The shrinkage strain during the contraction stage.

The maximum principal stress experienced through the whole demolding process in the nanoimprints was calculated by the numerical model. Due to the low surface energy of fluorinated materials[7, 53, 179], the stresses at the interface reached the fracture criterion during the shrinkage stage. In Abaqus, there is a variable that tells the percentage of maximum traction damage initiation criterion, called “CSMAXSCRT”. Fig. V-6 (a) showed a contour plot of the ratio for stresses at the interface and the maximum nominal stress. Since the shrinkage contracted towards the PET web, the top wall first reached the fracture criterion. The far end of the nanoimprints reached a lower ratio of the fracture stress. At the end of the shrinkage stage, all the cohesive elements at the interface reached the initial fracture stress, as shown in Fig. V-6(b). The percentage of stress over the maximum nominal stress was plotted in Fig. V-6(c). Next, once the zero-thickness cohesive elements reached the fracture toughness criterion, the adhesive layer failed.

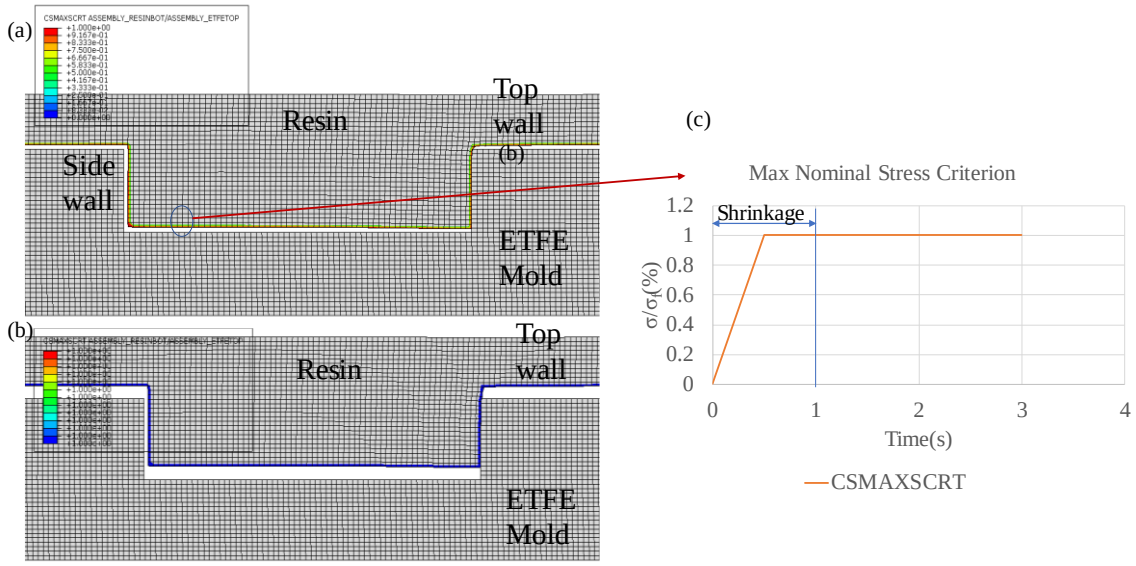

Fig. V-6 (a) contour plot of the ratio of stresses at the interface and the fracture stress criterion (the top wall reaches first reaches fracture stress criterion) (b) all the walls reached fracture criterion (c) the percent ratio of stresses and the fracture stress plotted by time sequence

The initiation of crack at the interface was started during the shrinkage stage. The degradation of the zero-thickness cohesive elements was monitored as a ratio of work potential over fracture energy, as shown in Fig. V-7(a). Once the ratio of fracture energy in the cohesive elements approached 100%, the elements would fail. The fracture ratio increased as the location moved downward, this was caused by the far end of the nanoimprints accumulated more contraction which increased the fracture energy in the cohesive elements at the bottom wall. During the shrinkage stage, the contraction of the UV resin cause separation between the resist and the mold. Thus, the fracture energy accumulated as the time lapse, as shown in Fig. V-7 (b). Next, applying the bending strain to the resin caused fracture energy to increase. Eventually, as the separation at the interfaces increased, the work potential reached the fracture energy criterion, then the cohesive elements failed. The nanoimprints were detached from the ETFE mold.

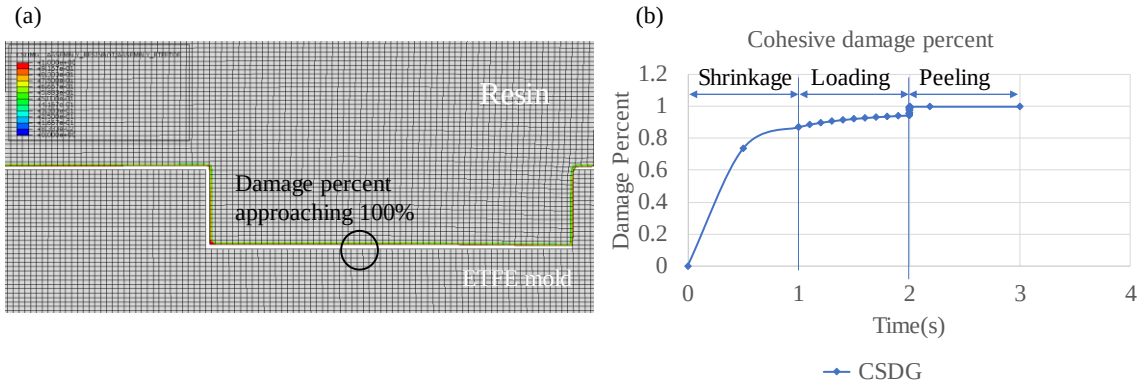

Fig. V-7 (a) scalar stiffness degradation for the cohesive surface at nodes (CSDMG) contour plot, the degradation percent was approaching 100% (b) degradation percent with time at the circle location in (a).

During the extraction process, the maximum principal stress in the nanoimprints was a high concern, which determined if the nanoimprints would be released without distortion or damage. Typical stress distribution contour plots during the extraction were shown in Fig. V-8(a) and (b). Stresses adjacent to the right sidewall of each nano-channel were relatively high due to the contraction of the polymer and bending stress. Fig. V-8(c) showed stress components experienced through the history of the whole demolding process. One should notice that the time axis in Fig. V-8(c) is not the actual time of the extraction process. The first two seconds are used to apply the boundary conditions for the numerical model. The extraction started at the time scale of 2.0s. During the shrinkage stage, the stresses increased linearly because the thermal contraction was applied uniformly. In the second stage, the stress in the second direction and the shear stress increased because of the contact between the resin and ETFE mold. Once extraction started, the cohesive elements were almost reached the fracture criterion, the stress caused by adhesive was reduced following the unloading path as shown in Fig. V-2. Due to the shrinkage and adhesive at the interface, as well as the stress concentration, the maximum principal stress was located at the spot shown in Fig. V-8(a). The value of the maximum principal stress was about 4.83MPa, which was mainly attributed to S22. Since the tensile strength of the resin is 5.73MPa, the nanoimprint can be released without any distortion or damage. One should notice that the stress reduced

steeply when the extraction started. This was because the process speed was high, which led to a high demolding speed. The extraction was happening 0.006s, thus, the Fig. V-8 (c) with the scale of time showed a steep reduction of stress.

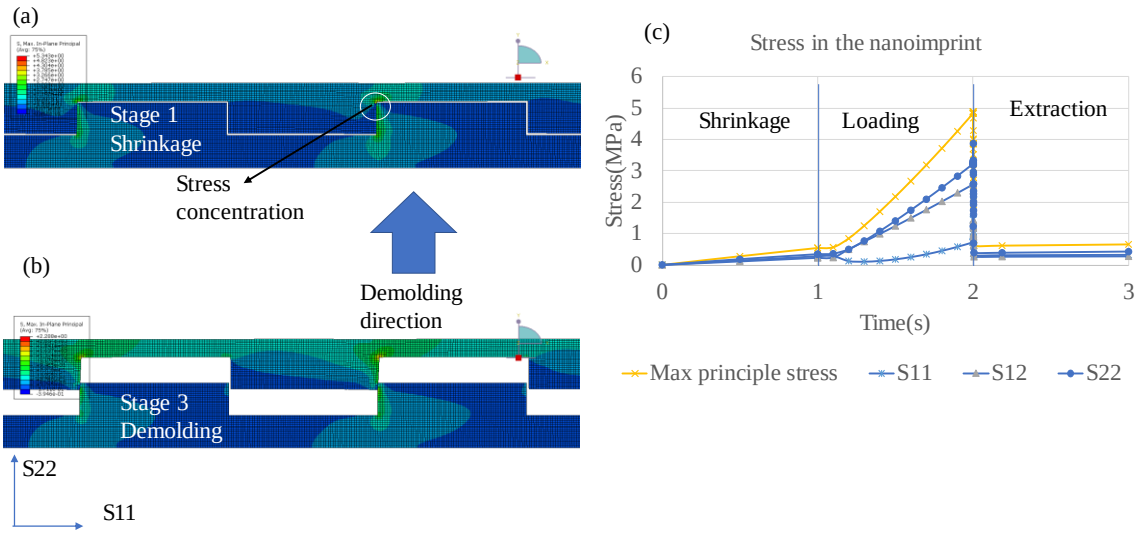

Fig. V-8 (a) Contour plot of maximum In-plane principal stress for the nanoimprints before extraction (b) Contour plot of maximum In-plane principal stress for the nanoimprints during extraction (c) Stress components and max principal stress experience through the history of the whole process for stress concentration spot at (a)

Extraction process under various process speed

As we have mentioned in chapter 2, the objective of this research is to develop simulation tools that can predict whether defect-free production can be produced. To achieve the objective of high-speed roll-to-roll manufacturing, the process speed is the most important parameter to be guaranteed. The process speed also affects many other parameters that have an impact on the roll-to-roll manufacturing process, such as, exposure time, curing level of the UV resin, material parameters as well as extraction speed. Therefore, in this section, the extraction process under various process speed will be explored. The prediction of whether defect-free production can be produced will be made.

Hundreds of thousands of line grating nanoimprints exist on the ETFE mold, to fulfill a simulation of the whole scale of the mold will cost a huge amount of computational resource. The

stress distribution showed replicability in the channels of the nanoimprints. A comparison between the simulations with 12 channels and 6 channels showed that the maximum principal stress convergence to a certain range of the values, as shown in Fig. V-9. To balance the computational cost and accuracy of the results, a representative simulation with 6 channels of the nanoimprints were conducted for various process speed.

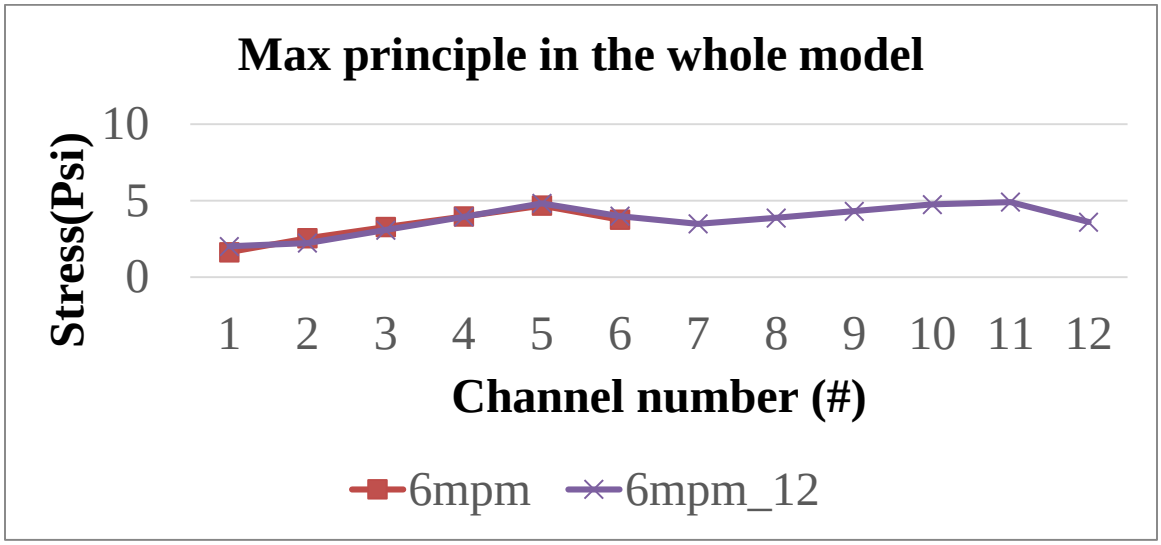

Fig. V-9 Comparison of simulations with 6 channels and 12 channels.

Under the process speed of 14mpm, the exposure time of UV light is approximately 2.08s. The material model is shown in Table V-2 Material property of UV resin under different process speed The results of the maximum principal stress throughout the whole history of the demolding process are shown in Fig. V-10. Since the maximum stress in the nanoimprints exceeds the tensile strength, the nanoimprints will be destroyed. The manufacturing process is based on a roll-to-roll continuous imprinting process. Thus, each of the nanoimprints will travel the failure channel, which means all nanoimprints will be destroyed or distorted.

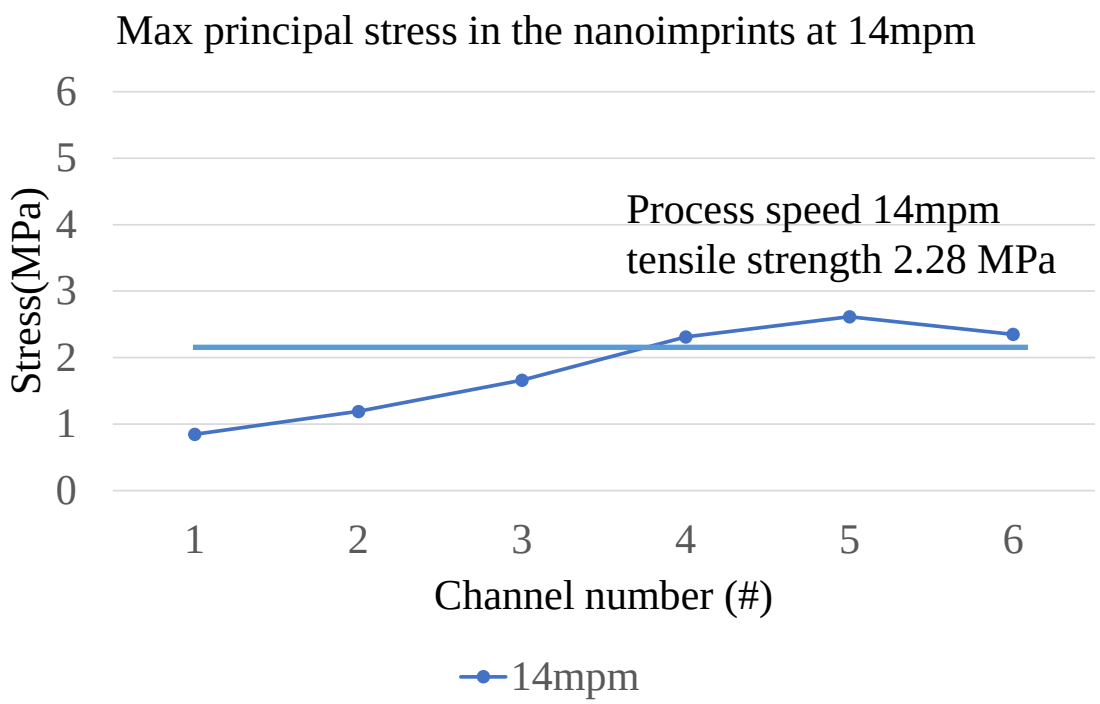

Fig. V-10 Maximum principal stress throughout the whole history of the demolding process under process speed of 14mpm

Under the process speed of 6mpm and 10mpm, the exposure time of UV light is approximately 4.8s and 2.88s respectively. The material model is shown in Table V-2 Material property of UV resin under different process speeds. The results of the maximum principal stress throughout the whole history of the demolding process under process speed of 6mpm and 10mpm are shown in Fig. V-11 and Fig. V-12, respectively. Under the process speed of 10mpm, the maximum stress in the nanoimprints exceeds the tensile strength, the nanoimprints will be destroyed. However, under the process speed of 6mpm, the maximum stress in the model throughout the whole history of the extraction process does not exceed the tensile stress. Therefore, the nanoimprints will be released from the ETFE mold successfully, so that defect-free production will be produced.

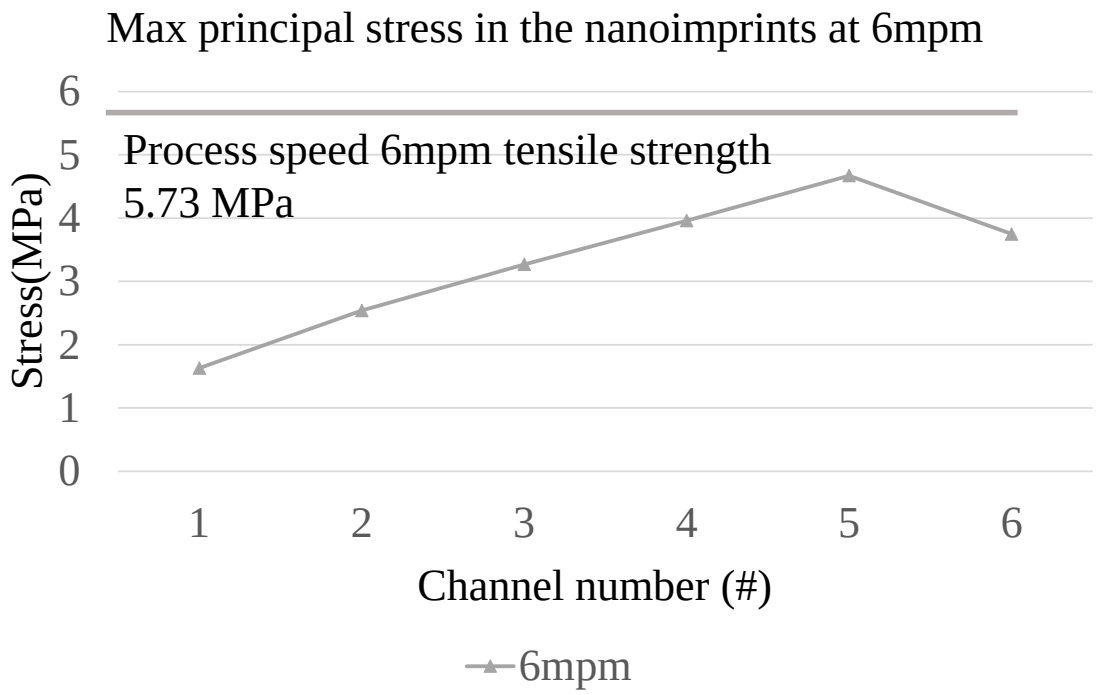

Fig. V-11 Maximum principal stress throughout the whole history of the demolding process under process speed of 6mpm

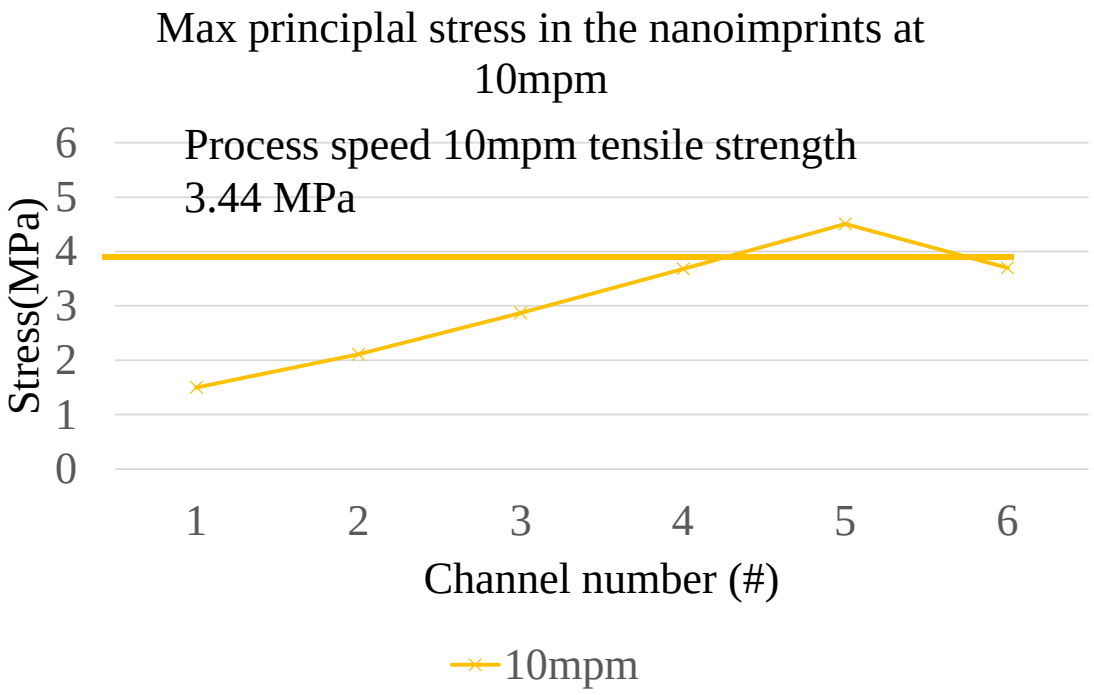

Fig. V-12 Maximum principal stress throughout the whole history of the demolding process under process speed of 10mpm

Effect of the aspect ratio of the nanoimprints

As indicated in the introduction, nanoimprints with a high aspect ratio (AR) are preferred not only in the microelectronics industry but also in many other fields[7, 53, 180, 181]. Investigating various aspect ratios of the grating nanoimprints is one of the purposes in this project. Therefore, the aspect ratio of one and five which are currently being manufacturing are investigated. Additionally, an even higher aspect ratio of 10 is also studied. Fig. V-13 (a) and (b) showed the stress distribution and the location of the maximum in-plane principal stress. The maximum principal stress in each numerical model experienced through the history of the whole demolding process was plotted in Fig. V-14. As the aspect ratio of the nanoimprints increased from 1 to 5, the maximum principal stress increased steeply. However, the increase of the max principal stress was relatively small from AR 5 to AR 10. The final maximum in-plane stress was the stress in the nanoimprints when cohesive elements fractured, as shown in Fig. V-7. The final stress showed the same trend as the maximum principal stress. Fig. V-14(b) showed the percentage of maximum principal stress over ultimate tensile strength. The maximum principal stress levels indicate the nanoimprints were not close to failure. Therefore, the nanoimprints of high aspect ratio can be released from the mold without any distortion or damage under the current curing level given the cured resin strength and shrinkage of UV15.

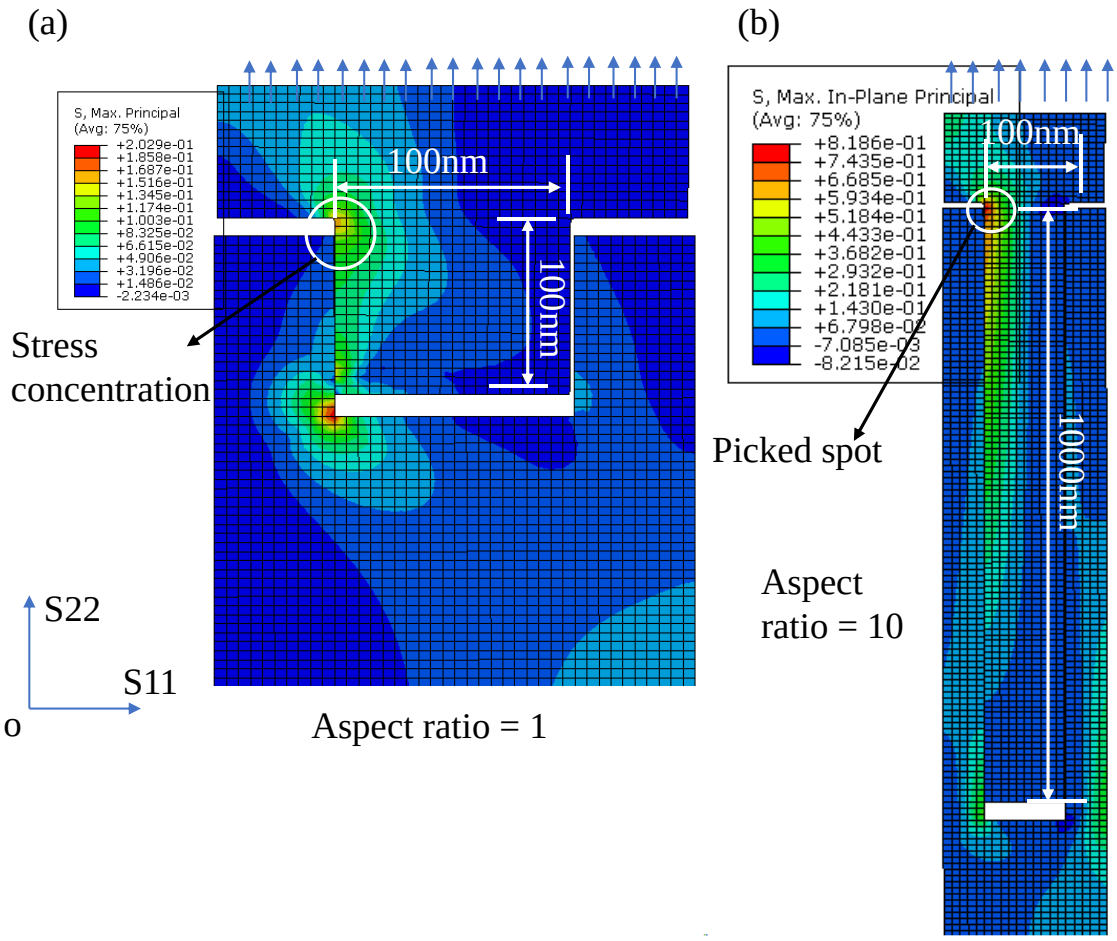

Fig. V-13 (a) Contour plot of Maximum in-plane principal stress for nanoimprints for AR=1. (b) Contour plot of Maximum in-plane principal stress for nanoimprints for AR=10

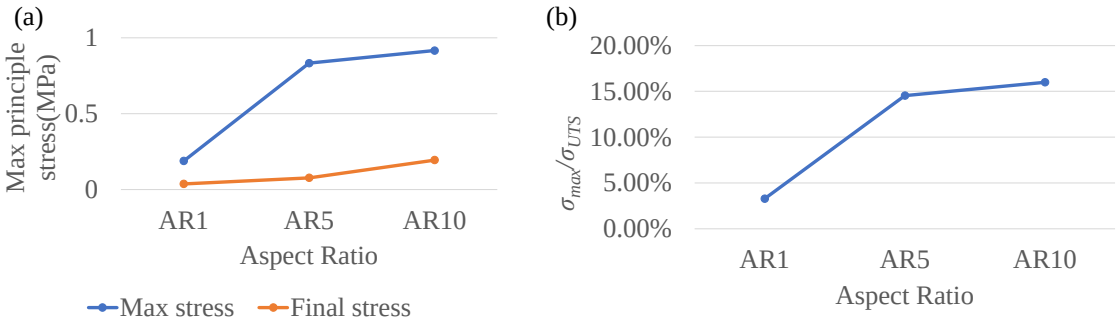

Fig. V-14(a) Maximum in-plane principal stress for nanoimprints experienced through the whole demolding process (b) Maximum principal stress in the nanoimprints over ultimate tensile stress of the UV 15 at the curing level of 2.6W/cm2 for 5s

5.6 Summary

A method of exploring imprint extraction from imprint roller molds was developed. The method employs the finite element method simulation. The maximum stresses occurred in the root areas of the nanoimprints in contact with the ETFE mold. The internal stresses in the imprints are affected by resin shrinkage as well as friction and adhesion at the interfaces during extraction. The process speed of the continuous roll-to-roll manufacturing can influence the potential for imprint damage during extraction. Once the process speed reached a certain level, the internal stress in the nanoimprints would exceed the tensile strength, which led to failure. The simulation method will assist in scaling of UV-NIL R2R manufacturing to commercial production velocities that can be limited by the resin cure level at the peel roller where imprint extraction is occurring. The numerical simulation model can be an effective tool to predict whether defect-free production can be produced. This tool can also provide guidance to optimize the operating parameters in the manufacturing and structure of the equipment for roll-to-roll manufacturing.

CHAPTER VI

VI. Laboratory experimental validation

6.1 Introduction

In the research that has been conducted it has become apparent how UV resin selection affects machine development and ultimately the ability to conduct the process successfully at speeds that will support commercial viability. In chapter 3, we have demonstrated how the properties of the UV cured resin are not attained instantaneously on exposure to UV light[173]. Modulus and tensile strength increase initially with exposure where cross-linking of the polymer resins initiate but also increase with dark curing time where the cross-linking between polymer chains continue after exposure. Commercial UV-NIL processes that are economically successful require speed and productivity which are attributes of roll-to-roll (R2R) manufacturing processes. To achieve success requires the strength of the curing UV resin to be sufficient that (1) the nanoimprints can be extracted from the mold on the imprint roller without damage and (2) the imprinted resin adhered to a carrier web must be able to withstand the bending stresses that result from peeling from the imprint roller without failure. Extraction failures are nano failures wherein imprinted nanofeatures cannot be extracted from the mold without local failure of the features. These types of failures have been documented to increase with the aspect ratio of the imprinted nanofeatures[182]. Extraction failures will be the focus of this section. As we have discussed in

Chapter 5, a numerical simulation is established to predict if the defect-free production can be produced. In this section, the focus will be on failures related to peeling that can affect the commercial productivity of a UV-NIL R2R manufacturing process. The experimental results will be a validation for the extraction simulation. The development of a UV-NIL demonstration surface using R2R manufacturing processes will also be shown.

The experimental effort and results presented were produced as a result of a combined effort by Good[183] and Lucca research teams at Oklahoma State University and Guo research team at the University of Michigan[184].

6.2 Experimental setup

The experimental setup used in this project was developed at Oklahoma State University, as shown in Fig. VI-1 and Fig. IV-13. Our earlier research had employed a reverse gravure coater to apply UV resin to a polyester prior to entry of the nip between the backup and imprint rollers. We found that we could better control imprint quality by nip coating where we would introduce a reservoir of UV resin at the convergence of the web on the backup roller with the imprint roller. To maintain a reservoir of resin with increased process speed required us to meter additional resin at the convergence. We employed this coating method in this research.

The purpose of a peel roller is to control the point of separation between the imprinted resin/web and the imprint roller. Without a peel roller control of web tension is very difficult. Consider an adhesive tape dispenser whereby hand we extract a needed amount of tape. A jerking motion while extracting the tape is common and is associated with the point of separation oscillating at the tangent exit of the tape web from the roll. This jerking motion will not allow a steady extraction of the imprinted web from the mold on the imprint roller resulting in imprint defects. Thus, a peel roller is a necessary entity but it does introduce other complexities to the strains the curing resin is subjected to. The UV resin used in this research was UV15, a cationic resin

developed by Master Bond[2]. The imprint mold was a St. Gobain[3] ETFE (ethylene tetrafluoroethylene) polymer film that had been thermally imprinted with a wire grid pattern by the Guo team at the University of Michigan. The ETFE has low surface energy and the mold was bounded by 3M[4] 5461 tape which is also low surface energy to enhance the release of the cured imprinted resin from the mold. Here the goal is for the UV15 resin to adhere to the polyester web and not to the mold or the imprint roller. As the uncured resin is applied to the web there is no internal strain. The web coated with resin conforms to the imprint roller and the resin is exposed to UV light and curing begins. As the imprinted web approaches the exit of the imprint roller we will first consider the case where no peel roller is present. As the web leaves the imprint roller and moves into the exit span, tensile bending strains of approximate magnitude $h/(2R_{IR})$ will occur in the resin. Here *h* is the thickness of the web and is assumed very largely compared to the resin coating thickness and R_{IR} is the radius of the imprint roller. If a peel roller is employed the bending strain will increase to a higher level of $h/(2R_{IR})$ plus $h/(2R_{PR})$ where R_{PR} is the radius of the peel roller. The bending stress in the resin will be whatever the modulus of the resin is at the stage of curing at the exit (E) times the total bending strain. If that bending stress exceeds the ultimate tensile stress of the resin, also dependent on the stage of curing at the exit, cracks will result in defects in the imprinted resin.

[2] Master Bond Inc., 154 Hobart St, Hackensack, NJ 07601, USA
[3] St. Gobain Specialty Films, 717 Plantation Street, Worcester, MA 01605, USA
[4] 3M Company, 2501 Hudson Rd, Maplewood, MN 55144, USA

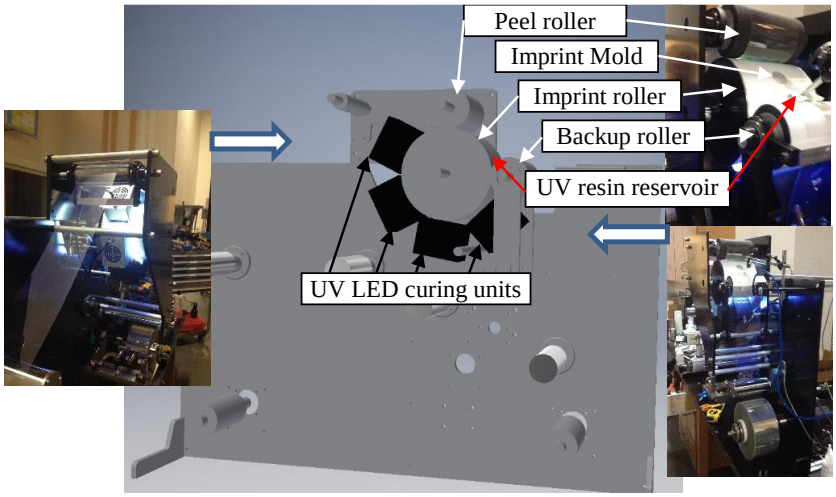

Fig. VI-1 OSU UV-NIL R2R process machine

6.3 Experimental results

The test results in Fig. VI-2 demonstrate that imprint quality and bending failure cracks are dependent on the R2R process speed, which is in line with our numerical simulation. In Fig. VI-2 note that diffraction patterns are witnessed over the width of the replicate areas at 4.5 and 6 mpm process speeds. The diffraction patterns are a quick visual means of determining whether the imprint mold has successfully been replicated. Note at process speeds of 10-20 mpm that (1) diffraction patterns have diminished and (2) that bending failure cracks have appeared. Both artifacts are indications that the resin was insufficiently cured when the web/resin was peeled from the imprint roller. This demonstrates how the mechanical properties of the resin at the time of peel are important in determining the quality of imprint at the nano-scale in terms of diffraction and at the macro-scale in terms of visible crack flaws.

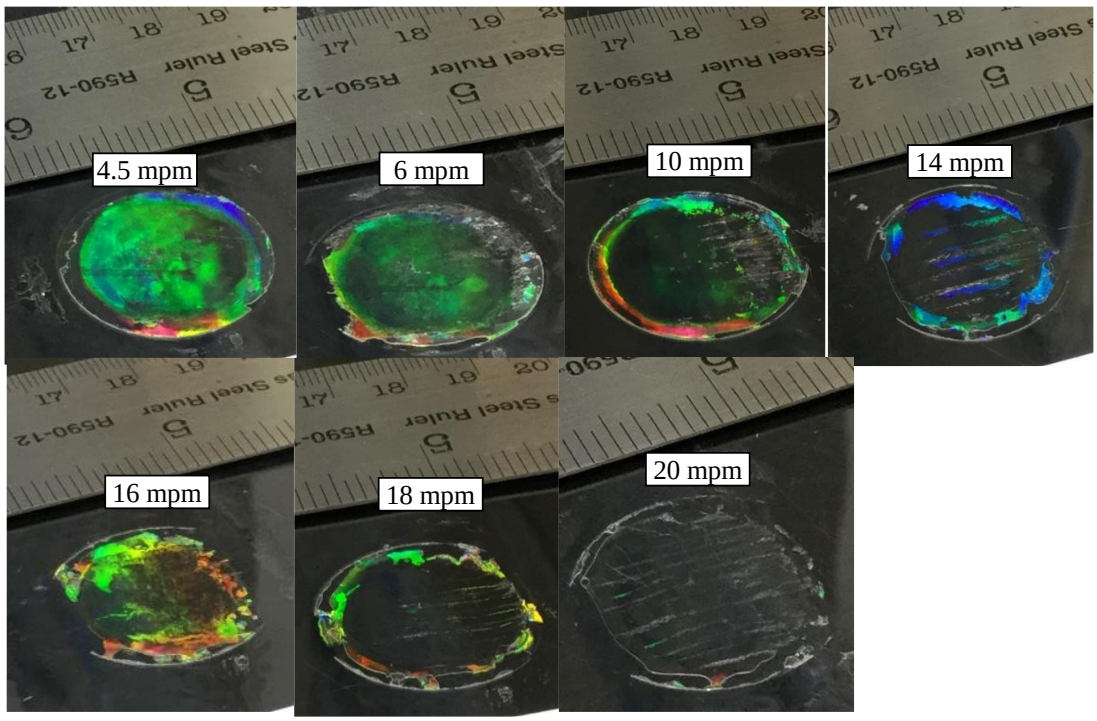

Fig. VI-2 Test results as a function of process speed

Imprints from the 3 mpm trial and the used imprint mold were provided to the Dr.Lucca team at OSU. Five imprints were provided and were labeled with numbers from 6 to 10. Imprints 6 through 9 were measured with atomic force microscopy (AFM) since the 10th was not complete. For each imprint 2 or 3 AFM scans were performed using a scan size of 10 µm by 5 µm. Cross-sections of the AFM scans were used to measure the period and depth of the imprinted gratings. The ETFE mold used to create the imprints was also measured with AFM.

Horizontal 1-D power spectral density (PSD) analysis performed with the AFM software showed all the gratings had a 1.25 µm period. Measurements of the period from individual sections averaged around 1.26 µm. The periodicity was consistent across the measured areas and the measured values are summarized in. The depth measured along the cross-sections tended to vary, but the maximum depth ranged from 120 nm to 180 nm. The mold and imprints displayed similar characterization as expected. The characterization was consistent with the silicon wafer mold that

produced the mold and ultimately the imprints. The maximum depth of the mold and imprints was somewhat less than the 240 nm depth of the silicon wafer grating, an indication that the thermal imprinting did not fully replicate the wafer in the ETFE film.

Table VI-1 Summary of measured period and maximum depth of imprints processed at 3mpm

		Period (μm)	Maximum Depth (nm)
Mold	Area 1	1.25	175
	Area 2	1.25	180
Imprint 6	Area 1	1.28	180
	Area 2	1.27	185
	Area 3	1.26	180
Imprint 7	Area 1	1.27	150
	Area 2	1.26	145
Imprint 8	Area 1	1.26	120
	Area 2	1.26	175
Imprint 9	Area 1	1.25	165
	Area 2	1.26	155

The mold could not be scanned with AFM near the center since it was not possible to obtain a stable contact between the mold and the stage, but it was possible to scan close to the edge. Two scans of 10 μm by 5 μm were measured, using the same settings used for the imprints, with exception of the speed which was halved. Horizontal 1-D PSD analysis and individual cross-sections indicated a period of 1.25 μm. The maximum depth of the mold was consistent with the maximum depth of 180 nm found on the gratings. The depth varied across the scanned areas of the mold. Fig. VI-3 displays the data acquired on Imprint 6 and is demonstrative of the data acquired for Imprints 7-9 and the mold.

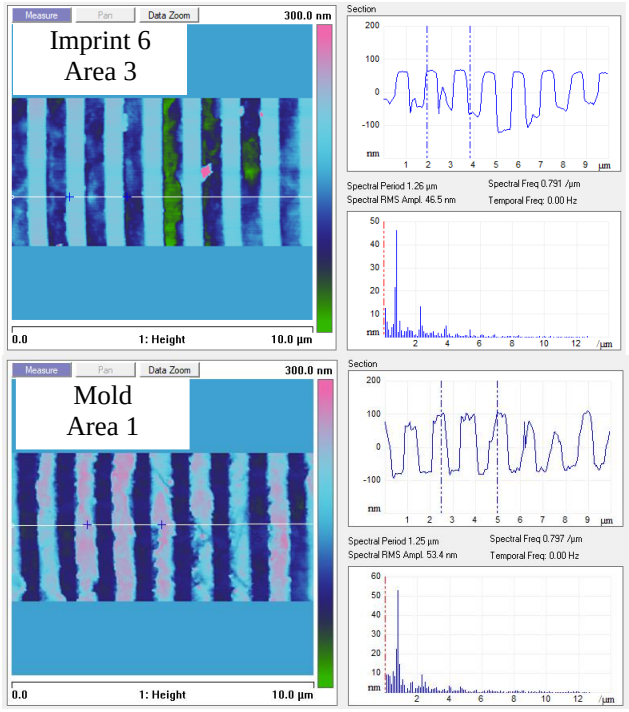

Fig. VI-3 Example Characterization of the Mold and an Imprint

6.4 Validation of extraction simulation

The geometry of nano-scale extraction simulation is based on the period and depth of the ETFE mold and nanoimprints, as shown in Fig. VI-3. As we discussed in section 0, the internal stress of the nanoimprints as a function of process speed is demonstrated. The maximum principal stress throughout the whole history of demolding cannot exceed the tensile strength of the UV 15 at the curing level under the process speed of 6mpm. Fig. VI-4 shows the comparison between the numerical simulation and the experiment on the process line. Since each nanofeatures will travel through the channel where the nanofeature will be failed, all the nanofeatures are potentially distorted and destroyed.

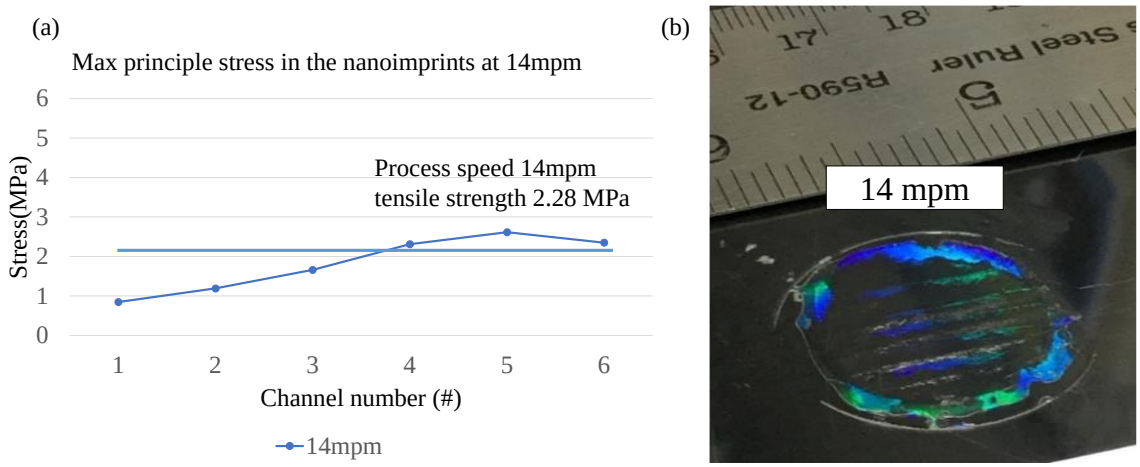

Fig. VI-4 Result of extraction simulation and the experiments in the process line at process speed of 14mpm

Fig. VI-5 and Fig. VI-6 demonstrate the comparison of maximum principal stress in the nanoimprints predicted by the extraction simulation under the process speed of 10mpm and 6mpm, respectively. Under the process speed of 10mpm, the simulation predicts the failure of nanoimprints, which is in line with the results of the experiment. As shown in Fig. VI-6, the simulation predicts that the nanoimprints can be extracted without defects. The pattern of the experiment result also shows good visual diffraction.

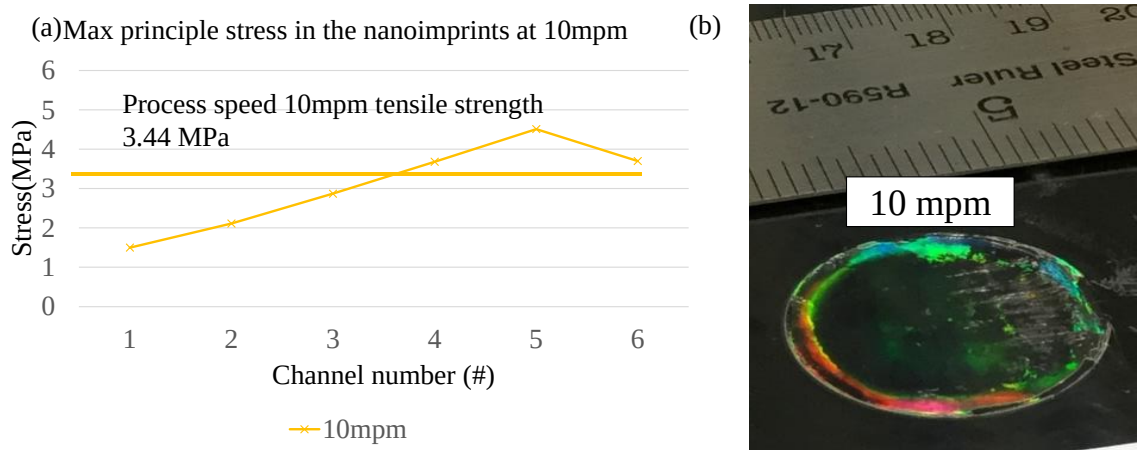

Fig. VI-5 Result of extraction simulation and the experiments in the process line at process speed of 10mpm

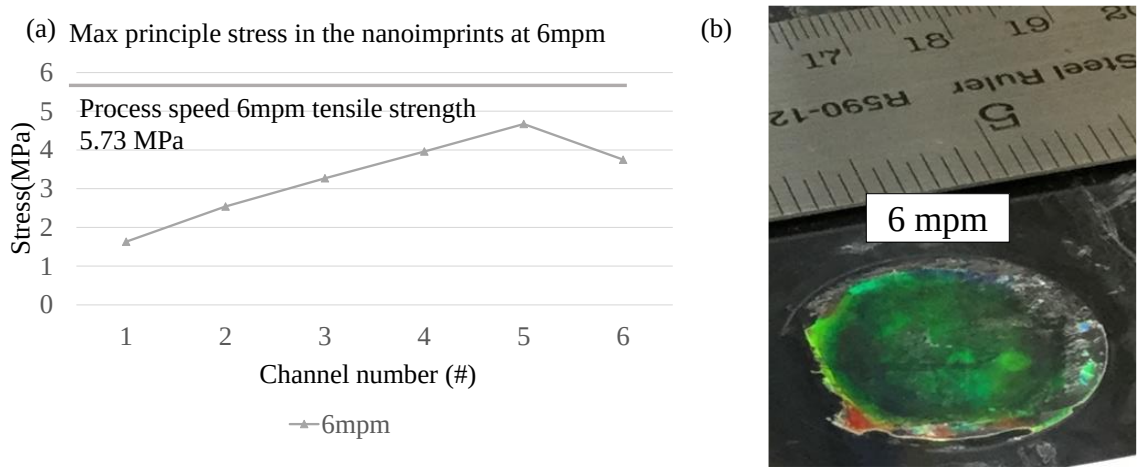

Fig. VI-6 Result of extraction simulation and the experiments in the process line at process speed of 6mpm

6.5 Summary

Laboratory trials have shown that the diffraction of the nanoimprints is a simple way to check if nanoimprints are produced. Based on the results of the experimental validation, the prediction of the numerical simulation tool developed in chapter 4 and chapter 5 demonstrates a good agreement with the results of trials in the laboratory.

CHAPTER VII

VII. Conclusion, Findings and Future work

7.1 Conclusions

Roll-to-roll UV NIL is a highly complex process. The imprinting part involving nip contact and resin curing is simulated by the macro-scale model. Successful extraction of nanoimprints from molds is also an important facet of R2R UV NIL processes. A nano-scale simulation tool that can predict whether extraction will be successful or not is also developed. Based on the results of the experiments and numerical simulations, several conclusions can be drawn as follows:

- The macro-scale simulation provides a method to investigate the slippage between the resin and the imprint roller. The slippage could be eliminated by adjusting the operation parameters. The predominant parameter in controlling slippage is the imprinted web exit tension.
- A method of exploring imprint extraction from imprint roller molds under various process speeds, which can predict extraction defects, was developed. Higher aspect-ratio nanoimprints have more difficulties to be extracted from the mold.
- Experimental means were developed to determine the material mechanical properties, such as, Young's modulus, adhesive properties, friction properties, as well as the ultimate shear strength, as affected by process speed, that were necessary input for the

simulations.

- The diffraction of the nanoimprints is a method to check the defects rapidly. The experimental nano-imprint trial results are consistent with the prediction of the simulation tools under the process speeds of 6mpm, 10mpm, and 14mpm.
- By combining these two numerical models at different scales, the simulation tool can fully predict the success of producing defect-free nanoimprints. This simulation tool provides a guide for manufacturers to reach optimal operation parameters.

This will enable those who design imprinted surfaces based on geometric requirements to predict whether that surface can be commercially produced. This will also enable UV-NIL manufacturing to move from a trial-and-error approach to a predictive mode, where extraction success can be known prior to moving to the manufacturing environment.

7.2 Future work

To get high-quality nanofeatures on the web, there are unknown areas of the process to be further explored.

- In the semiconductor industry, the high aspect ratio nanoimprints with various shapes are preferred to build smaller transistors. Simulations of typical aspect ratio line grating nanoimprints were explored. However, for the practical semiconductor industry, higher aspect ratios with other typical shapes of the nanoimprint need to be explored.
- The assumption that the UV resin behaves elastically under the current manufacturing process prevents the simulation of a wider range of process speeds. If the process speed decreases, the UV resin may behave differently. To conquer this limitation, the material behavior of the UV resin should be further explored. Based on the current knowledge of this resin, time-resolved mechanical spectroscopy (TRMS) measurements on the rheometer during curing can fully characterize the material properties of the UV resin, although at relatively long times compared to the industrial process. In addition, further measurements of the dynamic moduli for a broader range of frequency

at the same UV intensity need to be conducted to develop a relevant viscoelastic model.

- The adhesive property at the interface between the resin and the imprint roller was represented by a friction law using a penalty method. The resin stuck to the ETFE mold after a certain amount of UV irradiation. Characterizing the contact property combining friction with adhesive properties should improve the accuracy of the simulation. The author met convergence difficulties when attempting to develop such simulations. This model coupling the friction and adhesive properties in a dynamic simulation needs to be explored.

REFERENCES

1. Perret, C., C. Gourgon, F. Lazzarino, J. Tallal, and S. Landis, *Characterization of 8-in. wafers printed by nanoimprint lithography.* Microelectronic Engineering, 2004. **73**: p. 172-177.
2. Han, C., Z. Yu, W. Jian, J.O. Tegenfeldt, R.H. Austin, E. Chen, and S.Y. Chou, *Fabrication of 10 nm enclosed nanofluidic channels.* Applied Physics Letters, 2002. **81**(1): p. 174-176.
3. Pisignano, D., L. Persano, M.F. Raganato, P. Visconti, R. Cingolani, G. Barbarella, L. Favaretto, and G. Gigli, *Room-Temperature Nanoimprint Lithography of Non-thermoplastic Organic Films.* Advanced Materials, 2010. **16**(6): p. 525-529.
4. Shibata, M., A. Horiba, Y. Nagaoka, H. Kawata, M. Yasuda, and Y. Hirai, *Process-simulation system for UV-nanoimprint lithography.* Journal of vacuum science & technology. B, Microelectronics and nanometer structures: processing, measurement, and phenomena: an official journal of the American Vacuum Society, 2010. **28**(6): p. C6M108-C6M113.
5. Chou, S.Y., P.R. Krauss, and P.J. Renstrom, *Imprint of sub-25 nm vias and trenches in polymers.* Applied physics letters, 1995. **67**(21): p. 3114-3116.
6. Kooy, N., K. Mohamed, L.T. Pin, and O.S. Guan, *A review of roll-to-roll nanoimprint lithography.* Nanoscale Research Letters, 2014. **9**(1): p. 320-320.
7. Ahn, S.H. and L.J. Guo, *High log peed Roll-to ln oll Nanoimprint Lithography on Flexible Plastic Substrates.* Advanced Materials, 2010. **20**(11): p. 2044-2049.
8. Blevins, R.D., *Applied fluid dynamics handbook.* New York, Van Nostrand Reinhold Co., 1984, 568 p., 1984.
9. Pfiffer, J., *Internal pressures in a wound roll of paper.* Tappi Journal, 1966. **49**: p. 342-347.
10. Golaz, B., V. Michaud, Y. Leterrier, and J.A.E. Månson, *UV intensity, temperature and dark-curing effects in cationic photo-polymerization of a cycloaliphatic epoxy resin.* Polymer, 2012. **53**(10): p. 2038-2048.
11. Chan-Park, M.B., Y. Lam, P. Laulia, and S. Joshi, *Simulation and investigation of factors affecting high aspect ratio UV embossing.* Langmuir, 2005. **21**(5): p. 2000-2007.
12. CO.LTD., M., *UV 15 Product Information.* From "https://www.masterbond.com/tds/uv15", 2019. **Acessed at 01/15/2019**.
13. Lorenz, H., M. Despont, N. Fahrni, N. LaBianca, P. Renaud, and P. Vettiger, *SU-8: a low-cost negative resist for MEMS.* Journal of Micromechanics and Microengineering, 1997. **7**(3): p. 121.
14. Cheng, X., L.J. Guo, and P.F. Fu, *Room-temperature, low-pressure nanoimprinting based on cationic photopolymerization of novel epoxysilicone monomers.* Advanced Materials, 2005. **17**(11): p. 1419-1424.
15. Yeo, L., Y. Lam, M.B. Chan-Park, S. Joshi, and D. Hardt, *Demolding of high aspect ratio polymeric micro-patterning.* International Journal of Nanoscience, 2005. **4**(04): p. 543-549.
16. Worgull, M., M.P. Heckele, J.F. Hétu, and K. Kabanemi, *Modeling and optimization of the hot embossing process for micro-and nanocomponent fabrication.* Journal of Micro/Nanolithography, MEMS, and MOEMS, 2006. **5**(1): p. 011005.
17. Park, S., Z. Song, L. Brumfield, A. Amirsadeghi, and J. Lee, *Demolding temperature in thermal nanoimprint lithography.* Applied Physics A, 2009. **97**(2): p. 395-402

18. Yeo, L.P., S.C. Joshi, Y.C. Lam, M.B. Chan-Park, and D.E. Hardt, *Numerical analyses of peel demolding for UV embossing of high aspect ratio micro-patterning.* Microsystem Technologies, 2009. **15**(4): p. 581-593.
19. Dirckx, M.E. and D.E. Hardt, *Analysis and characterization of demolding of hot embossed polymer microstructures.* Journal of Micromechanics and Microengineering, 2011. **21**(8): p. 085024.
20. Sipani, V., A.B.J.J.o.P. Scranton, and P.A. Chemistry, *Kinetic studies of cationic photopolymerizations of phenyl glycidyl ether: termination/trapping rate constants for iodonium photoinitiators.* 2003. **159**(2): p. 189-195.
21. Higham, A.K., C.A. Bonino, S.R. Raghavan, and S.A.J.S.M. Khan, *Photo-activated ionic gelation of alginate hydrogel: real-time rheological monitoring of the two-step crosslinking mechanism.* 2014. **10**(27): p. 4990-5002.
22. Guo, L.J., X. Cheng, and C.F. Chou, *Fabrication of Size-Controllable Nanofluidic Channels by Nanoimprinting and Its Application for DNA Stretching.* Nano Letters, 2003. **4**(1): p. 69-73.
23. Chou, S.Y., P.R. Krauss, W. Zhang, L. Guo, and L. Zhuang, *Sub-10 nm imprint lithography and applications.* Journal of Vacuum Science & Technology B: Microelectronics and Nanometer Structures Processing, Measurement, and Phenomena, 1997. **15**(6): p. 2897-2904.
24. Guo, L.J. *New development of nanoimprint technology*. in *International Microprocesses & Nanotechnology Conference*. 2004.
25. Chou, S.Y., P.R. Krauss, and P.J. Renstrom, *Imprint Lithography with 25Nanometer Resolution.* Science, 1996. **272**(5258): p. 85-87.
26. Guo, L.J., *Nanoimprint lithography: methods and material requirements.* Advanced materials, 2007. **19**(4): p. 495-513.
27. Haisma, J., M. Verheijen, K.V.D. Heuvel, and J.V.D. Berg, *Mold-assisted nanolithography: A process for reliable pattern replication.* Journal of Vacuum Science & Technology B Microelectronics & Nanometer Structures Processing Measurement & Phenomena, 1996. **14**(6): p. 4124-4128.
28. Colburn, M., S.C. Johnson, M.D. Stewart, S. Damle, T.C. Bailey, B. Choi, M. Wedlake, T.B. Michaelson, S.V. Sreenivasan, and J.G. Ekerdt, *Step and flash imprint lithography: A new approach to high-resolution patterning.* Proc Spie, 1999. **3676**(3676): p. 379-389.
29. Ruchhoeft, P., M. Colburn, B. Choi, and H. Nounu, *Patterning curved surfaces: Template generation by ion beam proximity lithography and relief transfer by step and flash imprint lithography.* Journal of Vacuum Science & Technology B Microelectronics & Nanometer Structures Processing Measurement & Phenomena, 1999. **17**(6): p. 2965-2969.
30. Stewart, M.D., S.C. Johnson, S.V. Sreenivasan, D.J. Resnick, and C.G. Willson, *Nanofabrication with step and flash imprint lithography*. 2005.
31. Kim, E.K. and C.G. Willson, *Thermal analysis for step and flash imprint lithography during UV curing process.* Microelectronic engineering, 2006. **83**(2): p. 213-217.
32. Schift, H., *Nanoimprint lithography: An old story in modern times? A review.* Journal of Vacuum Science & Technology B Microelectronics & Nanometer Structures Processing Measurement & Phenomena, 2008. **26**(2): p. 458.
33. Plachetka, U., M. Bender, and A. Fuchs, *Wafer scale patterning by soft UV-Nanoimprint Lithography.* Microelectronic Engineering, 2004. **73**(1): p. 167-171.
34. Vogler, M., S. Wiedenberg, M. Mühlberger, I. Bergmair, T. Glinsner, H. Schmidt, E.B. Kley, and G. Grützner, *Development of a novel, low-viscosity UV-curable polymer system for UV-nanoimprint lithography.* Microelectronic Engineering, 2007. **84**(5): p. 984-988.
35. Lee, J.J., S.Y. Park, K.B. Choi, and G.H. Kim, *Nano-scale patterning using the roll typed UV-nanoimprint lithography tool.* Microelectronic Engineering, 2008. **85**(5-6): p. 861-865.
36. Alkaisi, M.M. and K. Mohamed, *Three-dimensional patterning using ultraviolet nanoimprint lithography*, in *Lithography*. 2010, InTech.
37. Guo, L.J., *Recent progress in nanoimprint technology and its applications.* Journal of Physics D Applied Physics, 2004. **37**(11): p. 123-141.
38. Cheng, X., L.J. Guo, and P.F. Fu, *Room-Temperature, Low-Pressure Nanoimprinting Based on Cationic Photopolymerization of Novel Epoxysilicone Monomers.* Advanced Materials, 2010. **17**(11): p. 1419-1424.
39. Yi, P., W. Hao, C. Zhang, L. Peng, and X. Lai, *Roll-to-roll UV imprinting lithography for*

micro/nanostructures. Journal of Vacuum Science & Technology B, 2015. **33**(6).
40. Resnick, D.J., W.J. Dauksher, D. Mancini, K.J. Nordquist, T.C. Bailey, S. Johnson, N. Stacey, J.G. Ekerdt, C.G. Willson, and S.V. Sreenivasan, *Imprint lithography for integrated circuit fabrication.* Journal of Vacuum Science & Technology B Microelectronics & Nanometer Structures, 2003. **21**(21): p. 2624 - 2631.
41. Perret, C., C. Gourgon, F. Lazzarino, J. Tallal, S. Landis, and R. Pelzer, *Characterization of 8-in. wafers printed by nanoimprint lithography.* Microelectronic Engineering, 2004. **73**(1): p. 172-177.
42. Hiroshima, H. and M. Komuro, *Control of Bubble Defects in UV Nanoimprint.* Japanese Journal of Applied Physics, 2007. **46**(9B): p. 6391-6394.
43. Hiroshima, H. and M. Komuro, *UV-nanoimprint with the assistance of gas condensation at atmospheric environmental pressure.* Journal of Vacuum Science & Technology B Microelectronics & Nanometer Structures, 2007. **25**(25): p. 2333-2336.
44. Hiroshima, H. *Quick Cavity Filling in UV Nanoimprint Using Pentafluoropropane*. in *Microprocesses & Nanotechnology, Digest of Papers*. 2008.
45. Morihara, D., H. Hiroshima, and Y. Hirai, *Numerical study on bubble trapping in UV-nanoimprint lithography.* Microelectronic Engineering, 2009. **86**(4): p. 684-687.
46. Matsui, S., H. Hiroshima, Y. Hirai, and M. Nakagawa, *Breakthrough achievement in nanoimprint lithography using PFP condensable gas.* Journal of Photopolymer Science and Technology, 2014. **27**(1): p. 61-72.
47. Hao, W., P. Yi, L. Peng, and X. Lai, *Study on bubble defects in roll-to-roll UV imprinting process for micropyramid arrays. I. Experiments.* Journal of Vacuum Science & Technology B, 2016. **34**(2): p. 021201.
48. Peng, L., H. Wu, P. Yi, and X. Lai, *Study on bubble defects in roll-to-roll UV imprinting process for micropyramid arrays II: Numerical study.* Journal of Vacuum Science & Technology B, 2016. **34**(5).
49. Tan, H., A. Gilbertson, and S.Y. Chou, *Roller nanoimprint lithography.* Journal of Vacuum Science & Technology B, 1998. **16**(6): p. 3926-3928.
50. Ahn, S., J. Cha, H. Myung, S.M. Kim, and S. Kang, *Continuous ultraviolet roll nanoimprinting process for replicating large-scale nano- and micropatterns.* Applied Physics Letters, 2006. **89**(21): p. 443.
51. Lan, S., H. Lee, J. Ni, S. Lee, and M. Lee. *Survey on roller-type nanoimprint lithography (RNIL) process*. in *Smart Manufacturing Application, 2008. ICSMA 2008. International Conference on*. 2008. IEEE.
52. Dumond, J.J. and Y.L. Hong, *Recent developments and design challenges in continuous roller micro- and nanoimprinting.* Journal of Vacuum Science & Technology B Microelectronics & Nanometer Structures, 2012. **30**(1): p. 0801.
53. Se Hyun, A. and G. L Jay, *Large-area roll-to-roll and roll-to-plate nanoimprint lithography: a step toward high-throughput application of continuous nanoimprinting.* Acs Nano, 2009. **3**(8): p. 2304-2310.
54. Ok, J.G., S.H. Ahn, M.K. Kwak, and L.J. Guo, *Continuous and high-throughput nanopatterning methodologies based on mechanical deformation.* Journal of Materials Chemistry C, 2013. **1**(46): p. 7681-7691.
55. Maury, P., D. Turkenburg, N. Stroeks, P. Giesen, I. Barbu, E. Meinders, A.V. Bremen, N. Iosad, R.V.D. Werf, and H. Onvlee, *Roll-to-roll UV imprint lithography for flexible electronics.* Microelectronic Engineering, 2011. **88**(8): p. 2052-2055.
56. Yoshikawa, H., J. Taniguchi, G. Tazaki, and T. Zento, *Fabrication of high-aspect-ratio pattern via high throughput roll-to-roll ultraviolet nanoimprint lithography.* Microelectronic Engineering, 2013. **112**(12): p. 273-277.
57. Ren, Y. and J.K. Good. *The Nip Mechanics of Nano-Impression Lithography in Roll-to-Roll Process Machines*. in *Proceedings of the Fourteenth International Conference on Web Handling*. 2017.
58. Iyoshi, S., H. Miyake, K.-i. Nakamatsu, and S. Matsui, *UV-curable resins appropriate for UV nanoimprint.* Journal of Photopolymer Science and Technology, 2008. **21**(4): p. 573-581.
59. Sakai, N., *Photo-curable resin for UV-nanoimprint technology.* Journal of Photopolymer Science and Technology, 2009. **22**(2): p. 133-145.
60. Lu, J.H. and J.P. Youngblood, *Adhesive bonding of carbon fiber reinforced composite using UV-curing epoxy resin.* Composites Part B Engineering, 2015. **82**: p. 221-225.

61. Schmidt, L.E., Y. Leterrier, D. Schmäh, J.A.E. Månson, D. James, E. Gustavsson, and L.S.J.J.o.A.P.S. Svensson, *Conversion analysis of acrylated hyperbranched polymers UV-cured below their ultimate glass transition temperature.* 2007. **104**(4): p. 2366-2376.
62. Schmidt, L.E., Y. Leterrier, J.M. Vesin, M. Wilhelm, and J.A.E. Månson, *Photorheology of Fast UV-Curing Multifunctional Acrylates.* 2005. **290**(11): p. 1115-1124.
63. Yang, L., J. Yang, J. Nie, and X.J.R.A. Zhu, *Temperature controlled cationic photo-curing of a thick, dark composite.* 2017. **7**(7): p. 4046-4053.
64. Crivello, J.V.J.J.o.M.S., Part A: Pure and A. Chemistry, *Effect of temperature on the cationic photopolymerization of epoxides.* 2008. **45**(8): p. 591-598.
65. Schift, H. and L. Heyderman, *Nanorheology–squeeze flow in hot embossing of thin films.* Alternative Lithography–Unleashing the Potentials of Nanotechnologys, Kluwer Academic Publishers, London, 2004.
66. Seo, S.M., T.I. Kim, and H.L. Hong, *Simple fabrication of nanostructure by continuous rigiflex imprinting.* Microelectronic Engineering, 2007. **84**(4): p. 567-572.
67. Heyderman, L.J., H. Schift, C. David, J. Gobrecht, and T. Schweizer, *Flow behaviour of thin polymer films used for hot embossing lithography.* Microelectronic Engineering, 2000. **54**(3): p. 229-245.
68. Lee, H., *Effect of imprinting pressure on residual layer thickness in ultraviolet nanoimprint lithography Effect of imprinting pressure on residual layer thickness in ultraviolet nanoimprint lithography.* Journal of Vacuum Science & Technology B Microelectronics & Nanometer Structures Processing Measurement & Phenomena, 2005. **23**(3): p. 1102-1106.
69. Lee, H.J., H.W. Ro, C.L. Soles, R.L. Jones, E.K. Lin, W.L. Wu, and D.R. Hines, *Effect of initial resist thickness on residual layer thickness of nanoimprinted structures.* Journal of vacuum science & technology. B, Microelectronics and nanometer structures: processing, measurement, and phenomena: an official journal of the American Vacuum Society, 2005. **23**(6): p. 3023-3027.
70. Schmitt, H., L. Frey, H. Ryssel, M. Rommel, and C. Lehrer, *UV nanoimprint materials: Surface energies, residual layers, and imprint quality.* Journal of vacuum science & technology. B, Microelectronics and nanometer structures: processing, measurement, and phenomena: an official journal of the American Vacuum Society, 2007. **25**(25): p. 785-790.
71. Gomez-Constante, J.P., P.R. Pagilla, and K.R. Rajagopal. *Effect of the processing and transport parameters on mold filling in roll-to-roll nanoimprint lithography*. in *IWEB*. 2019. Stillwater, OK, US.
72. Kang, J.H., K.S. Kim, and K.W. Kim, *Molecular dynamics study of pattern transfer in nanoimprint lithography.* Tribology Letters, 2007. **25**(2): p. 93-102.
73. Taga, A., M. Yasuda, H. Kawata, and Y. Hirai, *Impact of molecular size on resist filling process in nanoimprint lithography: Molecular dynamics study.* Journal of vacuum science & technology. B, Microelectronics and nanometer structures: processing, measurement, and phenomena: an official journal of the American Vacuum Society, 2010. **28**(6): p. C6M68-C6M71.
74. Koyama, M., M. Shirai, H. Kawata, Y. Hirai, and M. Yasuda, *Computational study on UV curing characteristics in nanoimprint lithography: Stochastic simulation.* Japanese Journal of Applied Physics, 2017. **56**(6S1): p. 06GL03.
75. Jian, Y.H. and P.H. Zhao, *Computer Simulation on Intensity Distribution of UV Irradiation System.* Applied Mechanics & Materials, 2010. **34-35**: p. 591-594.
76. Qualls, R.G. and J.D. Johnson, *Bioassay and dose measurement in UV disinfection.* Appl Environ Microbiol, 1983. **45**(3): p. 872-877.
77. Ignasi, S.E., D.M. Hargreaves, and P. Gianluca Li, *Evaluation of the intrinsic photocatalytic oxidation kinetics of indoor air pollutants.* Environmental Science & Technology, 2007. **41**(6): p. 2028.
78. Puma, G.L.I., K. Jen Nee, and B. Alberto, *Modeling of an annular photocatalytic reactor for water purification: oxidation of pesticides.* Environmental Science & Technology, 2004. **38**(13): p. 3737-45.
79. Wang, Z., J. Liu, Y. Dai, W. Dong, S. Zhang, and J. Chen, *CFD modeling of a UV-LED photocatalytic odor abatement process in a continuous reactor.* Journal of Hazardous Materials, 2012. **215-216**(4): p. 25-31.
80. Wang, Z., J. Liu, Y. Dai, W. Dong, S. Zhang, and J. Chen, *Dimethyl Sulfide Photocatalytic*

Degradation in a Light-Emitting-Diode Continuous Reactor: Kinetic and Mechanistic Study. Industrial & Engineering Chemistry Research, 2011. **50**(13): p. 7977-7984.
81. Hirai, Y., *UV-nanoimprint lithography (NIL) process simulation.* Journal of Photopolymer Science and Technology, 2010. **23**(1): p. 25-32.
82. Kirchner, R., L. Nüske, A. Finn, B. Lu, and W.J. Fischer, *Stamp-and-repeat UV-imprinting of spin-coated films: Pre-exposure and imprint defects.* Microelectronic Engineering, 2012. **97**(3): p. 117-121.
83. Guo, Y., G. Liu, Y. Xiong, and Y. Tian, *Study of the demolding process—implications for thermal stress, adhesion and friction control.* Journal of Micromechanics and Microengineering, 2006. **17**(1): p. 9.
84. Hirai, Y., S. Yoshida, and N. Takagi, *Defect analysis in thermal nanoimprint lithography.* Journal of Vacuum Science & Technology B: Microelectronics and Nanometer Structures Processing, Measurement, and Phenomena, 2003. **21**(6): p. 2765-2770.
85. Song, Z., J. Choi, B.H. You, J. Lee, and S. Park, *Simulation study on stress and deformation of polymeric patterns during the demolding process in thermal imprint lithography.* Journal of Vacuum Science & Technology B: Microelectronics and Nanometer Structures Processing, Measurement, and Phenomena, 2008. **26**(2): p. 598-605.
86. Song, Z., B.H. You, J. Lee, and S. Park, *Study on demolding temperature in thermal imprint lithography via finite element analysis.* Microsystem technologies, 2008. **14**(9-11): p. 1593-1597.
87. Amirsadeghi, A., J.J. Lee, and S. Park, *A simulation study on the effect of cross-linking agent concentration for defect tolerant demolding in UV nanoimprint lithography.* Langmuir, 2012. **28**(31): p. 11546-11554.
88. Yeo, L., S. Joshi, Y. Lam, M.B. Chan-Park, and D. Hardt, *Numerical analyses of peel demolding for UV embossing of high aspect ratio micro-patterning.* Microsystem Technologies, 2009. **15**(4): p. 581-593.
89. Tochino, T., T. Shiotsu, K. Uemura, M. Yasuda, H. Kawata, and Y. Hirai, *Impact of resist shrinkage on the template release process in nanoimprint lithography.* Journal of Vacuum Science & Technology B, Nanotechnology and Microelectronics: Materials, Processing, Measurement, and Phenomena, 2014. **32**(6): p. 06FG08.
90. Chalvin, F., N. Nakamura, T. Tochino, M. Yasuda, H. Kawata, and Y. Hirai, *Impact of template stiffness during peeling release in nanoimprint lithography.* Journal of Vacuum Science & Technology B, 2016. **34**(6): p. 06K403.
91. Song, Z., J. Choi, B.H. You, and J. Lee, *Simulation study on stress and deformation of polymeric patterns during the demolding process in thermal imprint lithography.* Journal of Vacuum Science & Technology B Microelectronics & Nanometer Structures, 2008. **26**(2): p. 598-605.
92. Ye, X., Y. Ding, Y. Duan, H. Liu, and B. Lu, *Effects of exposure time on defects and demolding force in soft ultraviolet nanoimprint lithography.* Journal of Vacuum Science & Technology B, 2009. **27**(27): p. 2091-2096.
93. Shirai, M., K. Uemura, K. Shimomukai, T. Tochino, and Y. Hirai, *Effect of elastic modulus of UV cured resist on demolding force.* Journal of Vacuum Science & Technology B, 2016. **34**(6).
94. Jiang, W., Y. Ding, H. Liu, B. Lu, Y. Shi, J. Shao, and L. Yin, *Two-step curing method for demoulding in UV nanoimprint lithography.* Microelectronic Engineering, 2008. **85**(2): p. 458-464.
95. Liu, H., Y. Ding, W. Jiang, Q. Lian, L. Yin, Y. Shi, and B. Lu, *Novel imprint lithography process used in fabrication of micro/nanostructures in organic photovoltaic devices.* Journal of Micro/Nanolithography, MEMS, and MOEMS, 2009. **8**(2): p. 021170.
96. Liu, H., W. Jiang, Y. Ding, Y. Tang, B. Lu, H. Lan, Y. Shi, and L. Yin, *A novel loading and demoulding process control in UV nanoimprint lithography.* Microelectronic Engineering, 2009. **86**(1): p. 4-9.
97. Houle, F.A., C.T. Rettner, D.C. Miller, and R. Sooriyakumaran, *Antiadhesion considerations for UV nanoimprint lithography.* Applied Physics Letters, 2007. **90**(21): p. 4124-31.
98. Ahn, S.H. and L.J. Guo. *High-speed roll-to-roll nanoimprint lithography on flexible substrate and mold-separation analysis*. in *Advanced Fabrication Technologies for Micro/Nano Optics and Photonics II*. 2009. International Society for Optics and Photonics.
99. Good, J.K. and D.R. Roisum, *Winding: machines, mechanics and measurements*. 2008: DEStech Publications, INC.

100. Hertz, H.R., *Uber die Beruhrung fester elastischer Korper und Uber die Harte.* Verhandlung des Vereins zur Beforderung des GewerbefleiBes, Berlin, 1882: p. 449.
101. Radzimovsky, E.I., *Stress distribution and strength condition of two rolling cylinders pressed together.* 1953.
102. Bentall, R.H. and K.L. Johnson, *Slip in the rolling contact of two dissimilar elastic rollers.* International Journal of Mechanical Sciences, 1967. **9**(6): p. 389-404.
103. Bentall, R. and K. Johnson, *An elastic strip in plane rolling contact.* International Journal of Mechanical Sciences, 1968. **10**(8): p. 637-663.
104. Hahn, H.T. and M. Levinson, *Indentation of an elastic layer bonded to a rigid cylinder—II. Unidirectional slipping with Coulomb friction ☆.* International Journal of Mechanical Sciences, 1974. **16**(7): p. 503-514.
105. Hahn, H.T. and M. Levinson, *Indentation of an elastic layer(s) bonded to a rigid cylinder—I. Quasistatic case without friction ☆.* International Journal of Mechanical Sciences, 1974. **16**(7): p. 489-502.
106. Batra, R.C., *Rubber Covered Rolls---The Nonlinear Elastic Problem.* Journal of Applied Mechanics, 1980. **47**(1): p. 82-86.
107. Batra, R., *Quasistatic indentation of a rubber-covered roll by a rigid roll.* International Journal for Numerical Methods in Engineering, 1981. **17**(12): p. 1823-1833.
108. Soong, T.C. and C. Li, *The steady rolling contact of two elastic layer bonded cylinders with a sheet in the nip.* International Journal of Mechanical Sciences, 1981. **23**(5): p. 263-273.
109. Soong, T.C. and C. Li, *The Rolling Contact of Two Elastic-Layer-Covered Cylinders Driving a Loaded Sheet in the Nip.* Journal of Applied Mechanics, 1981. **48**(4): p. 889.
110. Rand, T. and L.G. Eriksson, *Physical properties of newsprint rolls during winding.* Tappi, 1973. **56**(6): p. 153-156.
111. Pfeiffer, J., *Nip forces and their effect on wound-in tension [Paper production]*. TAPPI, 1977.
112. Good, J., J. Hartwig, and R. Markum. *A Comparison of Center and Surface Winding Using the Wound-In-Tension Method*. in *Proceedings of the Fifth International Conference on Web Handling*. 1999.
113. Pfeiffer, J.D., *Mechanics of a rolling nip on paper webs.* Tappi, 1968. **51**(8): p. A77-&.
114. Good, J., *Predicting internal stresses in centerwound rolls with an undriven nip roller.* Tappi journal, 1991. **74**: p. 101-109.
115. Hakiel, Z., *Nonlinear model for wound roll stress.* Tappi journal, 1987. **70**(5): p. 113-117.
116. Good, J., Z. Wu, and M. Fikes, *The internal stresses in wound rolls with the presence of a nip roller.* Journal of applied mechanics, 1994. **61**(1): p. 182-185.
117. Steves, R.E., *Effect of Nip Load on Wound-on-tension in Surface Winding*. 1997, Oklahoma State University.
118. Good, J., B. Kandadai, and R. Markum, *A New Method for Measurement of Wound-In-Tension in Webs Wound into Rolls.* Journal of Pulp and Paper Science, 2009. **35**(1): p. 17-23.
119. Jiang, W., *Development of non-interfering wound-on-tension measurement method.* Dissertations & Theses - Gradworks, 2014.
120. Good, J.K. and Z. Wu, *The Mechanism of Nip-Induced Tension in Wound Rolls.* Asme Journal of Applied Mechanics, 1993. **60**(4): p. 942.
121. Jorkama, M., *Contact mechanical model for winding nip*. 2001: Helsinki University of Technology.
122. Jorkama, M. and R. von Hertzen, *The mechanism of nip-induced tension in winding.* Journal of pulp and paper science, 2002. **28**(8): p. 280-284.
123. Good, J.K., *Modelling nip induced tension in wound rolls.* Proceedings of the Sixth International Conference on Web Handling, 2001.
124. Ärölä, K. and R.V. Hertzen, *Development of sheet tension under a rolling nip on a paper stack.* International Journal of Mechanical Sciences, 2005. **47**(1): p. 110-133.
125. Arola, K. and R.v. Hertzen. *Strain-inducing mechanism of a rolling nip on a paper stack*. in *Proceedings of the Seventh International Conference on Web Handling*
2003.
126. Kandadai, B.K. and J.K. Good. *Modeling wound rolls using explicit FE methods*. in *Proceedings of the 9th International Conference on Web Handling*. 2007.
127. Kandadai, B.K. and J.K. Good. *Finite element analysis of winding nip mechanics*. in *Proceedings*

of the 10th International Conference on Web Handling. 2009.
128. Corcione, C.E., A. Greco, and A. Maffezzoli, *Time–temperature and time-irradiation intensity superposition for photopolymerization of an epoxy based resin.* Polymer, 2005. **46**(19): p. 8018-8027.
129. Schmidt, L.E., D. Schmäh, Y. Leterrier, and J.A.E. Månson, *Time-intensity transformation and internal stress in UV-curable hyperbranched acrylates.* Rheologica Acta, 2007. **46**(5): p. 693-701.
130. FA, H., A. Fornof, H. Trung, S. Raoux, R. Sooriyakumaran, H. Ito, and M. Hart, *Nanoimprint materials systems.* Journal of Photopolymer Science and Technology, 2008. **21**(4): p. 563-572.
131. Suzuki, R., N. Sakai, A. Sekiguchi, Y. Matsumoto, R. Tanaka, and Y. Hirai, *Evaluation of curing characteristics in UV-NIL resist.* Journal of Photopolymer Science and Technology, 2010. **23**(1): p. 51-54.
132. Tanabe, T., N. Fujii, M. Matsue, and H. Kawata, *Impact of exposure doses on demolding process in UV nanoimprint lithography.* Journal of Vacuum Science & Technology B Microelectronics & Nanometer Structures, 2010. **28**(6): p. 1239-1241.
133. Vacche, S.D., V. Geiser, Y. Leterrier, and J.A.E. Månson, *Time-intensity superposition for photoinitiated polymerization of fluorinated and hyperbranched acrylate nanocomposites.* Polymer, 2010. **51**(2): p. 334-341.
134. Emami, N., K.J. Söderholm, and L.A. Berglund, *Effect of light power density variations on bulk curing properties of dental composites.* Journal of Dentistry, 2003. **31**(3): p. 189-196.
135. Khan, S., I. Plitz, and R.J.R.a. Frantz, *In situ technique for monitoring the gelation of UV curable polymers.* 1992. **31**(2): p. 151-160.
136. Sang, S.L., A. Luciani, and J.A.E. Månson, *A rheological characterisation technique for fast UV-curable systems.* Progress in Organic Coatings, 2000. **38**(3): p. 193-197.
137. Claesson, H., E. Malmström, M. Johansson, A. Hult, M. Doyle, and J.A.E. Månson, *Rheological behaviour during UV-curing of a star-branched polyester.* Progress in Organic Coatings, 2002. **44**(1): p. 63-67.
138. Furukawa, T., F.A. Houle, D.L. Casher, and D.C. Miller. *Characterization of vinyl ether UV-cure nanoimprint resist*. in *Alternative Lithographic Technologies*. 2009. International Society for Optics and Photonics.
139. Suzuki, R., N. Sakai, T. Ohsaki, A. Sekiguchi, H. Kawata, and Y. Hirai, *Study on curing characteristic of UV nanoimprint resist.* Journal of Photopolymer Science and Technology, 2012. **25**(2): p. 211-216.
140. Payne, J.A., L.F. Francis, and A.V.J.J.o.a.p.s. McCormick, *The effects of processing variables on stress development in ultraviolet-cured coatings.* 1997. **66**(7): p. 1267-1277.
141. Odian, G., *Principles of polymerization*. 2004: John Wiley & Sons.
142. Maffezzoli, A. and R.J.T.A. Terzi, *Effect of irradiation intensity on the isothermal photopolymerization kinetics of acrylic resins for stereolithography.* 1998. **321**(1-2): p. 111-121.
143. Fujii, N., T. Tanabe, T. Hirasawa, H. Kawata, N. Sakai, and Y. Hirai, *Impact of De-molding Force on Exposure Dosage in UV-Nanoimprint Process.* Journal of Photopolymer Science and Technology, 2009. **22**(2): p. 181-184.
144. Nishino, T., R. Suzuki, H. Kawata, and Y. Hirai, *Dependence of de-molding force on process conditions in UV nanoimprint.* Journal of Photopolymer Science and Technology, 2011. **24**(1): p. 101-104.
145. Bryant, R. and W. Dukes, *The measurement of the shear strength of adhesive joints in torsion.* British Journal of Applied Physics, 1965. **16**(1): p. 101.
146. E229-97, A., *Standard test method for shear strength and shear modulus of structural adhesives*. www.astm.org.
147. Jojibabu, P., M. Jagannatham, P. Haridoss, G.J. Ram, A.P. Deshpande, and S.R. Bakshi, *Effect of different carbon nano-fillers on rheological properties and lap shear strength of epoxy adhesive joints.* Composites Part A: Applied Science and Manufacturing, 2016. **82**: p. 53-64.
148. D1002, A., *Standard test method for apparent shear strength of single-lap-joint adhesively bonded metal specimens by tension loading*. www.astm.org.
149. Czech, Z., J. Kabatc, A. Kowalczyk, D. Sowa, and E. Madejska, *Application of selected 2-methylbenzothiazoles AS cationic photoreactive crosslinkers for pressure-sensitive adhesives based on acrylics.* International Journal of Adhesion & Adhesives, 2015. **58**: p. 1-6.

150. De Gee, A., C. Davidson, and A. Smith, *A modified dilatometer for continuous recording of volumetric polymerization shrinkage of composite restorative materials.* Journal of Dentistry, 1981. **9**(1): p. 36-42.
151. De Boer, J., R. Visser, and G. Melis, *Time-resolved determination of volume shrinkage and refractive index change of thin polymer films during photopolymerization.* Polymer, 1992. **33**(6): p. 1123-1126.
152. Geiser, V., Y. Leterrier, and J.A.E. Månson, *Conversion and shrinkage analysis of acrylated hyperbranched polymer nanocomposites.* Journal of Applied Polymer Science, 2010. **114**(3): p. 1954-1963.
153. Park, J.W., G.S. Shim, J.G. Lee, S.W. Jang, H.J. Kim, and J.N. Choi, *Evaluation of UV Curing Properties of Mixture Systems with Differently Sized Monomers.* Materials, 2018. **11**(4): p. 509.
154. Vallin, Ö., K. Jonsson, and U. Lindberg, *Adhesion quantification methods for wafer bonding.* Materials Science and Engineering: R: Reports, 2005. **50**(4-5): p. 109-165.
155. Lacombe, R., *Adhesion measurement methods: theory and practice*. 2005: CRC Press.
156. Mittal, K., *Adhesion measurement of films and coatings: a commentary.* Adhesion measurement of films and coatings, 1995. **1**.
157. Evans, A., M. Rühle, B. Dalgleish, and P. Charalambides, *The fracture energy of bimaterial interfaces.* Metallurgical Transactions A, 1990. **21**(9): p. 2419-2429.
158. Taniguchi, J., T. Kawasaki, Y. Tokano, Y. Kogo, I. Miyamoto, M. Komuro, H. Hiroshima, N. Sakai, and K. Tada, *Measurement of adhesive force between mold and photocurable resin in imprint technology.* Japanese journal of applied physics, 2002. **41**(6S): p. 4194.
159. Hiroshima, H., *Release force reduction in UV nanoimprint by mold orientation control and by gas environment.* Journal of Vacuum Science & Technology B: Microelectronics and Nanometer Structures Processing, Measurement, and Phenomena, 2009. **27**(6): p. 2862-2865.
160. Hong, L., W. Xia, Z. Li, X. Jiang, Q. Wang, and Y. Jie, *Photoreversible Resists for UV Nanoimprint Lithography (UV-NIL).* Acs Applied Materials & Interfaces, 2010. **2**(7): p. 2076-2082.
161. Lai, Y.-H. and D.A. Dillard, *A study of the fracture efficiency parameter of blister tests for films and coatings.* Journal of adhesion science and technology, 1994. **8**(6): p. 663-678.
162. Yeo, L., Y. Yan, Y. Lam, and M.B. Chan-Park, *Design of experiment for optimization of plasma-polymerized octafluorocyclobutane coating on very high aspect ratio silicon molds.* Langmuir, 2006. **22**(24): p. 10196-10203.
163. Chen, C.-f. and K. Wharton, *Characterization and failure mode analyses of air plasma oxidized PDMS–PDMS bonding by peel testing.* RSC advances, 2017. **7**(3): p. 1286-1289.
164. Jambhapuram, M., *Viscoelastic pheomena in Roll-to-Roll manufacturing.* Thesis of Oklahoma state university, 2020.
165. Kawashita, L., D. Moore, and J.G. Williams, *Protocols for the measurement of adhesive fracture toughness by peel tests.* The Journal of Adhesion, 2006. **82**(10): p. 973-995.
166. Genesky, G.D. and C. Cohen, *Toughness and fracture energy of PDMS bimodal and trimodal networks with widely separated precursor molar masses.* Polymer, 2010. **51**(18): p. 4152-4159.
167. Lake, G. and A. Thomas, *The strength of highly elastic materials.* Proceedings of the Royal Society of London. Series A. Mathematical and Physical Sciences, 1967. **300**(1460): p. 108-119.
168. Griffith, A.A., *VI. The phenomena of rupture and flow in solids.* Philosophical transactions of the royal society of london. Series A, containing papers of a mathematical or physical character, 1921. **221**(582-593): p. 163-198.
169. Sih, G.C., *Mechanics of fracture initiation and propagation: surface and volume energy density applied as failure criterion*. Vol. 11. 2012: Springer Science & Business Media.
170. Orowan, E., *Energy criteria of fracture*. 1954, Massachusetts Inst of Tech Cambridge Dept of Mechanical Engineering.
171. Good, J.K. *Modeling Rubber Covered Rollers in Web Lines*. in *Proceedings of the Sixth International Conference on Web Handling* 2001. Web Handling Research Center, Stillwater, Oklahoma
172. Johnson, K.L., *Contact mechanics.* Journal of Tribology, 1985. **108**(4): p. 464.
173. Chen, X., M. Jamhapuram, R. Markum, S. Qi, D. Lucca, and J. Good, *Challenges for Scaling UV NIL to Production Speeds using Roll-to-Roll Manufacturing1.* International conference on Nanoimprint and nanoprint Technologies 2019.
174. Blackman, B., H. Hadavinia, A.J. Kinloch, and J. Williams, *The use of a cohesive zone model to*

study the fracture of fibre composites and adhesively-bonded joints. International journal of fracture, 2003. **119**(1): p. 25-46.
175. Amirsadeghi, A., J.J. Lee, and S. Park, *Surface adhesion and demolding force dependence on resist composition in ultraviolet nanoimprint lithography.* Applied surface science, 2011. **258**(3): p. 1272-1278.
176. Amirsadeghi, A., J.J. Lee, and S. Park, *Polymerization shrinkage stress measurement for a UV-curable resist in nanoimprint lithography.* Journal of Micromechanics and Microengineering, 2011. **21**(11): p. 115013.
177. Shibata, M., A. Horiba, Y. Nagaoka, H. Kawata, M. Yasuda, and Y. Hirai, *Process-simulation system for UV-nanoimprint lithography.* Journal of Vacuum Science & Technology B, Nanotechnology and Microelectronics: Materials, Processing, Measurement, and Phenomena, 2010. **28**(6): p. C6M108-C6M113.
178. Hudson, A., S. Martin, M. Hubert, and J. Spelt, *Optical measurements of shrinkage in UV-cured adhesives.* J. Electron. Packag., 2002. **124**(4): p. 352-354.
179. Kawaguchi, Y., F. Nonaka, and Y. Sanada, *Fluorinated materials for UV nanoimprint lithography.* Microelectronic Engineering, 2007. **84**(5-8): p. 973-976.
180. *Nanoimprint lithography: Emergent materials and methods ofactuationLewis.* 2019.
181. Afhea, J.A., *A study of nanotextured surface production for bactericidal surfaces on orthopaedic implants using the hydrothermal method*. 2019, Queensland University of Technology.
182. Yoshikawa, H., J. Taniguchi, G. Tazaki, and T. Zento, *Fabrication of high-aspect-ratio pattern via high throughput roll-to-roll ultraviolet nanoimprint lithography.* Microelectronic Engineering, 2013. **112**: p. 273-277.
183. Ron Markum, J.K.G., *Process and UV-NIL R2R Machnie Development.* NSF report, 2020.
184. Good, J.K., Guo, L. J, Pagilla, P.R. and Lucca, D. A., *Roll-to-roll nanoimpirnting to scale manufacturing of metasurfaces for photonics and optoelectronics* National science foundation, 2020. **year 4 progress report**(NSF award 4635636).

VITA

Xin Chen

Candidate for the Degree of

Doctor of Philosophy

Dissertation: Simulation Study on Nip Contact Mechanics and Mold Extraction for Predicting Defects in Roll-to-Roll UV Nanoimprint Lithography

Major Field: Mechanical Engineering

Biographical:

Education:

Completed the requirements for the Doctor of Philosophy in Mechanical Engineering at Oklahoma State University, Stillwater, Oklahoma in December, 2020.

Completed the requirements for the Master of Science in Mechanical Engineering at Northeastern University, Shenyang, China in 2017.

Completed the requirements for the Bachelor of Science in Mechanical Engineering at Wuhan University of Technology, Wuhan, China in 2013.